THESIS FOR THE DEGREE OF DOCTOR OF PHILOSOPHY

Extending Transient Plane Source-Based Measurements for Accurate Determination of Thermal Properties

ZIJIN ZENG

Department of Chemistry and Chemical Engineering

CHALMERS UNIVERSITY OF TECHNOLOGY

Gothenburg, Sweden 2025

Extending Transient Plane Source-Based Measurements for Accurate Determination of Thermal Properties

ZIJIN ZENG
ISBN 978-91-8103-327-4

Doktorsavhandlingar vid Chalmers tekniska högskola
Ny serie nr 5784
ISSN 0346-718X
https://doi.org/10.63959/chalmers.dt/5784

Department of Chemistry and Chemical Engineering
Chalmers University of Technology
SE-412 96 Gothenburg
Sweden
Telephone + 46 (0)31-772 1000

Cover:
A graph displays the temperature response of the probe over time in a typical Transient Plane Source measurement, set against a background of meshes — a key component in numerical simulations using the finite-element method. The three pencil sketches represent the TPS probes for layer measurements and the setup for heat capacity measurement, respectively.

Chalmers Digitaltryck
Gothenburg, Sweden 2025

This project has received funding from the European Union's Horizon 2020 research and innovation programme under grant agreement No 955837

Extending Transient Plane Source-Based Measurements for Accurate Determination of Thermal Properties

Zijin Zeng

Department of Chemistry and Chemical Engineering
Chalmers University of Technology

ABSTRACT

The Transient Plane Source (TPS) method is a widely used technique for measuring the thermal properties of isotropic materials, including the thermal conductivity, the thermal diffusivity, and the specific heat capacity. To accommodate various sample geometries and samples with directional properties, several variants of the TPS method have been developed.

One variant was designed to characterize micrometre-thick layers with a low thermal conductivity ($< 2\ \mathrm{W/(m \cdot K)}$), which involves sandwiching the layer between the TPS probe and backing substrates. By assuming one-dimensional (1D) heat flux across the layer after a certain period, its thermal conductivity can be estimated by incorporating Fourier's law in the calculation. However, thermal contact resistance impedes heat conduction and leads to significant errors. This thesis shows that introducing a liquid interface material, e.g., deionized water, effectively reduces R_c and enables arcuate thermal conductivity determination (errors < 4 %) from measurements of layers with different thicknesses.

Once the layer has either a higher thermal conductivity ($> 2\ \mathrm{W/(m \cdot K)}$) or a greater thickness (> 600 μm), the measured thermal conductivity tends to be significantly overestimated, as the heat flux across the layer can no longer be assumed to be 1D. To overcome this limitation, the Layer 2D model, which accounts for 2D heat flux within the layer, was proposed. This model extends the measurable range of thermal conductivity by an order of magnitude (up to $20\ \mathrm{W/(m \cdot K)}$) and thickness by about three times (up to 2000 μm), while maintaining errors below 10 %.

Another TPS variant was developed that allows to directly characterize the specific heat capacity. In this approach, the sample is placed in a holder that is attached to the TPS probe. Although the sample-holder assembly is surrounded by thermal insulation, the influence of heat loss increases over time and eventually introduces substantial errors, particularly for low thermal conductivity samples. To address this issue, a novel data analysis method assisted by finite element simulations was proposed, which allows for precise estimation of heat loss and thus accurate determination of the heat capacity (error < 4 %).

Overall, this study offers critical insights that significantly extend the applicability of TPS measurements, thereby contributing to the advancement of thermal property characterization.

Keywords: Transient Plane Source method, thermal conductivity, finite element simulation, specific heat capacity, data analysis, polymer.

PUBLICATIONS

This thesis consists of an extended summary of the following appended papers:

Paper I **Liquid Interface for Accurate Intrinsic Thermal Conductivity Measurements of Polymer Films Using the Transient Plane Source Method**
Zijin Zeng, Przemyslaw Sowinski, Christian Müller, and Besira Mihiretie
Journal of Thermal Science and Engineering Applications, ***2025****, 17(11), 111008*
https://doi.org/10.1115/1.4069207

Paper II **Extending the Transient Plane Source Scanning Method for Determining the Specific Heat Capacity of Low Thermal Conductivity Materials through a Numerical Study**
Zijin Zeng, Christian Müller, and Besira Mihiretie
Thermochimica Acta, **2024**, 742, 179883
https://doi.org/10.1016/j.tca.2024.179883

Paper III **Poly (benzodifurandione) Coated Silk Yarn for Thermoelectric Textiles**
Mariavittoria Craighero, Qifan Li, Zijin Zeng, Chunghyeon Choi, Youngseok Kim, Hyungsub Yoon, Tiefeng Liu, Przemyslaw Sowinski, Shuichi Haraguchi, Byungil Hwang, Besira Mihiretie, Simone Fabiano, and Christian Müller
Advanced Science, ***2024****, 11(38), 2406770*
https://doi.org/10.1002/advs.202406770

Paper IV **Improved Transient Plane Source Measurements of Layer–Substrate Structures via a Semi-Analytical Temperature Response Model**
Zijin Zeng, Johan Gustavsson, Christian Müller, and Besira Mihiretie
Manuscript in preparation

Paper V **Prediction of the thermal conductivity of polypropylenes and propylene copolymers based on crystallinity or elastic modulus**
Przemyslaw Sowinski, Zijin Zeng, Ewa Piorkowska-Galeska, Besira Mihiretie, Mathis Brette Mortensen, Ergang Wang, and Christian Müller
Manuscript in preparation

CONTRIBUTION REPORT

Paper I — Main author. B.M. and C.M. conceptualized the study. Z.Z. performed all the measurements and corresponding simulations, visualized the data, and wrote the original draft. P.S. provided support in the analysis of DSC data. Z.Z., B.M. and C.M. reviewed and edited the original draft. C.M. and B.M. supervised the overall study.

Paper II — Main author. Z.Z. conceptualized the study with the help of B.M., performed all the measurements and simulations, visualized the data, and wrote the original draft. C.M. and B.M. supervised the overall study.

Paper III — Co-author. M.C., Q.L. and C.M. conceptualized the study. M.C., Q.L., Y.K. prepared samples and performed characterization. Z.Z. carried out the device-level numerical simulations and wrote the related content in the manuscript, M.C., C.M., Q.L., and S.F. wrote the manuscript.

Paper IV — Main author. Z.Z. conceptualized the study with the help of B.M.. Z.Z. performed all the measurements and simulations, visualized the data, and wrote the original draft. J.G. took charge of the new sensor fabrication. Z.Z. wrote the original draft and revised it together with B.M. and C.M.. C.M. and B.M. supervised the overall study.

Paper V — Co-author. P.S., C.M., design and conceptualized the study, P.S., Z.Z. performed the measurements, B.M., E.W. performed molecular-weight determination, Z.Z. carried out uncertainty analysis in TPS measurements and wrote the related content in the manuscript, under the supervision of B.M., P.S., C.M. visualized the data, and wrote the original draft, C.M. supervised the overall study, All authors: read and commented on the manuscript.

TABLE OF CONTENT

1. Introduction

1.1 Heat conduction

1.1.1 Thermal properties and heat equations

Heat transfer is the exchange of thermal energy driven by temperature gradients. It is a ubiquitous phenomenon throughout the universe spanning an extraordinary range of scales — from tiny atoms to enormous galaxies. Furthermore, heat transfer plays a vital role in various industries, including energy, electronics, aerospace, and manufacturing. A comprehensive understanding of heat transfer improves device performance and reduces energy consumption, paving the way for a more sustainable future.

There are three mechanisms in heat transfer [1]: conduction, convection, and radiation. Heat conduction is the process by which thermal energy is transmitted through a material without any macroscopic movement of the substance itself. Conversely, convection refers to heat transfer through relative motion of portions of the heated body. Radiation is in turn the process by which heat is transferred directly between distant portions of the body by electromagnetic radiation.

In heat conduction, there is a linear relationship between the temperature gradient (∇T, in $\mathrm{K/m}$) and the heat flux (q, in $\mathrm{W/m^2}$). This relationship is called Fourier's law and expressed as follows [1]:

$$q = -\lambda \nabla T \tag{1.1}$$

where the minus sign indicates the direction of heat flow from regions of high to regions of low temperatures, the constant of proportionality λ is thermal conductivity, a material property measured in $\mathrm{W/(m \cdot K)}$.

At the macroscopic scale, thermal conductivity can be expressed as the product of density (ρ), specific heat capacity (C_p) and thermal diffusivity (α) [1]:

$$\lambda = \alpha \rho C_p \tag{1.2}$$

where α (in $\mathrm{mm^2/s}$) quantifies the rate at which temperature diffuses through a material. Considering energy conservation in an isotropic element, the following heat equation in a three-dimensional (3D) Cartesian coordinate system can be used to describe heat conduction [1]:

$$\rho C_p \frac{\partial T}{\partial t} + \nabla q = Q \tag{1.3}$$

where $T(x, y, z, t)$ represents the temperature at a position (x, y, z) and time t, and Q (in $\mathrm{W/m^3}$) is the power generated per unit volume.

1.1.2 Heat conduction in polymers

In solids, heat conduction is generally considered to arise from lattice vibrations and electron migration at the microscopic scale. Therefore, the thermal conductivity is normally expressed as the sum of the contributions from phonons (λ_{ph}) and electrons (λ_e) [2]:

$$\lambda = \lambda_{ph} + \lambda_e \tag{1.4}$$

Based on the kinetic theory of gases and its extension, λ_{ph} can be further expressed as [3, 4]:

$$\lambda_{ph} = \frac{1}{3} \rho C_p v l \tag{1.5}$$

where v denotes the average phonon velocity, and l is the phonon mean free path.

In metals and highly doped semiconductors, λ_e is considered to be proportional to the electrical conductivity (σ) based on the prediction of the Wiedemann–Franz law [5]:

$$\lambda_e = \dot{L} \sigma T \tag{1.6}$$

where $\dot{L}$ is the Lorenz number, and T is the absolute temperature.

In insulating polymers, heat transport is dominated by λ_{ph}. However, λ_{ph} of polymers is generally isotropic and small, typically 0.1 - 0.5 $\mathrm{W/(m \cdot K)}$, due to structural disorder and weak inter-chain coupling [6-8]. In highly doped conjugated polymers with high conductivity, the contribution of λ_e becomes significant and can be described by Eq 1.6 [5]. On the other hand, when an oriented structure is introduced, for example through mechanical processing [9-11] or advanced deposition techniques [12, 13], the thermal conductivity of polymers can become anisotropic and significantly higher.

1.2 Techniques for measuring thermal properties

Accurate determination of thermal properties is essential for both scientific research and engineering. For instance, reliable information about the thermal conductivity enables accurate correlation between material microstructure and its performance, thereby advancing the development in material design [11, 14, 15]. In engineering, accurate thermal conductivity values are a prerequisite for reliable thermal simulations [16-18]. Even minor inaccuracies in thermal conductivity can lead to significant errors in temperature predictions [17], potentially resulting in design failures and substantial economic losses.

1.2.1 Measuring thermal conductivity and/or thermal diffusivity

Numerous well-established techniques are available to measure the thermal conductivity, thermal diffusivity, or both, in bulk materials and thin layers [19, 20]. Based on the time dependence of the thermal response to be measured, these techniques can be broadly classified as steady-state or transient methods.

Steady-state methods measure a time independent temperature response. The Guarded Hot Plate (GHP) [21] and Heat Flow Meter (HFM) [22] are two commercialized and widely used examples. These two methods measure the heat flux across a thick slab sample and the resulting time difference. Subsequently, the thermal conductivity can be calculated directly using Fourier's law. Steady-state methods are straightforward but have two main limitations: (1) they require long measurement times

to achieve a time-independent state, and (2) they cannot be used to measure thermal diffusivity or heat capacity.

Transient methods offer faster measurements but involve greater complexity. These methods can be further categorized into two types: contact and contactless methods, depending on whether the sensing element is in physical contact with the specimen. Transient contactless methods, primarily based on optical techniques, include time-domain thermoreflectance (TDTR) [23, 24], frequency-domain thermoreflectance (FDTR) [25, 26] and laser flash analysis (LFA) [27]. A major advantage of these methods, especially thermoreflectance, is the disregard of thermal contact resistance (R_c) between the specimen and the sensing element, enabling the characterization of nanometer- to micrometer-thick films. However, these methods often require depositing a transducer layer (e.g., gold [28, 29], aluminum [15, 30], graphite [31]) on the sample surface. The transducer facilitates the conversion between optical and thermal energy, which however tends to increase both the time and complexity of the measurement process.

Transient contact methods comprise the 3w method [32], the temperature wave analysis (TWA) method [33], and the transient plane source (TPS) method [34]. The 3w method is a frequency-dependent method employing a metal sensor deposited on the sample surface. This method allows for the measurement of the thermal conductivity of submicrometer-thick films, which are thin compared to other contact methods [35]. TWA, another frequency-dependent method, is utilized to measure cross-plane thermal diffusivity of micrometer-thick films. The determination of thermal conductivity is achieved by multiplying the measured thermal diffusivity by a given volumetric heat capacity [36]. The TPS method in turn is a time-dependent technique offering versatile and nondestructive testing. For isotropic bulk samples, the TPS method can simultaneously determine thermal conductivity and diffusivity, which can be used to determine volumetric heat capacity. For uniaxial anisotropic bulk samples ($\lambda_x = \lambda_y \neq \lambda_z$), the TPS method can determine λ_x and λ_z provided volumetric heat capacity is known [34].

1.2.2 Measuring heat capacity

There are several methods available for measuring heat capacity, including drop calorimetry [37, 38], Differential Scanning Calorimetry (DSC) [37], TPS-based methods [34, 39], TDTR [24, 40, 41] and FDTR [40, 42]. Drop calorimetry determines the heat capacity by dropping a heated specimen of known temperature into a coolant and measuring the resulting temperature change. This is a rapid and straightforward technique yet requires careful management of heat loss. DSC obtains heat capacity and other thermal properties by measuring the heat flow associated with the average temperature change of a sample. It requires a small sample volume, typically 40 – 100 µl [43], so that a uniform temperature within the sample can be easily achieved [44, 45]. Through slight modifications, TDTR [24, 40, 41] and FDTR [40, 42] as optical methods can also be utilized to measure heat capacity of bulk and thin films.

In contrast to DSC, the TPS method requires relatively large samples. From a single measurement, the thermal conductivity and thermal diffusivity can be determined simultaneously, thereby enabling the indirect estimation of volumetric heat capacity using Eq. 1.2. However, this method is limited to isotropic and homogenous samples. To enable the measurement of anisotropic and/or inhomogeneous samples, the TPS method has been extended to the Transient Plane Source Scanning (TPSS) method [39], which is explained in detail in Section 1.3.4 of this thesis.

1.3 The TPS methods and its variants

1.3.1 Measurement setup and theory

In TPS measurements, a probe consisting of a metal foil covered by insulation sheets is utilized (Fig. 1.1 a). The metal foil serves as the sensing element, typically made of a pure nickel spiral, although alternatives include spirals made of molybdenum [46], a nickel–polymer composite [47] for printable sensors, and platinum for low-temperature measurements [48]. The insulation sheets, most commonly polyimide (Kapton), provide both electrical insulation and mechanical support for the spiral.

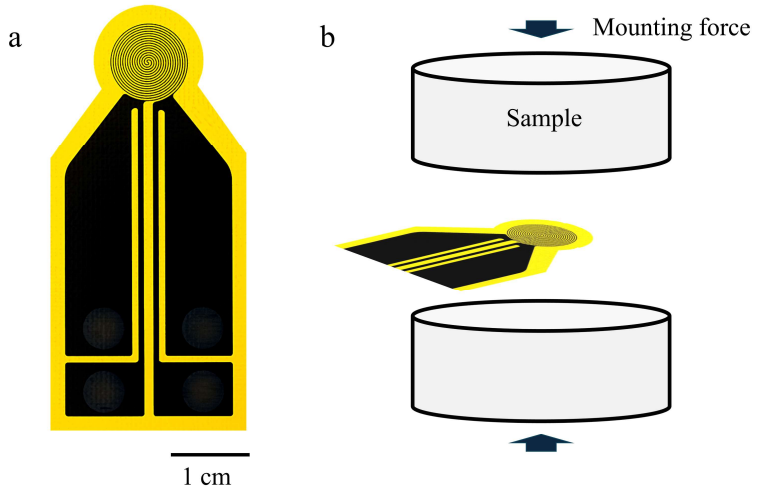

Figure 1.1. (a) Profile of a TPS sensor encapsulated in insulation layers of polyimide, with the sensing (upper) part featuring a spiral. (b) Schematic of a standard TPS measurement of bulk samples.

For the measurement of bulk materials, the TPS probe is sandwiched between two samples with identical properties (Fig. 1.1 b). A mounting force is applied to enhance the physical contact within the sample–probe assembly. During a measurement, the metal spiral performs two functions simultaneously: (1) it heats up the surrounding material with a constant power, and (2) it functions as a thermometer, detecting the resulting temperature response ($\Delta T(t)$, Fig. 1.2 a) through the resistance of the sensor ($R(t)$). Assuming a small temperature perturbation, a linear approximation can be applied to relate $\Delta T(t)$ and $R(t)$ [34]:

$$R(t) = R_0[1 + a \cdot \Delta T(t)] \tag{1.7}$$

where R_0 is the initial resistance of the nickel spiral and a represents the temperature coefficient of resistance of the spiral.

In general, the temperature response can be regarded as consisting of two components [34]:

$$\Delta T(t) = \Delta T_s(t) + \Delta T_a(t) \tag{1.8}$$

where $\Delta T_s(t)$ denotes the temperature increase of the sample surface in immediate contact with the probe, and $\Delta T_a(t)$ represents an additional temperature difference

caused by the thermal resistance between the sample and the probe. In case of bulk measurements, $\Delta T_a(t)$ typically reaches a constant value shortly after the measurement begins.

By assuming (1) that the spiral can be approximated as a series of concentric, equally spaced circular line sources, and (2) that the heat wave generated by the probe does not reach the sample boundary so that the sample can be assumed as "semi-infinite", the thermal properties can be related to the temperature response at the sample surface [34]:

$$\Delta T_s(\tau) = P(\pi^{3/2} r\lambda)^{-1} D(\tau) \quad and \quad \tau = \left(\frac{t-t_c}{\theta}\right)^{1/2}, \quad \theta = \frac{r^2}{\alpha} \tag{1.9}$$

where P is the heating power supplied by the sensor, r is the radius of the sensor, t_c denotes the time correction factor compensating for hardware and software delays, and $D(\tau)$ is a dimensionless time function. For isotropic bulk samples, the general form of $D(\tau)$ can be expressed as [34]:

$$D(\tau) = [m(m+1)]^{-2} \int_0^{\tau} \sigma^{-2} \left[\sum_{n=1}^{m} n \sum_{k=1}^{m} k \exp\left(\frac{-(n^2+k^2)}{4m^2\sigma^2}\right) I_0\left(\frac{nk}{2m^2\sigma^2}\right)\right] \mathrm{d}\sigma \tag{1.10}$$

where m denotes the number of concentric ring sources, σ is an integration variable related to dimensionless time, and I_0 is the first kind modified Bessel function of the zeroth order.

To determine the thermal properties, a least-squares iterative process is employed to fit the measured $\Delta T(t)$ with respect to α and t_c. The optimal results of α and t_c are those that produce a linear relationship between $D(\tau)$ and $\Delta T(t)$, as illustrated in Fig. 1.2 b. Subsequently, the thermal conductivity can be calculated from the slope of this line according to Eq. 1.9. Optionally, the volumetric heat capacity can be calculated from the ratio between thermal conductivity to thermal diffusivity.

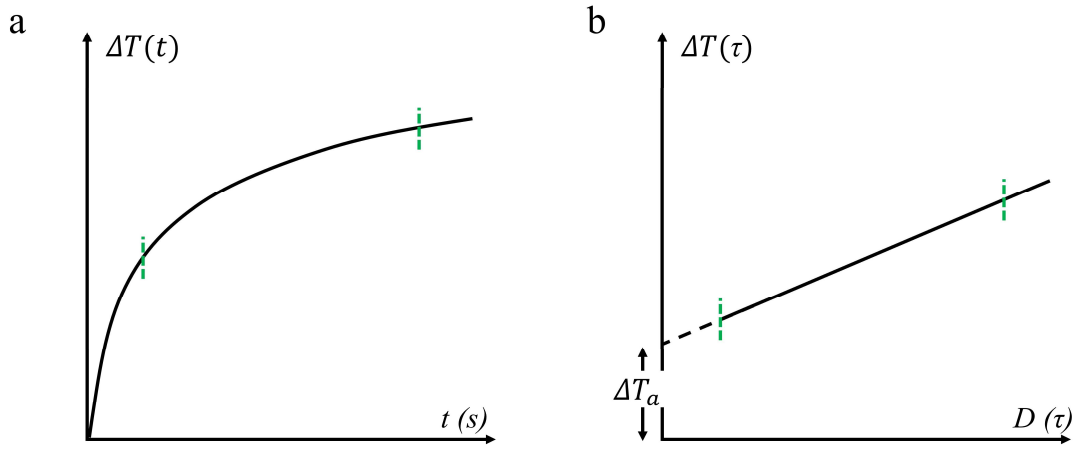

Figure 1.2. A typical temperature increase of the sensor versus (a) time and (b) dimensionless time during a TPS measurement. The data between two green dashed lines are used in the iterative process to determine the thermal properties.

Over the past two decades, the TPS method has evolved into several variants to accommodate diverse measurement requirements and different sample geometries. For example, its algorithm has been modified to allow the characterization of samples with various shapes, including rods [49], slabs [50, 51], and thin layers [52, 53]. In addition, the probe design and measurement procedure has been upgraded to enable direct measurements of the specific heat capacity, namely the Transient Plane Source Canning (TPSS) method [39]. This thesis focuses on TPS measurements on thin layers and TPSS measurements, two widely adopted methods with significant potential for further improvement. The principles and limitations of these methods are presented in Section 1.3.3 and Section 1.3.4, with corresponding solutions discussed in Sections 3 and 4, respectively.

1.3.2 Key concepts

Before delving into the detailed measurement procedures and theory, several key concepts are explained and defined in this subsection.

Probing depth

The probing depth represents the distance of a heat wave has travelled within the sample, which can be given by [34]:

$$\Delta p(t) = k\sqrt{\alpha t} \tag{1.11}$$

where k is a constant dependent on the sensitivity of the temperature recordings. A typical value of k in the TPS measurement is $k = 2$ [54].

To ensure the validity of the semi-infinite assumption and the applicability of Eq. 1.9, $\Delta p(t_{\max})$ must be smaller than the shortest distance between the probe and any sample boundary, i.e., the available probing depth (Δp_{avail}). Here, $t_{\max}$ denotes the final time point of the recorded data used in the fitting process.

Thermal contact resistance

Thermal contact resistance (R_c) is caused by imperfect contact between different components [55, 56]. The presence of R_c can significantly impede the conduction of heat during thermal conductivity measurements and might lead to inaccurate results. In case of measurements of bulk samples, R_c leads to a positive constant offset of $\Delta T(t)$ compared to the ideal case without thermal contact resistance. In such cases, the influence of R_c can be mitigated by excluding the initial data points from the fitting process. In case of measurements of thin layers, however, the influence of R_c is intertwined with the thermal properties of sample. This complication and a simple resolution will be discussed in Section 1.3.3 and Section 3, respectively.

Sensitivity

Sensitivity refers to the ratio between the change of the output with regard to the corresponding change in an input parameter [57, 58]. In TPS measurements, the sensitivity of $\Delta T(t)$ to a parameter x can be defined as [59, 60]:

$$S_x(t) = \frac{\partial \ln(\Delta T(t))}{\partial \ln(x)} \approx \frac{x\,\delta(\Delta T(t))}{\Delta T(t)\,\delta(x)} \tag{1.12}$$

where δ presents a small perturbation.

Sensitivity analysis can be used to evaluate whether a parameter can be reliably extracted from a measurement. Comparing the sensitivities with regard to different parameters further reveals potential mutual correlation. When multiple parameters, e.g., λ and α in bulk measurements, exhibit sufficiently high sensitivities and low correlation, they can be determined accurately and simultaneously.

Time window

The time window is defined as the data segment $[t_{\min}, t_{\max}]$ utilized in the fitting process. In a measurement of bulk samples, there are specific criteria for $t_{\min}$ and $t_{\max}$ respectively:

(1) $t_{\min}$ should be sufficiently large, typically on the order of 10 – 100 ms [34, 54], to mitigate the influence of thermal contact resistance at the beginning of the measurement;

(2) $t_{\max}$ should satisfy the dimensionless criterion $0.3 < t_{\max}\,\alpha/r^2 < 1.0$ to ensure a reliable simultaneous determination of λ and α [34]. This condition can also be expressed in terms of probing depth as $1.1\,r < \Delta p(t_{\max}) < 2.0\,r$. Considering that $\Delta p(t_{\max})$ must also be smaller than Δp_{avail}, the condition is further refined to $1.1\,r < \Delta p(t_{\max}) < \min\{2.0\,r, \Delta p_{\text{avail}}\}$.

Below is an example illustrating the fitting results against the selection of the time window (Fig. 1.3). In this case, the sample is an isotropic polymer with a Δp_{avail} of 4 mm, and the probe utilized has a radius of 3.2 mm (see details in Paper V). Within the data range satisfying $1.1\,r < \Delta p(t_{\max}) < \Delta p_{\text{avail}}$, the fitting results show good variance of 1.6 %, even though different measurement parameters were employed. These results show that the selection of time window plays a vital role for the fitting process and should be carefully considered.

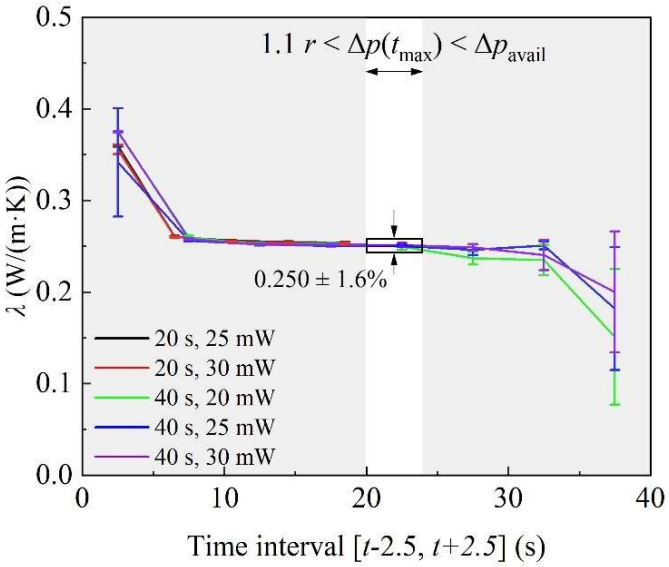

Fig. 1.3 Thermal conductivity obtained for different measurement parameters and time windows. *Unpublished data in Paper V.*

1.3.3 TPS measurements on thin layers

This type of TPS measurement requires a sample layer to be positioned between the probe and a bulk material of relatively high thermal conductivity (Fig. 1.4 b). A specialized probe with a wide nickel spiral (Fig. 1.4 a) is utilized to approximate an ideal circular heat source. Under these conditions, the dimensionless time function $D(\tau)$ reduces to [58, 61]:

$$D_{\mathrm{o}}(\tau) = \int_0^{\tau} \mathrm{d}\sigma\sigma^{-2} \int_0^1 v\,\mathrm{d}v \int_0^1 u\,\mathrm{d}u \cdot \exp\left(-\frac{u^2+v^2}{4\sigma^2}\right) I_0\left(\frac{uv}{2\sigma^2}\right) \qquad (1.13)$$

where variable v and u represent normalized radial coordinates.

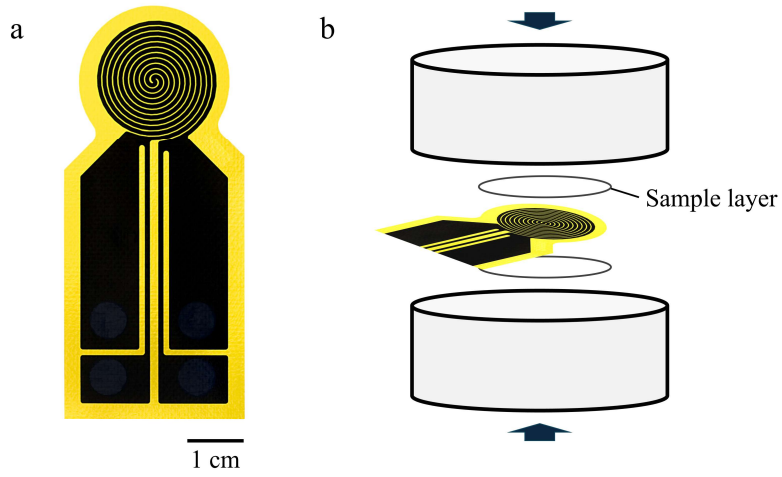

Fig. 1.4 (a) Profile of a specially designed TPS sensor used for characterization of thin layers. (b) Schematic of a TPS measurement for sample layers.

For a layer with a low thermal conductivity (λ_l) and a small thickness (L) compared to the sensor radius, one-dimensional heat flow between the probe and the bulk material is assumed. Under this assumption, the total thermal resistance between them can be estimated using the following equation [34]:

$$R_{tot} = \frac{2\pi r^2 \Delta T_a}{P} \tag{1.14}$$

In this case, the total thermal resistance consists of the sum of the thermal resistance caused by the layer ($R_l = L/\lambda_l$) and thermal contact resistance:

$$R_{tot,l} = R_l + R_{c,p-l} + R_k + R_{c,l-b} \tag{1.15}$$

where R_k is the thermal resistance caused by the Kapton insulation sheet, $R_{c,p-l}$ is the thermal contact resistance between the probe and the layer, and $R_{c,l-b}$ represents the thermal contact resistance between the layer and the backing bulk material.

In a measurement without a layer between the probe and the bulk materials (similar to Fig. 1.1 b), the following expression can be written in a similar way:

$$R_{tot,b} = R_k + R_{c,p-b} \tag{1.16}$$

By comparing $R_{tot,l}$ and $R_{tot,b}$, it is possible to estimate the apparent thermal conductivity of the sample layer ($\lambda_{l,a}$), which includes the influence of thermal contact resistance:

$$R_{tot,l} - R_{tot,b} \approx L/\lambda_{l,a} \tag{1.17}$$

Owing to thermal contact resistance, the currently used implementation of the TPS method cannot directly determine the intrinsic thermal conductivity of layers. The measured apparent thermal conductivity is typically much lower than the intrinsic thermal conductivity [62, 63]. Moreover, to satisfy the one-dimensional heat-flux assumption, sample layers must have a thermal conductivity below $2\ \mathrm{Wm^{-1}K^{-1}}$ and thickness below $600\ \mu\mathrm{m}$ [49].

There are several studies on the improvement of TPS measurements with respect to these limitations. Ahadi et al. [64] mitigated the influence of thermal contact resistance by comparing measurements of layers with varying thickness, which allows for estimation of the intrinsic thermal conductivity. This approach, known as *the slope method*, has been reported to achieve an accuracy of approximately 7–15 % [63-65]. The method implicitly assumes that thermal contact resistance remains constant across measurements on layers of different thicknesses, but this assumption is not explicitly justified and could lead to significant errors. Zhang et al. [62] systematically studied the influence of non-1D heat flux through FEM simulations and provided an empirical function for results calibration. This approach is applicable only in limited cases and does not comprehensively address non-one-dimensional heat-flux effects.

1.3.4 Transient Plane Source Scanning (TPSS) measurements

The TPSS method is an adaptation of the standard TPS technique, employing the same type of probe but mounted on a specially designed sample holder (Fig. 1.5 a). This modification allows for the direct determination of the specific heat capacity, which can subsequently be used to calculate the anisotropic thermal conductivity.

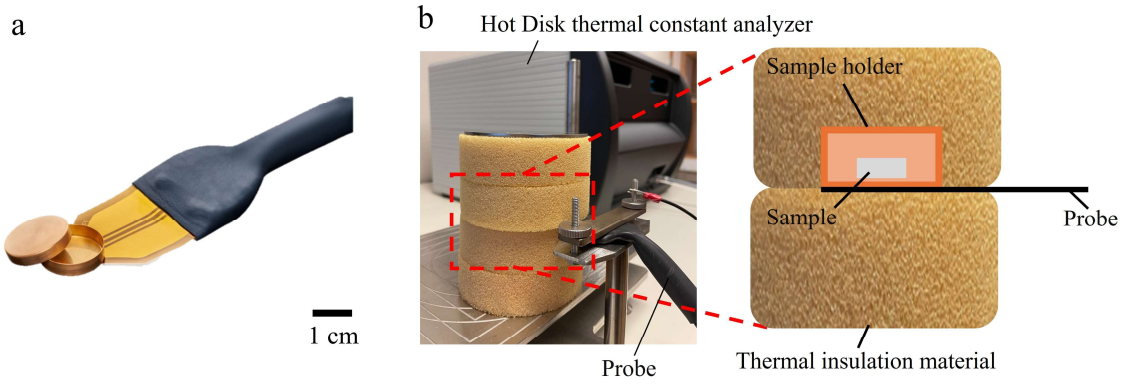

Fig. 1.5 (a) A probe attached to a sample holder for a TPSS measurement. (b) Image of a sample heat capacity measurement setup (left), with a cross-sectional diagram showing the internal structure (right). Figure reproduced with permission from Paper II; Copyright 2024 (CC-BY), Elsevier.

There are two steps involved in the TPSS methods. The first step, known as the holder measurement, requires a temperature record with an empty sample holder embedded in pieces of an insulation material. This step provides information about the heat capacity of the holder and the heat loss during the measurement. Here, heat loss refers to the thermal energy transferred into the surrounding insulation material rather than into the sample. Once an internal non-varying temperature gradient (Ref. [39] and Paper II, section 2.2) is established in the sample holder, typically after 10 s [49], $\Delta T_h(t)$ recorded by the probe can be considered representative of the entire holder. Accordingly, the holder measurement can be described by the following conservation equation [39]:

$$P_h = [(mC_p)_h + f_h(t)]\frac{d}{dt}\big(\Delta T_h(t)\big) \tag{1.18}$$

where P_h is the power supplied by the probe in the holder measurement, m the is mass, $(mC_p)_h$ denotes the heat capacity of the sample holder. Given good thermal insulation, it is assumed that a heat loss function, denoted as $f(t)$ [39], can be utilized to describe the heat loss by $Q(t) = \frac{d}{dt}\big(\Delta T(t)\big)f(t)$. Here, $f_h(t)$ represents the heat loss function that describes the holder measurement.

The second step, referred to as the sample measurement (Fig. 1.5 b), involves a temperature recording with a sample inside the sample holder. Similarly, the sample-

holder assembly requires a certain period of time to establish an internal non-varying temperature gradient (Ref. [39] and Paper II, section 2.2), after which $\Delta T_h(t)$ recorded by the probe can be regarded representative of the entire assembly. Consequently, the sample measurement can be described by the following equation [39]:

$$P_s = [(mC_p)_h + (mC_p)_s + f_s(t)]\frac{d}{dt}\left(\Delta T_s(t)\right) \tag{1.19}$$

where P_s is the power provided from the probe during the sample measurement, $(mC_p)_s$ represents the heat capacity of sample, and $f_s(t)$ is the heat loss function in the sample measurement.

The period of time for internal non-varying temperature gradient of holder-sample assembly can be approximated by $2 \cdot L^2/\alpha$, where L is sample thickness and α represents thermal diffusivity of sample [49]. In practice, data from the fixed time window $[2 \cdot L^2/\alpha, 4 \cdot L^2/\alpha]$ are typically utilized for calculating C_p of sample (Paper II, section 2.2). If $\Delta T_s(t)$ and $\Delta T_h(t)$ are linear and closely aligned in this time window, $f_h(t)$ can be used to approximate $f_s(t)$. Consequently, the following equation can be used to calculate the heat capacity of a sample [39]:

$$\frac{\overline{P_s}}{\delta_s} - \frac{\overline{P_h}}{\delta_h} = \left(mC_p\right)_s \tag{1.20}$$

where $\overline{P}$ is the average heating power from the probe and δ is the average rate of temperature increase, defined as $\frac{d}{dt}\overline{\Delta T(t)}$.

The TPSS technique is generally applicable to centimeter-scale samples whose thermal conductivity is above approximately 1 $\mathrm{W/(m \cdot K)}$ [49]. For materials with a lower conductivity, the influence of heat loss becomes significant and leads to underestimation of heat capacity. Consequently, the TPSS method cannot reliably characterize a broad range of industrial materials, such as polymers, wood and textiles. Berge et al. [66] conducted a systematic investigation of TPSS measurements of high-thermal-conductivity materials and proposed a setup to mitigate heat loss. However, the application of TPSS to low thermal conductivity materials remains unexplored.

1.4 Numerical simulation of TPS measurements

Numerical simulation can be used to obtain approximate solutions to governing equations when analytical solutions are unavailable or impractical due to complex geometries, boundary conditions, or material properties [60, 67]. Mesh-based numerical methods are among the most robust and practical approaches [68-70]. A key step of mesh-based numerical methods is discretizing the computational domain into a mesh, thereby approximating differential operators with algebraic equations that can be solved iteratively.

Based on the discretization framework, methods are commonly classified into the finite difference method (FDM) [68], finite volume method (FVM) [69], and finite element method (FEM) [70]. The FDM discretizes the computational domain into a structured grid and directly approximates derivatives using finite differences, while the FVM divides the domain into control volumes and enforces local conservation laws by integrating the governing equations over each volume. FEM in turn discretizes the computational domain into small elements and uses shape functions to approximate the solution. Mesh-based numerical methods have been widely applied to various engineering problems, including the design of thermoelectric generators [71, 72], the analysis of polymer flow during injection molding [73] or extrusion [74], and the detailed study of TPS measurements [59, 60, 62, 75-80].

FEM and FVM are commonly used in TPS studies to offer insights of measurement design and accuracy. Mihiretie et al. [75] developed an accurate FEM model to investigate the current density and temperature distribution of a probe, gaining more understanding of TPS measurements. Zhang and Tao et al. applied FVM to study the influence of the probe geometry [62, 78] and radiation [76, 77] in TPS measurements. Emanuel et al. [79, 80] utilized the FEM method to generate reference TPS data for verification of analytical models. Zheng et al. [59, 60] performed a detailed sensitivity analysis through comprehensive FEM-based numerical calculations, providing thorough information for selecting time windows as part of the fitting process.

2. Aims of this thesis

This thesis aims to enhance the scope of TPS-based measurements by broadening their applicability and improving their accuracy, thereby contributing to the fields of thermal characterization and material development. With focus on the limitations of the current implementation of the technique, the following scientific and engineering questions are considered and addressed:

For TPS measurements of layers:

Can the intrinsic thermal conductivity of thin layers be determined with high accuracy? (Section 3)

How does thermal contact resistance affect the results of layer measurements, and can its influence be mitigated? (Section 3.2)

How does the non-1D heat flux across the sample layer impact the measurement results, and can such effects be incorporated into the theoretical framework? (Section 3.3)

For TPSS measurements:

Can the specific heat capacity of low-thermal-conductivity samples be accurately determined? (Section 4)

How does the heat loss influence the measurement results, and are there data-analysis methods available to compensate for it? (Section 4.2)

3. Extended TPS measurement for layer characterization

In this chapter, I discuss how the TPS method can be employed to determine the intrinsic thermal conductivity of films or thin layers. The effect of thermal contact resistance on the measurements is first systematically examined, and an effective mitigation strategy is introduced (Section 3.1). (Section 3.1). Furthermore, I propose a new mathematical model accounting for the non-1D heat flux across the layer, which considerably expands the scope of the TPS method (Section 3.2).

3.1 Deconvolution of thermal contact resistance

3.1.1 The influence of thermal contact resistance

I have fabricated two types of polymer layers using high-density polyethylene (HDPE) and polypropylene (PP), respectively. These polymers are widely used with well-known thermal (Table 3.1) and mechanical properties, making them suitable for evaluating the TPS measurement. Specifically, HDPE and PP were hot-pressed into a circular layer with a diameter of 30 mm and thicknesses ranging from approximately 30 to 400 μm. More properties regarding the hot-pressed polymers are available in Paper I.

Table 3.1 Polymer properties. The error corresponds to the measurement uncertainty. a. Measured by the TPS measurements of bulk samples. b. Determined from the mass and volume of the samples. c. Obtained by DSC measurements.

Material	λ (W/(m · K))	ρ (kg/m^3)	C_p (J/(kg · K))
HDPE	0.465 ± 0.023[a]	950 ± 29[b]	1923 ± 38[c]
PP	0.269 ± 0.013[a]	900 ± 27[b]	1613 ± 32[c]

I conducted two rounds of measurements on the same set of samples. In the first round, thermal conductivity of layers was determined strictly according to the TPS procedure described in Section 1.3.3. Different levels of mounting force were applied to the measurement assembly to investigate their influence on the results. The second round was conducted in a similar manner, but with thermal interface materials applied between the probe, sample layers, and backing bulk material to enhance thermal contact. The backing material used in this study was stainless steel with a thermal conductivity of 13.5 W/(m · K). The thermal interface materials include deionized water and silicone oil, enabling non-destructive measurement of micrometre-thick polymer layers.

In the first round of measurements, virtually all determined thermal conductivities are significantly lower than their respective reference values—0.465 W/(m · K) for HDPE and 0.269 W/(m · K) for PP (Table 3.1). I attribute these lower values to the presence of thermal contact resistance, which impedes heat conduction and increases the total thermal resistance between the layer and the backing bulk material. Thicker layers display higher values of determined thermal conductivity. I associate this with their larger intrinsic thermal resistance, which makes the influence of thermal contact resistance less significant.

Furthermore, I observed that a higher mounting force resulted in higher values of determined thermal conductivity, particularly in the case of HDPE. This increase likely resulted from reduced thermal contact resistance under a higher mounting force. Notably, thin HDPE layers (< 50 μm) exhibit anomalously higher values of thermal conductivity under high mounting force of 300 N, likely owing to their softer nature, which results in better contact with the sensor and the backing bulk material. I expect the relatively larger

thermal conductivity observed in PP layers thinner than 80 µm to arise from the same reason.

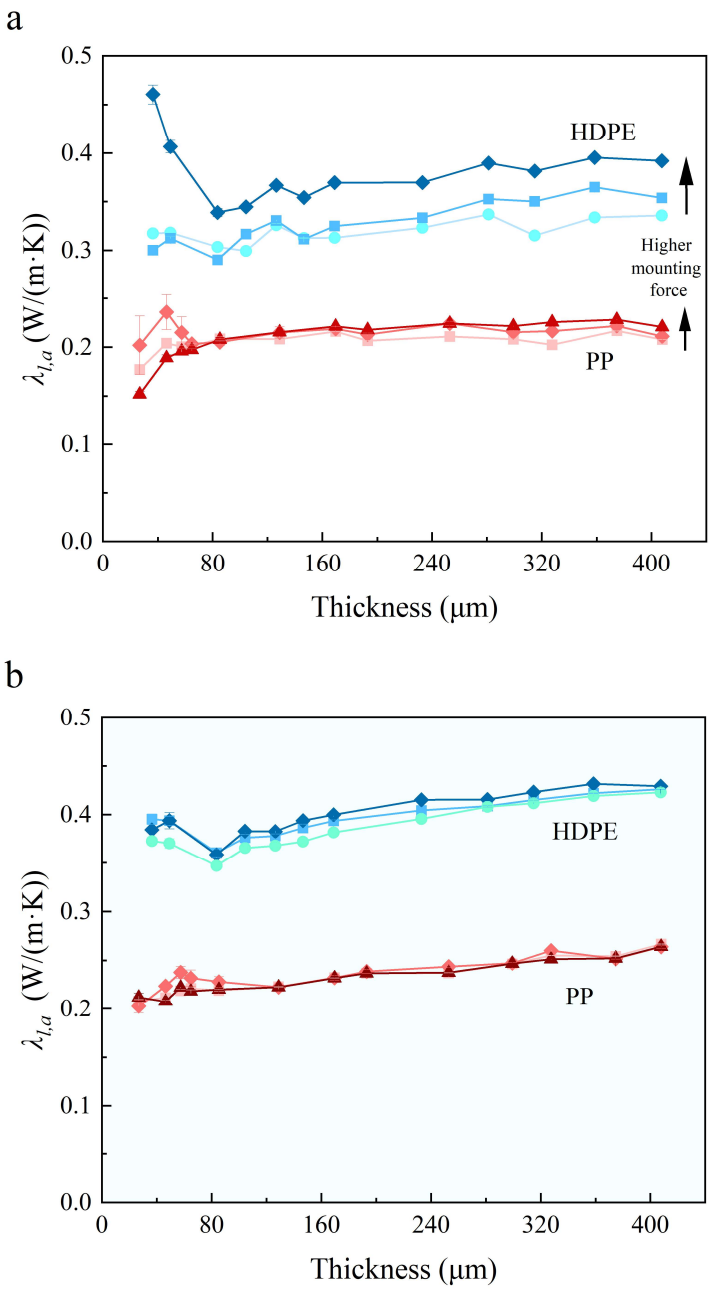

Fig. 3.1 Comparison of determined thermal conductivity values as a function of layer thickness: (a) without a TIM; (b) with deionized water as the TIM. Mounting forces applied by the pressure stand: ● 0 N, ■ 50 N, ◆ 300 N, ▲ 550 N. Figures reproduced with permission from Paper I; Copyright 2025, American Society of Mechanical Engineers.

In a second round of measurements, ionized water was introduced as a TIM. The determined thermal conductivity values exhibited significantly reduced dependence on the mounting force. Moreover, these values are higher than the previous cases without any TIM, which can be attributed to reduced thermal contact resistance. Despite this increase, the determined values of thermal conductivity are still noticeably lower than the reference values, with a difference of up to approximately 25 % in cases of both HDPE and PP. This implies that the introduction of a TIM did not completely eliminate thermal contact resistance.

3.1.2 The slope method

When assuming that the thermal contact resistance remains identical across different layer thicknesses, the measured $R_{tot,l} - R_{tot,b}$ can be written as a linear function of layer thickness L:

$$R_{tot,l} - R_{tot,b} = L/\lambda_l + C \tag{3.1}$$

where C denotes the additional thermal contact resistance introduced by a sample layer.

Based on this equation, a linear fit can be applied to the measurement data, whose slope corresponds to the reciprocal of the intrinsic thermal conductivity ($1/\lambda_l$). This approach is therefore referred to as the slope method.

To extract the intrinsic thermal conductivity, the experiment results in Fig.3.1 a,b are expressed in the form $R_{tot,l} - R_{tot,b}$ and linear fits are applied to these data (Fig. 3.2). Data points from layers thinner than 80 μm are excluded from the fitting owing to large fluctuations.

In case of measurements without a TIM, the slope decreases with increasing mounting force (Fig. 3.2 a), which corresponds to a higher thermal conductivity (see Table 2 in Paper I). Specifically, the extracted thermal conductivity of HDPE increases from 0.343 to 0.411 $\mathrm{W/(m \cdot K)}$, while that of PP increases from 0.209 to 0.230 $\mathrm{W/(m \cdot K)}$. However, these values remain lower compared to the reference values, with a difference of up to 26 % in case of HDPE and 22 % in case of PP.

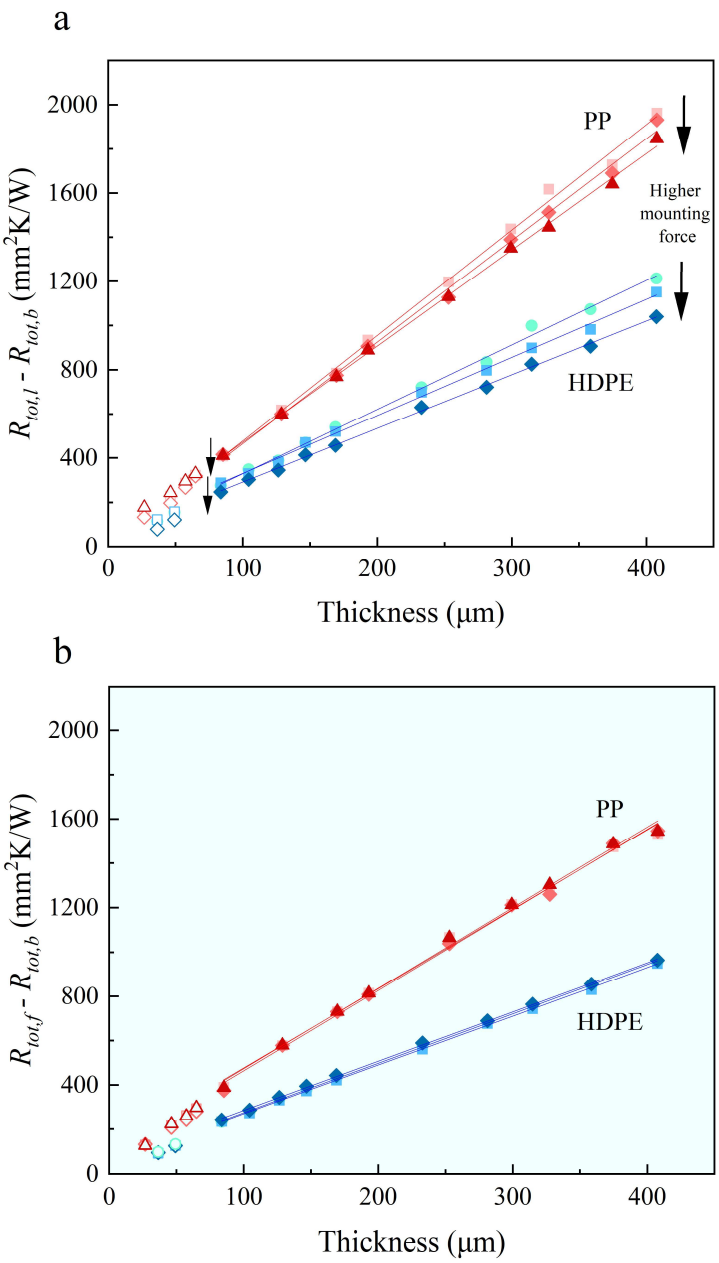

Fig. 3.2 (a) $R_{tot,l} - R_{tot,b}$ as a function of layer thickness, along with linear fits: (a) without a TIM; (b) with deionized water as the TIM. Data points from the specimens thinner than 80 μm (open symbols) were excluded from the fitting. Mounting forces applied by the pressure stand: ● 0 N, ■ 50 N, ◆ 300 N, ▲ 550 N. Figures reproduced with permission from Paper I; Copyright 2025, American Society of Mechanical Engineers.

With the introduction of ionized water, the fitted lines corresponding to different mounting forces nearly overlap (Fig. 3.2 b). The extracted values of thermal

conductivity are more consistent across different mounting forces, with a variation of approximately 1 %, indicating a negligible dependence on mounting force. Finally, the average value of extracted thermal conductivity across different mounting forces is (0.450 ± 0.003) $\mathrm{W/(m \cdot K)}$ for HDPE and (0.277 ± 0.004) $\mathrm{W/(m \cdot K)}$ for PP. These values agree with the reference values obtained from the TPS measurements on bulk materials, differing by approximately 4 %.

3.1.3 The influence of sample number

In the previous section, the slope method was applied to data from numerous samples of varying thicknesses. This section, in turn, discusses the minimum number of samples required by the slope method to achieve precise results with low uncertainty. Using fewer samples can reduce the time and effort required for each measurement, but the influence of measurement uncertainty may be more significant.

I first applied the slope method to data from only two pairs of samples (2×2), extracted from Fig. 3.2 b. The extracted thermal conductivity is denoted as $\lambda_{l,2}$ and plotted against the thickness difference between the two samples pairs (Fig. 3.3 a). In general, the values of $\lambda_{l,2}$ show greater scatter when the thickness difference is small, but become more consistent as the thickness difference increases. Overall, the average values of $\lambda_{l,2}$ is 0.448 $\mathrm{W/(m \cdot K)}$ with a standard deviation of 0.022 $\mathrm{W/(m \cdot K)}$ (5 %) for HDPE, and 0.289 $\mathrm{W/(m \cdot K)}$ with a standard deviation of 0.065 $\mathrm{W/(m \cdot K)}$ (22 %) for PP (Table 3.2). When only considering the sample pairs with a thickness difference larger than 200 µm, the average values of $\lambda_{l,2}$ are (0.451 ± 0.006) $\mathrm{W/(m \cdot K)}$ (1 %) for HDPE and (0.277 ± 0.013) $\mathrm{W/(m \cdot K)}$ (5%) for PP, with markedly smaller uncertainties.

Similarly, the slope method was applied to the data from three pairs of samples (3×2) to obtain the intrinsic thermal conductivity ($\lambda_{l,3}$). The values of $\lambda_{l,3}$, plotted against the largest thickness difference between the samples, are less scattered compared to the case of $\lambda_{l,2}$, especially when the thickness difference is small. Overall, the standard deviation is 0.012 $\mathrm{W/(m \cdot K)}$ (7 %) for HDPE and 0.019 $\mathrm{W/(m \cdot K)}$ (5 %) for PP.

Lastly, the intrinsic thermal conductivity values obtained from four pairs of samples ($\lambda_{l,4}$) are examined. Notably, the values of $\lambda_{l,4}$ exhibit substantially smaller standard

deviations than the previous cases: 0.008 $\mathrm{W/(m \cdot K)}$ (2 %) for HDPE and 0.009 $\mathrm{W/(m \cdot K)}$ (3 %) for PP.

Based on the current analysis, several sample combinations can be recommended for a precise determination of the intrinsic thermal conductivity of layers with low standard deviation (< 0.02 $\mathrm{W/(m \cdot K)}$). For example, one suitable combination consists of 2×2 layers thicker than 80 µm with a thickness difference exceeding 200 µm. Another appropriate combination consists of 4×2 sample layers, each thicker than 80 µm.

To demonstrate the applicability of the proposed sample combinations, the first one was applied to characterize regio-regular poly(3-hexylthiophene) (P3HT) layers, yielding an intrinsic thermal conductivity of (0.296 ± 0.030) $\mathrm{W/(m \cdot K)}$. This result is comparable to the thermal conductivity of P3HT films or bulk material prepared by other methods, such as drop casting (0.21 $\mathrm{W/(m \cdot K)}$) [81], spin coating (0.27 $\mathrm{W/(m \cdot K)}$) [82], cold pressing (0.19 $\mathrm{W/(m \cdot K)}$) [83], and drop casting followed by cold pressing (0.33 $\mathrm{W/(m \cdot K)}$) [84].

Table 3.2 Comparison of average λ_l and standard deviation obtained from datasets with varying number of samples.

Thermal conductivity ($\mathrm{W/(m \cdot K)}$)	$\lambda_{l,2}$	$\lambda_{l,3}$	$\lambda_{l,4}$
HDPE	0.448 ± 0.022	0.448 ± 0.012	0.446 ± 0.008
PP	0.289 ± 0.065	0.278 ± 0.019	0.269 ± 0.009

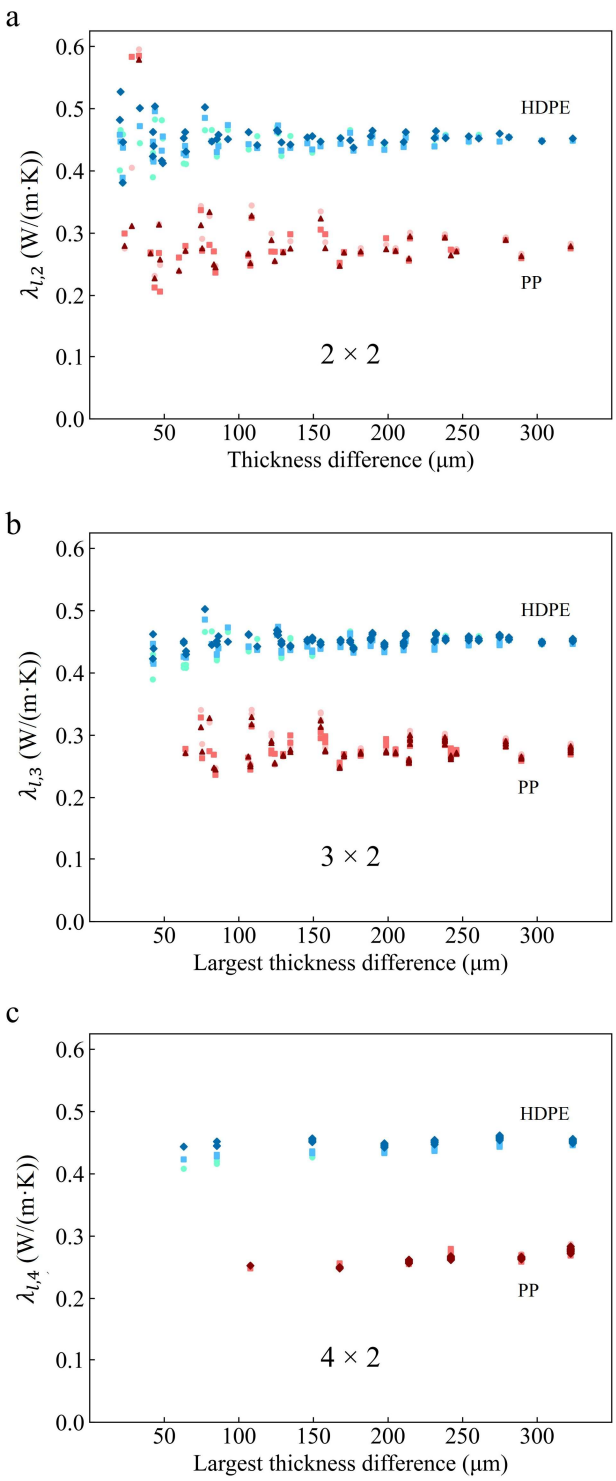

Fig. 3.3 Variation in extracted λ_l of HDPE and PP as a function of thickness difference for different mounting forces (● 0 N, ■ 50 N, ◆ 300 N, ▲ 550 N), across various systems: (a) 2×2, (b) 3×2, (c) 4×2 samples. Figures adapted with permission from Paper I; Copyright 2025, American Society of Mechanical Engineers.

3.2 Theoretical optimization considering non-1D heat flux

3.2.1 The influence of non-1D heat flux across the layer

The conventional TPS model for layer measurements (denoted as the Layer 1D model) assumes 1D heat flux across the layer, which imposes limitations on the layer properties (thermal conductivity < 2 $W/(m \cdot K)$ and thickness < 600 μm) and sensor geometry (radius > 11 mm). The actual heat flux is not strictly 1D, i.e., the edge region of the layer beyond the coverage of the probe conducts heat in the radial direction (see Fig. 7 in Paper I for details). This radial heat flux is more significant if the thermal conductivity or thickness of the layer is larger and eventually leads to considerable errors.

To quantify the errors (ε, defined by Eq. 10 in Paper I) caused by radial heat flux within the layer, I measured various layers with a thermal conductivity ranging from 0.2 to 20 $W/(m \cdot K)$ and a thickness from 500 to 2000 μm, including poly(methyl methacrylate) (PMMA), glass, zirconium dioxide (ZrO_2), stainless steel, and alumina (see Table 3.3 for material properties). The backing substrate was stainless steel for all cases. Contour maps are plotted based on measured results to show how ε changes with layer thermal conductivity and thickness (Fig. 3.4). Due to a pronounced overall gradient, the data of layers thinner than 500 μm was obtained by extrapolation based on the measurement data (Table S1 in Paper IV).

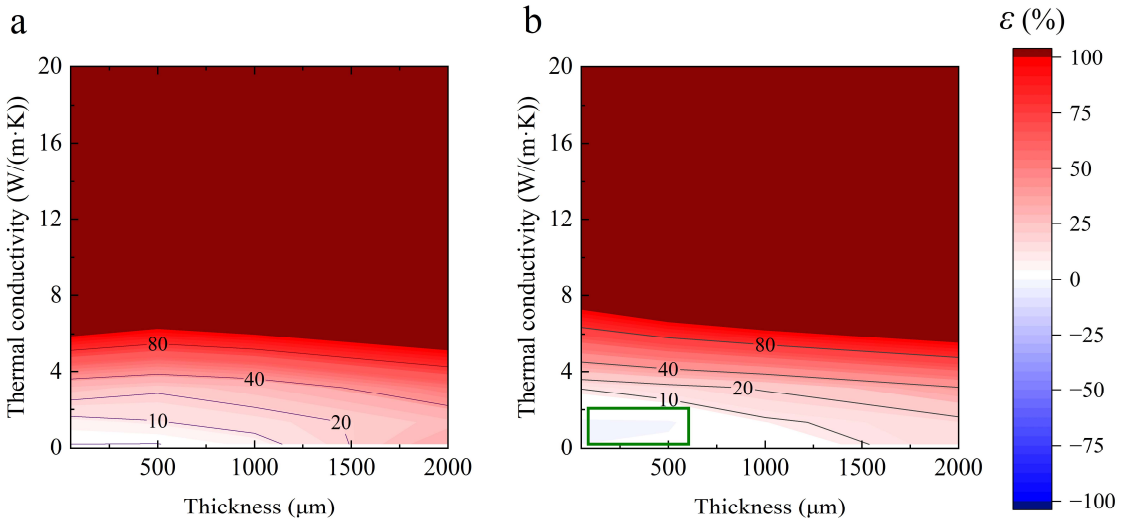

Fig. 3.4 Contour maps of the error ε in layer thermal conductivity determined using the conventional Layer 1D model, based on measurements with probes of different radii: (a) 6.6 mm (b) 11 mm. The green frame in (b) indicates the original applicability of the TPS method for characterizing layers using a sensor with a radius larger than 11 mm. *Unpublished data in Paper IV.*

In the case of a 6.6 mm probe (Fig. 3.4 a), a low ε (< 10 %) is observed for thin layers with low thermal conductivity. However, ε increases considerably with increasing thickness or thermal conductivity, which implies that the 1D heat flux assumption is not valid under these conditions. It should be noted that the effect of this invalidation overshadows that of thermal contact resistance, ultimately leading to an overestimation of the layer thermal conductivity. In the case of a 11 mm sensor (Fig. 3.4 b), the region with a low ε (< 10 %) is slightly enlarged, likely due to the larger probe-to-layer thickness ratio, which as a result of the heat flux across the layer more closely resembles the assumed 1D scenario. However, a higher thermal conductivity or thickness still leads to a considerably larger ε. This indicates that increasing the radius, in this case by 67 %, is not an effective way to broaden the applicability of the conventional Layer 1D model.

Table 3.3 Material properties. [a] Measured by TPS measurements on bulk samples. The measurement accuracies are ± 2 % for thermal conductivity and ± 7 % for thermal diffusivity [34]. [b] Calculated from mass and volume. [c] Measured by the Transient Plane Source Scanning method, with a measurement accuracy of approximately 5 %.

Material	Thermal conductivity $(\mathrm{W}/(\mathrm{m}\cdot\mathrm{K}))$	Thermal diffusivity $(\mathrm{mm}^2/\mathrm{s})$	Density $(\mathrm{kg}/\mathrm{m}^3)$	Specific heat capacity $(\mathrm{J}/(\mathrm{kg}\cdot\mathrm{K}))$
PMMA	0.21[a]	0.12[a]	1180[b]	1464[c]
Glass	1.34[a]	0.81[a]	2172[b]	766[c]
ZrO_2	3.15[a]	1.23[a]	6220[b]	412[c]
Stainless steel	13.5[a]	3.60[a]	8150[b]	460[a]
Alumina	22.3[a]	7.26[a]	3775[b]	815[c]

3.2.2 The Layer 2D model

To extend the measurement capability, a model accounting for 2D heat flux (referred to as the Layer 2D model) was developed based on the following physical configuration. In cylindrical coordinates, a semi-infinite substrate is in perfect thermal contact with a radially infinite overlying layer of thickness L. This layer-substrate assembly, initially at zero reference temperature, is suddenly subjected to heating across a circular area of radius R and a constant and uniform density φ. The governing equation of heat diffusion in the solids is [1]:

$$\frac{\partial^2 T_i}{\partial r^2} + \frac{\partial T_i}{r\,\partial r} + \frac{\partial^2 T_i}{\partial z^2} = {\alpha_i}^{-1}\frac{\partial T_i}{\partial t} \tag{3.2}$$

where T_i represents the temperature response of the solids to the heating, α_i denotes thermal diffusivity, and $i = l$ or s corresponds to the layer and the substrate, respectively.

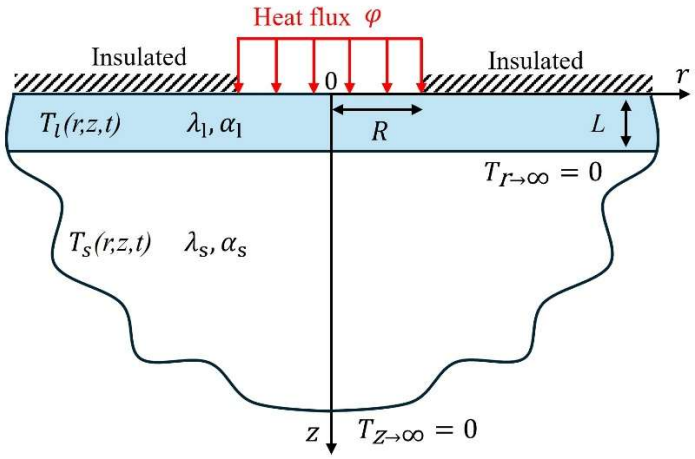

Fig. 3.5 Schematic of a semi-infinite substrate with a layer, subjected to localized heating.

The boundary conditions are given by:

$$-\lambda_l \frac{\partial T_l}{\partial z}\Big|_{z=0} = \begin{cases} \varphi \ (r \le R) \\ 0 \ \ (r > R) \end{cases} \tag{3.3}$$

$$T_i(r, z, 0) = 0 \tag{3.4}$$

$$T_l(r \to \infty) = 0 \tag{3.5}$$

$$T_s(z \to \infty) = 0 \tag{3.6}$$

where λ represents the thermal conductivity. At the interface between the layer and the substrate where $z = L$ the following conditions apply:

$$T_l(z = L) = T_s(z = L) \tag{3.7}$$

$$-\lambda_l \frac{\partial T_l}{\partial z}\Big|_{z=L} = -\lambda_s \frac{\partial T_s}{\partial z}\Big|_{z=L} \tag{3.8}$$

After derivation (see Paper IV for details), the average temperature of the heating area (ΔT_{avg}) can be written as:

$$\Delta T_{\text{avg}} = \frac{2\varphi}{\lambda_l} \int_0^\infty \frac{J_1^2(\beta R)}{\beta} \mathcal{L}^{-1}\left(\frac{1}{q_l p} \cdot \frac{\lambda_s q_s \tanh(L q_l) + \lambda_l q_l}{\lambda_l q_l \tanh(L q_l) + \lambda_s q_s}\right) d\beta \tag{3.9}$$

where J_1 denotes the first-order Bessel function of the first kind, $\mathcal{L}^{-1}$ represents the inverse Laplace operator, β is the Hankel variable, $q_i = \sqrt{\beta^2 + p/\alpha_i}$, and p is the Laplace variable.

At a later stage of the measurement, the heat flux across the layer achieves a quasi-steady state, where the contribution of α_l to ΔT_{avg} becomes negligible. Under this condition, it is assumed that $\alpha_l = \alpha_s$, which allows the term inside the inverse Laplace transform (K) to be simplified:

$$K = \frac{1}{pq_l} \cdot \frac{q_s \tanh(Lq_l) + c \cdot q_l}{c \cdot q_l \tanh(Lq_l) + q_s} \approx \frac{1}{pq_l} \cdot \frac{c(w^2+3)+3w}{(w^2+3)+3cw} \tag{3.10}$$

where $w = q_s L$ and $c = \lambda_l / \lambda_s$ (Detailed derivation is available in the Supporting Information of Paper IV).

Upon taking the inverse Laplace transform of simplified K, the following equation can be written to predict ΔT_{avg}:

$$\Delta T_{\text{avg,2D}} = \frac{2\varphi}{\lambda_l} \int_0^{\infty} \frac{J_1^2(\beta R)}{\beta} \frac{(A+D)}{F} \, d\beta \tag{3.11}$$

where

$$A = c(\beta^4 L^4 - 3\beta^2 L^2 + 9) \cdot \text{erf}\left(\beta \sqrt{\alpha_s t}\right)$$

$$D = 3\beta L(1 - c^2)(3 + \beta^2 L^2)$$

$$F = 9\beta L + 3\beta^3 L^3 (2 - 3c^2) + \beta^5 L^5$$

3.2.3 Results and discussion

To evaluate the accuracy of the Layer 2D model, the average temperature T_{avg} calculated from different models are compared:

• **Layer 1D model**: An analytical model assuming 1D heat flux across the layer (based on Eq. 1.8 where $\Delta T_a(t) \approx \frac{\varphi L}{\lambda_l}$, or Eq. 29 in Paper IV).

• **Layer 2D model**: A semi-analytical model accounting for 2D heat flux across the layer (based on Eq. 3.11).

• **Simplified FEM model**: A FEM model representing the simplified physical configuration shown in Fig. 3.5, used as a reference to validate the analytical models (see Section 2.3.1 in Paper IV).

As implied by its underlying assumption, the conventional Layer 1D model agrees well with the FEM results when the layer has both a low thermal conductivity and a small thickness (bottom group in Fig. 3.6 a), corresponding to an almost one-dimensional heat flux across the layer. However, the increase of either thermal conductivity or layer thickness significantly enlarges the difference between the Layer 1D model and the simplified FEM model.

In contrast, the Layer 2D model exhibits good agreement with the FEM results across a broad range of thermal conductivities (up to 20 $\mathrm{W\,m^{-1}\,K^{-1}}$) and thicknesses (up to 2000 μm). In general, there is a time delay before the Layer 2D model achieves close agreement with the FEM results (Fig. 3.6 a-d). This delay results from the simplification of heat diffusion within the layer in the equation, namely the assumption $\alpha_l = \alpha_s$. Therefore, this delay depends on both the layer thickness and thermal diffusivity, as confirmed by the results of sensitivity analysis (Fig. 6 in Paper IV).

When layer and substrate share identical properties (Fig. 3.6 c, stainless steel layer on a stainless steel substrate), all scenarios with different thicknesses converge to the case of a semi-infinite substrate heated by a circular heat source. Consequently, the T_{avg} values remain identical across different layer thicknesses in both the simplified FEM model and Layer 2D model. The Layer 2D model closely aligns with the FEM throughout the whole period without any delay, as the assumption $\alpha_l = \alpha_s$ is always fulfilled in these cases.

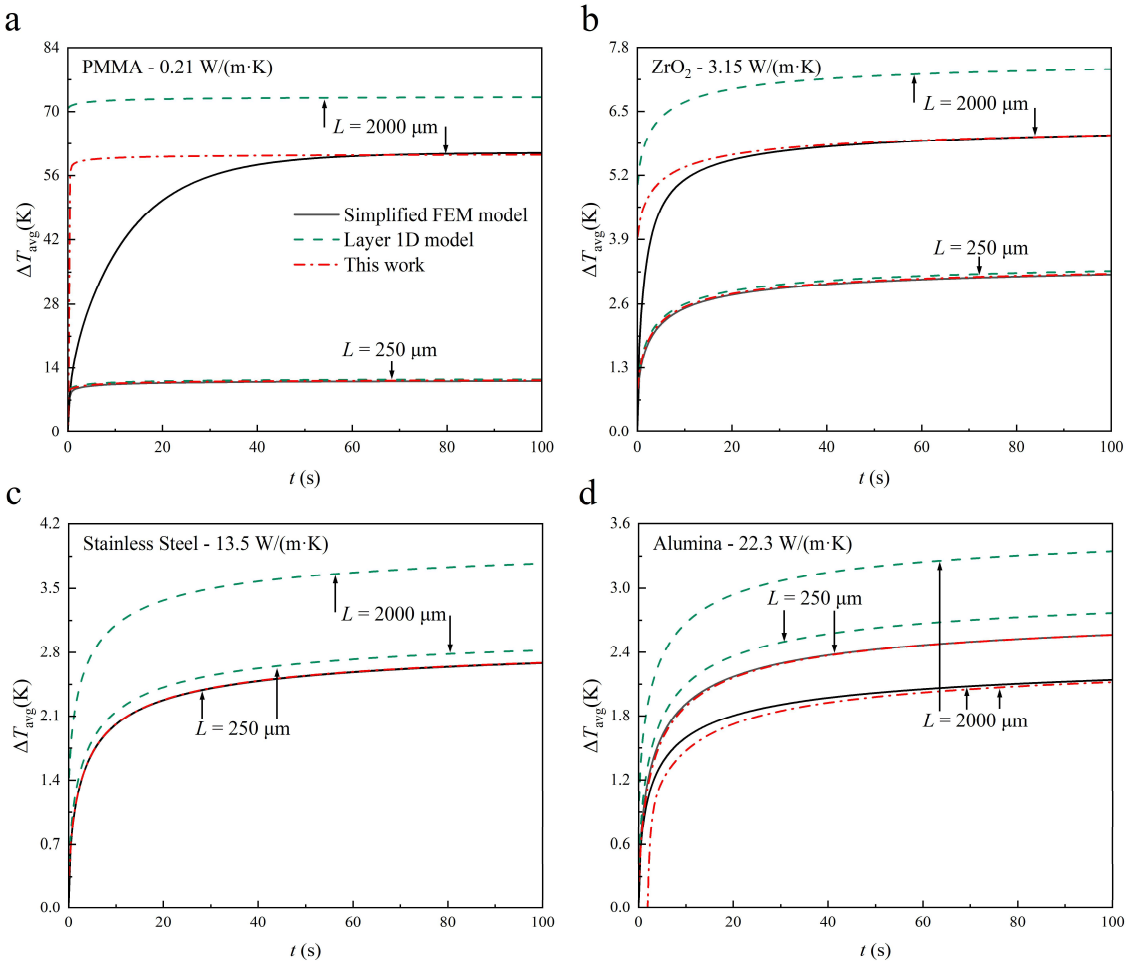

Fig. 3.6 Comparison of T_{avg} obtained using different models (Layer 1D model: green dashed line, Layer 2D model: red dash-dot line, FEM model: black solid line), for a heating area radius of 6.6 mm: (a) PMMA layer, (b) ZrO_2 layer, (c) stainless steel layer, and (d) alumina layer. The substrate in all cases is stainless steel, and the heating power is 1 W. *Unpublished data in Paper IV.*

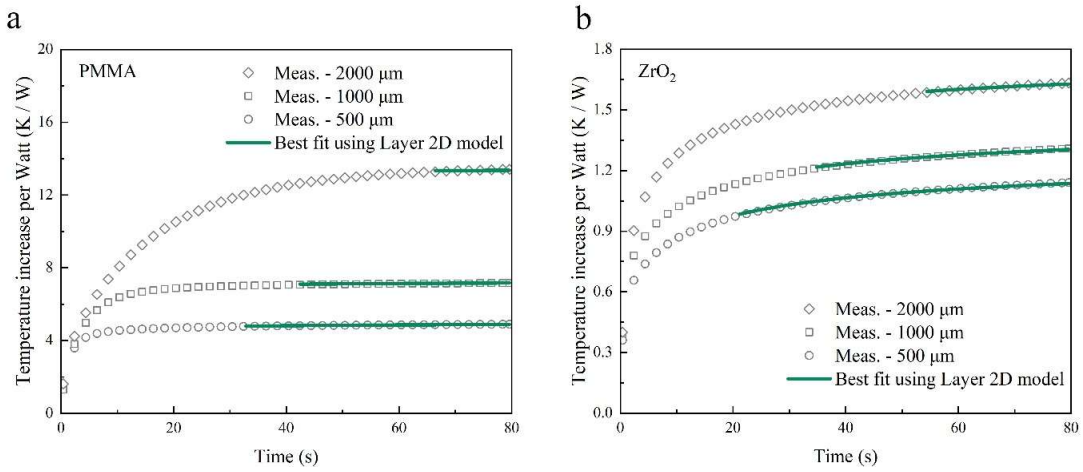

Fig. 3.7 Exemplary comparison between experimental data and the fitted data for (a) a glass layer and (b) a ZrO_2 layer. *Unpublished data in Paper IV.*

The Layer 2D model, with the consideration of the thermal resistance caused by the Kapton sheets (Eq. 34 in Paper IV), is subsequently utilized to fit the experimental data and to determine the layer thermal conductivity. An iterative algorithm is implemented to automatically select an appropriate time range for the fitting (see Sections 3.3 and 3.4 in Paper IV for details). After fitting, the best-fit curve and the corresponding layer thermal conductivity are obtained.

The best fits show good agreement with the experimental data within the selected fitting range (Fig. 3.7 a, b). Moreover, the determined thermal conductivity agrees with the reference values in most cases (except for thinnest stainless steel and alumina layers), with errors ε less than 7 % (Table 3.4), thereby validating the Layer 2D model and fitting procedure.

Table 3.4 Thermal conductivity values determined from experimental data using the Layer 2D model. Each value represents the average of three repeated measurements, with the associated error given as the maximum difference among them.

	Layer thickness (μm)	Thermal conductivity (W/(m · K))				
		PMMA	Glass	ZrO_2	Stainless steel	Alumina
Probe A (R = 6.6 mm)	500	0.198 ± 0.001	1.35 ± 0.01	3.17 ± 0.18	13.8 ± 0.4	14.7 ± 0.1
	1000	0.196 ± 0.001	1.37 ± 0.02	3.15 ± 0.03	13.4 ± 0.3	22.4 ± 0.8
	2000	0.207 ± 0.001	1.33 ± 0.01	3.14 ± 0.01	13.9 ± 0.4	23.8 ± 0.2
Probe B (R = 11 mm)	500	0.206 ± 0.001	1.38 ± 0.03	3.11 ± 0.06	12.7 ± 0.6	18.4 ± 0.7
	1000	0.209 ± 0.011	1.42 ± 0.01	3.13 ± 0.06	13.9 ± 0.1	19.8 ± 0.6
	2000	0.212 ± 0.002	1.39 ± 0.06	3.22 ± 0.02	13.4 ± 0.3	22.6 ± 1.0

To reveal the distribution of ε with respect to layer thickness and thermal conductivity, contour maps are plotted based on the results in Table 3.4. In case of both a 6.6 mm and a 11 mm probe, the region with low ε covers vast majority of the plot (Fig. 3.8 a, b), in contrast to the small low ε area obtained utilizing the Layer 1D model (Fig. 3.4). I attribute this significant improvement to the consideration of two-dimensional heat flux in the Layer 2D model. For layers thicker than approximately 750 μm or with a thermal conductivity lower than about 8 $\mathrm{W/(m \cdot K)}$, ε is lower than 5 %. Only thermally thin layers (upper left corner) exhibit a value of ε lower than 10 %, indicating an underestimation of the layer thermal conductivity. I ascribe this underestimation to thermal contact resistance between the components, which impedes thermal conduction and leads to a higher temperature response of the probe.

To obtain complete distribution of ε, the Layer 2D model is further employed to determine the layer thermal conductivity from simulated measurement data generated by a detailed FEM model (inset in Fig. 3.8 c). This detailed FEM model accounts for thermal contact resistance and the actual pattern of the probe (see Section 2.3.2 in Paper IV for detailed description of the model). It covers two thermal contact conditions between the probe, sample layer, and substrate: (1) good thermal contact, represented by a 5 μm-thick TIM with a thermal conductivity of 3 $\mathrm{W/(m \cdot K)}$, and (2) inferior

thermal contact, represented by a TIM of 1 $\mathrm{W/(m \cdot K)}$. In this analysis, ε is calculated as the relative difference between the determined thermal conductivity from the Layer 2D model and the input value in the FEM simulation.

Generally, the distribution of ε obtained from the simulated data (Fig. 3.8 c-f) agrees with that from the experimental data (Fig. 3.8 a, b), showing similar underestimations of thermal conductivity in thermally thin layers. In the cases of TIM of 3 $\mathrm{W/(m \cdot K)}$, ε is generally low (< 10 %) for layers thicker than 250 µm in both cases of 6.6 mm and 11 mm sensors. For low thermal conductivity layers (< 2 $\mathrm{W/(m \cdot K)}$), the magnitude of ε remains small even when the layer thickness is as low as 50 µm. Compared with the conventional Layer 1D model (green frame, Fig. 3.8 d), the measurement applicability is significantly extended, enabling accurate characterization (ε < 10 %) of layers with thermal conductivities up to 20 $\mathrm{W/(m \cdot K)}$ and thicknesses up to 2000 µm.

When the thermal contact resistance is higher (Fig. 3.8 e, f), the underestimation observed for thin layers becomes more pronounced, indicating that thermal contact resistance is the primary limiting factor of the Layer 2D model. These results are closer to the measurement results observed in Fig. 3.8 a, b. Overall, minor systematic errors caused by thermal contact resistance remain acceptable for thick layers and can be mitigated by improving thermal contact, for example, by using a TIM with a higher thermal conductivity of 3 $\mathrm{W/(m \cdot K)}$.

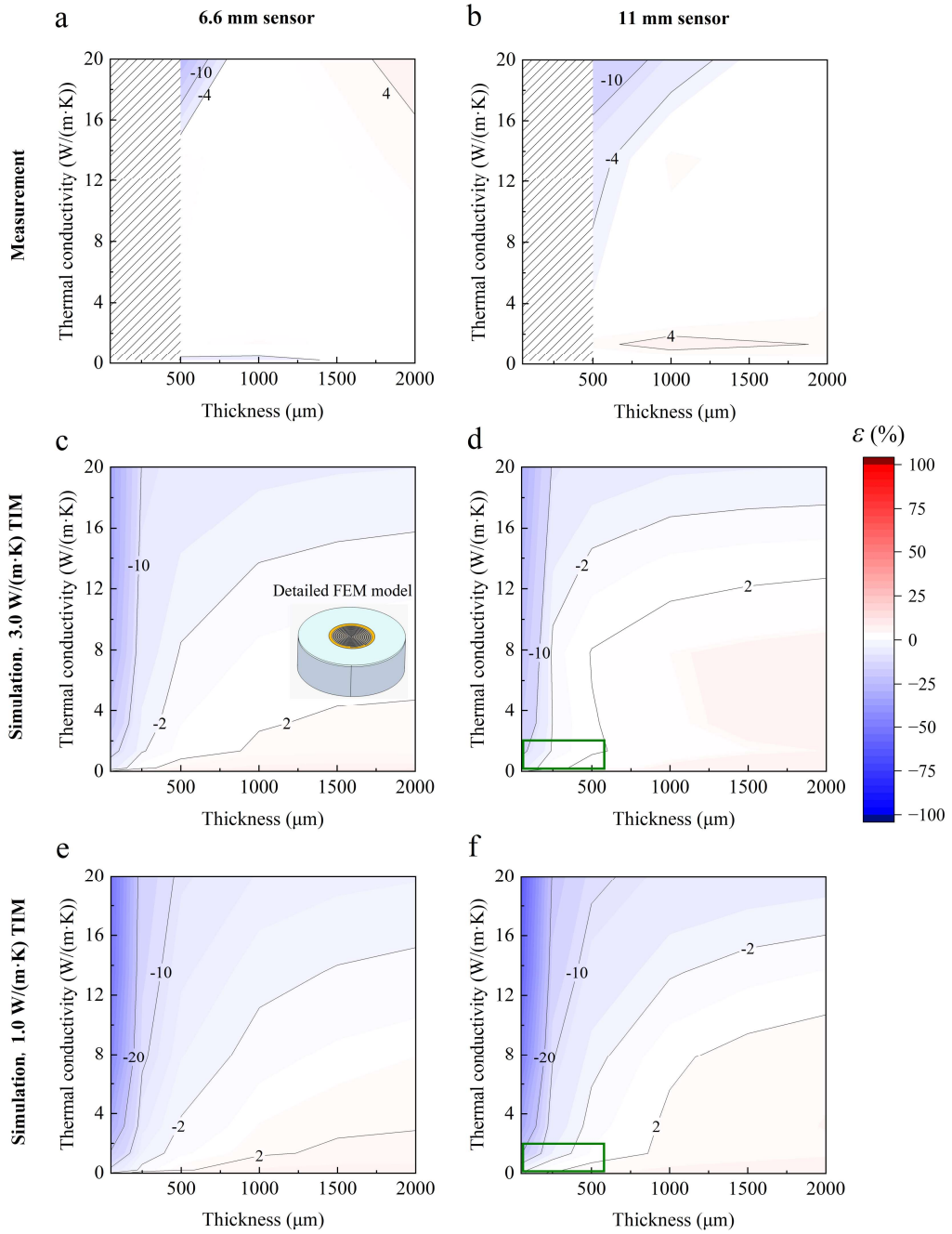

Fig. 3.8 Contour maps of the error ε in layer thermal conductivity determined using the Layer 2D model based on different datasets: (a) experimental data, 6.6 mm probe; (b) experimental data, 11 mm probe; (c) simulated data, 6.6 mm probe, TIM of 3 W/(m · K), (d) simulated data, 11 mm probe, TIM of 3 W/(m · K), (e) simulated data, 6.6 mm probe, TIM of 1 W/(m · K), (f) simulated data, 6.6 mm probe, TIM of 1 W/(m · K). Since the data for layers thinner than 500 μm was not experimentally obtained, the corresponding regions in (a, d) are shaded. *Unpublished data in Paper IV.*

4. Extended TPSS measurement

In this chapter, the current implementation of TPPS method for C_p measurements is investigated across samples with a wide range of thermal conductivities from 0.2 – 398.0 $\mathrm{W/(m \cdot K)}$ (section 4.1), providing a comprehensive understanding of current limitations of TPSS measurements. To address these limitations, a general solution is then introduced (Section 4.2) and discussed (Section 4.3).

4.1 Influence of heat loss

Three types of samples, including copper, glass, and PMMA, are measured at room temperature (293 K). Their C_p values are calculated from data within the corresponding recommended time ranges (Table 4.1) according to the conventional theory described in Section 1.3.4. Reference values from DSC or the Dynamic Plane Source method (DPS) [85, 86] are provided for comparison (Fig. 4.1 a). Overall, the TPSS values for copper and glass agree with the reference values, while the TPSS value for PMMA is considerably lower.

Table 4.1 Three types of samples and their corresponding time ranges for C_p calculation according to Section 1.3.4.

Material	Recommended time range
Copper	20 – 40 s
Glass	40 – 80 s
PMMA	120 – 240 s

To gain deeper insights into the results obtained from TPSS measurements, C_p values are recalculated using a sliding window of width 0.8s, i.e., [t - 0.4 s, t + 0.4 s], rather than the fixed time window in Table 4.1. Here, t denotes the central point of the time window. This analysis decomposes the fixed time range into small sub-windows for C_p calculation, providing finer temporal resolution to track the evolution of the calculated C_p over time and to help diagnose the cause of the observed deviation.

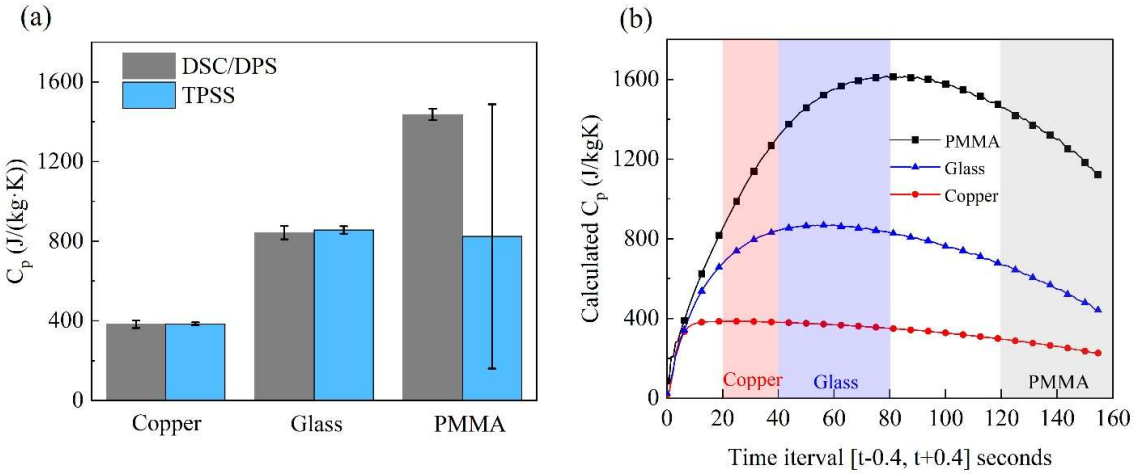

Fig. 4.1 (a) Comparison of the C_p values obtained from the TPSS method with reference values from DSC (glass, PMMA) or DPS [85, 86] (copper). The error bars represent the maximum variation of calculated C_p obtained using sliding time windows within the recommended time ranges. (b) C_p values calculated using sliding time windows with a width of 0.8 s. Figures reproduced with permission from Paper II; Copyright 2024 (CC-BY), Elsevier.

Generally, the recalculated C_p values of all samples exhibit an initial increase followed by a decrease over time (Fig. 4.1 b). The extent of this increase corresponds to the time required for the sample-holder assembly to establish a non-varying internal temperature gradient state, which is related to the thickness and the thermal diffusivity of the sample. In the case of copper, the duration of the increasing phase is comparatively short, about 10 s, owing to its high thermal diffusivity, compared to around 50 s for glass and 80 s for PMMA.

After the initial increase, the calculated C_p of copper stays consistent with the reference value, showing only a minimal drop (~ 1 %) within the recommended time range of 20 – 40 s (red shaded region in Fig. 4.1 b). This implies that the TPSS theory accurately describes the measurement in this time range. Beyond 40 s, however, the calculated C_p of copper shows a continuous decline, likely due to inaccuracies in heat loss compensation using Eq. 1.20 during the later stage of the measurement. In the case of glass, the decline in the calculated C_p is slightly larger (~ 3 %) within the recommended time range (blue range in Fig. 4.1 b), while for PMMA it is estimated to be dramatically larger, exceeding 80 % when the whole recommended time range is considered (grey range and beyond). Note that the data beyond 160 s for PMMA was not experimentally obtained but extrapolated using a linear fit to the preceding data. Overall, the calculation of C_p appears to be increasingly affected by inaccuracies in heat loss compensation, especially in the later stages of the measurement.

4.2 A Well-Tuned FEM Model

To fully understand why the C_p is underestimated and ultimately to develop a method that allows to obtain accurate results, I conducted a series of FEM studies (Fig. 4.2). First, I developed a 2D model to replicate the measurement setup (Fig. 4.3, Table 4.2) and use it to simulate the temperature response (step 1). Based on this model, a subsequent sensitivity analysis is conducted to identify the key material parameters that dominant the temperature response during the TPSS holder measurement (step 2). In addition to these studies, which obtains the temperature response with input material properties, I performed inverse studies to estimate the values of the identified key parameters based on the temperature response from the holder measurement (step 3). The FEM model incorporating these estimated parameter values is hereafter referred to as the *well-tuned model*. Finally, I import the data from the sample measurement to the well-tuned model for a subsequent inverse study to estimate the heat capacity of various samples (step 4).

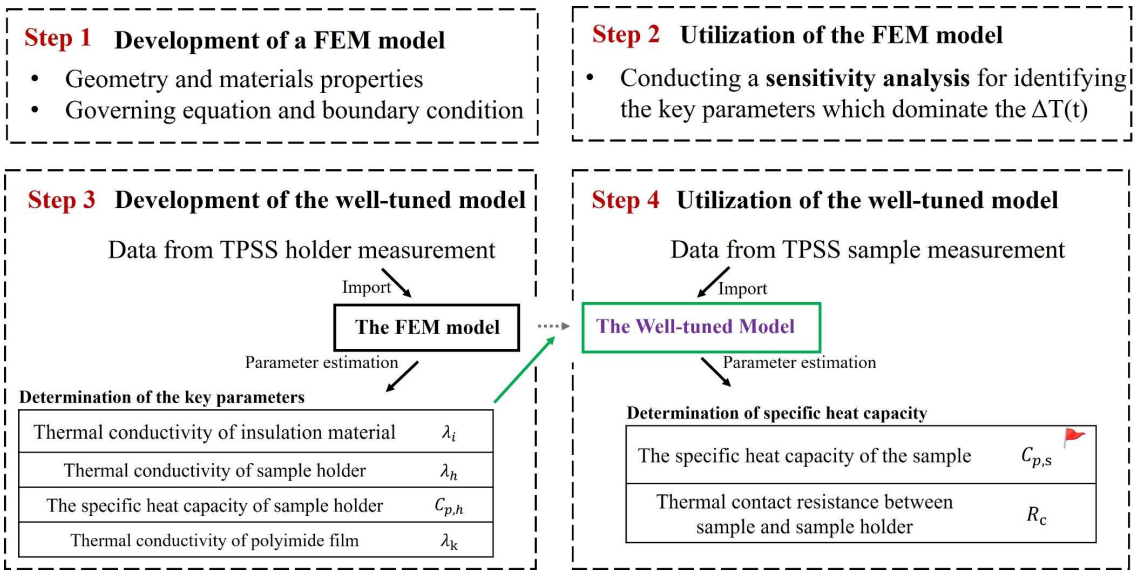

Fig. 4.2 Framework for developing and utilizing the well-tuned model to determine C_p of samples (Paper II). Figure reproduced with permission from Paper II; Copyright 2024 (CC-BY), Elsevier.

In step 1, the 2D simulation model was simplified based on the following assumptions:

- The heat transfer between measurement setup and ambient environment is negligible (adiabatic boundary condition).
- Heat transfer via convection and radiation within the setup is negligible.
- The measurement setup is axisymmetric, rendering the effects from sensor leads and the non-circular shape of the sample negligible.
- Material properties remain constant during the measurement.
- The spiral sensing element of the sensor can be represented by an ideal circular boundary heat source.

A detailed visualization of each component in the model is achieved through a 3D representation, obtained by rotating the 2D geometry, along with dimensional details (Fig. 4.3) that correspond to the experimental TPSS counterpart.

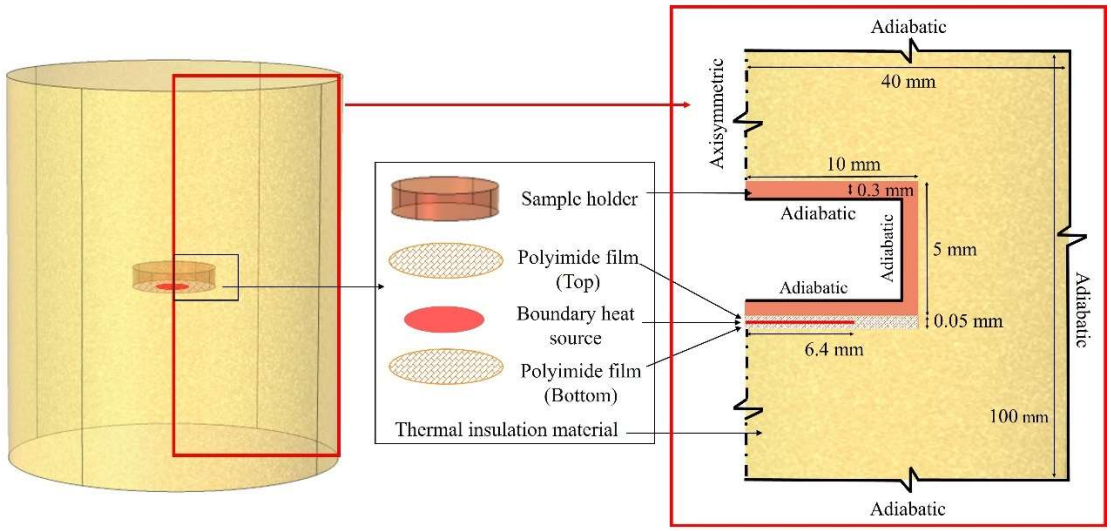

Fig. 4.3 Schematic of the model with its cross-sectional view. Selected components have been scaled to accommodate the wide range of dimensions and ensure all elements remain discernible. The sensing element is represented by an ideal circular boundary heat source (marked in red). Figure reproduced with permission from Paper II; Copyright 2024 (CC-BY), Elsevier.

The governing equations for transient heat conduction are employed in the simulation model. Prior to carried out systematic simulations, a mesh independence analysis was performed to determine the optimum mesh configuration for accuracy and computational efficiency (Fig. S1 in Papper II).

In step 2, a sensitivity analysis identified three parameters as most critical to the temperature response in the holder measurement: the thermal conductivity and the specific heat of the sample holder (λ_h and $C_{p,h}$) as well as the thermal conductivity of the thermal insulation material (λ_i). In addition, the thermal conductivity of Kapton sheets (λ_K) is also of interest. Since an ideal circular boundary heat source is used to represent the spiral sensing element, λ_K in the simulation serves as an equivalent thermal conductivity that enables the idealized source to replicate the behaviour of the actual spiral. Consequently, these four parameters (see step 3 in Fig. 4.3) are estimated based on the holder measurement data in the next step.

Table 4.2 Summary of the component properties used in the model. Errors in the table represent the estimated measurement uncertainty. a. Measured by the TPS measurement for slab samples [50, 51]. b. Calculated based on the specific heat capacity of the ingredients. c. Calculated from mass and volume. d. Measured by the TPS measurement for bulk samples [34]. e. Literature values [87].

Component	Material	$\lambda\,(\mathrm{W/(m\cdot K)})$	C_p $(\mathrm{J/(kg\cdot K)})$	ρ $(\mathrm{kg/m^3})$
Sample holder	Gold alloy	44 ± 10^{a}	177 ± 9^{b}	1065 ± 32^{c}
Thermal insulation material	Polyimide foam	0.039 ± 0.002^{d}	1090^{e}	6.6 ± 0.2^{c}
Insulation layer	Polyimide sheet	0.12^{e}	1090^{e}	1420^{e}

The model used in step 3 retains the same physical framework as that developed in step 1, but the four key parameters are initially unknown. These parameters are subsequently obtained through a fitting process that adjusts their values until the simulated temperature response closely aligns with the measured response. The fitting procedure minimizes the following objective function:

$$J = \sum_{n=t}^{t+\Delta t}\left[\Delta\hat{T}_n(\lambda_h, C_{p,h}, \lambda_i, \lambda_K) - \Delta T_n\right]^2/2 \tag{4.1}$$

where J denotes the least-square objective value, $\Delta\hat{T}_n$ represents the simulated average temperature increase of the sensor and ΔT_n is the measured average temperature increase, both evaluated at various time points t.

The fitting was carried out with a derivative-free optimization method called the bound optimization by quadratic approximation (BOBYQA) [88]. The core principle of the BOBYQA method involves iteratively approximating the objective function with a suitable quadratic model.

Once the four key parameters have been determined, the sample domain is introduced into the well-tuned model, and a subsequent fitting process is performed to estimate the heat capacity of the sample (step 4), along with the thermal contact resistance between the sample and sample holder. Similar to the conventional TPPS

method, only a part of the sample measurement data is utilized in the fitting process (Table 4.1)

4.3 Results and discussion

After step 3, the simulated temperature response from the well-tuned model agrees well with the measured data (Fig. 4.4 a), with deviations of less than 1 % for every data point. It should be noted that only the measured data with a heating power of 80 mW was utilized to estimate the four key parameters. Nevertheless, even when the heating power varied widely (40 – 120 mW), the good agreement between simulation and measurement remains, demonstrating the reliability of the well-tuned model. The estimated values of the four key parameters from step 3 are summarized in Table 4.3.

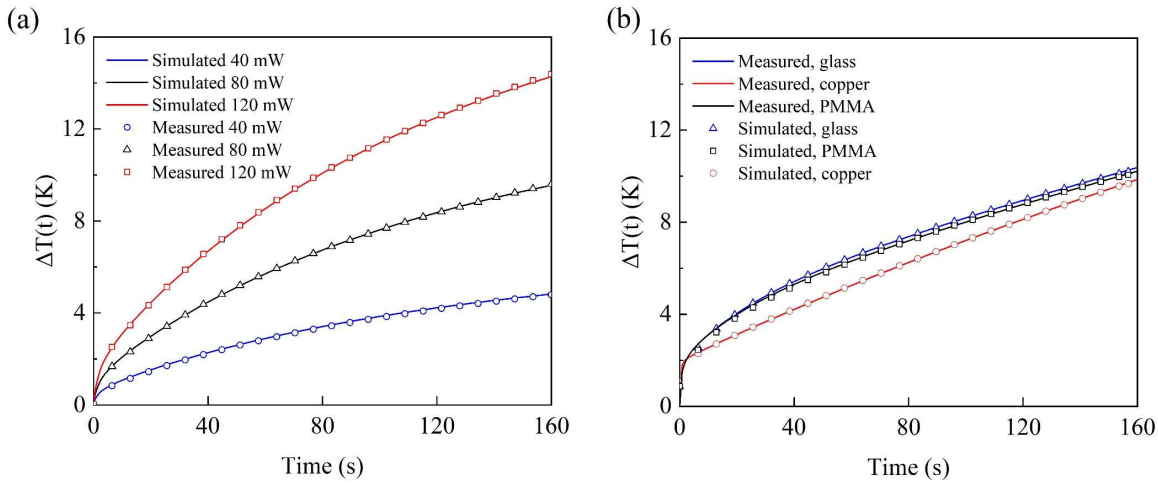

Fig. 4.4 Comparison between measured $\Delta T(t)$ (symbols) and simulated $\Delta T(t)$ (solid lines) in the case of (a) holder measurement and (b) sample measurement. Figures reproduced with permission from Paper II; Copyright 2024 (CC-BY), Elsevier.

Table 4.3 Estimated values of the four key parameters from the fitting process in step 3. Errors represent the standard deviation of repeated measurements.

Parameter	Estimated value
λ_h	34.6 ± 1.1 W/(mK)
λ_i	0.057 ± 0.001 W/(mK)
λ_K	0.017 ± 0.002 W/(mK)
$C_{p,h}$	154 ± 4 J/(kg · K)

Similarly, the simulated temperature response from the well-tuned model in step 4 closely aligns with measured data across different samples (Fig. 4.4 b). The estimated values of sample C_p are extracted and summarized in Table. 4.4. In general, these C_p values closely match the corresponding reference values, with an average difference of less than 4.4 %. This agreement demonstrates the ability of the well-tuned model to accurately determine C_p from experimental data.

In addition to the estimation of C_p, I used the well-tuned model to perform a heat balance analysis, revealing the distribution of heat accumulation among the different components. This analysis aims to provide deeper insight into how inaccuracies in heat loss affect the results of conventional TPSS measurements.

In the case of the holder measurement (Fig. 4.5 a), the rate of heat accumulation in the sample holder decreases over time. In contrast, the rate of heat accumulation in the insulation material, i.e., the heat loss, steadily increases and eventually surpasses that of the sample holder at around 60 s. By the end of the measurement, heat loss accounts for a substantial 74 % of the overall power supplied by heating.

Table 4.4 Comparison between C_p estimated by the well-tuned model and corresponding reference values from DSC or DPS [85, 86] measurements. The uncertainty of each estimation is lower than 4 % (see Section 4.1, Paper II), while the errors on the average values represent the standard deviation of repeated measurements.

C_p $(\mathrm{J/(kg \cdot K)})$	Trial	Copper	Glass	PMMA
Sample A	1	382	836	1393
	2	386	837	1427
	3	381	836	1382
Sample B	4	378	781	1477
	5	380	777	1473
	6	381	783	1491
Sample C	7	380	802	1402
	8	383	806	1402
	9	379	802	1403
Average		381 ± 19	807 ± 40	1428 ± 71
Reference		384 ± 19	843 ± 34	1437 ± 29

In the case of the copper measurement (Fig. 4.5 b), the heat accumulation in the sample holder and the heat loss is similar to those observed as part of the holder measurement. In addition, a substantial fraction of the heat is absorbed by the copper sample, resulting in smaller portion of heat loss compared to the holder measurement.

With knowledge of the heat loss, the shape of the heat loss function in the conventional TPSS theory can be extracted by $f(t) = Q(t)/\frac{d}{dt}\big(\Delta T(t)\big)$. In the case of copper measurements, the difference between $f_h(t)$ and $f_s(t)$ remains below 8 % within the recommended time ranges from 20 to 40 s (Fig. 4.5 c). However, the difference gradually increases over time, reaching 48 % by the end of the measurement, which is consistent with the observed deviation (see Fig. 4.1 b). In the case of PMMA measurements, there is no clear period during which $f_h(t)$ and $f_s(t)$ consistently exhibit

a close relationship. The difference between them reaches 20 % at the end of the measurement.

Furthermore, I determined the relative inaccuracies in heat loss calculation (ϵ_Q) using the following equation:

$$\epsilon_Q(t) = \frac{f_r(t)\frac{d}{dt}(T_s(t)) - Q_s(t)}{P_s} \tag{4.2}$$

where Q_s is the rate of heat loss during the sample measurement.

In the case of copper, $\varepsilon_Q(t)$ remains within 1 % during the recommended time range (Fig. 4.5 d, red region), which contributes to the accurate determination of the C_p of copper. For PMMA, $\varepsilon_Q(t)$ ranges from 3 % to 10 % within the recommended time range of 120 s to 160 s (Fig. 4.5 d, blue region). A high positive $\varepsilon_Q(t)$ indicates that the heat loss is overestimated, which contributes to an underestimate of the specific heat capacity of PMMA.

In this chapter, I have discussed a series of FEM simulations that allow me to investigate the reason for the underestimated results from TPSS measurements. A well-tuned model was described with its key material properties tuned based on data from a holder measurement. This model enables the accurate determination of sample C_p from given data obtained from sample measurements. Moreover, a heat balance analysis was carried out based on the simulated data from the well-tuned model. The analysis revealed that the conventional TPSS theory tends to overestimate the heat loss in the sample measurements when the measurement time is large, thereby leading to an underestimated heat capacity especially for low thermal conductivity samples.

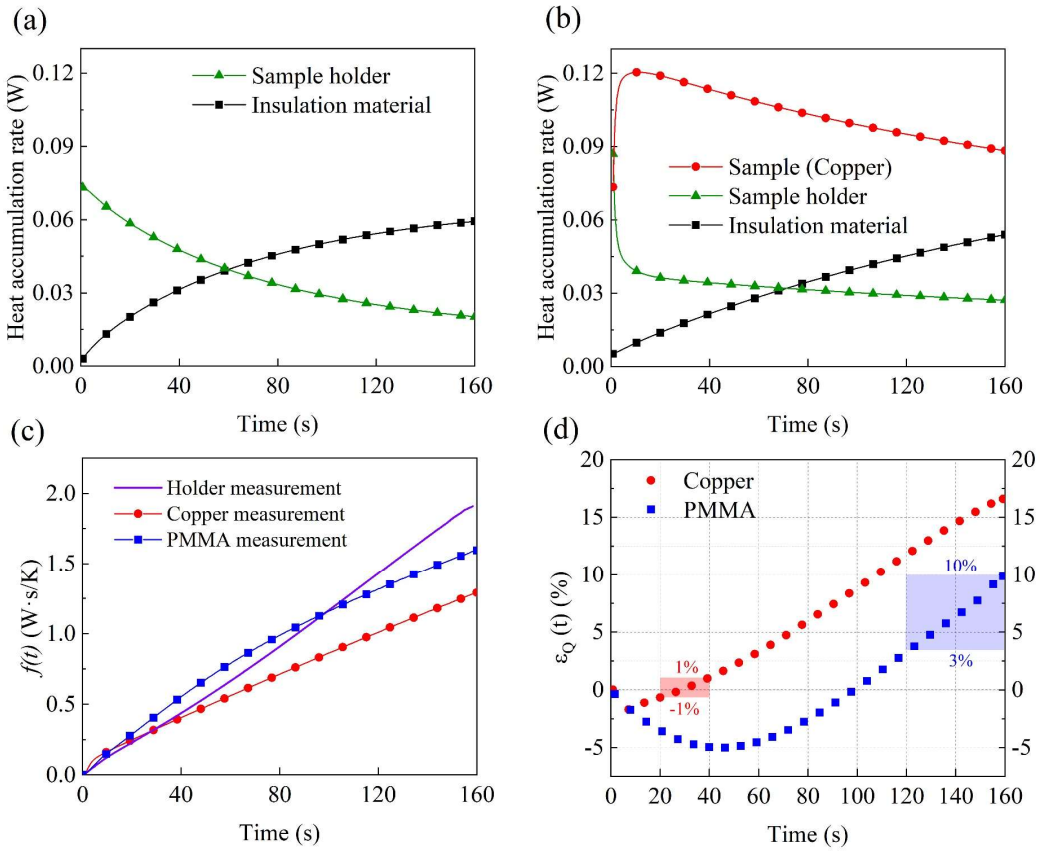

Fig. 4.5 (a) The rate of heat accumulation by different components during the holder measurement and (b) during the sample measurement. (c) Comparison between the heat loss function $f(t)$ associated with the holder measurement and the sample measurement of copper and PMMA. (d) Relative error of heat loss determination in the case of copper and PMMA, calculated using Eq. 4.2. Figures reproduced with permission from Paper II; Copyright 2024 (CC-BY), Elsevier.

5. Role of thermal conductivity on thermoelectric devices

Knowledge about thermal transport and the thermal conductivity is important for the optimization of numerous advanced devices [71, 72]. This section examines how FEM simulations can be used to understand the heat transport and the performance of a thermoelectric generator (TEG). TEGs are introduced in Section 5.1, followed by a thorough discussion of the simulation model and results in Section 5.2.

5.1 Thermoelectric generator

Thermoelectric materials can directly convert thermal into electrical energy through the thermally driven accumulation of charge carriers (holes and electrons) [89, 90]. This phenomenon, known as the Seebeck effect, can be described by the following equation:

$$\Delta V = -S\Delta T_{te} \tag{5.1}$$

where ΔT_{te} denotes the temperature difference across the thermoelectric material, S is a material parameter called the Seebeck coefficient, and ΔV is the potential difference generated as a result of the temperature difference.

There will be a thermal resistance (R_c) between the thermoelectric materials and the heat source and heat sink [91, 92], which is typically considered to be connected in series with the thermal resistance of thermoelectric material (R_{te}) (Fig. 5.2). Hence, the following equation can be used to estimate ΔT_{te} [91]:

$$\Delta T_{te} = \Delta T_{hc} \cdot \frac{R_{te}}{R_c + R_{te}} \tag{5.2}$$

where ΔT_{hc} is the temperature difference between the heat source and heat sink.

Thermoelectric materials are typically fabricated into legs with cuboid or cylindrical geometries, characterized by a cross-sectional area (A_{te}) and length (L_{te}).

Consequently, the thermal resistance R_{te} and electrical resistance ($R_{e,te}$) of a thermoelectric leg can be expressed as:

$$R_{te} = \frac{L_{te}}{\lambda A_{te}} \text{ and } R_{e,te} = \frac{L_{te}}{\sigma A_{te}} \tag{5.3}$$

where λ and σ denote the thermal and electrical conductivities of the thermoelectric material, respectively.

Thermoelectric materials are further classified as p-type or n-type depending on their majority charge carriers [89, 90]. In p-type materials, holes are the dominant charge carriers and the Seebeck coefficient is positive ($S_p > 0$), whereas in n-type materials, electrons are the dominant charge carriers and the Seebeck coefficient is negative ($S_n < 0$). Typically, one p-type and one n-type leg form the basic unit (Fig. 5.1), or thermocouple, of a TEG. A TEG can be regarded as M pairs of thermocouples that are electrically connected in series and thermally connected in parallel. Under load matching conditions, TEGs deliver their maximum power (P_{max}) [91]:

$$P_{max} = \frac{{V_{oc}}^2}{4R_{e,int}} = \frac{(M \cdot V_{te})^2}{4R_{e,int}} = \frac{(M \cdot S_{tc} \cdot \Delta T_{tc})^2}{4R_{e,int}} \tag{5.4}$$

where V_{oc} is the open circuit voltage of the TEG, M is the number of thermocouples within the TEG, and $S_{tc} = S_p - S_n$ is the effective Seebeck coefficient of the thermocouple. $R_{e,int}$ denotes the total internal electric resistance of the TEG, which consists of the electrical resistance of thermoelectric legs and the electrical contact resistance between them.

There are multiple ways to optimize the performance of TEGs. From a thermal perspective (Eqs. 5.1-5.4), decreasing the thermal conductivity of the thermoelectric materials increases R_{te} and V_{oc}, eventually resulting in a higher P_{max}. From an electrical perspective (Eqs. 5.3-5.4), reducing the electrical resistance of the thermoelectric legs or the electrical contact resistance increases P_{max}.

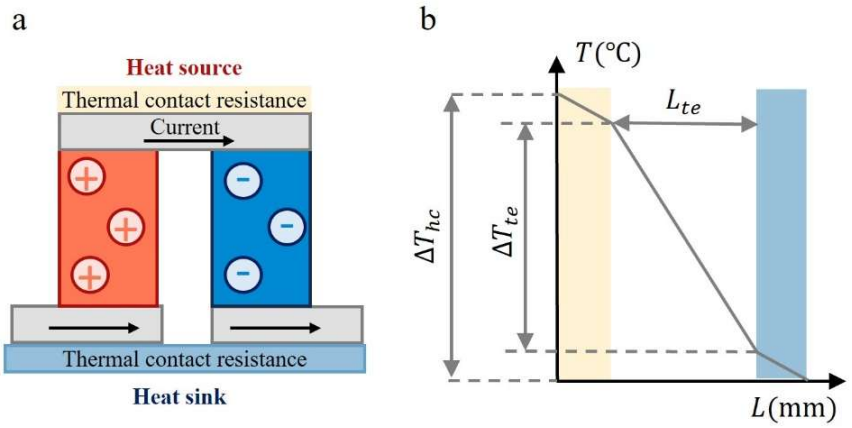

Fig. 5.1 (a) Schematic of a thermocouple, consisting of a pair of p-type (red) and n-type (blue) legs, placed between a heat source and a heat sink. The temperature difference induces diffusion of charge carriers (holes: positive signs, electrons: negative signs), balanced by a drift current. (b) Relationship between ΔT_{hc} and ΔT_{te}: the latter is smaller owing to thermal contact resistance. Figures reproduced with permission from Ref [91]; Copyright 2020 (Creative Commons CC-BY), Elsevier.

5.2 Thermoelectric textile and corresponding simulations

Recent advancements in organic thermoelectric materials have enabled the integration of TEGs into textiles [91, 93, 94], referred to as thermoelectric textiles, for powering small wearable electronics within the Internet of Things (IoT) framework. In this section, I present a thermoelectric textile that employs two state-of-the-art organic thermoelectric materials: poly(3,4-ethylenedioxythiophene):poly(styrenesulfonate) (PEDOT:PSS) and poly(benzodifurandione) (PBFDO) as the p- and n-type material, respectively. These two materials are coated on silk yarns, respectively, which were hand-sewn through a felt wool forming eight thermocouples by the co-authors in Paper III (Fig. 5.2 a).

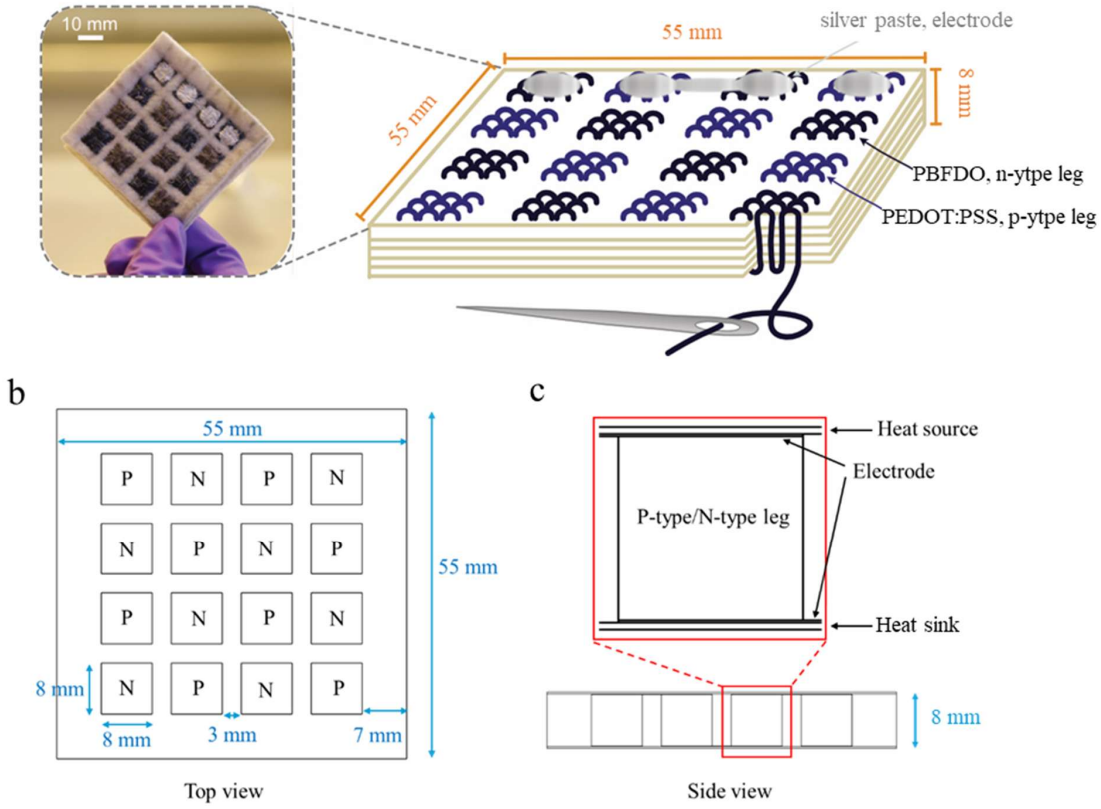

Fig. 5.2 (a) Schematic and photograph of the thermoelectric textile, which was fabricated by Chunghyeon Choi, Hyungsub Yoon and Dr. Mariavittoria Craighero. (b) Top view and (c) side view of the FEM model of the thermoelectric textile, along with the corresponding dimensions. Figures reproduced with permission from Paper III; Copyright 2024 (CC-BY), WILEY.

To investigate potential strategies for optimizing the performance of the thermoelectric textile, a corresponding FEM model was developed (Fig. 5.2 a-b, see Paper III for details). The simulated V_{oc} and P_{max} agree with the measured values (Fig. 6 b in Paper III), which validates the FEM model. Using the validated model, I first investigated the influence of the TEG thickness (L_{te}) and electrical contact resistance of each thermocouple ($R_{e,tc}$) (Fig. 5.3 a). A larger L_{te} results in a larger thermal resistance of thermoelectric legs R_{te} and thus a larger V_{oc}. However, it also increases the internal electrical resistance of the TEG, which leads to a decline of P_{max} at large L_{te}. The interplay between thermal and electrical contact resistances determines the optimal L_{te} with highest P_{max} . $R_{e,tc}$ also plays a significant role in the TEG

performance. In the case of $R_{e,tc} = 1\ \Omega$, for example, P_{max} reaches 1.95 μW for an optimal L_{te} of 5.0 mm. This value of P_{max} is more than three times higher, while the value of L_{te} is approximately half, compared to the case of $R_{e,tc} = 9.1\ \Omega$.

Furthermore, I investigated the influence of the number of coated yarns that make up each thermocouple leg (Fig. 5.3 b), quantified by the thread count (N_t). Because the thermal conductivity of coated yarns (approximately 0.18 $\mathrm{W/(m \cdot K)}$) is considerably higher than that of wool (0.056 $\mathrm{W/(m \cdot K)}$) [91], a larger N_t leads to a higher effective thermal conductivity of a leg, which decreases the temperature difference across each leg and hence reduces V_{oc}. On the other hand, a larger N_t results in a lower electrical resistance of the textile thermopile, eventually leading to a slightly higher P_{max} at the optimal L_{te}. Owing to the smaller temperature difference, increasing the thread count does not appear to be an effective way to improve P_{max}. For instance, tripling N_t from 90 to 270 results in only a modest 15 % increase in P_{max}, with an optimal L_{te} of around 23 mm, which is already too thick for practical wearable applications.

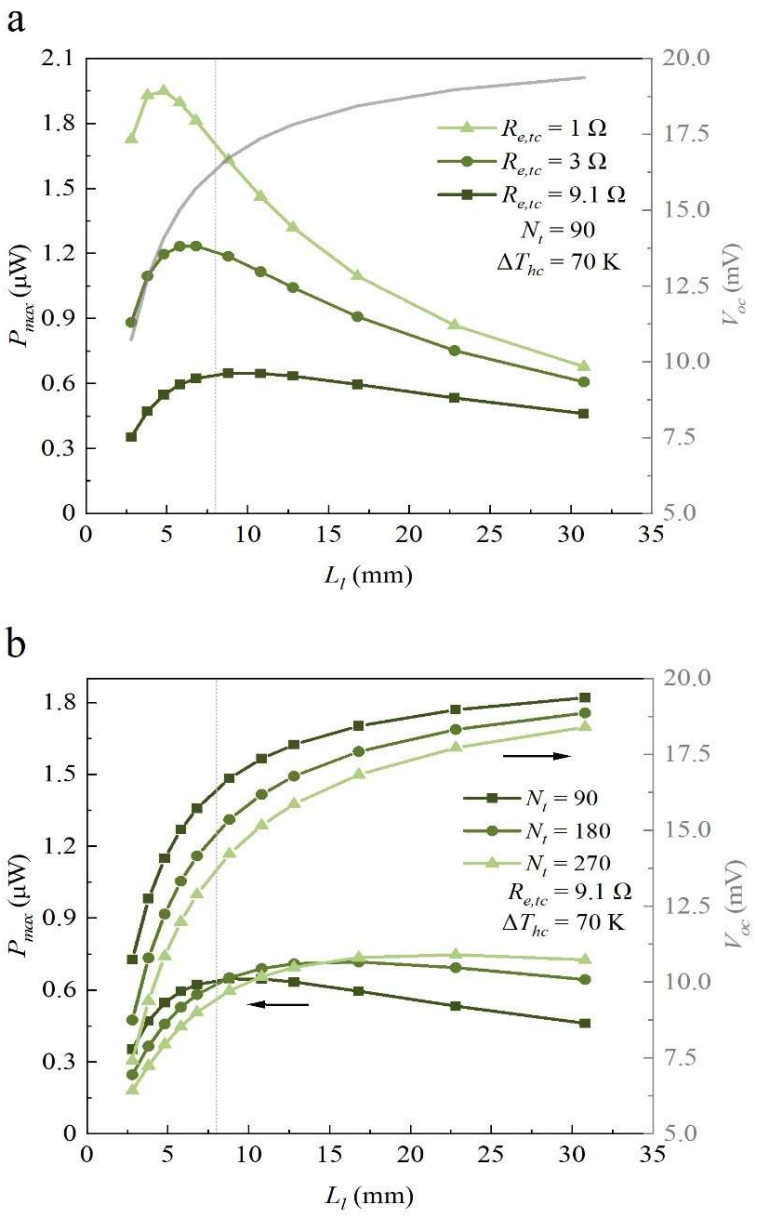

Fig. 5.3 (a) Simulated P_{max} (right) and V_{oc} (left) of the thermoelectric textile as a function of leg length (L_{te}), under a thread count (N_t) of 90 and different electrical contact resistances per thermocouple ($R_{e,tc}$). The vertical grey line at L_{te}= 8 mm represents the actual thickness of the textile. (b) Simulated P_{max} (right) and V_{oc} (left) of the thermoelectric textile as a function of leg length (L_{te}), under a $R_{e,tc}$ of 9.1 Ω and different values of N_t. Figures reproduced with permission from Paper III; Copyright 2024 (CC-BY), WILEY.

6. Conclusions and outlook

In this thesis, I present improvements to TPS-based measurements that enhance their applicability and accuracy, contributing to the broader field of thermal property characterization.

For thin layers, I demonstrated that their intrinsic thermal conductivity can be accurately determined using TPS measurements, rather than being limited to their apparent thermal conductivity (Paper I). Through systematic investigations, I found that the influence of thermal contact resistance is significant and cannot be compensated for simply by comparing results across layers of different thicknesses (the slope method). This is because the thermal contact resistance can vary with the layer thickness—thicker layers tend to exhibit lower pliability and larger thermal contact resistance. This is at odds with the underlying assumption of the slope method and led to errors of up to 26 % in case of micrometer-thick polyolefin layers.

With introduction of a liquid interface material, e.g., deionized water, the correlation between layer thickness and thermal contact resistance was alleviated. Consequently, non-destructive and accurate characterization of polyolefin layers was achieved using the slope method, with errors below 4 %. Furthermore, I demonstrated that as few as two pairs of samples can yield precise results, with a standard deviation below 0.02 $\mathrm{W/(m \cdot K)}$, provided that their thickness differs by more than 200 μm.

In addition, I comprehensively quantified the errors arising from non–one-dimensional heat flux across the layer, which can increase dramatically to over 100 % with increasing layer thermal conductivity and thickness (Paper IV). To maintain acceptable errors ($<$ 10 %), multiple constraints on layer properties (thermal conductivity < 2 $\mathrm{W/(m \cdot K)}$ and thickness $<$ 600 μm) and sensor geometry (radius $>$ 11 mm) must be strictly followed.

To extend the applicability of TPS measurements, I proposed the Layer 2D model (Paper IV), which accounts for non-one-dimensional heat flux across the layer, along with an iterative algorithm that automatically selects time range for data analysis. The Layer 2D model substantially relaxes these constraints, expanding the applicable range of layer thermal conductivity by an order of magnitude (up to 20 $\mathrm{W/(m \cdot K)}$) and thickness by about three times (up to 2000 μm) (Fig. 5.1). More importantly, the Layer 2D model enables the use of a new TPS probe for layer characterization, featuring a radius of only 6.6 mm. Measurements and finite element simulations further indicate that errors below 10 % can be achieved, provided that the thermal contact resistance is mitigated—for example, by using a thermal interface material with a conductivity greater than 3 $\mathrm{W/(m \cdot K)}$.

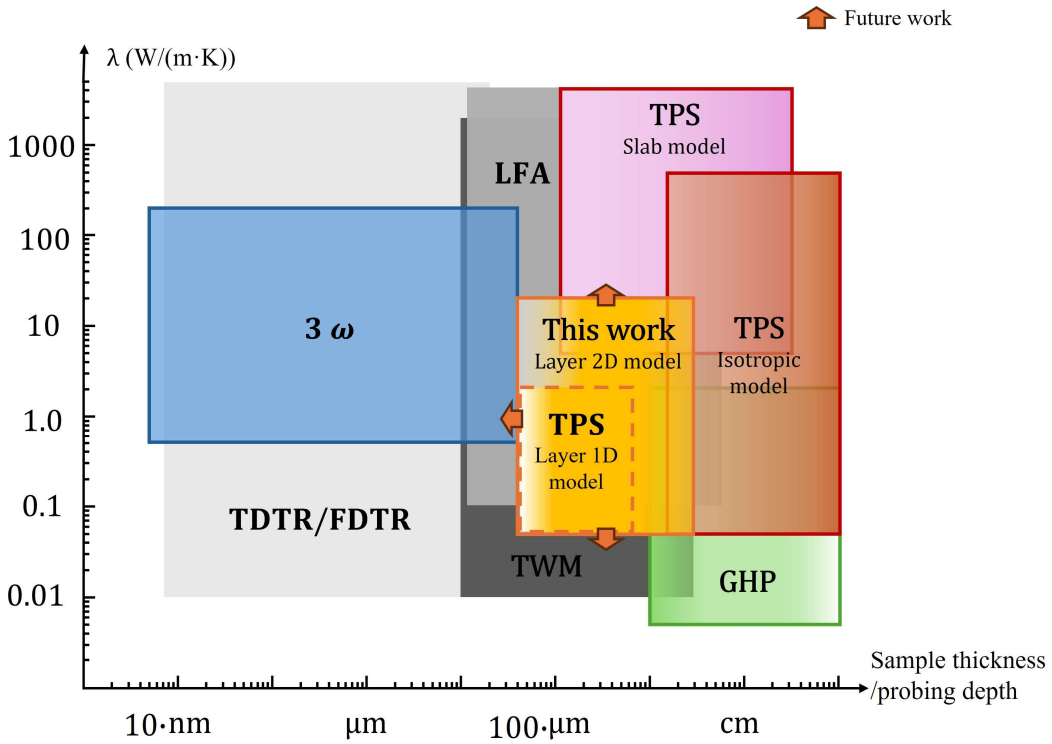

Fig. 5.1 Comparison of sample thickness/probing depth and thermal conductivity ranges across multiple commercial methods: TPS [49], TDTR [95], FDTR [96], 3-ω [97], LFA [98], TWM [99] and GHP [100]. Colored regions with frames indicate the specifications of the methods for directly measuring thermal conductivity, while the greyscale areas represent those for measuring thermal diffusivity. Arrow signs denote the potential directions for future enhancement in the TPS method.

In case of TPSS measurements for direct heat capacity determination (Paper II), I demonstrated that the inaccuracies for low thermal conductivity samples ($< 1\ \mathrm{W/(m \cdot K)}$) arise from incorrect estimation of heat loss. This error increases over time and can reach as high as 43 % for low conductivity materials such as PMMA. To precisely quantify the heat loss, a numerical model based on the finite element method was developed, with its key material properties tuned using the data of the holder measurement (without a sample). Subsequently, this model was utilized to analyze the sample measurement data and estimate the heat capacity of the samples. The estimated values agree with the reference specific heat capacity, showing a difference of approximately 4 %. Overall, this data analysis approach extends the applicability of TPPS measurements to samples with a thermal conductivity as low as $0.19\ \mathrm{W/(m \cdot K)}$ (Fig. 5.2), including many polymers, textiles, and laminated materials.

Through finite element simulations (Paper III), I showed that thermal transport and thermal conductivity play a crucial role in the design of TEGs. In thermoelectric textiles, the internal thermal resistance of the thermoelectric legs, influenced by the leg thickness and the number of yarns coated with thermoelectric materials, must be carefully considered. The interplay between internal thermal and electrical resistances ultimately determines the optimal performance of these textiles.

The continuous advancement of technology introduces increasingly demanding requirements for thermal property measurements. Due to material scarcity or functional design constraints, many advanced materials are now fabricated as small samples or as nano- to micrometer-thin layers, making accurate thermal characterization particularly challenging. While the TPS method has proven highly effective for bulk materials, future developments in probe design and modeling may extend its applicability to micro- and nanoscale systems (Fig. 5.1). Meanwhile, the rapid rise of electric vehicles has driven growing interest in the thermal properties of batteries. To preserve structural integrity and realistic heat transfer pathways, measurements are preferably performed on complete cells rather than disassembled components. However, the heterogeneous structures of prismatic batteries and the curved surfaces of cylindrical batteries demand advanced mathematical models and carefully designed measurement procedures. To achieve accurate property extraction, corresponding sensitivity analyses are essential to

assess parameter identifiability of fitting process. Overall, although a number of validated methods exist for thermal property characterization, the field now faces not only unprecedented opportunities but also challenges with regard to meeting the demands of emerging technologies.

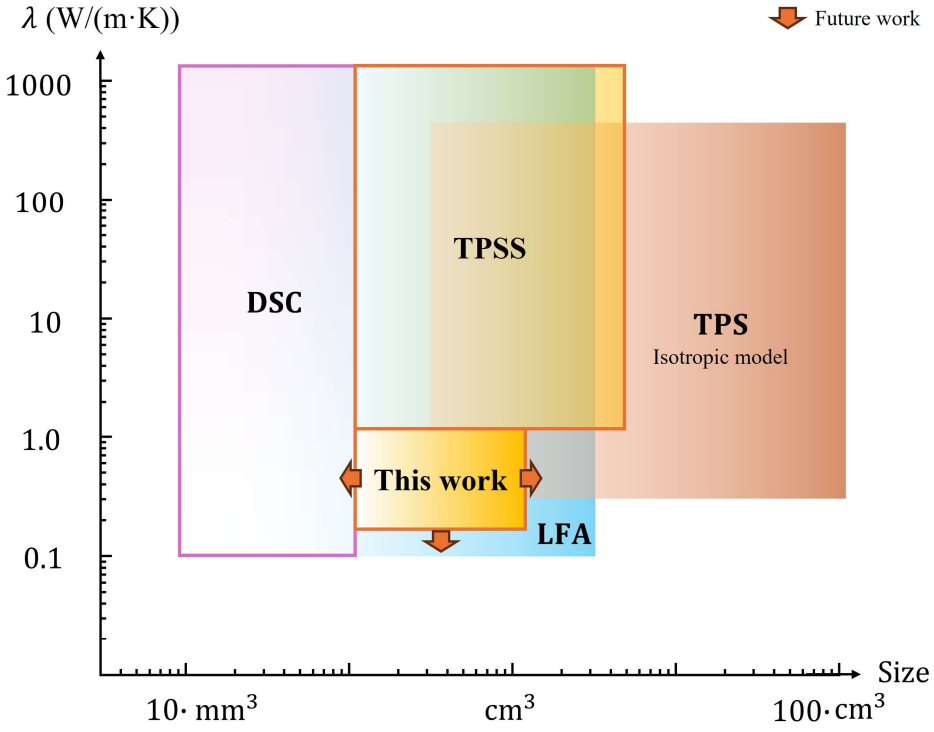

Fig. 5.2 Comparison of sample size and thermal conductivity ranges across multiple commercial methods: DSC [101], LFA [98, 102], TPSS [49], and the TPS isotropic model [49]. Colored regions with frames indicate the specifications applicable to both isotropic and non-isotropic samples, while greyscale areas represent ranges applicable only to isotropic samples. Arrow signs denote the potential directions for future enhancement in the TPSS method.

ACKNOWLEDGMENTS

There is a Chinese idiom, “白驹过隙,” which expresses how quickly time passes — literally, “time flies like a white pony flashing past a narrow gap.” I have never felt this sense of fleeting time more keenly. I can still easily recall how excited I was when I received the news of acceptance for the PhD position from Besira and Christian four years ago. I clearly remember the fabulous and colorful autumn scenery, yet also the frosty feeling when I landed alone in Sweden on October 22, 2021. Thankfully, four years later, I now have the opportunity to defend my PhD degree, supported by my supervisors, colleagues, friends, and family. I am deeply grateful.

I would like to express my sincere gratitude to my supervisor at Chalmers, Prof. Christian Müller, for your excellent supervision and scientific guidance, which have helped me grow into a more capable researcher. It has been a great pleasure to be part of your group, learning fascinating knowledge about polymers. I will never forget the inspiring ideas you shared with us — such as the “attention test with a gorilla passing through” and “organic semiconductor chlorophyll” — which have truly encouraged me to think differently. I am sure that what I have learned from you will guide me throughout life.

I would like to express my sincere gratitude to my supervisor at Hot Disk AB, Dr. Besira Mihiretie, for your unwavering support in both academia and life, which has helped me grow tremendously. You guided me as I adapted to a new life in Sweden, introduced me to the world of TPS techniques, and consistently supported me whenever I was in need. I truly enjoyed our discussions on science and engineering — I could not have achieved what I have today without your guidance and encouragement.

My sincere thanks go to Prof. Andreas Dahlin, my examiner, and Prof. Itai Panas, my study director, for ensuring that my studies stayed on track. I am also grateful to Prof. Ergang Wang for providing computational resources during my research. Finally, I extend my gratitude to Prof. Bijan Adl-Zarrabi for his valuable comments during my Licentiate defense.

I am deeply grateful to all my colleagues at Hot Disk AB. In particular, my heartfelt thanks go to Anton Ma, Andrey Sizov, Wayne Dilles, and Bitnoori Lee for our valuable scientific and everyday discussions; Carina Jannesson and Anna Vallin for their kind support and daily assistance; Tomas Nyqvist, Albin Otterberg, Teo Nyqvist, and Lukas Nyqvist for their fantastic hardware support; Anders Isacson and Thomas Gustafsson for their excellent software support; and Jesper Löfman for his amazing photography skills.

Special thanks go to Silas Gustafsson and Lars Hälldahl, who founded Hot Disk 30 years ago and made everything possible. I would also like to express my sincere appreciation to Mattias Gustavsson, Henrik Otterberg, and Johan Gustavsson for their continued dedication to the operation of Hot Disk and Kagaku.

Throughout my PhD, I truly enjoyed being surrounded by amazing colleagues from Müller's group. I have always believed that I can learn a great deal from colleagues, not only from supervisors. Mavi and Joost, it was a great pleasure to share the entire PhD journey with you both within the same HORATES consortium. Mavi, you are a fantastic team player — your patience, optimism, and willingness to help others made every collaboration enjoyable and productive. Joost, you have truly inspired me with your clear vision and your dedication to pursuing it without reservation. I would also like to thank Przemyslaw for being one of my few co-authors over the past few years. I have learned so much from you, both about polymers and about life. I am also grateful to Judy for our daily chats in my mother tongue, Cantonese — they always brought me comfort. I would like to express my gratitude to all members of the group for their kindness and for fostering such a positive and collaborative research environment: Amin, Andrii, Jan, Jessica, Jochen, Judith, Meghna, Shuichi, Ts-Pei, and Vero.

I would also like to thank all the lovely people from the 8th floor. Thank you, Lotta and Sara, for being so helpful and for taking such good care of the floor. Thank you, Alex H and Krzysztof, for the thrilling tennis matches we had. Thank you, Krzysztof and Monika, for organizing so many interesting events for us. Thank you, Monika and Albin, for keeping my plant alive — it has lasted longer than any other I've grown! Thank you all for making the 8th floor feel as close as a family: Mathis, Ruby, Vale,

Jinhui, Jess, Yixu, Jinnan, Megan, Pablo, Purin, Ting, and Lidiya. I will always remember the wonderful moments we shared together.

My sincere thanks go to Prof. Mariano Campoy, Dr. Sebastian Reparaz, Jiali, Paolo, and Kai for the wonderful time during my first secondment at ICMAB in Barcelona. I am also grateful to Prof. Igor Zozoulenko, Najmeh, and Qifan for the fantastic experience during my second secondment at LiU in Linköping.

I am deeply thankful to Zhiwei Lu, who has always shared valuable experiences with me and cared for me like an elder brother. I am also thankful to Shuaiqiao Peng for the wonderful times we spent together during vacations and for his thoughtful advice and inspiring insights.

I would like to thank my tennis teammates from Team Landvetter — Jesper R, Aniroodh, Alfred, and Gabriel. I will never forget the joyful and sweet moments we had on the court.

Finally, and most importantly, I would like to express my deepest gratitude to my family. I am especially grateful to my wife, Jinmin, who has been by my side for the past ten years. You always stood with me, offering love, understanding, and unwavering support — especially during the most challenging moments of my studies. I look forward with joy to continuing our journey together and building our future hand in hand.

I would also like to thank my parents, who raised me and provided the best environment for me to grow up. Your love, guidance, and unwavering support have shaped who I am today. Thank you for your encouragement, for always believing in me, and for being my strongest source of strength throughout my life.

BIBLIOGRAPHY

[1] H.S. Carslaw, J.C. Jaeger, Conduction of Heat in Solids, Oxford Science Publications, New York, 2000.

[2] R. Hanus, R. Gurunathan, L. Lindsay, M.T. Agne, J. Shi, S. Graham, G. Jeffrey Snyder, Thermal transport in defective and disordered materials, Applied Physics Reviews 8 (3) (2021) 031311.

[3] J.M. Ziman, Electrons and phonons: the theory of transport phenomena in solids, Oxford University Press, 2001.

[4] F.W. Sears, G.L. Salinger, Thermodynamics, kinetic theory, and statistical thermodynamics, Addison-Wesley Reading, 1975.

[5] A. Sommerfeld, H. Bethe, Elektronentheorie der Metalle, Springer-Verlag, 2013.

[6] X. Qian, J. Zhou, G. Chen, Phonon-engineered extreme thermal conductivity materials, Nature Materials 20 (9) (2021) 1188-1202.

[7] C. Huang, X. Qian, R. Yang, Thermal conductivity of polymers and polymer nanocomposites, Materials Science and Engineering: R: Reports 132 (2018) 1-22.

[8] H. Chen, V.V. Ginzburg, J. Yang, Y. Yang, W. Liu, Y. Huang, L. Du, B. Chen, Thermal conductivity of polymer-based composites: Fundamentals and applications, Progress in Polymer Science 59 (2016) 41-85.

[9] K. Kurabayashi, Anisotropic thermal properties of solid polymers, International Journal of Thermophysics 22 (1) (2001) 277-288.

[10] S. Ronca, T. Igarashi, G. Forte, S. Rastogi, Metallic-like thermal conductivity in a lightweight insulator: solid-state processed ultra high molecular weight polyethylene tapes and films, Polymer 123 (2017) 203-210.

[11] Y. Xu, D. Kraemer, B. Song, Z. Jiang, J. Zhou, J. Loomis, J. Wang, M. Li, H. Ghasemi, X. Huang, Nanostructured polymer films with metal-like thermal conductivity, Nature Communications 10 (1) (2019) 1771.

[12] Y. Xu, X. Wang, J. Zhou, B. Song, Z. Jiang, E.M. Lee, S. Huberman, K.K. Gleason, G. Chen, Molecular engineered conjugated polymer with high thermal conductivity, Science advances 4 (3) (2018) eaar3031.

[13] A. Shanker, C. Li, G.-H. Kim, D. Gidley, K.P. Pipe, J. Kim, High thermal conductivity in electrostatically engineered amorphous polymers, Science Advances 3 (7) (2017) e1700342.

[14] D. Kraemer, G. Chen, A simple differential steady-state method to measure the thermal conductivity of solid bulk materials with high accuracy, Review of Scientific Instruments 85 (2) (2014) 025108.
[15] X. Qian, Z. Ding, J. Shin, A.J. Schmidt, G. Chen, Accurate measurement of in-plane thermal conductivity of layered materials without metal film transducer using frequency domain thermoreflectance, Review of Scientific Instruments 91(6) (2020) 064903.
[16] G. Xia, L. Cao, G. Bi, A review on battery thermal management in electric vehicle application, Journal of Power Sources 367 (2017) 90-105.
[17] Y. Xie, Y. Fan, R. Yang, K. Zhang, B. Chen, S. Panchal, Y. Zhang, Influence of uncertainty of thermal conductivity on prediction accuracy of thermal model of lithium-ion battery, IEEE Transactions on Transportation Electrification 10 (4) (2024) 8713-8727.
[18] Z. Wang, J. Ma, L. Zhang, Finite element thermal model and simulation for a cylindrical Li-ion battery, IEEE Access 5 (2017) 15372-15379.
[19] D. Zhao, X. Qian, X. Gu, S.A. Jajja, R. Yang, Measurement techniques for thermal conductivity and interfacial thermal conductance of bulk and thin film materials, Journal of Electronic Packaging 138 (4) (2016) 040802.
[20] Ľ. Kubičár, V. Boháč, P. Gaal, D. Apostolescu, Review of several dynamic methods of measuring thermophysical parameters, Proc. of 24th Int. Conf. on Thermal Conductivity/12th Int. Thermal Expansion Symposium", Technomic Publishing Co., Lancaster, PA, 1999, pp. 135-149.
[21] ISO 8302:1991, Thermal insulation — Determination of steady-state thermal resistance and related properties — Guarded hot plate apparatus.
[22] ISO 8301:1991, Thermal insulation — Determination of steady-state thermal resistance and related properties — Heat flow meter apparatus.
[23] D.G. Cahill, Analysis of heat flow in layered structures for time-domain thermoreflectance, Review of Scientific Instruments 75 (12) (2004) 5119.
[24] P. Jiang, X. Qian, R. Yang, Tutorial: Time-domain thermoreflectance (TDTR) for thermal property characterization of bulk and thin film materials, Journal of Applied Physics 124 (16) (2018) 161103.
[25] A.J. Schmidt, R. Cheaito, M. Chiesa, Characterization of thin metal films via frequency-domain thermoreflectance, Journal of Applied Physics 107 (2) (2010) 024908.
[26] J.A. Malen, K. Baheti, T. Tong, Y. Zhao, J.A. Hudgings, A. Majumdar, Optical measurement of thermal conductivity using fiber aligned frequency domain thermoreflectance, Journal of Heat Transfer 133 (8) (2011) 081601.

[27] ISO 22007-4:2024, Plastics — Determination of thermal conductivity and thermal diffusivity — Part 4: Light flash method.
[28] J. Yang, E. Ziade, A.J. Schmidt, Uncertainty analysis of thermoreflectance measurements, Review of Scientific Instruments 87 (1) (2016) 014901.
[29] L.A. Pérez, K. Xu, M.R. Wagner, B. Dörling, A. Perevedentsev, A.R. Goñi, M. Campoy-Quiles, M.I. Alonso, J.S. Reparaz, Anisotropic thermoreflectance thermometry: A contactless frequency-domain thermoreflectance approach to study anisotropic thermal transport, Review of Scientific Instruments 93 (3) (2022) 034902.
[30] J. Zhu, D. Tang, W. Wang, J. Liu, K.W. Holub, R. Yang, Ultrafast thermoreflectance techniques for measuring thermal conductivity and interface thermal conductance of thin films, Journal of Applied Physics 108(9) (2010) 094315.
[31] Y.-H. Zhao, Z.-K. Wu, S.-L. Bai, Thermal resistance measurement of 3D graphene foam/polymer composite by laser flash analysis, International Journal of Heat and Mass Transfer 101 (2016) 470-475.
[32] D.G. Cahill, Thermal conductivity measurement from 30 to 750 K: the 3ω method, Review of Scientific Instruments 61 (2) (1990) 802-808.
[33] ISO 22007-3:2008, Plastics — Determination of thermal conductivity and thermal diffusivity — Part 3: Temperature wave analysis method.
[34] ISO 22007-2:2022, Plastics — Determination of thermal conductivity and thermal diffusivty — Part 2: Transient plane heat source (hot disc) method.
[35] C. Dames, Measuring the thermal conductivity of thin films: 3 omega and related electrothermal methods, Annual Review of Heat Transfer 16 (2013).
[36] T. Hashimoto, Y. Matsui, A. Hagihara, A. Miyamoto, Thermal diffusivity measurement of polymer films by the temperature wave method using joule-heating, Thermochimica Acta 163 (1990) 317-324.
[37] ISO 19628:2024, Fine ceramics (advanced ceramics, advanced technical ceramics) — Thermophysical properties of ceramic composites — Determination of specific heat capacity.
[38] J. Suurkuusk, I. Wadsö, Design and testing of an improved precise drop calorimeter for the measurement of the heat capacity of small samples, The Journal of Chemical Thermodynamics 6 (7) (1974) 667-679.
[39] M. Gustavsson, N. Saxena, E. Karawacki, S. Gustafsson, Specific heat measurements with the hot disk thermal constants analyser, Thermal Conductivity 23, CRC Press, 1995, pp. 56-65.

[40] J. Liu, J. Zhu, M. Tian, X. Gu, A. Schmidt, R. Yang, Simultaneous measurement of thermal conductivity and heat capacity of bulk and thin film materials using frequency-dependent transient thermoreflectance method, Review of Scientific Instruments 84 (3) (2013) 034902.
[41] J. Liu, B. Yoon, E. Kuhlmann, M. Tian, J. Zhu, S.M. George, Y.-C. Lee, R. Yang, Ultralow thermal conductivity of atomic/molecular layer-deposited hybrid organic–inorganic zincone thin films, Nano Letters 13 (11) (2013) 5594-5599.
[42] E. Ziade, Wide bandwidth frequency-domain thermoreflectance: Volumetric heat capacity, anisotropic thermal conductivity, and thickness measurements, Review of Scientific Instruments 91 (12) (2020) 124901.
[43] C.E. Bernardes, A. Joseph, M.E.M. Da Piedade, Some practical aspects of heat capacity determination by differential scanning calorimetry, Thermochimica Acta 687 (2020) 178574.
[44] J.D. Menczel, L. Judovits, R.B. Prime, H.E. Bair, M. Reading, S. Swier, Thermal Analysis of Polymers: Fundamentals and Applications, WILEY, 2009.
[45] R.L. Danley, Comparison of simulated and actual DSC measurements for first-order transitions, Thermochimica Acta 409 (2) (2004) 111-119.
[46] S.E. Gustafsson, E. Karawacki, M.A. Chohan, Thermal transport studies of electrically conducting materials using the transient hot-strip technique, Journal of Physics D: Applied Physics 19 (5) (1986) 727.
[47] C. Cao, Z. Jia, L. Yang, H. Li, Y. Tao, Q. Zhong, Z. Xu, C. Luo, Z. Chen, Printed Heating and Temperature-Sensing Film in Transient Plane Source Sensor and its Application in Measuring Thermal Conductivity, IEEE Sensors Journal 25 (1) (2024).
[48] P. Zhao, Q. Wang, An improved platinum probe used for transient plane source method at cryogenic temperatures, Applied Thermal Engineering 270 (2025) 126207.
[49] Hot Disk Thermal Constants Analyser — Instruction Manual, Hot Disk AB, Sweden, downloaded in 2023.
[50] M. Gustavsson, E. Karawacki, S.E. Gustafsson, Thermal conductivity, thermal diffusivity, and specific heat of thin samples from transient measurements with hot disk sensors, Review of Scientific Instruments 65 (12) (1994) 3856-3859.
[51] Y. He, Rapid thermal conductivity measurement with a hot disk sensor: Part 1. Theoretical considerations, Thermochimica Acta 436 (1-2) (2005) 122-129.
[52] J. Gustavsson, M. Gustavsson, S. Gustavsson, On the Use of the Hot Disk Thermal Constants Analyser for Measuring the Thermal Conductivity of Thin Samples of Electrically Insulating Materials, Thermal Conductivity 24, Technomic Publishing Co., Lancaster, PA, 1997, pp. 116-122.

[53] M. Gustavsson, L. Hälldahl, Thermal conductivity measurements of thin insulating layers deposited on high-conducting sheets, International Journal of Thermophysics 27 (1) (2006) 195-208.
[54] S.E. Gustafsson, B.M. Mihiretie, M.K. Gustavsson, Measurement of thermal transport in solids with the hot disc method, International Journal of Thermophysics 45 (1) (2024) 1.
[55] M.M. Yovanovich, Four decades of research on thermal contact, gap, and joint resistance in microelectronics, IEEE Transactions on Components and Packaging Technologies 28 (2) (2005) 182-206.
[56] M. Cooper, B. Mikic, M.M. Yovanovich, Thermal contact conductance, International Journal of Heat and Mass Transfer 12 (3) (1969) 279-300.
[57] V. Bohac, M.K. Gustavsson, L. Kubicar, S.E. Gustafsson, Parameter estimations for measurements of thermal transport properties with the hot disk thermal constants analyzer, Review of Scientific Instruments 71 (6) (2000) 2452-2455.
[58] Y. Jannot, Z. Acem, A quadrupolar complete model of the hot disc, Measurement Science and Technology 18 (5) (2007) 1229.
[59] Q. Zheng, S. Kaur, C. Dames, R.S. Prasher, Analysis and improvement of the hot disk transient plane source method for low thermal conductivity materials, International Journal of Heat and Mass Transfer 151 (2020) 119331.
[60] G. Jiaqi, S.B. Safiullah, L. Yang, Q. Ziyan, Q. Zheng, Improving the Accuracy of Transient Plane Source Thermal Conductivity Measurements: Novel Analytical Models, Fitting Approaches, and Systematic Sensitivity Analysis, International Journal of Heat and Mass Transfer 247 (2025) 127110.
[61] S.E. Gustafsson, Transient plane source techniques for thermal conductivity and thermal diffusivity measurements of solid materials, Review of Scientific Instruments 62 (3) (1991) 797-804.
[62] H. Zhang, M.-J. Li, W.-Z. Fang, D. Dan, Z.-Y. Li, W.-Q. Tao, A numerical study on the theoretical accuracy of film thermal conductivity using transient plane source method, Applied Thermal Engineering 72 (1) (2014) 62-69.
[63] B. Feng, Y.-H. Zhang, J. Tu, L.-W. Fan, Z.-T. Yu, Determination on the thermal conductivity and thermal contact resistance of thin composite phase change films as a thermal interfacial material, Case Studies in Thermal Engineering 33 (2022) 101979.
[64] M. Ahadi, M. Andisheh-Tadbir, M. Tam, M. Bahrami, An improved transient plane source method for measuring thermal conductivity of thin films: Deconvoluting thermal contact resistance, International Journal of Heat and Mass Transfer 96 (2016) 371-380.

[65] D. Landry, R. Flores, R.B. Goodman, Estimating the Thermal Conductivity of Thin Films: A Novel Approach Using the Transient Plane Source Method, ASME Journal of Heat and Mass Transfer 146 (3) (2024) 031004.
[66] A. Berge, B. Adl-Zarrabi, C.-E. Hagentoft, Determination of specific heat capacity by transient plane source, Frontiers of Architectural Research 2 (4) (2013) 476-482.
[67] J.N. Reddy, An introduction to the finite element method, McGraw-Hill Mechanical Engineering, 1993.
[68] J.C. Strikwerda, Finite difference schemes and partial differential equations, SIAM2004.
[69] W. Malalasekera, An introduction to computational fluid dynamics: the finite volume method, Pearson Prentice Hall, 2007.
[70] B. Szabó, I. Babuška, Finite Element Analysis: Method, Verification and Validation, John Wiley & Sons Inc, 2021.
[71] I. Brunetti, F. Ferrari, N.J. Pataki, S. Abdolhosseinzadeh, J. Heier, L.J.A. Koster, U. Lemmer, M. Kemerink, M. Caironi, Fully Screen‐Printed, Flexible, and Scalable Organic Monolithic Thermoelectric Generators, Advanced Materials Technologies 9 (11) (2024) 2302058.
[72] N.J. Pataki, N. Zahabi, Q. Li, P. Rossi, M. Cassinelli, M. Butti, M. Massetti, S. Fabiano, I. Zozoulenko, M. Caironi, A rolled organic thermoelectric generator with high thermocouple density, Advanced Functional Materials 34 (30) (2024) 2400982.
[73] C. Fernandes, A.J. Pontes, J.C. Viana, A. Gaspar‐Cunha, Modeling and Optimization of the Injection‐Molding Process: A Review, Advances in Polymer Technology 37 (2) (2018) 429-449.
[74] K. Wilczyński, A. Nastaj, A. Lewandowski, K.J. Wilczyński, K. Buziak, Fundamentals of global modeling for polymer extrusion, Polymers 11 (12) (2019) 2106.
[75] B. Mihiretie, D. Cederkrantz, A. Rosén, H. Otterberg, M. Sundin, S. Gustafsson, M. Karlsteen, Finite element modeling of the Hot Disc method, International Journal of Heat and Mass Transfer 115 (2017) 216-223.
[76] H. Zhang, W.-Z. Fang, Y.-M. Li, W.-Q. Tao, Experimental study of the thermal conductivity of polyurethane foams, Applied Thermal Engineering 115 (2017) 528-538.
[77] H. Zhang, Y. Li, W. Tao, Effect of radiative heat transfer on determining thermal conductivity of semi-transparent materials using transient plane source method, Applied Thermal Engineering 114 (2017) 337-345.

[78] H. Zhang, Y.-M. Li, W.-Q. Tao, Theoretical accuracy of anisotropic thermal conductivity determined by transient plane source method, International Journal of Heat and Mass Transfer 108 (2017) 1634-1644.

[79] M. Emanuel, M. Bhouri, S.L. Ackermann, D. Groulx, J. Maassen, Temperature fields generated by a circular heat source (CHS) in an infinite medium: Analytical derivation and comparison to finite element modeling, International Journal of Heat and Mass Transfer 126 (2018) 1265-1274.

[80] M. Emanuel, M. Bhouri, J. Furlotte, D. Groulx, J. Maassen, Temperature fields generated by a circular heat source (CHS) in an infinite isotropic medium: Treatment of contact resistances with application to thin films, International Journal of Heat and Mass Transfer 137 (2019) 677-689.

[81] Q. Wei, C. Uehara, M. Mukaida, K. Kirihara, T. Ishida, Measurement of in-plane thermal conductivity in polymer films, AIP Advances 6 (4) (2016) 045315.

[82] S. Kommandur, S. Yee, A suspended 3-omega technique to measure the anisotropic thermal conductivity of semiconducting polymers, Review of Scientific Instruments 89 (11) (2018) 114905.

[83] C. Bounioux, P. Díaz-Chao, M. Campoy-Quiles, M.S. Martín-González, A.R. Goni, R. Yerushalmi-Rozen, C. Müller, Thermoelectric composites of poly (3-hexylthiophene) and carbon nanotubes with a large power factor, Energy & Environmental Science 6 (3) (2013) 918-925.

[84] D. Kiefer, L. Yu, E. Fransson, A. Gómez, D. Primetzhofer, A. Amassian, M. Campoy‐Quiles, C. Müller, A solution‐doped polymer semiconductor: insulator blend for thermoelectrics, Advanced Science 4 (1) (2017) 1600203.

[85] B.M. Suleiman, S. Malinarič, Transient techniques for measurements of thermal properties of solids: data evaluation within optimized time intervals, WSEAS Transactions on Heat and Mass Transfer 1 (8) (2006).

[86] E. Karawacki, B.M. Suleiman, Dynamic plane source technique for simultaneous determination of specific heat, thermal conductivity and thermal diffusivity of metallic samples, Measurement Science and Technology 2 (8) (1991) 744.

[87] A.C. Lua, J. Su, Isothermal and non-isothermal pyrolysis kinetics of Kapton® polyimide, Polymer Degradation and Stability 91 (1) (2006) 144-153.

[88] M.J. Powell, The BOBYQA algorithm for bound constrained optimization without derivatives, Cambridge NA Report NA2009/06, University of Cambridge, Cambridge 26 (2009) 26-46.

[89] J. He, T.M. Tritt, Advances in thermoelectric materials research: Looking back and moving forward, Science 357 (6358) (2017) eaak9997.

[90] H. Jouhara, A. Żabnieńska-Góra, N. Khordehgah, Q. Doraghi, L. Ahmad, L. Norman, B. Axcell, L. Wrobel, S. Dai, Thermoelectric generator (TEG) technologies and applications, International Journal of Thermofluids 9 (2021) 100063.

[91] A. Lund, Y. Tian, S. Darabi, C. Müller, A polymer-based textile thermoelectric generator for wearable energy harvesting, Journal of Power Sources 480 (2020) 228836.

[92] R. Bjørk, The universal influence of contact resistance on the efficiency of a thermoelectric generator, Journal of Electronic Materials 44 (8) (2015) 2869-2876.

[93] L. Wang, K. Zhang, Textile‐based thermoelectric generators and their applications, Energy & Environmental Materials 3 (1) (2020) 67-79.

[94] H.M. Elmoughni, A.K. Menon, R.M. Wolfe, S.K. Yee, A textile‐integrated polymer thermoelectric generator for body heat harvesting, Advanced Materials Technologies 4 (7) (2019) 1800708.

[95] Product Brochure: Thermoreflectance by Pulsed Light Heating — NanoTR/PicoTR, NETZSCH-Gerätebau GmbH, Germany, downloaded in 2025, https://analyzing-testing.netzsch.com/_Resources/Persistent/e/a/8/4/ea840caa68a102ac687d929eb4a68f8038ad9751/Thermoreflectance.pdf.

[96] Product Brochure: TF-LFA L54 — Thin Film Laser Frequency Analyzer, LINSEIS GmbH, Germany, downloaded in 2025, https://www.linseis.com/en/instruments/electrical-property/thin-film-thin-film-analysis/tf-lfa-l54/.

[97] Product Brochure: Thin film analyzer, LINSEIS GmbH, Germany, downloaded in 2025, https://www.linseis.com/en/instruments/electrical-property/thin-film-thin-film-analysis/tfa-l59/#downloads.

[98] Product Brochure: Light Flash Apparatus — LFA 467 HyperFlash® Series, NETZSCH-Gerätebau GmbH, Germany, downloaded in 2025, https://analyzing-testing.netzsch.com/en/products/thermal-diffusivity-and-conductivity/lfa-467-hyper-flash-light-flash-apparatus.

[99] Product Brochure: ai-Phase Mobile M3 type, ai-Phase Co., Ltd., Japan, downloaded in 2025, https://www.ai-phase.co.jp/englishpage/.

[100] Guarded Hot Plate Series — GHP 500, GHP 600, GHP 900 and GHP 900 S, NETZSCH TAURUS Instruments GmbH, Germany, downloaded in 2025, https://analyzing-testing.netzsch.com/_Resources/Persistent/8/5/4/f/854f5bef1cb8b34949e2838af12cca495c87caff/NTA_Guarded_Hot_Plate_Series_en_web.pdf.

[101] Product Brochure: Crucibles for Thermal Analysis, METTLER TOLEDO Group, Switzerland, downloaded in 2025, https://www.mt.com/se/sv/home/library/product-brochures/lab-analytical-instruments/crucible_brochure.html.

[102] E1461 – 07, Standard Test Method for Thermal Diffusivity by the Flash Method.

Paper I

Liquid Interface for Accurate Intrinsic Thermal Conductivity Measurements of Polymer Films Using the Transient Plane Source Method

Journal of Thermal Science and Engineering Applications

ASME Journal of Thermal Science and Engineering Applications
Online journal at:
https://asmedigitalcollection.asme.org/thermalscienceapplication

Liquid Interface for Accurate Intrinsic Thermal Conductivity Measurements of Polymer Films Using the Transient Plane Source Method

Zijin Zeng[1]
Department of Chemistry and Chemical Engineering,
Chalmers University of Technology,
Gothenburg 41296, Sweden;
Hot Disk AB,
SvenHultins Gatan 9A,
Gothenburg 41288, Sweden
e-mail: zijin@chalmers.se

Przemyslaw Sowinski
Department of Chemistry and Chemical Engineering,
Chalmers University of Technology,
Gothenburg 41296, Sweden
e-mail: sowinski@chalmers.se

Christian Müller
Department of Chemistry and Chemical Engineering,
Chalmers University of Technology,
Gothenburg 41296, Sweden
e-mail: christian.muller@chalmers.se

Besira Mihiretie[1]
Hot Disk AB,
SvenHultins Gatan 9A,
Gothenburg 41288, Sweden
e-mail: besira.mihiretie@hotdiskinstruments.com

Characterizing the thermal properties of micrometer-thin films is crucial for optimizing their performance in a broad range of engineering applications. The transient plane source (TPS) method is widely used for measuring bulk materials, but its direct application to thin films fails due to thermal contact resistance. By comparing TPS measurements across films of varying thicknesses, it is possible to compensate for the influence of thermal contact resistance and extract the intrinsic thermal conductivity. However, this method still suffers from significant errors, e.g., as high as 26% in case of polyolefin films, since its underlying assumption—thermal contact resistance remains identical for films of different thickness—does not always hold true for actual measurements. Here, we demonstrate that these errors can be effectively reduced to 4% by incorporating a liquid thermal interface material. Specifically, the intrinsic cross-plane thermal conductivities of high-density polyethylene, isotactic polypropylene, and regioregular poly(3-hexylthiophene) films are determined to be 0.450, 0.277, and 0.296 W/(m · K), respectively. Moreover, these measurements exhibit remarkable reproducibility, achieving a standard deviation below 0.02 W/(m · K) when the film thickness is sufficiently varied. Furthermore, potential systematic errors are investigated through a comprehensive numerical study. Overall, this study offers critical insights that considerably extend the applicability of TPS measurements for thin films. [DOI: 10.1115/1.4069207]

Keywords: heat conduction, transient plane source method, measurement techniques, heat and mass transfer, thermophysical properties

1 Introduction

Polymer films with micrometer-scale thickness play an important role in various engineering applications, with their mechanical, electrical, optical, and thermal properties significantly impacting their performance [1]. Among these properties, the thermal conductivity is of particular importance, especially in the fields of energy harvesting/storage and electronics [2–4]. For instance, in the case of fuel cells, the thermal conductivities of proton exchange membranes and gas diffusion layers critically influence the internal temperature distribution and thus the device performance [5,6]. Similarly, in the case of organic thermoelectric generators, the thermal conductivity governs the temperature difference across the generator, impacting the efficiency of power generation [7,8]. Furthermore, recent studies have demonstrated that insulating polymer films processed in the solid state can feature a high thermal conductivity, thereby facilitating the thermal management of electronics [9–11].

There are numerous measurement techniques available for assessing the thermal conductivity of micrometer-thick films [12–20]. They can be broadly categorized into contact and contactless methods, depending on whether the sensing element physically contacts the specimen or not [12,20]. Contactless methods, predominantly based on optics, include time-domain thermoreflectance [13,14], frequency-domain thermoreflectance [15–17], and laser flash analysis (LFA) [18,19,21]. One of the common advantages of contactless methods is the disregard of thermal contact resistance (R_C) between the specimen and the sensing element [12,20]. Yet, these methods often require the deposition of a transducer layer (e.g., gold [22,23], aluminum [24,25], graphite [26]) on the sample surface. This layer facilitates the conversion of thermal responses into detectable optical signals, which however tends to increase both the time and complexity of the measurement process.

Contact methods include the guarded hot plate (GHP) method [27], the 3ω method [28,29], the temperature wave analysis (TWA) method [30], and the transient plane source (TPS) method [31]. The GHP method is a steady-state method with the advantages

[1]Corresponding authors.

Manuscript received April 16, 2025; final manuscript received July 17, 2025; published online August 4, 2025. Assoc. Editor: Stephen A Solovitz.

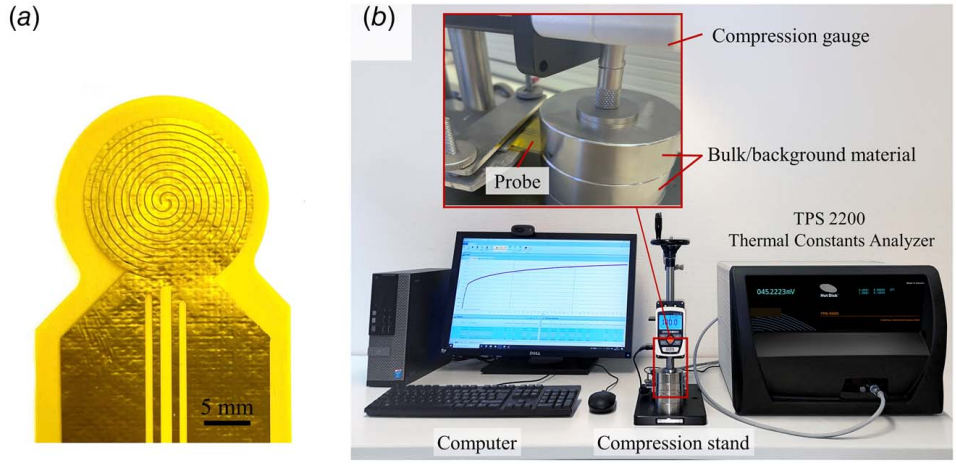

Fig. 1 (*a*) Probe profile featuring a nickel bifilar spiral sandwiched between polyimide layers and (*b*) the configuration of a TPS measurement using a compression stand

of simplicity and high accuracy [27]. The 3ω method, a frequency-dependent technique, necessitates a metal sensor deposited on the sample surface. This method allows for the measurement of the thermal conductivity of submicrometer-thick films, which are thinner than those measurable by other contact methods [28,29]. TWA is another frequency-dependent method for film specimens that is only employed for cross-plane thermal diffusivity measurements. The determination of thermal conductivity is achieved by multiplying the measured thermal diffusivity with the volumetric heat capacity [32].

The TPS method in turn is a time-dependent technique offering versatile and nondestructive testing [31,33,34]. Initially developed for characterizing bulk materials, it has been extended to determine the cross-plane thermal conductivity of films with a thermal conductivity ranging from 0.05 W/(m · K) to 2 W/(m · K) [31,35–37].

TPS measurements utilize a probe made of a nickel spiral covered by insulation layers that provide electrical insulation and mechanical support (Fig. 1(*a*)). When measuring bulk materials, this probe is positioned between two identical specimens and a mounting force is applied to enhance physical contact within the specimen–probe assembly (Fig. 1(*b*)). The probe heats the specimens through the Joule heating, and the resulting thermal response of the probe ($\Delta T(t)$) is simultaneously recorded over time [31] (Fig. 2(*a*)). ΔT can be further written as a function of dimensionless time τ (Fig. 2(*b*)), which is normalized with respect to the probe radius (r) and thermal diffusivity (α) of the bulk material [31,37]

$$\Delta T(\tau) = \Delta T_{\mathrm{a}} + P(\pi^{3/2} r\lambda)^{-1} D(\tau)$$
$$\text{where} \quad \tau = (t/\theta)^{1/2}, \quad \theta = r^2/\alpha \tag{1}$$

where P represents the power output of the probe, λ is the thermal conductivity of the bulk material, and ΔT_{a} is the additional temperature increase caused by the total thermal resistance between the probe and the bulk material. ΔT_{a} reaches a constant value shortly after the measurement begins [31]. $D(\tau)$ is a function of dimensionless time τ, which depends on the type of probe [31,33]

$$D(\tau) = \int_0^{\tau} d\sigma\sigma^{-2} \int_0^1 v dv \int_0^1 u du \times \exp\left(-\frac{u^2+v^2}{4\sigma^2}\right) I_0\left(\frac{uv}{2\sigma^2}\right) \tag{2}$$

where σ is an integration variable related to dimensionless time. The variables v and u are normalized radial coordinates, and I_0 is a modified Bessel function.

To determine the thermal properties of the bulk material, a least-squares iterative process is employed to fit the recorded $\Delta T(t)$ using Eq. (1). This fitting process establishes a linear relationship between $\Delta T(\tau)$ and $D(\tau)$. The slope of the linear relationship is associated with the thermal conductivity of the bulk material, while its intercept at $D(\tau) = 0$ reveals the additional temperature increase ΔT_{a} (Fig. 2(*b*)). ΔT_{a} can be utilized to estimate the total thermal resistance (R_{tot}) between the probe and the bulk material, which impedes heat conduction from the probe to the bulk material [31,37]

$$P = 2S\Delta T_{\mathrm{a}}/R_{\mathrm{tot}} \tag{3}$$

where S is the area of the probe.

Equation (3) assumes that heat conduction between the probe and the bulk material is one-dimensional (1D). This assumption holds when the thickness of the insulation layer is markedly smaller than the probe diameter. However, this simplification can introduce errors that vary with the thickness and thermal conductivity of the sample [38].

To determine the thermal conductivity of thin films, a two-step process is employed. First, the background material is measured, which is referred to as the background measurement (Fig. 2(*c*)). By performing the fitting process on the thermal response data ($\Delta T_{\mathrm{b}}(t)$, Fig. 2(*a*)), the additional temperature increase ($\Delta T_{\mathrm{a,b}}$, Fig. 2(*b*)) is obtained. This increase is further used to estimate the total thermal resistance ($R_{\mathrm{tot,b}}$), which consists of the thermal resistance caused by the insulation layer (R_{i}) and the thermal contact resistance between the probe and bulk material ($R_{\mathrm{c-b}}$)

$$R_{\mathrm{tot,b}} = R_{\mathrm{i}} + R_{\mathrm{c,p\text{-}b}} \tag{4}$$

Then, two thin-film specimens, e.g., two polymer films, are positioned between the probe and the background material while keeping the measurement conditions unchanged (Fig. 2(*d*), referred to as the film measurement). Similarly, the thermal response data ($\Delta T_{\mathrm{f}}(t)$, Fig. 2(*a*)) are obtained to estimate the additional temperature increase ($\Delta T_{\mathrm{a,\,f}}$, Fig. 2(*b*)) and the total thermal resistance ($R_{\mathrm{tot,f}}$). $R_{\mathrm{tot,f}}$ in this case can then be written as

$$R_{\mathrm{tot,f}} = R_{\mathrm{i}} + R_{\mathrm{c,p\text{-}f}} + R_{\mathrm{f}} + R_{\mathrm{c,f\text{-}b}} \tag{5}$$

where $R_{\mathrm{c,p\text{-}f}}$ is the thermal contact resistance between the probe and the film specimen, $R_{\mathrm{c,f\text{-}b}}$ denotes the thermal contact resistance between the film and the background material, and R_f represents the thermal resistance caused by the film specimen. The intrinsic cross-plane thermal conductivity ($\lambda_\perp$) of the films is given by

$$R_f = \delta/\lambda_\perp \tag{6}$$

where δ is the thickness of the film specimen. However, introducing the film specimens imposes an additional thermal contact resistance (denoted as C) compared to the background measurement.

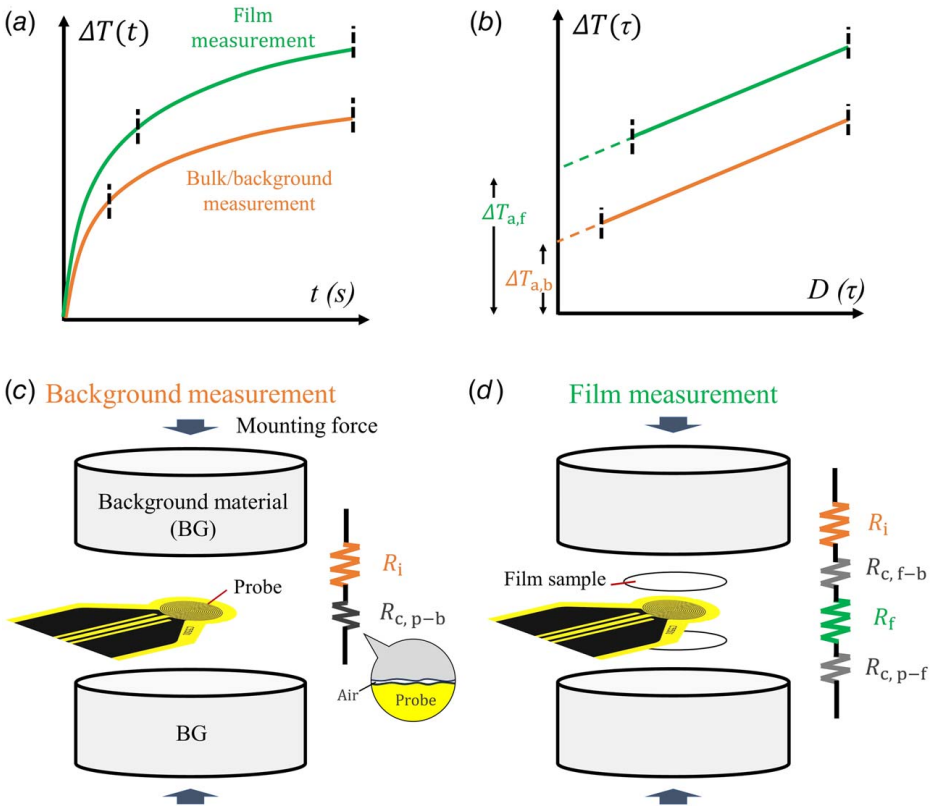

Fig. 2 (*a*) Thermal response of the probe over time (*t*) during a background measurement and a film measurement, respectively. The thick dashed lines define the range of data utilized for determining the properties of the bulk/background material; (*b*) thermal response of the probe as a function of dimensionless time (τ) in a background measurement and a film measurement, respectively. The intercepts ($\Delta T_{a,f}$, $\Delta T_{a,b}$) are utilized for determining the properties of the film specimens; (c) schematic of a background measurement and its thermal network between the probe and the background material. The inset illustrates the contact between the BG and the probe; (*d*) schematic of a film measurement and the corresponding thermal network.

Mathematically, this can be expressed as

$$R_{\text{tot,f}} - R_{\text{tot,b}} = \delta/\lambda_{\perp} + C = \delta/\lambda_{\perp,\text{a}} \tag{7}$$

In the current approach, the TPS method directly measures the apparent thermal conductivity ($\lambda_{\perp,\text{a}}$) of the film. This value includes the effect of the additional thermal contact resistance and as a result the measured thermal conductivity is typically lower than the intrinsic cross-plane thermal conductivity [38,39].

Determining the intrinsic cross-plane thermal conductivity using the TPS method is feasible by comparing measurements of films with varying thickness [39,40]. This approach, referred to as the slope method, has been reported to achieve an accuracy of approximately 7–15% [39,40]. The slope method requires a linear fitting of measured $R_{\text{tot, f}} - R_{\text{tot,b}}$ against film thickness. The slope of the fit represents the reciprocal of the intrinsic cross-plane thermal conductivity ($1/\lambda_{\perp}$). This method by default assumes that R_{C} (including $R_{\text{c,p-f}}$ and $R_{\text{c,f-b}}$) remains identical across measurements of samples with different thicknesses.

However, this underlying assumption of identical R_{C} may not hold true and could lead to significant errors, particularly when the sensor and film specimens have uneven surfaces. Our results demonstrate that such errors can easily reach a value of 26%. Additionally, systematic errors arise from the assumption of 1D heat conduction across the film specimen [38,41], which has not been investigated and quantified with regard to the slope method. Therefore, determining $\lambda_{\perp}$ of thin films with the TPS method is currently associated with considerable uncertainties.

In this work, high-density polyethylene (HDPE) and polypropylene (PP), two polymers with distinct thermal and mechanical properties, were primarily investigated. Additionally, poly(3-hexylthiophene) (P3HT), which has lately attracted significant interest in the context of energy conversion, was also measured. These materials were characterized using TPS measurements under varying measurement conditions, including changes in mounting force and the application of a thermal interface material (TIM). We found that the thermal contact resistance varied with film thickness, which differed from the assumption underlying the slope method and led to considerable deviations. However, using a thermal interface material effectively enhanced the measurements by reducing the variation in thermal contact resistance. In addition, the systematic error and reproducibility of the measurements were carefully evaluated.

2 Experiment

2.1 Materials. HDPE (547999, weight-average molecular weight (M_{W}) = 95 kg/mol, polydispersity index (PDI) = 5.3) and isotactic PP (427888, M_{W} = 250 kg/mol, PDI = 3.7) were obtained from Sigma-Aldrich, St. Louis, MO, and used as received. In addition, P3HT was obtained from Ossila, UK (M1010, M_{W} = 74 kg/mol, PDI = 2.1, regio-regularity = 97%) and used as received.

2.2 Sample Preparation. Free-standing polymer films were fabricated by hot pressing, using a laboratory press (LabPro 200) supplied by Fontijne Presses, the Netherlands, together with a

constant thickness film maker from Specac Ltd., Sheffield, UK. The press applied a force of 15 kN at temperatures that exceeded the melting temperature of the materials: 180°C for HDPE, 210°C for PP, and 290°C for P3HT. The hot-pressed films were subsequently cooled to room temperature at a rate of approximately 40°C/min. The thicknesses of the hot-pressed films were measured using a micrometer with a precision of 1 μm. Bulk polymer samples for reference measurements were hot pressed into cylindrical shapes with a thickness of 4 mm and a radius of 15 mm.

2.3 Pressure Distribution Tests. Prior to the TPS measurements of films, pressure distribution tests were conducted to assess the contact between the experimental components [42], such as background materials, the probe, and the film specimens. In this test, a pair of Prescale Films (i.e., pressure-sensitive films, including A-film and C-film) supplied by Fujifilm, Japan, was placed between the components to study the contact between them. A mounting force of 500 N was applied to the components and Prescale Films for 5 min. A-film is coated with a micro-encapsulated color-forming material, while the C-film is coated with a color-developing material. When used in pairs, these films respond to applied pressure by producing a red color at the point of contact. The intensity of the color correlates with the amount of pressure applied.

2.4 Thermal Conductivity Measurements. The TPS measurements of the film specimens were conducted using a TPS 2200 Thermal Constants Analyzer obtained from Hot Disk AB, Sweden. The probe utilized in the measurements had an effective radius of 11 mm and a 25 μm thick polyimide insulation layers on both sides (model 7854, Fig. 1(*a*)). The background material used was a stainless steel block with a thermal conductivity of 13.5 W/(m · K). A compression stand obtained from Hot Disk was employed for applying a mounting force of up to 550 N. Background measurements were conducted for each level of mounting force.

De-ionized water and silicone oil were employed as a TIM. The de-ionized water, supplied by Sigma-Aldrich, had a thermal conductivity of 0.59 W/(m · K) at room temperature. The silicone oil, sourced from Thermo Fisher Scientific, Waltham, MA, had a thermal conductivity of 0.14 W/(m · K) at room temperature. When using de-ionized water as a TIM, three repeated measurements were conducted within 1 h to avoid the influence of water evaporation. Optionally, sealing the gap between the two background materials with waterproof tape can effectively reduce the evaporation rate.

Two types of reference measurements were carried out: TPS measurements of bulk polymer samples and TWA measurements of pressed polymer films. These methods were selected because they are widely used and supported by international standards [30,31]. TPS measurements of bulk polymers used a sensor with a radius of 3.2 mm (model 5501), while TWA measurements of pressed polymer films employed an Ai-Phase Mobile M3 instrument supplied by Ai-Phase Co., Ltd., Tokyo, Japan.

2.5 Differential Scanning Calorimetry (DSC) Measurements. The specific heat capacity and melting characteristics of the pressed polymer films, including peak melting temperature (T_m) and enthalpy of melting (ΔH_m), were obtained using a DSC 2 instrument from Mettler Toledo, Columbus, OH. The specific heat capacity at room temperature was;obtained using the Sapphire method, with a heating rate of 2°C/min from 10 °C to 40°C. The melting characteristics were obtained from the first heating thermograms with a heating rate of 10°C/min from 20°C to 250°C.

2.6 Simulations. The heat transfer in solids module in COMSOL MULTIPHYSICS (version: 6.1) was utilized to study heat conduction in the TPS measurement setup.

3 Results and Discussion

3.1 Properties of Hot-Pressed Films and Bulk Samples. T_m and ΔH_m of the hot-pressed films were extracted from first heating DSC thermograms (Fig. 1(*a*) available in the Supplemental Materials on the ASME Digital Collection). The crystallinity (X_c) is calculated according to $(\Delta H_m/\Delta H_f^0) \times 100\%$, where ΔH_f^0 is the enthalpy of fusion. The crystallinity of the HDPE and PP films was determined to be 61% and 50%, respectively. The measured ΔH_m of P3HT agrees with the literature values [43]. More details are provided in Table 1 available in the Supplemental Materials.

The hot-pressed films had an average thickness ($\bar{t}$) varying from approximately 40 μm to 400 μm, across 12 distinct thickness levels. The coefficient of variation (CV) in thickness was calculated according to $CV = (\sigma/\bar{t}) \times 100\%$, where σ is the standard deviation of the five measured values taken at different locations on a single specimen. CV was then employed to quantify the flatness of the films (Fig. 1(*b*) available in the Supplemental Materials). Most films displayed a coefficient of variation lower than 3%, though films thinner than 80 μm showed higher variations.

The thermal conductivity of hot-pressed films determined by TWA ($\lambda_{\perp,TWA}$) was 0.488 ± 0.049 W/(m · K) for HDPE and 0.247 ± 0.025 W/(m · K) for PP. These values represent one of the two sets of reference values used in this study.

Another set of reference thermal conductivity values was derived using TPS measurements of bulk polymer samples (Table 1), where the thermal conductivity ($\lambda_{bulk,\ TPS}$) was 0.465 ± 0.023 W/(m · K) for HDPE and 0.269 ± 0.013 W/(m · K) for PP. The two sets of reference values are in good agreement, in particular when considering differences in sample preparation, with recorded differences of less than 8%. Additionally, these two sets of reference values fall within the range of thermal conductivity values reported in the literature: 0.42 W/(m · K) to 0.52 W/(m · K) for HDPE [44–46] and 0.22 W/(m · K) to 0.27 W/(m · K) for PP [47–49].

3.2 Pressure Distribution. Six pressure distribution tests with different arrangements of components were conducted. To assess the contact between two blocks of the background material, the first test was set up with an arrangement from the top to bottom comprising background material, Prescale Films, and background material (abbreviated as BG–Prescale Films–BG). The second test used an arrangement of BG–probe–Prescale Films–BG to study the contact between the probe and the background material. The remaining tests focused on the contact between film specimens

Table 1 Material properties

Material	λ (W/(m · K))	ρ (kg/m^3)	C_p (J/(kg · K))
HDPE	0.465[a]	950[b]	1923[c]
PP	0.269[a]	900[b]	1613[c]
Background material (stainless steel)	13.5[a]	8150[b]	460[a]
Insulation layer (polyimide)	0.18[d]	1420[e]	1090[e]
Probe (nickel)	91.4[f]	8900[f]	444[f]

[a]Determined by TPS measurements of bulk samples.
[b]Determined from the mass and volume of the samples.
[c]Obtained from the DSC Sapphire method.
[d]Obtained from a background measurement with de-ionized water as the TIM.
[e]Obtained from Ref. [50].
[f]Obtained from Ref. [38].

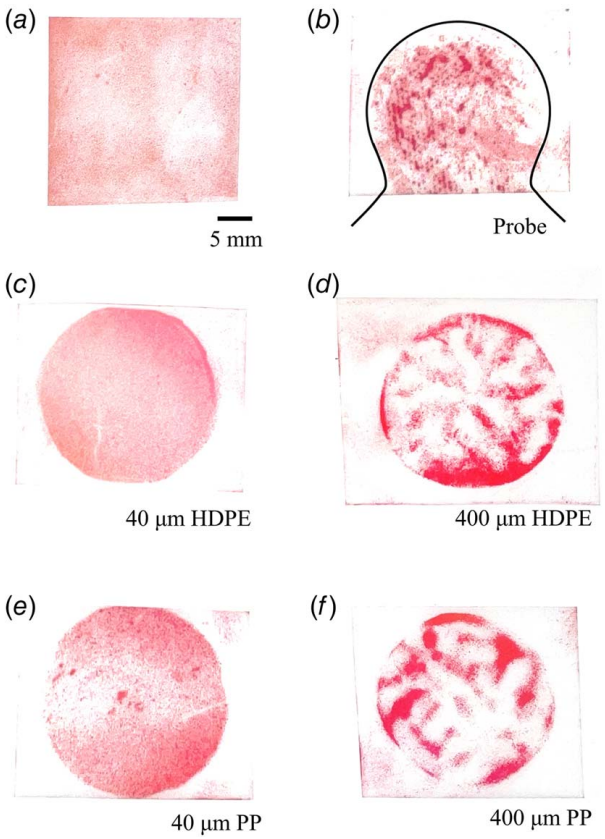

Fig. 3 The results of the pressure distribution test examining the contact between the background material and various components: (*a*) second block of the background material, (*b*) the probe, (c) a 40 μm-thick HDPE film, (*d*) a 400 μm-thick HDPE film, (e) a 40 μm-thick PP film, and (*f*) a 400 μm-thick PP film. The intensity of the coloration is related to the pressure level. To identify the position of the probe, a contour line in (*b*) is provided to represent the outer edge of the probe.

and the background material, using the arrangement BG–film specimen–Prescale Films–BG.

The first experiment showed an even distribution of color (Fig. 3(*a*)), suggesting a uniform pressure distribution between two blocks of the background material. The second experiment involving a probe demonstrated a heterogeneous and irregular coloration, characterized by small clusters of higher intensity (Fig. 3(*b*)). These clusters likely resulted from the bulges in the nickel pattern and polyimide surface, which can be seen in Fig. 1(*a*).

The tests involving a thin-film specimen (approximately 40 μm) displayed a more uniform and consistent color distribution (Figs. 3(*c*) and 3(*e*)). In contrast, thick film specimens (approximately 400 μm) led to a visibly larger and irregularly colored region (Figs. 3(*d*) and 3(*f*)). This irregularity is expected to be caused by the uneven surfaces and the low pliability of the thick films, showing the influence of film thickness on its surface properties.

3.3 Thermal Conductivity From Transient Plane Source Film Measurements

3.3.1 Measurement Without Thermal Interface Material. In the cases where TPS was carried out without a TIM, $\lambda_{\perp,a}$ of both HDPE and PP films (Fig. 4(*a*)) proved lower than the reference values obtained from the TWA and the TPS method for bulk materials (Table 1), which we attribute to the presence of thermal contact resistance. Generally, the thicker specimens displayed a higher apparent cross-plane thermal conductivity. This is because the thicker specimens possess a larger intrinsic thermal resistance ($R_f = \delta/\lambda_\perp$) and thus a larger $R_{tot,f}$, which diminished the influence of thermal contact resistance.

In addition, a higher mounting force led to an increase in the values of $\lambda_{\perp,a}$, particularly in the case of HDPE. This increase is attributed to a reduction in thermal contact resistance with greater mounting force. However, if the specimens are compressible, changes in mounting force may also alter their thickness, which in turn effects their thermal conductivity. Notably, HDPE films thinner than 50 μm exhibited anomalously higher values of $\lambda_{\perp,a}$ at a force of 300 N, likely due to the softer nature of thin HDPE films, which resulted in better contact with the probe and background materials.

Subsequently, we extracted the intrinsic thermal conductivity using the slope method (Fig. 4(*b*)). Data from the films thicker than 80 μm were utilized due to the low uncertainty in the determined thickness (Fig. 1(*b*) available in the Supplemental Materials). $R_{tot,f} - R_{tot,b}$ was initially plotted against the film thickness and fitted with a linear function. The uncertainty in the fit parameters (slope and intercept) was calculated in accordance with the methodology described in Refs. [40,51]. Afterward, $\lambda_\perp$ was obtained as the reciprocal of the slope from these fits (Table 2). Overall, the $\lambda_\perp$ values of HDPE and PP were still underestimated, showing a difference of up to 26% and 22%, respectively.

Moreover, the values of $\lambda_\perp$ also changed with the mounting force. When the external mounting force was increased, the $\lambda_\perp$ values of HDPE increased by 17% from 0.343 W/(m · K) to 0.411 W/(m · K), while those of PP increased by 9% from 0.209 W/(m · K) to 0.230 W/(m · K). Regardless, the highest values obtained were still significantly lower than reference values of 0.465 W/(m · K) for HDPE and 0.269 W/(m · K) for PP.

In addition, the influence of the mounting force differed with the specimen thickness (Fig. 4(*b*)). $R_{tot,f} - R_{tot,b}$ in the case of thin specimens decreased only slightly with increased mounting force (small arrows), whereas in the case of thicker specimens a more significant decrease was observed (big arrows). This indicates that there is greater potential for reducing R_c in case of thick films by applying a higher mounting force. Additionally, considering the uneven surfaces and reduced pliability of thicker films, we argue that these films tend to result in a higher R_c. This is at odds with the underlying assumptions of the slope method and thus resulted in errors.

A higher R_c in case of thick films leads to a higher total thermal resistance, resulting in a steeper slope of the linear fit and, consequently, a lower value of $\lambda_\perp$. This phenomenon likely contributes to the observed underestimation of the intrinsic thermal conductivity if no thermal interface material is used.

3.3.2 Measurements With Liquid Thermal Interface Material. TPS measurements with water as the TIM yielded higher values of thermal conductivity compared to the previous case without a TIM (Fig. 4(*c*)). The increase in $\lambda_{\perp,a}$ can be attributed to a reduction in thermal contact resistance. Despite this increase, the values of $\lambda_{\perp,a}$ of both HDPE and PP remained lower than their respective reference values, which we attribute to the fact that employing water did not completely eliminate thermal contact resistance.

Similarly, $R_{tot,f} - R_{tot,b}$ was again plotted against specimen thickness (Fig. 4(*d*)) and fitted to calculate $\lambda_\perp$ and the additional thermal contact resistance (intercept). Unlike the scenario without a TIM, the values of $\lambda_\perp$ were more consistent across different mounting forces, with a small difference of around 1% (Table 2). In case of HDPE, average values of $\lambda_\perp$ and the intercept over different mounting forces were 0.450 W/(m · K) and 55 mm^{2}K/W, respectively. In case of PP, average values were 0.277 W/(m · K) and 110 mm^{2}K/W, respectively. These values of $\lambda_\perp$ agreed well with the reference values from TPS measurements on bulk materials (Table 1) and the TWA method, differing by less than 4% and 11%, respectively.

Analogous measurements with a mounting force of 50 N were conducted using silicone oil as the TIM (Figs. 5(*a*) and 5(*b*)). In

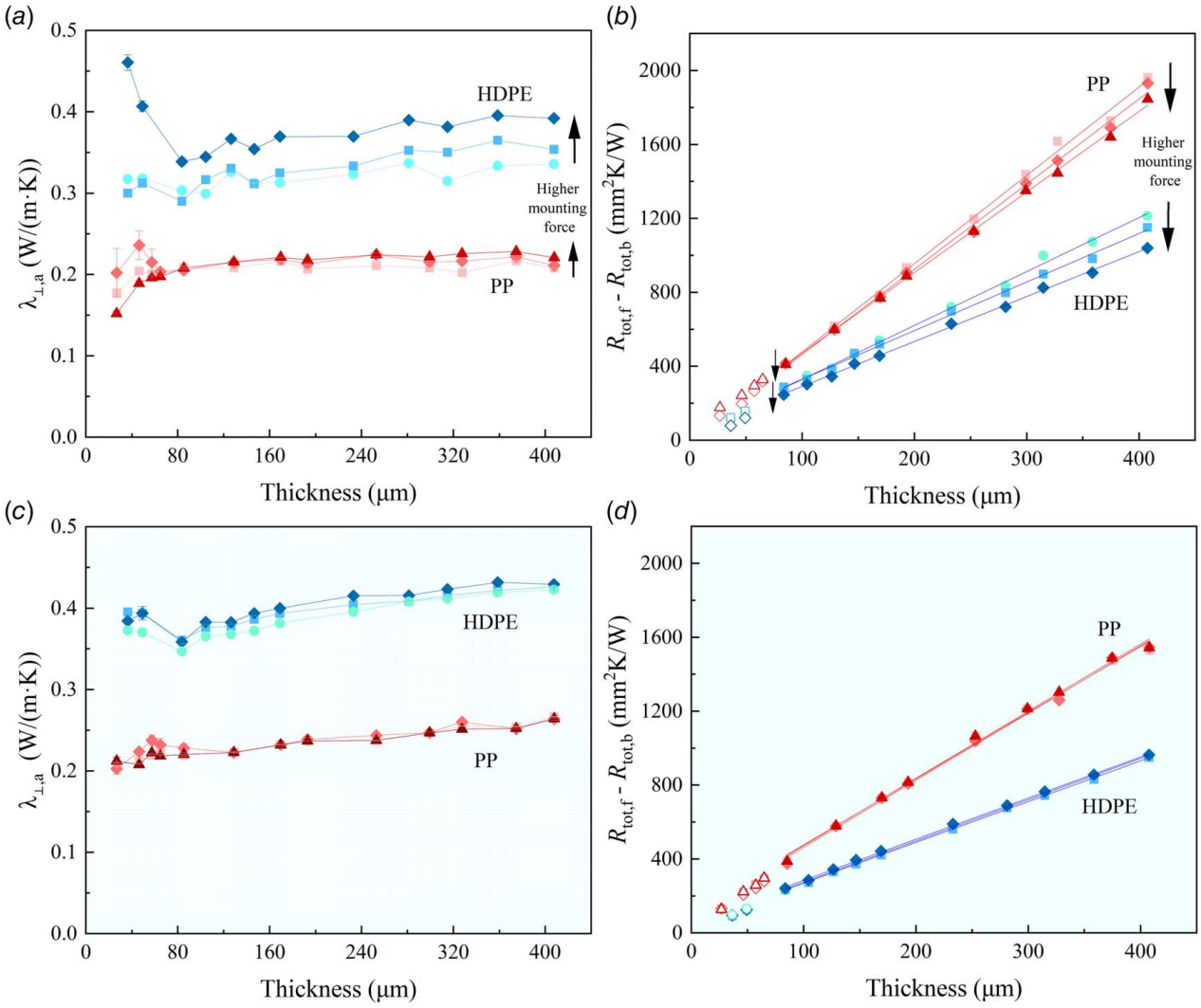

Fig. 4 Results of the TPS measurements of HDPE and PP films (mounting force: ● 0 N, ■ 50 N, ◆ 300 N, ▲ 550 N): (*a*) the values of the apparent thermal conductivity versus the film thickness, obtained from the measurements without a TIM; (*b*) $R_{tot,f} - R_{tot,b}$ as a function of the film thickness, along with linear fits. Data points from the specimens thinner than 80 μm (open symbols) were excluded from the fitting; (*c*) the values of the apparent thermal conductivity versus film thickness, obtained from the measurements using water as the TIM; (*d*) $R_{tot,f} - R_{tot,b}$ versus film thickness, along with the linear fits. Data points from specimens thinner than 80 μm (open symbols) were excluded from the fitting.

this case, $\lambda_\perp$ of HDPE and PP was calculated to be 0.435 W/(m · K) and 0.264 W/(m · K), respectively, similar to values obtained from the measurements with water as the TIM. Due to the low volatility of silicone oil, a high measurement stability was achieved. Specifically, the measurement results obtained for HDPE films under a mounting force of 500 N remained exceptionally stable for over 10 days, with an observed fluctuation of less than 0.5% (Fig. 5(*c*)). This also implies that the influence of creep is negligible in our measurements. However, the removal of silicone oil from the specimens at the end of measurement is normally more difficult compared to that of de-ionized water.

Table 2 The results from the slope method, including $\lambda_\perp$ (reciprocal of slope) and the additional thermal contact resistance (intercept)

Material	Mounting force (N)	$\lambda_\perp$(W/(m · K)) (without TIM)	Intercept (mm²K/W) (without TIM)	$\lambda_\perp$(W/(m · K)) (with water as TIM)	Intercept (mm²K/W) (with water as TIM)
HDPE	0	0.343 ± 0.007.	37.5 ± 14.5	0.447 ± 0.003	50.6 ± 4.1
	50	0.381 ± 0.007	67.3 ± 12.2	0.453 ± 0.003	48.5 ± 3.6
	300	0.411 ± 0.005	48.0 ± 7.7	0.449 ± 0.004	61.6 ± 4.5
PP	50	0.209 ± 0.005	0.2 ± 28.4	0.279 ± 0.007	118.3 ± 25.7
	300	0.217 ± 0.005	4.3 ± 25.8	0.276 ± 0.007	100.9 ± 24.0
	550	0.230 ± 0.003	35.6 ± 16.2	0.275 ± 0.007	110.0 ± 23.2

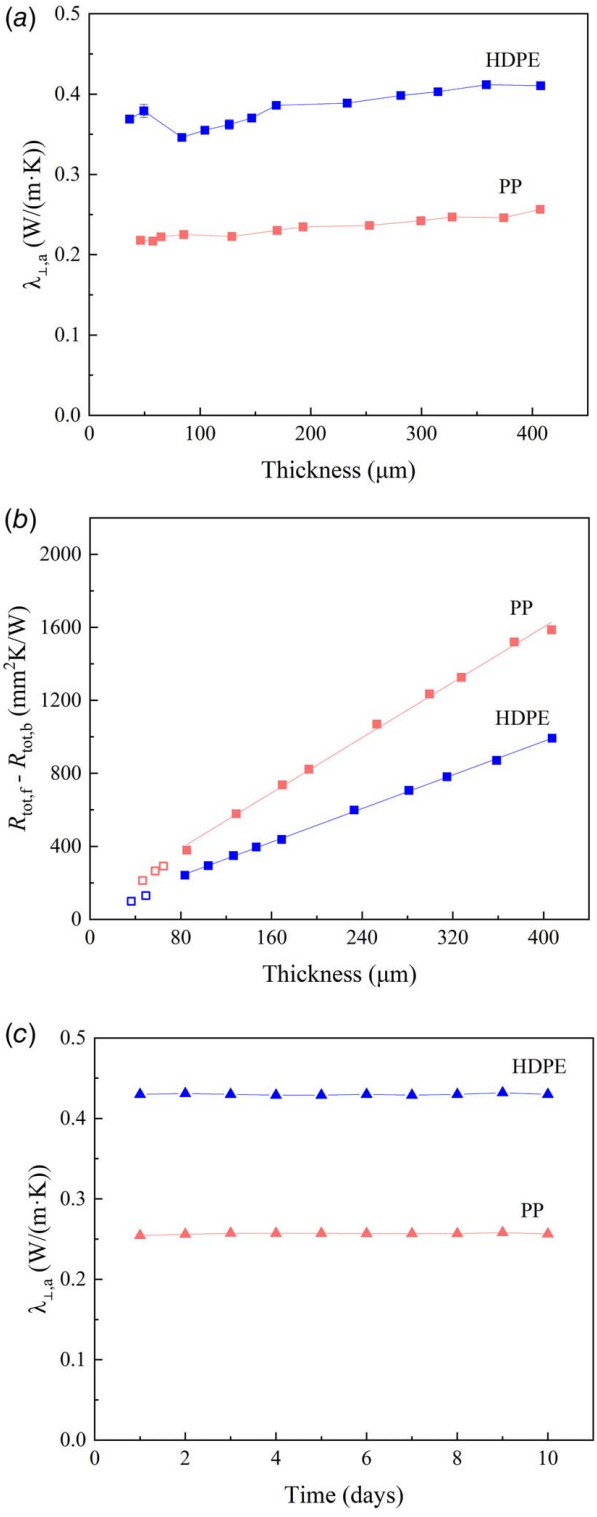

Fig. 5 Measurement results for HDPE and PP using silicone oil as the thermal interface material: (*a*) the values of $\lambda_{\perp,a}$ versus the film thickness for a mounting force of 50 N (■); (*b*) $R_{tot,f} - R_{tot,b}$ versus the film thickness for a mounting force of 50 N, along with linear fits. The data points from the specimens thinner than 80 μm (outlier open symbols) were excluded from the fitting; and (c) the values of $\lambda_{\perp,a}$ of 400 μm-thick HDPE and PP films versus time for a mounting force of 500 N (▲)

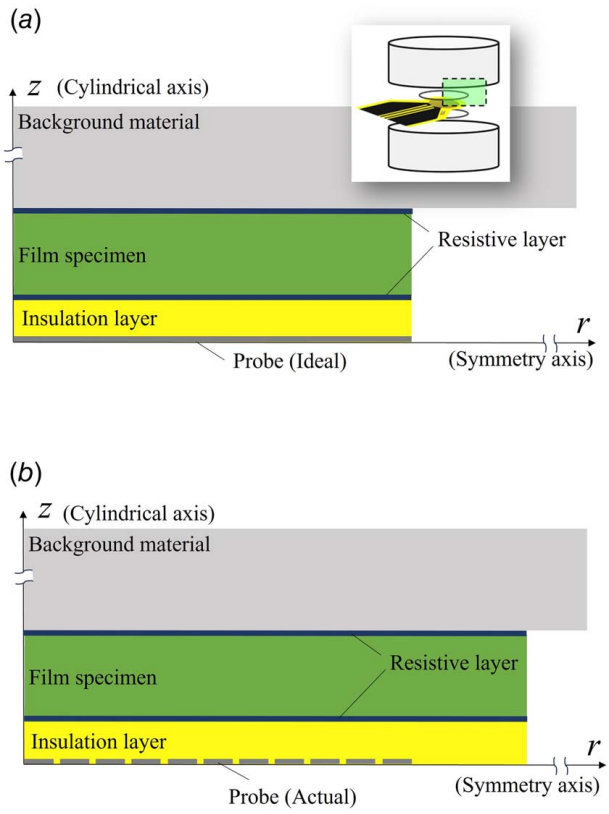

Fig. 6 Schematic depicting the two simulation models of TPS measurements involving de-ionized water that represent (*a*) the ideal and (*b*) the actual scenarios. The dashed frame in the inset indicates the computational domain.

3.4 Simulation. To investigate the systematic error caused by the assumption of 1D heat flow across the specimen, two simulation models were developed. Considering the axisymmetric heat conduction in the measurements, the models were reduced to two dimensions (2D) to improve computational efficiency [52,53]. The development of the 2D models relied on several key assumptions:

- The measurement setup, including the probe, background material, layers, and interfaces can be treated as axisymmetric.
- The bifilar probe can be approximated as a series of concentric and uniformly spaced ring sources.
- Heat transfer between the measurement components and the ambient environment is considered negligible (adiabatic boundary condition).
- Heat transfer via convection and radiation is considered negligible.
- Material properties are assumed to remain constant during the measurement.

One simulation model was developed to represent the ideal scenario where heat flow across the film specimen and the insulation layer is 1D (ideal scenario, Fig. 6(*a*)). In this model, an ideal heat source was depicted as a thin rectangle, transformable into a circular probe by rotation around the origin. The radius of the specimen layer, TIM layers, and insulation layers was set to be the same as the equivalent radius of the probe (11 mm).

The second model simulated the conditions of the actual measurements (Fig. 6(*b*)). A series of uniformly spaced thin rectangles with a height of 5 μm and a width of 800 μm was utilized to represent the double spiral probe. The space between the rectangles was 200 μm. In addition, the radius of the specimen and insulation layers was set to be 3 mm larger than that of the probe, consistent with the experimental setup.

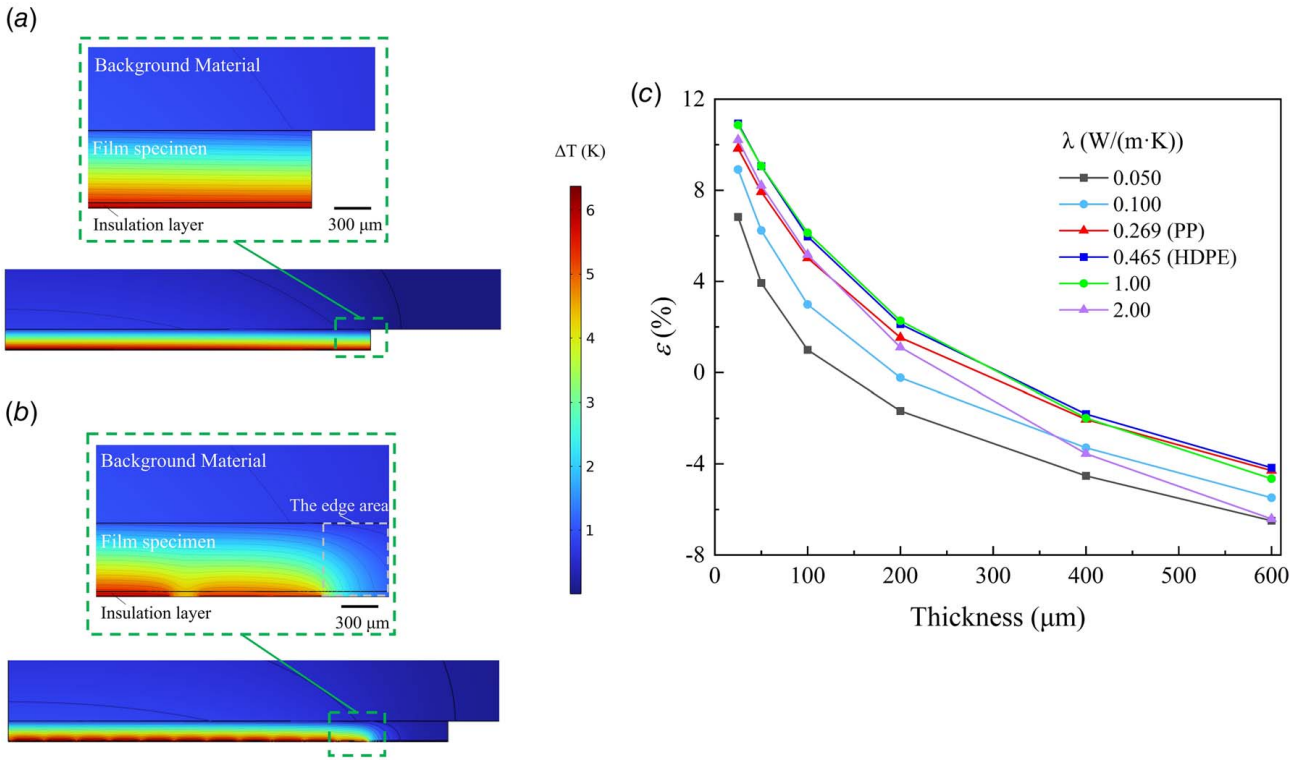

Fig. 7 Comparison of temperature distribution across the film specimen at the end of the measurement period (20 s) between the (*a*) ideal and (*b*) actual scenarios; and (c) difference in $R_{tot,f} - R_{tot,b}$ between the ideal and actual scenarios

The governing equations for heat conduction in the simulation are

$$\rho C_p \frac{\partial T}{\partial t} + \nabla q = Q \tag{8}$$

$$q = -\lambda \nabla T \tag{9}$$

where q is the heat flux by conduction and Q is the power supplied by the heat source. Thermal contact resistance in measurements using a TIM was considered and represented by equivalent thin resistive layers in the simulation model. The resistance of each layer was set to 28 mm^2K/W for HDPE measurements and 55 mm^2K/W for PP measurements, corresponding to half of the intercept obtained from the slope method (Table 2). The heating power and heating time of the probe were set to 1 W and 20 s, respectively, to align with the experimental conditions. The material properties, including λ, density (ρ), and the specific heat capacity (C_p), are listed in Table 1.

We first compare the simulated temperature distribution between the ideal and actual scenarios. In the ideal scenario, the isotherms are parallel within the film specimen, suggesting 1D heat conduction (Fig. 7(*a*)). However, in the actual scenario (Fig. 7(*b*)), the temperature distribution differs from the ideal scenario due to two factors. First, the actual double spiral probe has a slightly smaller heating area compared to an ideal circular probe with the same radius, which tends to result in a higher average temperature increase and thus an underestimated value of the thermal conductivity. Second, the radius of the insulation layer and the film specimen is slightly larger than that of the probe, which tends to create an additional edge area allowing heat to be conducted to the background material. This causes a lower average temperature increase, which results in an overestimation of $\lambda_\perp$.

The difference in $R_{tot,f} - R_{tot,b}$ between the ideal and actual scenarios (ϵ) was calculated according to

$$\epsilon = \left[\frac{(R_{tot,f} - R_{tot,b})_{act}}{(R_{tot,f} - R_{tot,b})_{idl}} - 1 \right] \times 100\% \tag{10}$$

where the subscript *idl* and *act* denote the ideal and actual scenarios, respectively. For a given sensor radius (11 mm in this case), ϵ varies depending on both the thickness and the thermal conductivity of the film specimens (Fig. 7(*c*)). In case of HDPE and PP, ϵ remains below 7% over the thickness range of 80–400 μm. Note that these values of ϵ will vary when a sensor with a different radius is utilized.

For thinner film specimens, the smaller area of the actual probe (the first factor) has a more pronounced effect, leading to an underestimated value of $\lambda_\perp$. This factor poses another challenge in evaluating thinner film specimens, alongside the aforementioned uncertainty in thickness determination. On the other hand, in case of thicker specimens, the influence of the additional edge area (the second factor) becomes more significant, resulting in an overestimated value of $\lambda_\perp$.

These systematic measurement errors at each thickness can accumulate and propagate into the final thermal conductivity value determined by the slope method. With knowledge of ϵ, the measured values of $R_{tot,f} - R_{tot,b}$ (Fig. 4(*d*)) were first adjusted and used to recalculate the thermal conductivity. By comparing the previous and recalculated thermal conductivity values (Table 2 available in the Supplemental Materials), the accumulated systematic errors were determined to be 4% for HDPE and 5% for PP.

To further reduce systematic errors, three general modifications to the probe are proposed so that the heat conduction during the measurement more closely resembles the ideal scenario: (1) increase of the probe radius, (2) narrowing of the gap within the double spiral, and (3) reduction of the thickness of the polyimide insulation layers.

3.5 Influence of Specimen Number. This section discusses the influence of the number of specimens (with different

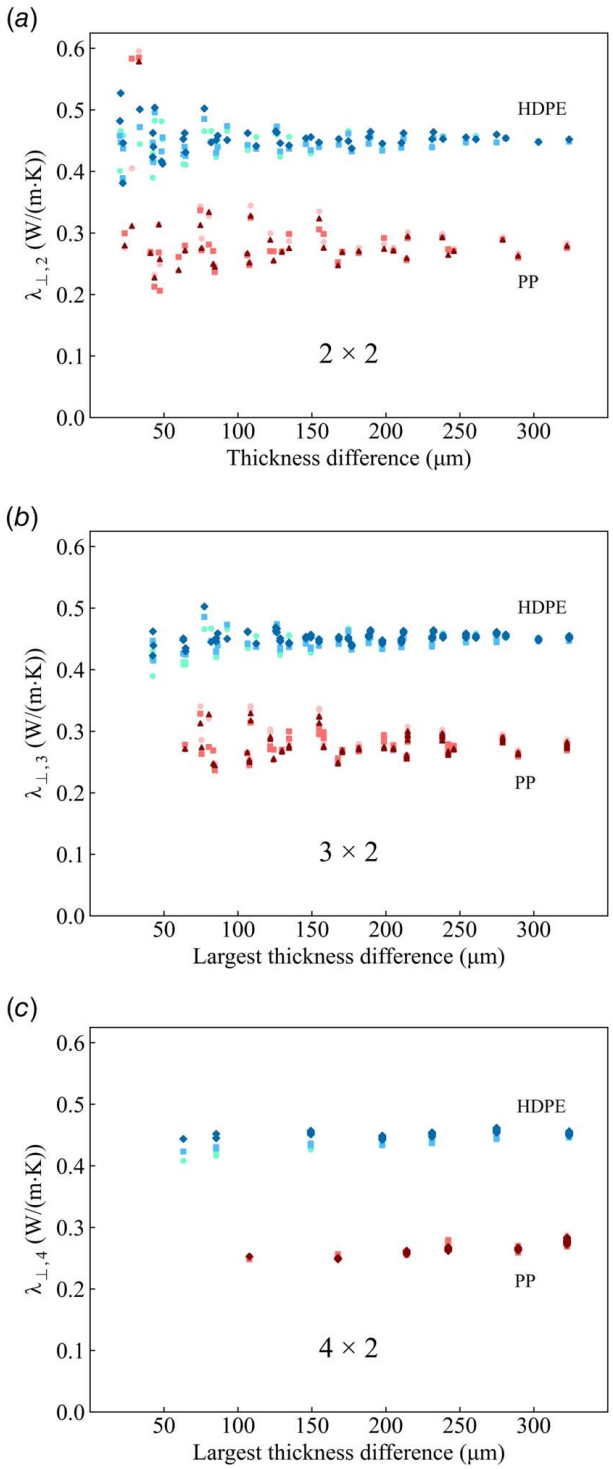

Fig. 8 Variation in $\lambda_\perp$ of HDPE and PP as a function of thickness difference for different mounting forces (● 0 N, ■ 50 N, ◆ 300 N, ▲ 550 N), across various systems: (*a*) 2 × 2, (*b*) 3 × 2, and (c) 4 × 2 datasets

thicknesses), providing insights into the reproducibility, and robustness of the TPS measurements when water is used as the TIM.

First, the intrinsic thermal conductivity calculated using only two pairs (2×2) of film specimens ($\lambda_{\perp,2}$) was examined. To achieve this, subsets of data from 2×2 specimens were extracted from Fig. 4(*d*) (solid symbols). For every subset, a linear regression was carried out, from which the slope and $\lambda_{\perp,2}$ were obtained. Subsequently, $\lambda_{\perp,2}$ values were plotted against the thickness difference between the 2×2 specimens (Fig. 8(*a*)).

Table 3 Comparison of $\lambda_\perp$ and standard deviation obtained from datasets with varying specimen numbers

Thermal conductivity (W/(m · K))	$\lambda_{\perp,2}$	$\lambda_{\perp,3}$	$\lambda_{\perp,4}$
HDPE	0.448 ± 0.022	0.448 ± 0.012	0.446 ± 0.008
PP	0.289 ± 0.065	0.278 ± 0.019	0.269 ± 0.009

First of all, the values of $\lambda_{\perp,2}$ were seen to evenly scatter across different mounting forces, indicating no dependence on the mounting force. In addition, the values of $\lambda_{\perp,2}$ were more scattered when the thickness difference was small. As the thickness difference increased, the values became more consistent. Overall, the standard deviation of $\lambda_{\perp,2}$ was 0.022 W/(m · K) (5%) for HDPE and 0.065 W/(m · K) (22%) for PP.

When the thickness difference was larger than 200 μm, the standard deviation significantly decreased to 0.006 W/(m · K) (1%) for HDPE and 0.013 W/(m · K) (5%) for PP. This suggests that 2×2 specimens with a significant thickness difference are likely sufficient for obtaining viable results of low uncertainty.

The intrinsic thermal conductivity obtained from 3×2 film specimens ($\lambda_{\perp,3}$) was also analyzed (Fig. 8(*b*)). With an additional specimen pair, the values of $\lambda_{\perp,3}$ were observed to be more consistent when the thickness difference was small, especially in the case of PP specimens. In case of both HDPE and PP, the standard deviation is less than 0.02 W/(m · K). Lastly, the intrinsic thermal conductivity from subsets with 4×2 specimens ($\lambda_{\perp,4}$) was evaluated (Fig. 8(*c*)). Differing from the preceding scenarios, the values of $\lambda_{\perp,4}$ in this case showed a much smaller standard deviation, especially when the thickness difference was small. Specifically, the standard deviation was 0.008 W/(m · K) (2%) for HDPE and 0.009 W/(m · K) (3%) for PP. All the results are summarized in Table 3.

Based on this analysis, two sets of specimens are recommended for precise TPS measurements with a standard deviation less of than 0.02 W/(m · K). The first set includes 2×2 specimens, each thicker than 80 μm, with a thickness difference exceeding 200 μm. The second set consists of 4×2 specimens, each thicker than 80 μm.

To illustrate the utility of the here proposed specimen set, 2×2 P3HT films with a thickness difference of over 200 μm were also measured, which gave an intrinsic cross-plane thermal conductivity of 0.296 ± 0.030 W/(m · K). This value is comparable to the thermal conductivity of P3HT films or bulk material prepared by other methods, such as drop casting (0.21 W/(m · K)) [54], spin coating (0.27 W/(m·K)) [55], cold pressing (0.19 W/(m · K)) [56], and drop casting followed by a cold pressing (0.33 W/(m · K)) [57].

4 Conclusions

In our measurements, thicker films led to a larger thermal contact resistance, likely due to their comparatively uneven surfaces and low pliability. This is at odds with the fundamental assumption of the slope method that heat conduction across the film is one-dimensional, leading to significant errors of up to 26% in case of HDPE. To address this issue, liquid thermal interface materials, e.g., de-ionized water or silicone oil, were introduced. The liquid thermal interface material ensured a consistent and low thermal contact resistance independent of film thickness, which enabled the precise extraction of the intrinsic cross-plane thermal conductivity. The extracted values for HDPE and PP agreed well with reference values, with a difference of 4%. This level of accuracy is comparable to the typical accuracy of 5% achieved by the LFA method for millimeter-thick samples.

Moreover, finite-element simulations were performed to quantify systematic errors arising from the assumption of one-dimensional heat conduction across the film specimens. The results indicate that the systematic error in the thermal conductivity of HDPE and

PP, determined via the slope method, is less than 5%. In addition, the simulations imply that samples with a thermal conductivity as low as 0.05 W/(m · K) and as high as 2 W/(m · K) can also be measured with a small error.

Finally, we observed that both the number of specimens and the thickness difference among them influence the overall precision of the measured intrinsic conductivity. Using as few as two specimens, provided they have sufficiently different thicknesses, can yield precise results with a standard deviation below 0.02 W/(m · K).

Hence, we propose a refined measurement procedure for efficient and reliable characterization of film specimens. The refined procedure involves the measurement of at least two sets of specimens with a significant thickness difference, application of a liquid thermal interface material (e.g., de-ionized water) to ensure a consistent and low thermal contact resistance, and subsequent use of the slope method to extract the intrinsic cross-plane thermal conductivity. In the future, it would be worthwhile to explore alternative liquid TIMs such as ethylene glycol for measurements under varying conditions.

Acknowledgment

This project has received funding from the European Union's Horizon 2020 research and innovation program under the Marie Skłodowska-Curie grant agreement No. 955837. The authors also wish to thank Dr. Silas Gustafsson for his insightful comments and Dr. Henrik Otterberg for his thorough language review.

Data Availability Statement

The datasets generated and supporting the findings of this article are obtainable from the corresponding author upon reasonable request.

References

[1] McKeen, L. W., 2017, *Film Properties of Plastics and Elastomers*, Elsevier, Amsterdam, The Netherlands.
[2] Tritt, T. M., 2005, *Thermal Conductivity: Theory, Properties and Applications*, Springer, Berlin, Germany.
[3] Yang, X., Liang, C., Ma, T., Guo, Y., Kong, J., Gu, J., Chen, M., and Zhu, J., 2018, "A Review on Thermally Conductive Polymeric Composites: Classification, Measurement, Model and Equations, Mechanism and Fabrication Methods," Adv. Compos. Hybrid Mater., **1**(2), pp. 207–230.
[4] Rao, Z., and Wang, S., 2011, "A Review of Power Battery Thermal Energy Management," Renew. Sustain. Energy Rev., **15**(9), pp. 4554–4571.
[5] Karimi, G., Li, X., and Teertstra, P., 2010, "Measurement of Through-Plane Effective Thermal Conductivity and Contact Resistance in PEM Fuel Cell Diffusion Media," Electrochim. Acta, **55**(5), pp. 1619–1625.
[6] Kandlikar, S. G., and Lu, Z., 2009, "Thermal Management Issues in a PEMFC Stack–A Brief Review of Current Status," Appl. Therm. Eng., **29**(7), pp. 1276–1280.
[7] Wang, Y., Yang, L., Shi, X.-L., Shi, X., Chen, L., Dargusch, M. S., Zou, J., and Chen, Z.-G., 2019, "Flexible Thermoelectric Materials and Generators: Challenges and Innovations," Adv. Mater., **31**(29), p. 1807916.
[8] Masoumi, S., O'Shaughnessy, S., and Pakdel, A., 2022, "Organic-Based Flexible Thermoelectric Generators: From Materials to Devices," Nano Energy, **92**, p. 106774.
[9] Xu, Y., Kraemer, D., Song, B., Jiang, Z., Zhou, J., Loomis, J., Wang, J., et al., 2019, "Nanostructured Polymer Films With Metal-Like Thermal Conductivity," Nat. Commun., **10**(1), p. 1771.
[10] Ronca, S., Igarashi, T., Forte, G., and Rastogi, S., 2017, "Metallic-Like Thermal Conductivity in a Lightweight Insulator: Solid-State Processed Ultra High Molecular Weight Polyethylene Tapes and Films," Polymer, **123**, pp. 203–210.
[11] Rodgers, P., Eveloy, V., Diana, A., Darawsheh, I., and Almaskari, F., 2017, "Mechanical and Heat Transfer Performance Investigation of High Thermal Conductivity, Commercially Available Polymer Composite Materials for Heat Exchange in Electronic Systems," ASME J. Therm. Sci. Eng. Appl., **9**(3), p. 031008.
[12] Zhao, D., Qian, X., Gu, X., Jajja, S. A., and Yang, R., 2016, "Measurement Techniques for Thermal Conductivity and Interfacial Thermal Conductance of Bulk and Thin Film Materials," ASME J. Electron Packag., **138**(4), p. 040802.
[13] Jiang, P., Qian, X., and Yang, R., 2018, "Tutorial: Time-Domain Thermoreflectance (TDTR) for Thermal Property Characterization of Bulk and Thin Film Materials," J. Appl. Phys., **124**(16), p. 161103.
[14] Capinski, W., Maris, H., Ruf, T., Cardona, M., Ploog, K., and Katzer, D., 1999, "Thermal-Conductivity Measurements of GaAs/AlAs Superlattices Using a Picosecond Optical Pump-and-Probe Technique," Phys. Rev. B, **59**(12), p. 8105.
[15] Schmidt, A. J., Cheaito, R., and Chiesa, M., 2009, "A Frequency-Domain Thermoreflectance Method for the Characterization of Thermal Properties," Rev. Sci. Instrum., **80**(9), p. 094901.
[16] Schmidt, A. J., Chen, X., and Chen, G., 2008, "Pulse Accumulation, Radial Heat Conduction, and Anisotropic Thermal Conductivity in Pump-Probe Transient Thermoreflectance," Rev. Sci. Instrum., **79**(11), p. 114902.
[17] Xu, K., Guo, J., Raciti, G., Goni, A. R., Alonso, M. I., Borrise, X., Zardo, I., Campoy-Quiles, M., and Reparaz, J. S., 2023, "In-Plane Thermal Diffusivity Determination Using Beam-Offset Frequency-Domain Thermoreflectance With a One-Dimensional Optical Heat Source," Int. J. Heat Mass Transfer, **214**, p. 124376.
[18] Min, S., Blumm, J., and Lindemann, A., 2007, "A New Laser Flash System for Measurement of the Thermophysical Properties," Thermochim. Acta, **455**(1–2), pp. 46–49.
[19] ISO 22007-4:2024, Plastics – Determination of Thermal Conductivity and Thermal Diffusivity.
[20] Abad, B., Borca-Tasciuc, D.-A., and Martin-Gonzalez, M., 2017, "Non-Contact Methods for Thermal Properties Measurement," Renew. Sustain. Energy Rev., **76**, pp. 1348–1370.
[21] Craddock, J. D., Burgess, J. J., Edrington, S. E., and Weisenberger, M. C., 2017, "Method for Direct Measurement of On-Axis Carbon Fiber Thermal Diffusivity Using the Laser Flash Technique," ASME J. Therm. Sci. Eng. Appl., **9**(1), p. 014502.
[22] Yang, J., Ziade, E., and Schmidt, A. J., 2016, "Uncertainty Analysis of Thermoreflectance Measurements," Rev. Sci. Instrum., **87**(1), p. 014901.
[23] Pérez, L. A., Xu, K., Wagner, M. R., Dörling, B., Perevedentsev, A., Goñi, A. R., Campoy-Quiles, M., Alonso, M. I., and Reparaz, J. S., 2022, "Anisotropic Thermoreflectance Thermometry: A Contactless Frequency-Domain Thermoreflectance Approach to Study Anisotropic Thermal Transport," Rev. Sci. Instrum., **93**(3), p. 034902.
[24] Qian, X., Ding, Z., Shin, J., Schmidt, A. J., and Chen, G., 2020, "Accurate Measurement of In-Plane Thermal Conductivity of Layered Materials Without Metal Film Transducer Using Frequency Domain Thermoreflectance," Rev. Sci. Instrum., **91**(6), p. 064903.
[25] Zhu, J., Tang, D., Wang, W., Liu, J., Holub, K. W., and Yang, R., 2010, "Ultrafast Thermoreflectance Techniques for Measuring Thermal Conductivity and Interface Thermal Conductance of Thin Films," J. Appl. Phys., **108**(9), p. 094315.
[26] Zhao, Y.-H., Wu, Z.-K., and Bai, S.-L., 2016, "Thermal Resistance Measurement of 3D Graphene Foam/Polymer Composite by Laser Flash Analysis," Int. J. Heat Mass Transfer, **101**, pp. 470–475.
[27] ISO 8302:1991. Thermal Insulation – Determination of Steady-State Thermal Resistance and Related Properties – Guarded Hot Plate Apparatus.
[28] Cahill, D. G., 1990, "Thermal Conductivity Measurement From 30 to 750 K: The 3ω Method," Rev. Sci. Instrum., **61**(2), pp. 802–808.
[29] Dames, C., 2013, "Measuring the Thermal Conductivity of Thin Films: 3 Omega and Related Electrothermal Methods," Annu. Rev. Heat Transf., **16**(16), pp. 7–44.
[30] ISO 22007-3:2008. Plastics – Determination of Thermal Conductivity and Thermal Diffusivity – Part 3: Temperature Wave Analysis Method.
[31] ISO 22007-2:2022. Plastics – Determination of Thermal Conductivity and Thermal Diffusivty – Part 2: Transient Plane Heat Source (Hot Disc) Method.
[32] Hashimoto, T., Matsui, Y., Hagihara, A., and Miyamoto, A., 1990, "Thermal Diffusivity Measurement of Polymer Films by the Temperature Wave Method Using Joule-Heating," Thermochim. Acta, **163**, pp. 317–324.
[33] Gustafsson, S. E., 1991, "Transient Plane Source Techniques for Thermal Conductivity and Thermal Diffusivity Measurements of Solid Materials," Rev. Sci. Instrum., **62**(3), pp. 797–804.
[34] Wereszczak, A. A., Emily Cousineau, J., Bennion, K., Wang, H., Wiles, R. H., Burress, T. B., and Wu, T., 2017, "Anisotropic Thermal Response of Packed Copper Wire," ASME J. Therm. Sci. Eng. Appl., **9**(4), p. 041006.
[35] Gustavsson, M., and Hälldahl, L., 2006, "Thermal Conductivity Measurements of Thin Insulating Layers Deposited on High-Conducting Sheets," Int. J. Thermophys., **27**(1), pp. 195–208.
[36] Gustavsson, J., Gustavsson, M., and Gustafsson, S., 1999, "On the Use of the Hot Disk Thermal Constants Analyser for Measuring the Thermal Conductivity of thin Samples of Electrically Insulating Materials," Thermal Conductivity, Vol. **24**, pp. 116–122.
[37] Instruction Manual, 2022. *Hot Disk Thermal Constants Analyser*, Hot Disk AB, Sweden.
[38] Zhang, H., Li, M.-J., Fang, W.-Z., Dan, D., Li, Z.-Y., and Tao, W.-Q., 2014, "A Numerical Study on the Theoretical Accuracy of Film Thermal Conductivity Using Transient Plane Source Method," Appl. Therm. Eng., **72**(1), pp. 62–69.
[39] Feng, B., Zhang, Y.-H., Tu, J., Fan, L.-W., and Yu, Z.-T., 2022, "Determination on the Thermal Conductivity and Thermal Contact Resistance of Thin Composite Phase Change Films as a Thermal Interfacial Material," Case Stud. Therm. Eng., **33**, p. 101979.
[40] Ahadi, M., Andisheh-Tadbir, M., Tam, M., and Bahrami, M., 2016, "An Improved Transient Plane Source Method for Measuring Thermal Conductivity of Thin Films: Deconvoluting Thermal Contact Resistance," Int. J. Heat Mass Transfer, **96**, pp. 371–380.
[41] Landry, D., Flores, R., and Goodman, R. B., 2024, "Estimating the Thermal Conductivity of Thin Films: A Novel Approach Using the Transient Plane Source Method," ASME J. Heat Transfer-Trans. ASME, **146**(3), p. 031004.
[42] Bachus, K. N., DeMarco, A. L., Judd, K. T., Horwitz, D. S., and Brodke, D. S., 2006, "Measuring Contact Area, Force, and Pressure for Bioengineering

Applications: Using Fuji Film and Tekscan Systems," Med. Eng. Phys., **28**(5), pp. 483–488.
[43] Koch, F. P. V., Rivnay, J., Foster, S., Müller, C., Downing, J. M., Buchaca-Domingo, E., Westacott, P., et al., 2013, "The Impact of Molecular Weight on Microstructure and Charge Transport in Semicrystalline Polymer Semiconductors-Poly (3-hexylthiophene), A Model Study," Prog. Polym. Sci., **38**(12), pp. 1978–1989.
[44] Cardarelli, F., 2008, *Materials Handbook: A Concise Desktop Reference*, Springer, Berlin, Germany.
[45] Ye, C.-M., Shentu, B.-Q., and Weng, Z.-X., 2006, "Thermal Conductivity of High Density Polyethylene Filled With Graphite," J. Appl. Polym. Sci., **101**(6), pp. 3806–3810.
[46] Feng, M., Pan, Y., Zhang, M., Gao, Q., Liu, C., Shen, C., and Liu, X., 2021, "Largely Improved Thermal Conductivity of Hdpe Composites by Building a 3D Hybrid Fillers Network," Compos. Sci. Technol., **206**, p. 108666.
[47] Weidenfeller, B., Höfer, M., and Schilling, F. R., 2004, "Thermal Conductivity, Thermal Diffusivity, and Specific Heat Capacity of Particle Filled Polypropylene," Compos. A: Appl. Sci. Manuf., **35**(4), pp. 423–429.
[48] Chen, L., Xu, H.-F., He, S.-J., Du, Y.-H., Yu, N.-J., Du, X.-Z., Lin, J., and Nazarenko, S., 2017, "Thermal Conductivity Performance of Polypropylene Composites Filled With Polydopamine-Functionalized Hexagonal Boron Nitride," PLOS One, **12**(1), p. e0170523.
[49] Kalakonda, P., Cabrera, Y., Judith, R., Georgiev, G. Y., Cebe, P., and Iannacchione, G. S., 2015, "Studies of Electrical and Thermal Conductivities of Sheared Multi-Walled Carbon Nanotube With Isotactic Polypropylene Polymer Composites," Nanomater. Nanotechnol., **5**, p. 2.
[50] Lua, A. C., and Su, J., 2006, "Isothermal and Non-Isothermal Pyrolysis Kinetics of Kapton Poyimide," Polym. Degrad. Stab., **91**(1), pp. 144–153.
[51] Montgomery, D. C., and Runger, G. C., 2010, *Applied Statistics and Probability for Engineers*, John Wiley & Sons, Hoboken, NJ.
[52] Zheng, Q., Kaur, S., Dames, C., and Prasher, R. S., 2020, "Analysis and Improvement of the Hot Disk Transient Plane Source Method for Low Thermal Conductivity Materials," Int. J. Heat Mass Transf., **151**, p. 119331.
[53] Zhang, H., Li, M., Fang, W., Dan, D., Li, Z., and Tao, W., 2014, "A Numerical Study on the Theoretical Accuracy of Film Thermal Conductivity Using Transient Plane Source Method," Appl. Therm. Eng., **72**(1), pp. 62–69.
[54] Wei, Q., Uehara, C., Mukaida, M., Kirihara, K., and Ishida, T., 2016, "Measurement of in-plane Thermal Conductivity in Polymer Films," AIP Adv., **6**(4), p. 045315.
[55] Kommandur, S., and Yee, S., 2018, "A Suspended 3-Omega Technique to Measure the Anisotropic Thermal Conductivity of Semiconducting Polymers," Rev. Sci. Instrum., **89**(11).
[56] Bounioux, C., Díaz-Chao, P., Campoy-Quiles, M., Martín-González, M. S., Goni, A. R., Yerushalmi-Rozen, R., and Müller, C., 2013, "Thermoelectric Composites of Poly (3-hexylthiophene) and Carbon Nanotubes With a Large Power Factor," Energy Environ. Sci., **6**(3), pp. 918–925.
[57] Kiefer, D., Yu, L., Fransson, E., Gómez, A., Primetzhofer, D., Amassian, A., Campoy-Quiles, M., and Müller, C., 2017, "A Solution-Doped Polymer Semiconductor: Insulator Blend for Thermoelectrics," Adv. Sci., **4**(1), p. 1600203.

Liquid Interface for Accurate Intrinsic Thermal Conductivity Measurements of Polymer Films Using the Transient Plane Source Method: Supplemental Material

Table S1. The properties of the hot-pressed films. Peak melting temperatures (T_m) and enthalpy of melting (ΔH_m) were extracted from first heating DSC thermograms. Crystallinity (X_c) is calculated by $(\Delta H_m / \Delta H_f^0) \times 100\%$, where ΔH_f^0 was the enthaply of fusion. ΔH_f^0 utilized for calculation was 293 J/g for 100% crystalline HDPE [1] and 209 J/g for 100% crystalline PP [2], respectively.

Material	$T_m(°C)$	$\Delta H_m(J/g)$	$X_c(\%)$
HDPE	129	179	61
PP	165	104	50
P3HT	233	22	-

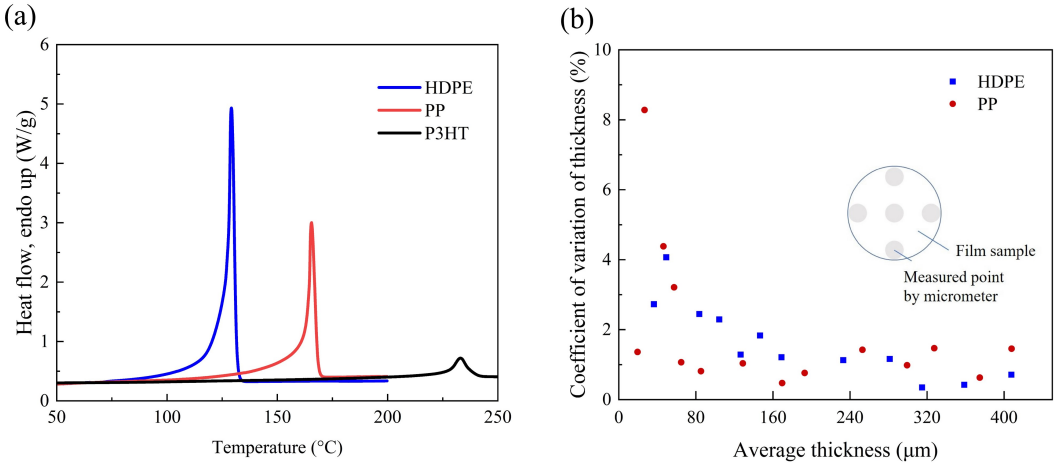

Fig. S1. Information regarding the hot-pressed polymer films. (a) DSC first heating thermograms. (b) The coefficient of variation of film thickness. The inset illustrates the locations of the measured points on each film specimen.

Table S2. The results from the slope method. (a) the original calculation with water as TIM. (b) recalculated results accounting for accumulated errors determined by the simulations.

Material	Mounting force (N)	$\lambda_{\perp}(\mathrm{W}/(\mathrm{m}\cdot\mathrm{K}))$ (original)	Intercept ($\mathrm{mm}^2\mathrm{K}/\mathrm{W}$) (original)	$\lambda_{\perp}(\mathrm{W}/(\mathrm{m}\cdot\mathrm{K}))$ (recalculated)	Intercept ($\mathrm{mm}^2\mathrm{K}/\mathrm{W}$) (recalculated)
HDPE	0	0.447	50.6	0.429	31.5
	50	0.453	48.5	0.428	21.2
	300	0.449	61.6	0.433	19.5
PP	50	0.279	118.3	0.266	72.1
	300	0.276	100.9	0.263	55.1
	550	0.275	110.0	0.262	63.6

REFERENCES

1. B. Wunderlich and G. Czornyj, "A study of equilibrium melting of polyethylene," Macromolecules **10**, 906–913 (1977).
2. J. Brandrup, E. H. Immergut, and W. McDowell, *Polymer handbook* (1975).

Paper II

Extending the Transient Plane Source Scanning Method for Determining the Specific Heat Capacity of Low Thermal Conductivity Materials through a Numerical Study

Thermochimica Acta

Thermochimica Acta 742 (2024) 179883

Contents lists available at ScienceDirect

Thermochimica Acta

journal homepage: www.elsevier.com/locate/tca

Extending the Transient Plane Source Scanning method for determining the specific heat capacity of low thermal conductivity materials through a numerical study

Zijin Zeng [a,b,*], Christian Müller [a], Besira Mihiretie [b]

[a] Department of Chemistry and Chemical Engineering, Chalmers University of Technology, Gothenburg, 41296, Sweden
[b] Hot Disk AB, Sven Hultins gatan 9A, Gothenburg, 41288, Sweden

ARTICLE INFO

Keywords:
Specific heat capacity
Transient plane source scanning method
Finite element method
Polymer
Sensitive analysis

ABSTRACT

In contrast to the conventional Transient Plane Source (TPS) method, the Transient Plane Source Scanning (TPSS) technique allows for the direct determination of the specific heat capacity and requires the use of a specially designed sample holder for accurate measurements. While this method correctly determines the specific heat capacity of samples with moderate and high thermal conductivity, it tends to underestimate the values for those with low thermal conductivity. This paper demonstrates that the underestimated specific heat capacity results from heat loss during the measurement process. To precisely quantify the heat loss, a numerical model based on the finite element method was developed, with key material properties tuned based on measurement data. This model can closely describe the curve of measured thermal response, thereby enabling the precise determination of the specific heat capacity. Consequently, this study introduces a novel approach that incorporates numerical simulation to enhance TPSS measurements of poorly conducting samples, providing a reliable alternative for determining the specific heat capacity.

1. Introduction

The specific heat capacity (C_p) refers to the energy necessary to raise the temperature of a unit mass of material by a finite difference in temperature [1]. It plays a vital role in the design of devices for thermal management. Accurate measurements are essential for optimizing system behavior in industries like aerospace [2,3], automotive [3–5], energy storage [6,7], construction [8–10] etc.

Calorimetry methods such as differential scanning calorimetry (DSC) [11], drop calorimetry [12], adiabatic calorimetry [13,14], and recently the Transient Plane Scanning Source (TPSS) method [15] are commonly used to directly measure C_p.

The Transient Plane Source (TPS) method has been used to characterize a wide range of materials, such as polymers [16,17], building materials [18], textiles [19,20], and graphene composites [21,22]. This method utilizes a thin metal structure in the shape of a double spiral, which performs two simultaneous functions: (1) it serves as a heat source through Joule heating of the spiral and hence the surrounding material, and (2) acts as a sensing element that records a response curve of temperature increase, $\Delta T(t)$, that results from the heating [23]. This response curve is referred to as the temperature transient or thermal response in the text below. Since the resistance of the sensor changes with temperature, the Joule heating alters the electrical resistance of the metal spiral, which disrupts the balance of the Wheatstone bridge. The resulting imbalance in voltage is measured with a sensitive voltmeter. Given the temperature coefficient of resistance, a, and the initial resistance, R_0, of the sensor, one can relate the average temperature change of the sensor to its electrical resistance over time, $R(t)$, as follows [24]:

$$R(t) = R_0[1 + a \cdot \Delta T(t)] \tag{1}$$

In this study, a nickel metal embedded between two protective polyimide (Kapton) films is utilized as the sensor (Fig. 1a), as it offers a well-defined temperature coefficient of resistance. Using this method, it is possible to calculate the thermal conductivity and thermal diffusivity from a single measurement of thermal response curve $\Delta T(t)$ according to Eq. (2) [23].

$$\Delta T(\tau) = P(\pi^{3/2} r \lambda)^{-1} D(\tau) \tag{2}$$

where P is the heating power from the sensor, r is the radius of the sensor, λ is the thermal conductivity of the specimen material, and $D(\tau)$

* Corresponding author at: Department of Chemistry and Chemical Engineering, Chalmers University of Technology, Gothenburg, 41296, Sweden.
E-mail addresses: zijin@chalmers.se (Z. Zeng), besira.mihiretie@hotdiskinstruments.com (B. Mihiretie).

https://doi.org/10.1016/j.tca.2024.179883
Received 12 August 2024; Received in revised form 18 October 2024; Accepted 19 October 2024
Available online 28 October 2024

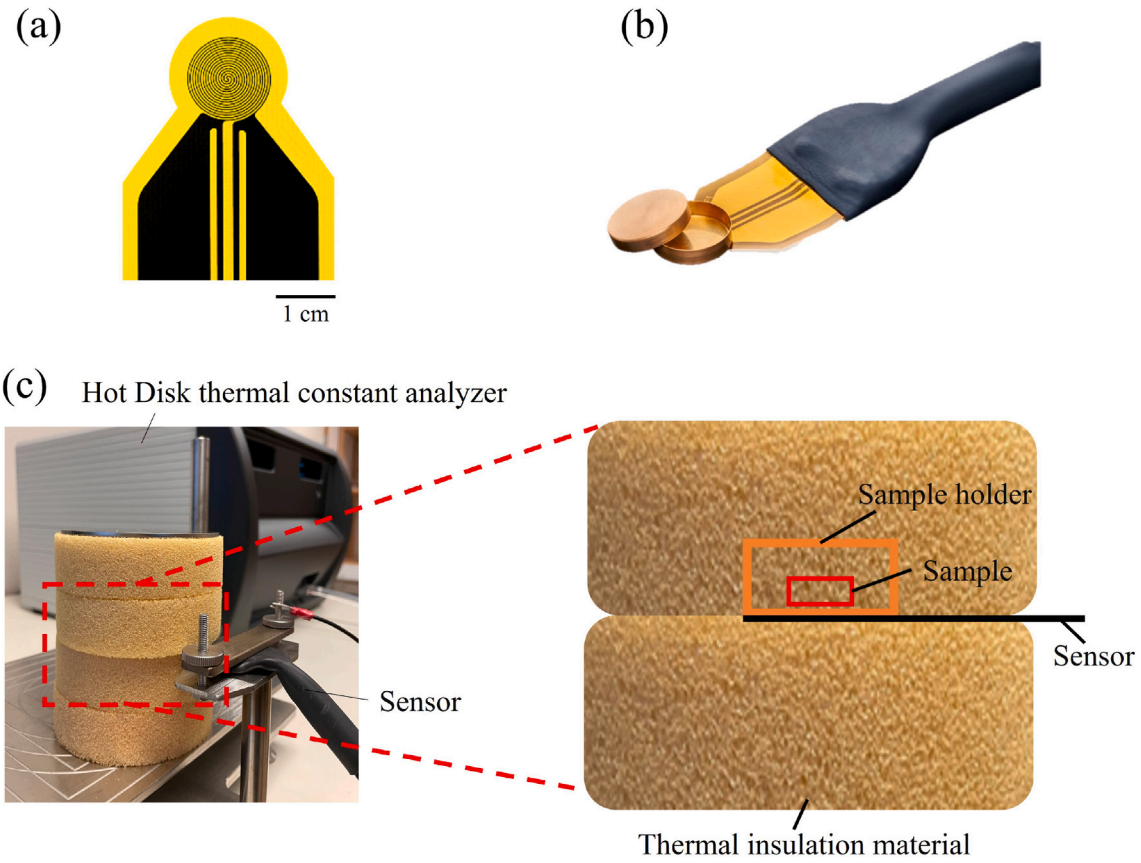

Fig. 1. Sensor profile and schematic of the measurement setup (a) Hot Disk Sensor 5501 insulated by polyimide films. (b) Gold sample holder attached to a Hot Disk Sensor 5501. (c) Schematic of a measurement with a sample.

is a dimensionless time function of τ, which is defined as a function of thermal diffusivity, α and measurement time, t [23].

$$\tau = \left(\frac{t}{\theta}\right)^{1/2} \quad and \quad \theta = r^2/\alpha \tag{3}$$

In instances where both thermal conductivity and thermal diffusivity can be simultaneously determined from an iterative data fitting of the experimentally recorded temperature transient in accordance with Eq. (2), the volumetric heat capacity, ρC_p, of a specimen with density ρ can be calculated using:

$$\rho C_p = \lambda/\alpha \tag{4}$$

Determining the ρC_p from λ and α is applicable to homogeneous isotropic materials like powders, pastes, and pure metals that feature a specific sample size and thermal transport properties [25]. This method offers a reliable and practical approach for determining the specific heat capacity of relatively large specimens. Following this approach, authors in ref [26] measured the C_p of polymers, including poly(methyl methacrylate) (PMMA), across a wide temperature range (from 25 K to 400 K).

Similarly, for a homogeneous slab specimen, the Hot Disk Slab method [27] allows for the simultaneous measurement of the in-plane thermal conductivity and thermal diffusivity using only one temperature transient, leading to the determination of the volumetric specific heat capacity. However, challenges may arise when dealing with small samples with high thermal conductivity even if isotropic, rod-shaped specimens, or extremely conductive slabs are investigated [25].

On the other hand, for materials that are anisotropic and/or inhomogeneous, like many of the contemporary samples produced in the industries mentioned earlier, using Eq. (4) to determine the C_p is not feasible. In fact, it is essential to know the volumetric heat capacity of materials beforehand if one aims to extract the direction-dependent thermal conductivity and thermal diffusivity from temperature transients [28,29]. This necessity motivated the development of the TPSS method, which utilizes the same experimental instrument (the thermal constant analyzer supplied by Hot Disk AB, Gothenburg, Sweden) as the TPS method but with the addition of sample holder and distinct algorithms (see Section 2 for more details). However, the TPSS method presents challenges when measuring materials with a thermal conductivity lower than approximately 1 W/(m K) [30].

It is also possible to employ the Dynamic Plane Source (DPS) approach [31,32] for characterizing the C_p of high-conductivity materials directly. This method is similar to the TPPS method but does not require a special sample holder. To accurately determine C_p with this method, certain criteria must be met. For example, the thermal mass of the sample must be significantly higher than that of the sensor, posing challenges for materials with a low thermal conductivity. Additionally, the thermal conductivity of the sample should be at least 100 times that of its insulating surroundings [25]. For example, using an expanded polystyrene foam (EPS) with a thermal conductivity close to 0.03 W/(m K) sets the approximate working range for the required thermal conductivity to greater than 3 W/(m K).

Numerous experimental and numerical investigations have been conducted to validate the standard TPS method [33–41] , and several sensitivity analyses have been carried out to provide valuable information for thermal properties identification and experimental design [42–44]. However, to the best of our knowledge, studies regarding the TPSS method are rare, and no study has been conducted to improve this method for low thermal conductivity materials.

In summary, the TPSS method is mainly suited for materials with a relatively high thermal conductivity (>1 W/(m K)). This study aims to

extend its applicability to low thermal conductivity materials, including most polymers. To achieve this, a finite element method (FEM) model is developed, which permits to optimize data fitting and analysis, and thus aids in identifying relevant parameters that may contribute to potential sources of error, such as heat loss to the surrounding insulation materials. By understanding these factors, a well-tuned simulation model is proposed that enables accurate data extraction of the C_p. The improvement of the developed model is then evaluated by testing it on a PMMA polymer, which has a low thermal conductivity of approximately 0.19 W/(m K) [45], as well as on glass (approximately 1.0 W/(m K)) and copper samples (approximately 398 W/(m K)).

2. The transient plane source scanning method

This section first introduces the experimental setup, the theoretical framework supporting the TPSS method, and the subsequent data analysis for C_p determination. It is followed by a systematic experimental study on representative samples, illustrating the current capabilities and limitations of the method.

2.1. Experimental setup and theory

As outlined in the previous section, the TPSS method necessitates an additional sample holder and enables the direct measurement of the C_p. In this study, the sample holder is made of a gold alloy with a gold purity of 75% (Fig. 1b).

Two steps are involved in the TPSS method [15]. First, a measurement is conducted with an empty sample holder, referred to as the holder measurement. This step provides crucial information regarding the C_p of the sample holder itself and the heat loss occurring during the measurement. The second step is to conduct a measurement with the sample placed inside the sample holder, referred to as the sample measurement. In both cases, the sample holder is sandwiched between insulation materials (Fig. 1c), which minimizes heat loss.

For the first step, the holder measurement, the specific heat capacity equation can be expressed as follows [15]:

$$P_h = [(mC_p)_h + f_h(t)]\frac{d}{dt}(\Delta T_h(t)) \tag{5}$$

where P_h represents the power input from the sensor during the holder measurement, $(mC_p)_h$ is the heat capacity of the sample holder, and $\frac{d}{dt}(\Delta T_h(t))$ represents the rate of temperature increase of the sensor. It is assumed that there exists a heat loss equation [15], denoted as $f(t)$, which governs the rate of heat loss during the measurement by $Q(t) = \frac{d}{dt}(\Delta T(t))f(t)$. $f_h(t)$ is the heat loss equation for the holder measurement.

During the second step, the sample measurement, we assume that the sensor adequately captures the thermal response of the sample after a certain time [15,25]. The total measurement time should be long compared to this certain time duration. A detailed discussion about how to decide the total measurement time can be found in Section 2.2. Based on these assumptions, Eq. (6) can be written for the sample measurement in a similar manner as Eq. (5) [15]:

$$P_s = [(mC_p)_h + (mC_p)_s + f_s(t)]\frac{d}{dt}(\Delta T_s(t)) \tag{6}$$

where P_s represents the power input from the sensor during the sample measurement, $(mC_p)_s$ is the heat capacity of the sample, $\frac{d}{dt}(\Delta T_s(t))$ represents the rate of temperature increase of the sensor during the sample measurement, and $f_s(t)$ is the heat loss equation for the sample measurement. The heating power during the sample measurement should be increased to achieve a similar temperature increase as observed for the holder measurement [30]. In the phase of the measurement where the $\Delta T_h(t)$ and $\Delta T_s(t)$ exhibit linear alignment, it is assumed that $f_h(t)$ is equivalent to $f_s(t)$. This assumption allows for the derivation of a final equation to calculate the heat capacity of the sample [15]:

$$\frac{\overline{P_s}}{\delta_s} - \frac{\overline{P_h}}{\delta_h} = (mC_p)_s \tag{7}$$

where $\overline{P}$ is the average power input from the sensor and δ is the average rate of temperature increase, defined as $\frac{d}{dt}\overline{\Delta T(t)}$.

Table 1
Three types of samples and the expected time ranges for calculating C_p.

Material	Expected time ranges
Copper	20–40 s
Glass	40–80 s
PMMA	120–240 s

2.2. The determination of total measurement time

In both case of the holder measurement and sample measurement, the measurement time should be longer than the time it takes to establish a non-varying temperature gradient inside the holder or holder-sample assembly. After the non-varying temperature gradient is established, the recorded $\frac{d}{dt}(\Delta T(t))$ of the sensor can represent that of the sample holder or holder-sample assembly, which is the foundation of Eq. (5) and Eq. (6).

In an ideal case, where a cylindrical sample is heated by a uniform and constant heat flux from its bottom surface (see inset of Fig. 2a), and assuming no heat loss, the time needed to establish a non-varying temperature gradient within the sample, known as the settling time, can be estimated by ${l_s}^2/\alpha$. Here, α denotes thermal diffusivity, l represents the characteristic length [15,25], and subscript s refers to the sample. The characteristic length of the sample is its height in the direction perpendicular to the sensor surface.

On the other hand, for a measurement where an additional sample holder is utilized (this work), the settling time could be estimated using $(\frac{l_s}{\sqrt{\alpha_s}} + \frac{l_h}{\sqrt{\alpha_h}})^2$, where subscript h denotes the sample holder [15,25]. In actual cases where the sample holder has a much higher thermal diffusivity than the sample, $2\,{l_s}^2/\alpha$ is utilized for calculating the settling time of the holder-sample assembly [25,30]. In addition, it is recommended that data analysis should focus on the time range between $2 \cdot l_s^2/\alpha$ to $4 \cdot l_s^2/\alpha$ seconds for the subsequent heat capacity calculation [25,30]. The time ranges based on this recommendation were utilized in the following section for C_p calculation.

2.3. Experimental results and data analysis

Utilizing the aforementioned two-step experimental procedure, the precise determination of the power delivered to the sample, which is instrumental in influencing the temperature throughout the entire bulk specimen, can be achieved. Furthermore, the average rate of temperature rise, δ, is calculated from the measured data within a recommended time range. This allows for the determination of the C_p using Eq. (7). Data from different time ranges were used to calculate the specific heat capacity of different samples. Table 1 provides an overview of the sample types and expected time ranges. The reason and the detailed methodology for deciding the time ranges are explained in Section 2.2. As outlined, the selection of the time range depends on the thickness and thermal diffusivity of the sample. It should be noted that the settling time of the gold sample holder must also be considered, which is circa 20 s; hence the earliest time range should start from 20 s.

To systematically evaluate the existing measurement method, we measured the temperature transient of samples with varying thermal diffusivity at room temperature (293 K). Exemplary temperature transients of the holder measurement and sample measurement of different samples are shown in Fig. 2b. Heating powers used during the measurements were as follows: 80 mW for the holder measurement, 160 mW for copper, and 130 mW for both copper and PMMA. These sample types consisted of 99% pure copper, float glass obtained from VWR, and atactic PMMA with a weight-average molecular weight (Mw) of 94 kg/mol and a polydispersity index (PDI) of 1.5, sourced from Polysciences. The thermal conductivity of PMMA at room temperature is expected to be approximately 0.19 W/(m K) [45].

The comparison of C_p of those samples is presented in Fig. 2c. The reference C_p of the glass and PMMA in Fig. 2c are determined using

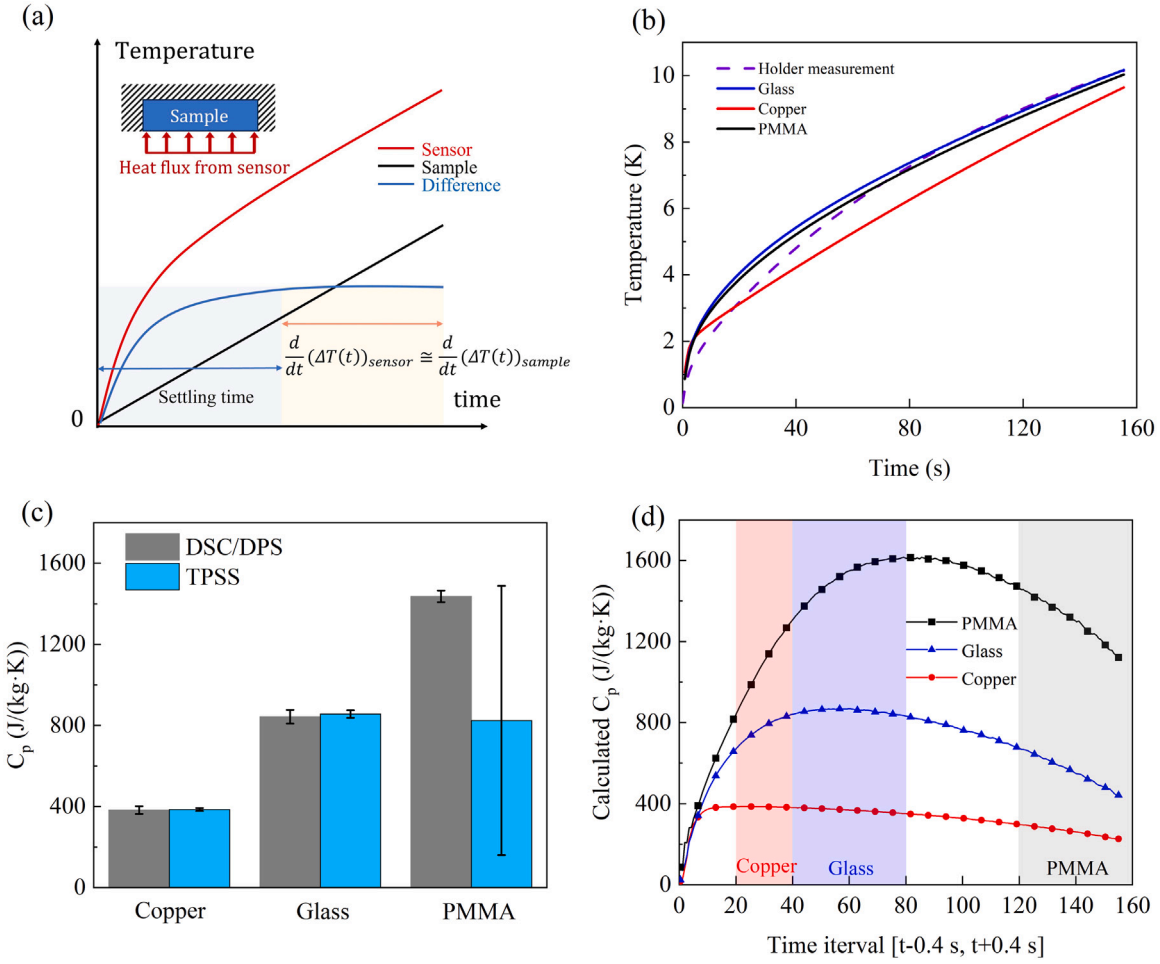

Fig. 2. (a) Comparison of average temperature increase between the sensor and sample in an ideal scenario, where a cylindrical sample is heated by a uniform heat flux from its bottom, with no heat loss (see inset). (b) Temperature transient (temperature increase over time) measured by the sensor in the holder measurement and the sample measurements. (c) Comparison between C_p of the samples at room temperature (293 K) obtained from the TPSS method and reference values from DSC[1](glass, PMMA) or DPS[2](copper). (d) The value of C_p calculated using moving time windows ([t-0.4 s, t+0.4 s]) with a short interval of 0.8 s.

DSC. Instead, the reference specific heat capacity of copper is obtained using the DPS method [32], which is reliable for samples with a high thermal conductivity. Each reported TPSS value of average C_p is based on three measurements. The error bars are related to the fluctuation of calculated C_p within corresponding time ranges (Fig. 2d).

The average TPSS values for copper and glass are in good agreement with the reference values, but the value for PMMA is significantly underestimated. To preliminarily investigate the cause of the underestimation, we recalculated the C_p using moving time windows [t-0.4 s, t+0.4 s] with a small interval of 0.8 s [41], instead of all the data from the expected time range. Here, t represents the central point of the time window. In our measurements, an interval of 0.8 s is used to record data across all three types of samples, serving as the thermal response sensing period. Consequently, this 0.8 s interval represents the smallest time window available for the determination of C_p. This analysis provides a more detailed insight into how the calculated values of C_p evolve over time.

It is observed that the calculated C_p of all the samples initially increases and then declines over time (Fig. 2d). The colored regions indicate the time ranges for calculating C_p of copper and glass. In the case of the copper sample, the increasing phase is notably shorter than that of the other samples, owing to its high thermal diffusivity. Within 20 s to 40 s, there is a range of data with a minimal fluctuation of around 1%. For the glass sample, the fluctuation of C_p from 40 s to 80 s is noticeably larger, around 3%. For copper and glass, a state could be reached where the heat loss has a relatively small impact on the measurement accuracy. However, when the data outside this state is used to calculate the C_p, the results are inaccurate. This implies that the measurement results are sensitive to the selection of the time window utilized for the calculation.

In contrast, for the PMMA sample, there is a 13% drop in C_p from 120 s to 160 s. If the data is extrapolated linearly to 240 s, the drop from 120 s to 240 s is expected to be even more significant. Since the calculated C_p of PMMA around 160 s is already much lower than the reference value and is expected to decrease further over time, the data from 160 s to 240 s were not experimentally obtained but extrapolated by a linear fit.

3. Numerical simulation

In this section, we present a simulation model using finite element method (FEM) (Section 3.1) and proceed to describe a modeling approach we term ‘a well-tuned model’, grounded in TPSS measurement data (Section 3.2).

[1] Measured using a DSC 2 calorimeter supplied by Mettler Toledo, Greifensee, Switzerland.

[2] Measured using a thermal constant analyzer supplied by Hot Disk AB, Gothenburg, Sweden.

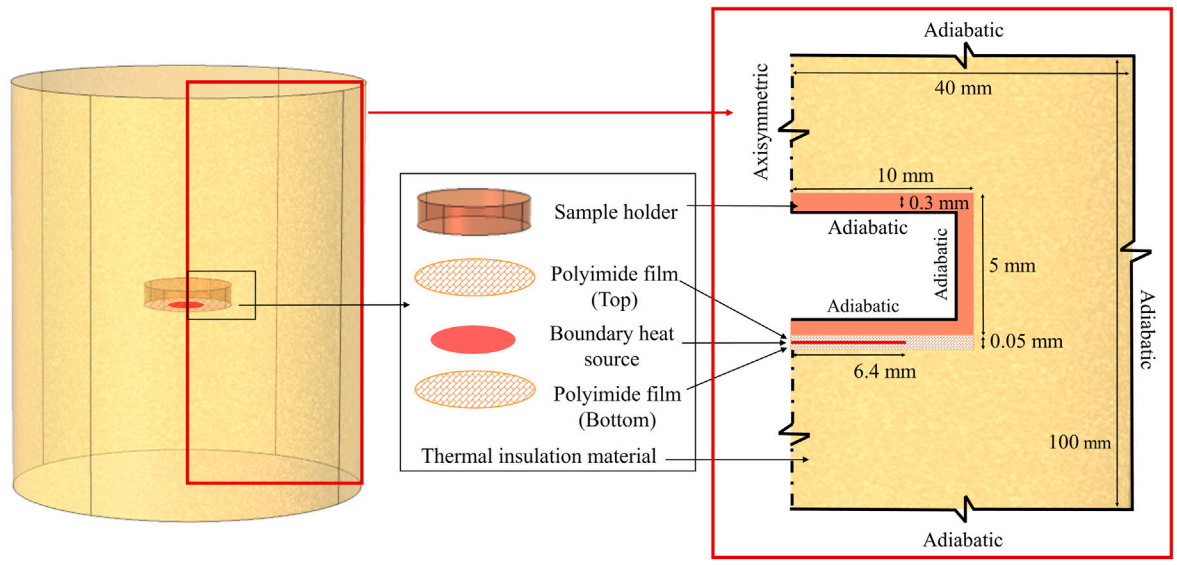

Fig. 3. Schematic of the model accompanied by its cross-sectional view. Selected components have been scaled in the cross-sectional view to accommodate the wide range of dimensions and ensure all elements are discernible. An ideal heat source with a circular boundary (marked in red) is used to represent the double spiral sensing element.

3.1. The development of a FEM model

A 3-dimensional (3D) FEM simulation of the TPSS experimental approach was reported in Ref. [46]. These simulation results demonstrated good agreement with high and moderately conducting materials. However, it was noted that for low thermal conductivity materials, the TPSS method tends to underestimate the C_p values, an issue this study aims to address. Due to the nearly axisymmetric nature of the measurement setup, its simulation model can be simplified to two dimensions (2D) [37,40]. For the current study, which involves the analysis of multiple parameters, a 2D simulation was chosen. This preference is due to its efficiency in accurately capturing heat transfer properties while also reducing the computational time. Furthermore, a mesh independence analysis was conducted to select the optimum mesh configuration for accuracy and computational efficiency (Fig. S1).

A detailed visualization of each component within the model is achieved through a 3D representation, crafted by rotating the 2D geometry, and is accompanied by dimensional details (Fig. 3) that correspond to the experimental TPSS counterpart.

To simplify the simulation model, the following assumption were made:

- The heat transfer between measurement setup and ambient environment is negligible (adiabatic boundary condition).
- Inside the setup, heat transfer via convection and radiation is negligible.
- The measurement setup is axisymmetric, which means the effect from sensor leads, and the non-circular shape of the sample, are negligible.
- Material properties are assumed to be constant during the measurement.
- The spiral sensing element of the sensor can be represented by an ideal circle boundary heat source.

Material properties utilized in these simulations are summarized in Table 2. The simulation utilized the heat transfer module for solids in COMSOL Multiphysics, and the governing equations for non-steady state heat conduction employed in the simulation are presented as follows:

$$\rho C_p \frac{\partial T}{\partial t} + \nabla q = \phi \tag{8}$$

$$q = -\lambda \nabla T \tag{9}$$

Table 2
Summary of the component properties used in the simulation for sensitivity analysis.

Component	Material	λ (W/(m K))	C_p (J/(kg K))	ρ (kg/m^3)
Sample holder	Gold alloy	44 ± 10[a]	177[b]	15500[c]
Insulation material	Polyimide foam	0.039 ± 0.002[d]	1090[e]	6.6[c]
Polyimide film	Polyimide	0.12[e]	1090[e]	1420[e]

[a] Measured by the Hot Disk slab method [27].
[b] Calculated based on the specific heat capacity of the ingredients.
[c] Calculated from mass and volume.
[d] Measured by the Hot Disk isotropic method [24].
[e] Obtained from Ref. [47].

where q denotes heat flux by conduction, while ϕ is the power supplied from the heat source. The thermal contact resistance, R_c, is integrated in the simulation model by assigning an equivalent thin resistive layer between the geometry of the sample and sample holder. The heat conduction across the resistive layer is governed by,

$$q = \frac{1}{R_c}(T_h - T_s) \tag{10}$$

where T_h and T_s are the temperature sample holder and the sample at their contact interface, respectively.

3.2. Development of the well-tuned model

The development and utilization of the well-tuned model consists of four steps (Fig. 4).

Firstly, a FEM model (Section 3.1) based on the actual experimental setup and the components used in the holder measurement (without sample) was developed.

Secondly, we employed the FEM model to conduct a sensitivity analysis to different material properties. According to the sensitivity analysis, we identify four crucial parameters that potentially influence the thermal response in the holder measurement to a significant degree.

Thirdly, these identified key parameters were finely tuned through a parameter estimation analysis that utilized data from the holder measurement, resulting in the well-tuned model which can closely describe the actual measurement.

In a final step, a sample was added to the well-tuned model, while the four key parameters obtained in the previous step were held constant. Sample measurement data were then incorporated into the model

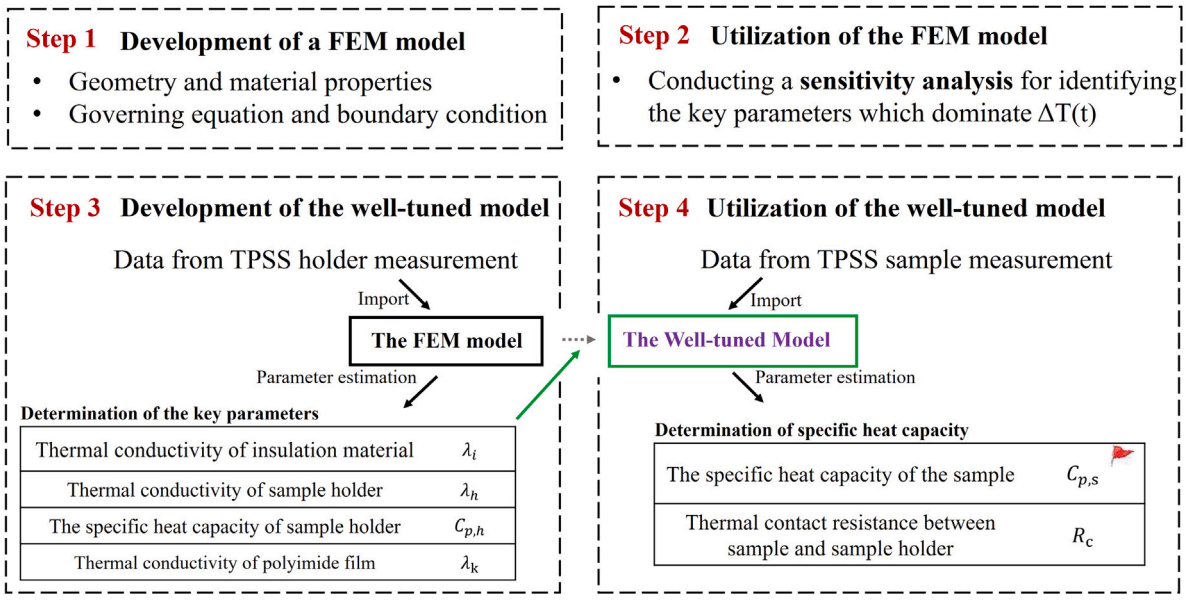

Fig. 4. The work flow of the simulation, including the development of the well-tuned model and its implementation.

for another parameter estimation analysis, enabling the determination of the C_p of the sample.

3.2.1. Sensitivity analysis

In the sensitivity study, a simulation based on the parameters in Table 2 was conducted to find out how a change in parameter x influences $\Delta T(t)$ in the measurement, namely the sensitivity coefficient $S_x(t)$. Following Ref. [42,48,49], we define $S_x(t)$ as the difference of thermal response caused by changing a parameter x by a certain tolerance of ϵ. To determine $S_x(t)$, a parameter sweep study is conducted with the target parameter being assigned to different values ($\epsilon = 0.1\%$), while keeping other parameters fixed. Using the equation below, $S_x(t)$ is calculated from the thermal response,

$$S_x(t) = \frac{\Delta T_{x+\epsilon}(t) - \Delta T_x(t)}{\epsilon} \tag{11}$$

The outcomes of $S_x(t)$ distinctly demonstrate that different parameters have specific impacts on $\Delta T(t)$, as illustrated in Fig. 5a and Fig. 5b. In the holder measurement, the sample holder plays a crucial role in the holder measurement, with its thermal conductivity (λ_h) and specific heat capacity ($C_{p,h}$) considerably affecting $\Delta T(t)$. The thermal conductivity of the insulation material (λ_i) also markedly influences $\Delta T(t)$ and its influence increases dramatically with time. Additionally, the thermal conductivity of the polyimide film (λ_k) is another parameter of interest. Since an ideal circular boundary heat source was employed to represent the spiral sensing element, λ_k in the simulation serves as an equivalent thermal conductivity that enables the ideal heat source to accurately replicate the behavior of the actual spiral. Therefore, these four parameters are selected to be tuned based on the data from the holder measurement.

In the parameter estimation, it is necessary to determine if the parameters being estimated exhibit linear correlation within the input data range. If such correlation exists, simultaneous estimation of the correlated parameters becomes infeasible [48]. During the period after 20 s, the sensitivity to λ_k (S_{λ_k}) and λ_h (S_{λ_h}) tends to remain constant. This implies that these two parameters are not correlated with the other two parameters, λ_i and $C_{p,h}$, whose sensitivity (S_{λ_i}, $S_{C_{p,h}}$) varies over time with different derivatives. S_{λ_i} has no linear correlation with $S_{C_{p,h}}$ throughout 160 s, while S_{λ_k} tends to be linearly correlated with S_{λ_h} after 20 s (Fig. S2a). The non-linear relationship between S_{λ_k} and S_{λ_h} from 10 s to 20 s still allows for the simultaneous estimation of these two parameters based on the measured data.

A sensitivity analysis was conducted for a measurement of copper (Fig. 5b). In this case, the sensitivity to the specific heat of the copper ($S_{C_{p,c}}$) increases over time, which is in agreement with other transient measurements of C_p in a thermal-insulated condition [50,51]. The sensitivity of the equivalent thermal contact resistance between the sample and the sample holder (S_{R_c}) remains constant at an appreciable level after a short period and does not correlate with $S_{C_{p,c}}$. Therefore, these two parameters could be estimated at the same time.

On the other hand, the sensitivity to λ_i (S_{λ_i}) and $C_{p,h}$ ($S_{C_{p,h}}$) rises over time. These two parameters were estimated in step 3 and utilized as the input parameters when estimating $C_{p,c}$. Relatively high sensitivity to these parameters suggests that their uncertainty has a greater influence on the final result of $C_{p,c}$. When considering the influence of λ_i, time windows starting after 20 s are preferred because of a higher relative sensitivity to the specific heat capacity of copper ($S_{C_{p,c}}/S_{\lambda_i}$, Fig. S2b). Meanwhile, $S_{C_{p,c}}/S_{C_{p,h}}$ remains relatively constant after 20 s, indicating the data after this time are comparable in terms of the potential influence of $C_{p,h}$.

Overall, λ_h, $C_{p,h}$, λ_i, and λ_k could be simultaneously identified in step 3, while the specific heat capacity of the sample ($C_{p,s}$) and R_c could be estimated in step 4.

3.2.2. Parameter estimation and model validation

The well-tuned model shares the same physical framework as the FEM model developed in the previous section. However, the four key material properties (λ_h, $C_{p,h}$, λ_i, λ_k) in the well-tuned model were determined through a parameter estimation study (step 3) based on the holder measurement data. Specifically, the data from 10 s to 160 s, with a heating power of 80 mW, were utilized. In step 4, the time windows immediately after the sample achieved a non-varying temperature gradient were utilized: 20 s to 40 s for copper, 40 s to 80 s for glass, and 120 s to 160 s for PMMA.

The parameter estimation study is based on the least-square method governed by the following equation,

$$J = \sum_{n=t}^{t+\Delta t} [\Delta \tilde{T}_n(\lambda_h, C_{p,h}, \lambda_i, \lambda_k) - \Delta T_n]^2/2 \tag{12}$$

where J is the least-square objective value, $\Delta \tilde{T}_n$ represents the simulated average temperature increase of the sensor and ΔT_n corresponds to the measured average temperature increase, both evaluated at various time points t.

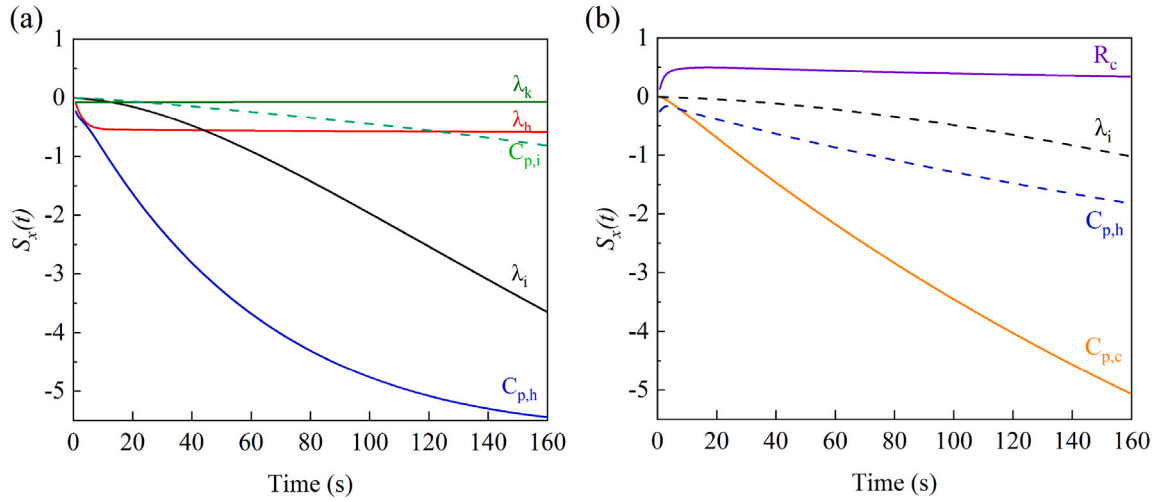

Fig. 5. (a) The sensitivity coefficient $S_x(t)$ for $C_{p,h}$, λ_i, λ_h, $C_{p,i}$ and λ_k obtained from the FEM model of the holder measurement. The sensitivity to the parameters estimated in step 3 are represented by solid lines. (b) $S_x(t)$ for $C_{p,c}$, $C_{p,h}$, R_c, and λ_i obtained from the FEM model of copper measurement. The sensitivity to the parameters estimated in step 4 are represented by solid lines.

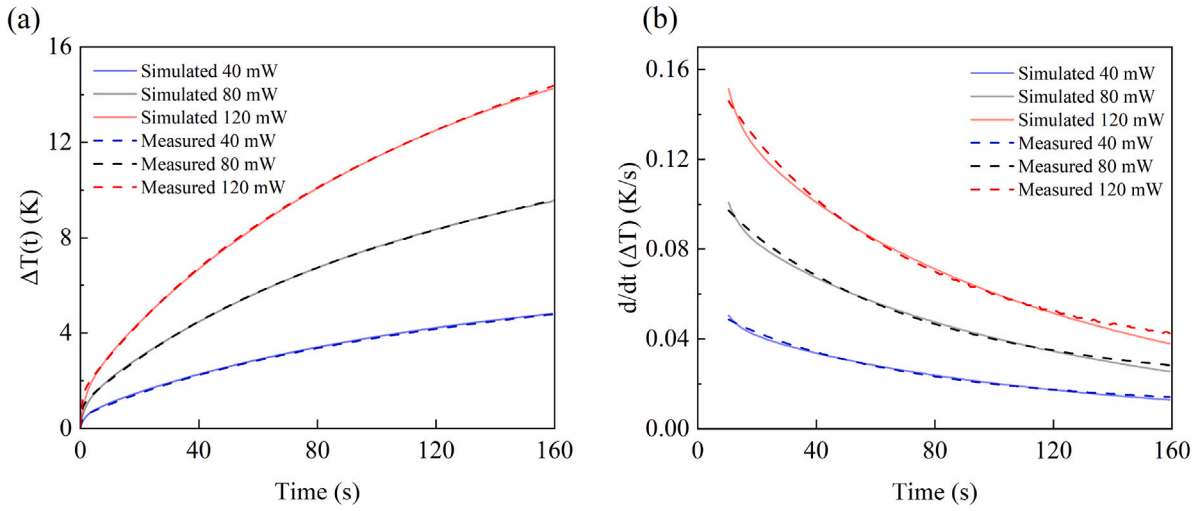

Fig. 6. (a) Comparison of the average $\Delta T(t)$ of the sensor between the measurements (dashed lines) and the well-tuned model (solid lines) for a heating power of 40 mW (blue), 80 mW (black), and 120 mW (red). (b) Comparison of the first derivative of $\Delta T(t)$ between the measurement and the well-tuned model.

Table 3
Average effective values from three trials of parameter estimation, each based on different sets of hold measurement data.

Parameter	Estimated value
λ_h (W/(m K))	34.6 ± 1.1
λ_i (W/(m K))	0.057 ± 0.001
λ_k (W/(m K))	0.017 ± 0.002
$C_{p,h}$ (J/(kg K))	153.5 ± 4.3

In the parameter estimation, a derivative-free optimization method, specifically the bound optimization by quadratic approximation (BOBYQA), has been employed. The core principle of the BOBYQA method involves iteratively approximating the objective function with a suitable quadratic model [52].

To validate the model resulting from this step, we initially compared the measured and simulated $\Delta T(t)$ for different power values (Fig. 6a). Note that only the measured data with a heating power of 80 mW was utilized in step 3. The maximum difference observed between the simulated and measured data was 1%, indicating that the model from step 3 accurately describes and predicts the thermal response. Furthermore, the derivatives of $\Delta T(t)$ from both the measurement and the simulation were compared (Fig. 6b), showing a good correlation between the two.

4. Results and discussion

4.1. Determination of $C_{p,s}$

The $\Delta T(t)$ obtained from the holder measurement was used to extract the four effective parameters: λ_h, $C_{p,h}$, λ_i, and λ_k (Table 3). However, the actual measurement setup is more intricate than this simulation model which is based on several assumptions (Section 3.1). For example, the actual sensing element (nickel spiral) is represented by an ideal boundary heat source. In addition, the sensor comprises two polyimide layers on opposite sides of the nickel wire with an adhesive layer in between. As a result, the estimated parameters are termed "effective values", whose sole purpose is to serve as calibration/fitting parameters for the next step of the simulation.

The parameters derived during step 3 were subsequently used in step 4 to determinate the specific heat capacity of the sample ($C_{p,s}$). The average $C_{p,s}$ of each sample in Table 4 were obtained from nine trials.

Table 4
The comparison between the reference value and the C_p of samples determined by the parameter estimation (step 4). The estimated values are based on nine trials for three samples (three trials for each sample).

C_p (J/(kg K))	Trial	Copper	Glass	PMMA
Sample A	1	381.8	836.1	1393.2
	2	385.8	837.4	1426.6
	3	381.4	836.0	1382.4
Sample B	4	377.5	781.3	1477.2
	5	379.7	777.3	1473.3
	6	380.8	782.7	1490.9
Sample C	7	379.2	801.8	1401.9
	8	383.2	806.1	1401.8
	9	379.4	801.7	1402.5
Average		381.0 ± 19.1	806.7 ± 40.3	1427.8 ± 71.4
Reference		384.2 ± 19.2[a]	843.3 ± 34.0[b]	1436.7 ± 28.7[b]

[a] Measured by DPS.
[b] Measured by DSC.

The average values are close to corresponding reference values, with an average difference of less than 4.4%. This demonstrates the ability of the model to accurately determine the $C_{p,s}$ based on experimental data.

However, it was anticipated that the results of $C_{p,s}$ were influenced by the uncertainty of input parameters, including the specific heat capacity of the insulation material ($C_{p,i}$), the thermal conductivity of the sample (λ_s), and the selection of the time window. The influence of these factors on the final result of $C_{p,s}$ can be investigated by varying these factors, respectively [33,53]. The results in Fig. S3 show that the estimated $C_{p,s}$ is weakly sensitive to the changes in $C_{p,i}$ and λ_s, and time window. Furthermore, considering that the uncertainties resulting from these factors are independent and small, Eq. (13) was employed to estimate the total uncertainty (U) in the parameter estimation process [50,53,54],

$$U = \sqrt{{U_{\Delta tw}}^2 + {U_{\Delta C_{p,i}}}^2 + {U_{\Delta \lambda_s}}^2} \tag{13}$$

where $U_{\Delta tw}$, $U_{\Delta C_{p,i}}$, and $U_{\Delta \lambda_s}$ are the fractional changes in the results of $C_{p,s}$ due to changes in the time window, $C_{p,i}$, and λ_s, respectively. The final uncertainty in parameter estimation was calculated to be 0.7%, 1.1% and 6.7% for copper, glass, and PMMA, given a 30% uncertainty in the three factors. When a reliable value of $C_{p,i}$ (uncertainty less than 10%) is used as an input parameter, the final uncertainty are 0.3%, 0.4%, and 4.3%, even with a 30% uncertainty in the other two factors.

Using the same method, the specific heat capacity of two other polymers at room temperature (293 K), namely high density polyethylene (HDPE) and poly(3-hexylthiophene) (P3HT), were determined to be 1942 ± 97 J/(kg K) and 1608 ± 80 J/(kg K), respectively. HDPE and P3HT were sourced from Sigma-Aldrich and Ossila, respectively. More detailed information including Mw and PDI are provided in Table S1.

4.2. Comparison of $\Delta T(t)$ between sample and the sensor

The calculation of $C_{p,s}$ in TPSS relies on a fundamental assumption: namely that the sensor can precisely capture the rate of average temperature change over time, $\frac{d}{dt}(\Delta T(t))$, for the entire sample. However, in real-world measurements, this assumption may not hold due to factors such as the presence of a sample holder and imperfect thermal insulation materials. In such cases, comparing the differences in $\Delta T(t)$ and $\frac{d}{dt}(\Delta T(t))$ between the sensor and the sample can provide valuable insights into potential errors.

For instance, in the case of copper, its average $\Delta T(t)$ shows a constant offset of around 2 K compared to that of the sensor after a few seconds (as shown in Fig. 7a). The 2 K difference in $\Delta T(t)$ emerges primarily from the thermal resistance between the sensor and the sample, alongside the internal thermal resistance of the sample itself.

In addition, $\frac{d}{dt}(\Delta T(t))$ of the sensor and the copper is compared (Fig. 7c). The difference between these two rates reduces to approximately 2% after a brief duration. This brief duration is estimated to be around 10 s. This duration can not only be attributed to the sensor (sample holder) inertia and thermal contact resistance, but also to the time needed to achieve a non-varying temperature gradient inside the sample. Note that in the TPSS measurement, this brief duration differs from that in the TPS measurement, which accounts for sensor thermal inertia and thermal contact resistance [42–44], but does not require consideration of the non-varying temperature gradient of the sample.

By contrast, the difference in $\Delta T(t)$ between PMMA and the sensor requires more time to reach its peak of around 4 K, and subsequently exhibits a noticeable decline over time (Fig. 7b). These characteristics are attributed to the low thermal diffusivity of PMMA. Likewise, we calculated the difference in $\frac{d}{dt}(\Delta T(t))$ between the PMMA sample and the sensor (Fig. 7d). Notably, this difference increases significantly during the first 100 s and then remains at around 11%. The larger difference in $\frac{d}{dt}(\Delta T(t))$ implies that, in the case of PMMA, heat is more difficult to conduct away from the sensor. This is due to both the thermal contact resistance and the low thermal conductivity of the sample.

4.3. Heat loss in the measurements

The thermal response curve $\Delta T(t)$ is influenced by multiple factors, including the heat capacity of both the sample and the sample holder, heat conduction between the sensor and the sample (thermal contact resistance and the thermal conductivity of the sample), and heat loss to the insulation material. Heat conduction between the sensor and the sample predominantly affects the initial stages of the measurement (for $t < 2 \cdot l_s^2/\alpha$), whereas heat loss becomes more significant over longer timescales.

In this section, the assumption regarding the heat loss equation is examined, namely $f_h(t) = f_s(t)$ (Section 2.1). This assumption holds when $\Delta T(t)$ in both measurements exhibits approximately linear behavior and they are aligned with each other [15]. However, in our measurements, we observe that $\Delta T(t)$ slightly deviates from linearity (Fig. 2b). This deviation arises from the heat loss to the insulation material, and it introduces a potential error in the determination of $C_{p,s}$ from Eq. (7). To gain deeper insight and to quantify the extent of heat loss, we conducted a comprehensive analysis of the heat balance utilizing the well-tuned model.

In the case of the holder measurement (Fig. 8a), the rate of heat accumulation in the sample holder decreases over time. Conversely, the rate of heat accumulation in the insulation material, or in other words, heat loss ($Q(t)$), steadily increases over time and eventually surpasses that of the sample holder at around the 60 s. Ultimately, it becomes three times greater than the heat accumulation in the sample holder, accounting for a substantial 74% of the overall heating power. A large heat loss is undesirable, as it implies that the actual experiment may deviate from ideal conditions.

In the case of the copper measurement (Fig. 8b), a similar trend of $\Delta T(t)$ can be observed for the sample holder and the insulation material. Additionally, a substantial fraction of the heat is directed to the copper sample, resulting in a smaller portion of heat entering the insulation material when compared to the holder measurement. This is the reason why the change in $\Delta T(t)$ during the sample measurement appears to follow a more linear trend compared to that during the holder measurement.

Knowing $Q(t)$ (Fig. 8a–b), we can calculate the unique heat loss function described in Section 2.1 as follows: $f(t) = Q(t)/\frac{d}{dt}(\Delta T(t))$. In the case of the copper sample, the difference between $f_h(t)$ and $f_s(t)$ remains small within the time window of 20 s to 40 s, varying within a range of ±8% (Fig. 8c). However, the difference gradually increases

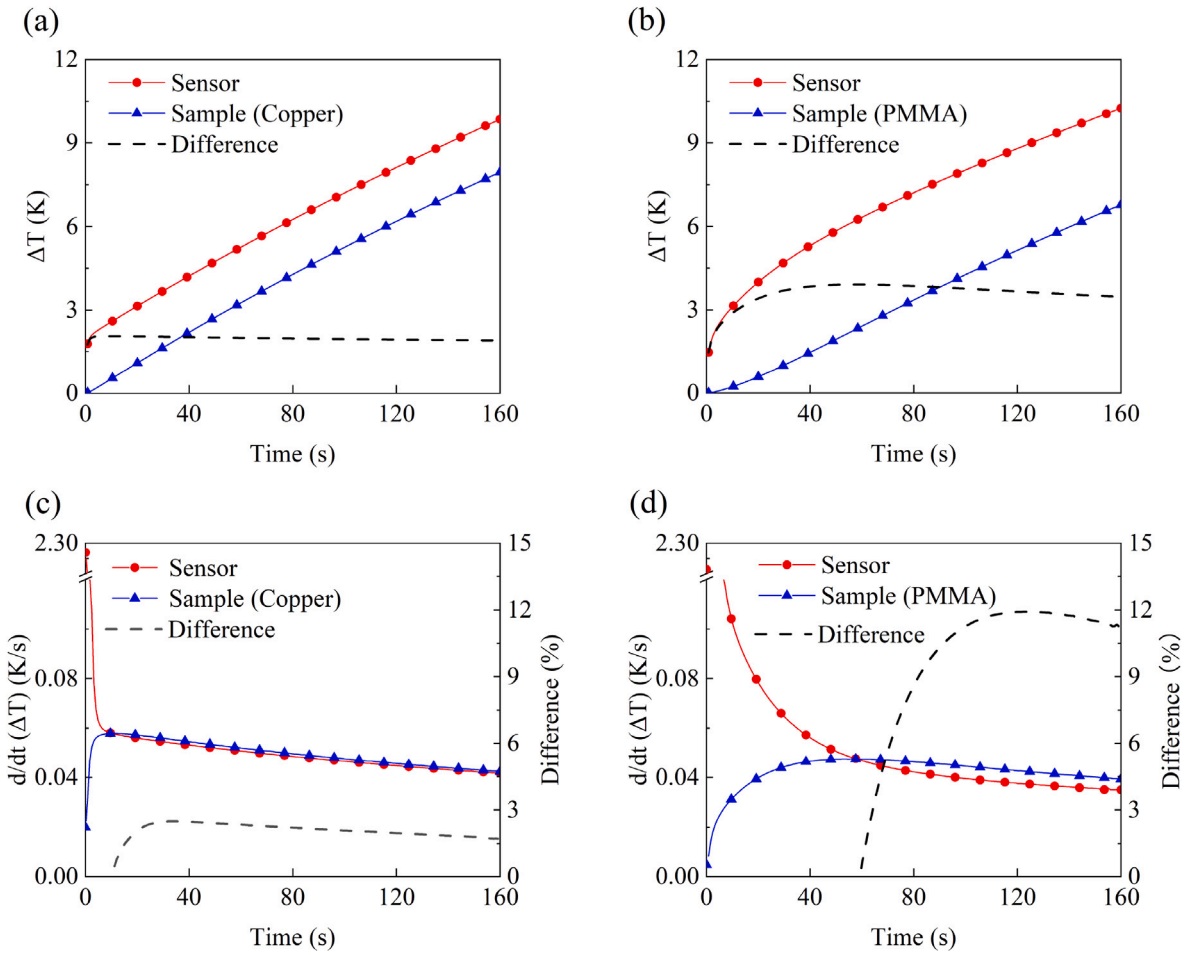

Fig. 7. Average $\Delta T(t)$ of the sensor and the sample for (a) copper and (b) PMMA. The corresponding $\frac{d}{dt}(\Delta T(t))$ for (c) copper and (d) PMMA. The dashed line in each plot represents the difference between the sensor and the sample.

over time and reaches 48% at the end of the measurement, in line with the observed trend of increasing underestimation of $C_{p,s}$ with time (Fig. 2b). For the PMMA sample, $f_h(t) \neq f_s(t)$ throughout the measurement. Initially, $f_h(t)$ is smaller than $f_s(t)$, but surpasses $f_s(t)$ after 100 s and ultimately becomes approximately 20% larger by the end of the measurement.

Furthermore, we estimated the percentage of error in the heat loss calculation relative to the heating power, referred to as $\varepsilon_Q(t)$ (Fig. 8d), using the formula below:

$$\varepsilon_Q(t) = \frac{f_h(t)\frac{d}{dt}(T_s(t)) - Q_s(t)}{P_s} \tag{14}$$

where $Q_s(t)$ represents the rate of heat loss in the sample measurement. For copper, $\varepsilon_Q(t)$ changes from −1% to 16% between 20 s and 160 s. Interestingly, $\varepsilon_Q(t)$ remains within ±1% during the time window of 20 s to 40 s (Fig. 8d, red region). This small value of $\varepsilon_Q(t)$ and the ability of the sensor to accurately capture the $\Delta T(t)$ of copper (Fig. 7a, c) are the reasons why $C_{p,c}$ calculated from this particular time window agrees with the reference value (Fig. 2c). For PMMA, $\varepsilon_Q(t)$ ranges from 3% to 10% within the time window of 120 s to 160 s. A higher $\varepsilon_Q(t)$ implies that the heat loss here is overestimated, which contributes to the underestimation of the specific heat capacity of PMMA ($C_{p,p}$).

In this section, we have quantified $Q(t)$ in both holder and sample measurements, relying on the results from the well-tuned model. It is evident that $Q(t)$ gradually increases over time, eventually accounting for a non-negligible portion of the total heat power. Subsequently, we have demonstrated that the difference between the heat loss equations $f_h(t)$ and $f_s(t)$ is indeed evident, especially in the later part of the measurements. This difference is believed to be the primary source of error in our experimental determination of $C_{p,s}$ for materials with a low thermal conductivity.

5. Conclusions

The objective of this study was to enhance the TPSS method to measure the specific heat capacity of materials with a low thermal conductivity. While the existing method is effective for determining the specific heat capacity of samples with moderate to high thermal conductivity ($\lambda > 1$ W/(m K)), the improved approach extends its applicability to materials with thermal conductivity as low as 0.19 W/(m K).

First, we conducted a series of TPSS experiments of select samples (copper, glass, and PMMA) with varying thermal conductivity to evaluate the measurement method. This analysis revealed both the capabilities and limitations of the TPSS method, particularly its tendency to underestimate the specific heat of samples with a low thermal conductivity. Following this, a well-tuned simulation model was developed and validated using the experiment data, with key material properties determined through a parameter estimation analysis. The simulation model was subsequently utilized to estimate the specific heat capacity of the samples. The estimated specific heat values showed good agreement with reference data, exhibiting a deviation of 4.4% and a small uncertainty. This alignment was achieved by analyzing data from a specific time range, which was determined based on the thickness and thermal diffusivity of each sample. For unknown samples, selecting an appropriate time range would be essential to ensure optimal results.

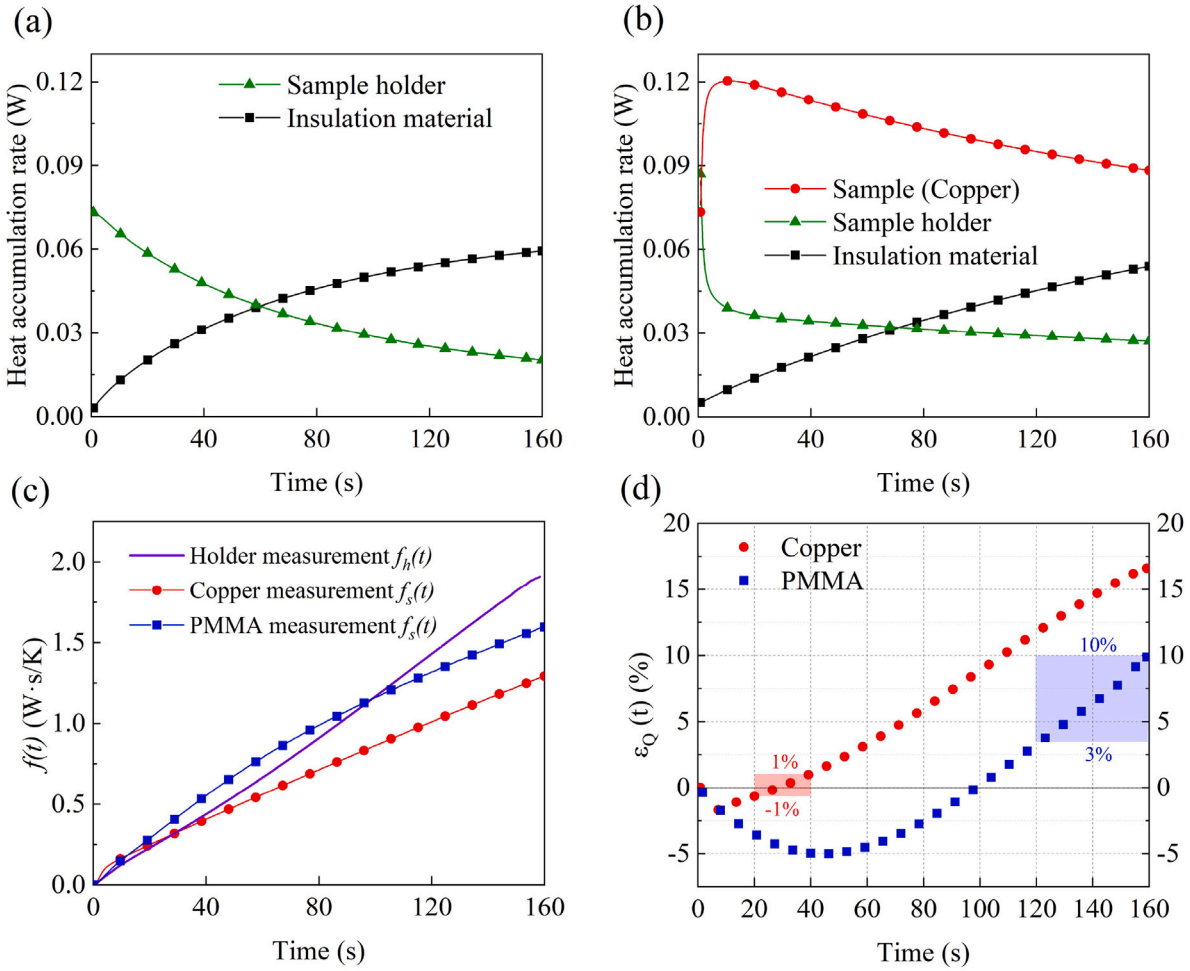

Fig. 8. The rate of heat accumulated in different components during (a) the holder measurement and (b) the sample measurement. (c) Comparison of the unique heat loss function that describes the holder measurement $f_h(t)$ and sample measurement $f_s(t)$. (d) The percentage of error in the heat loss calculation relative to the heating power, defined as $\varepsilon_Q(t)$.

Furthermore, the study illustrates that heat loss during the holder measurement and during the sample measurement could vary significantly, especially during longer measurement times, which is not anticipated in the conventional theory. This variation became evident through a heat balance analysis for each component (sample, sample holder, and thermal insulation material). The analysis led to the conclusion that inaccuracies in heat loss calculations are the primary reason for the underestimation of the specific heat capacity.

In summary, this work enhances the capabilities of the TPSS method by incorporating a well-tuned simulation model, offering a reliable alternative for determining the specific heat capacity of materials with low thermal conductivity.

CRediT authorship contribution statement

Zijin Zeng: Writing – review & editing, Writing – original draft, Visualization, Methodology, Investigation, Formal analysis, Data curation. **Christian Müller:** Writing – review & editing, Supervision, Resources, Project administration, Funding acquisition, Conceptualization. **Besira Mihiretie:** Writing – review & editing, Supervision, Resources, Project administration, Funding acquisition, Conceptualization.

Declaration of competing interest

The authors declare the following financial interests/personal relationships which may be considered as potential competing interests: Zijin Zeng and Besira Mihiretie are affiliates of Hot Disk AB and have a financial interest in the commercial success of the Hot Disk instrument. However, all scientific data and analyses presented in this paper are intended to meet standard scientific criteria for rigor and reproducibility. If there are other authors, they declare that they have no known competing financial interests or personal relationships that could have appeared to influence the work reported in this paper.

Acknowledgments

This project has received funding from the European Union's Horizon 2020 research and innovation program under the Marie Skłodowska-Curie grant agreement No 955837. The authors also wish to thank Dr. Silas Gustafsson for insightful discussion, and Dr. Henrik Otterberg for his thorough language review.

Appendix A. Supplementary data

Supplementary material related to this article can be found online at https://doi.org/10.1016/j.tca.2024.179883.

Data availability

Data will be made available on request.

References

[1] H. Carslaw, J. Jaeger, Heat Transfer in Solids, Second ed., Oxford University Press, Oxford, 1959.

[2] D.C. Deisenroth, M. Ohadi, Thermal management of high-power density electric motors for electrification of aviation and beyond, Energies 12 (2019) 3594, http://dx.doi.org/10.3390/en12193594.

[3] Y. Lv, G. Zhang, Q. Wang, W. Chu, Thermal management technologies used for high heat flux automobiles and aircraft: A review, Energies 15 (2022) 8316, URL https://www.mdpi.com/1996-1073/15/21/8316.

[4] G. Xia, L. Cao, G. Bi, A review on battery thermal management in electric vehicle application, J. Power Sources 367 (2017) 90–105, http://dx.doi.org/10.1016/j.jpowsour.2017.09.046.

[5] A. Loges, S. Herberger, P. Seegert, T. Wetzel, A study on specific heat capacities of Li-ion cell components and their influence on thermal management, J. Power Sources 336 (2016) 341–350, http://dx.doi.org/10.1016/j.jpowsour.2016.10.049.

[6] H. Zhang, J. Baeyens, G. Cáceres, J. Degreve, Y. Lv, Thermal energy storage: Recent developments and practical aspects, Prog. Energy Combust. Sci. 53 (2016) 1–40, http://dx.doi.org/10.1016/j.pecs.2015.10.003.

[7] S. Hasnain, Review on sustainable thermal energy storage technologies, Part I: heat storage materials and techniques, Energy Convers. Manage. 39 (1998) 1127–1138, http://dx.doi.org/10.1016/S0196-8904(98)00025-9.

[8] J. Lizana, R. Chacartegui, A. Barrios-Padura, J.M. Valverde, Advances in thermal energy storage materials and their applications towards zero energy buildings: A critical review, Appl. Energy 203 (2017) 219–239, http://dx.doi.org/10.1016/j.apenergy.2017.06.008.

[9] P. Shafigh, I. Asadi, N.B. Mahyuddin, Concrete as a thermal mass material for building applications-A review, J. Build. Eng. 19 (2018) 14–25, http://dx.doi.org/10.1016/j.jobe.2018.04.021.

[10] A.M. Khudhair, M. Farid, A review on energy conservation in building applications with thermal storage by latent heat using phase change materials, Energy Convers. Manag. (2021) 162–175, http://dx.doi.org/10.1016/S0196-8904(03)00131-6.

[11] Plastics — Differential scanning calorimetry (DSC) — Part 4: Determination of specific heat capacity, (ISO 11357-4:2021) 2021, URL https://www.iso.org/obp/ui/#iso:std:iso:11357:-4:ed-3:v1:en.

[12] Fine ceramics (advanced ceramics, advanced technical ceramics) — Thermophysical properties of ceramic composites — Determination of specific heat capacity, (ISO 19628:2017) 2017, URL https://www.iso.org/standard/62999.html.

[13] P.K. Gallagher, M.E. Brown, Handbook of Thermal Analysis and Calorimetry, first ed., Elsevier, Amsterdam, 2003.

[14] E.V. Boldyreva, V. Drebushchak, I. Paukov, Y.A. Kovalevskaya, T.N. Drebushchak, DSC and adiabatic calorimetry study of the polymorphs of paracetamol, J. Therm. Anal. Calorim. 77 (2004) 607–623, http://dx.doi.org/10.1023/B:JTAN.0000038998.47606.27.

[15] M. Gustavsson, N. Saxena, E. Karawacki, S. Gustafsson, Specific heat measurements with the hot disk thermal constants analyser, in: Thermal Conductivity 23, CRC Press, 1995, pp. 56–65.

[16] S.A. Al-Ajlan, Measurements of thermal properties of insulation materials by using transient plane source technique, Appl. Therm. Eng. 26 (2006) 2184–2191, http://dx.doi.org/10.1016/j.applthermaleng.2006.04.006.

[17] O. Almanza, M. Rodríguez-Pérez, J. De Saja, Applicability of the transient plane source method to measure the thermal conductivity of low-density polyethylene foams, J. Polym. Sci., Part B: Polym. Phys. 42 (2004) 1226–1234, http://dx.doi.org/10.1002/polb.20005.

[18] T. Log, S. Gustafsson, Transient plane source (TPS) technique for measuring thermal transport properties of building materials, Fire Mater. 19 (1995) 43–49, http://dx.doi.org/10.1002/fam.810190107.

[19] R. Penide-Fernandez, F. Sansoz, Anisotropic thermal conductivity under compression in two-dimensional woven ceramic fibers for flexible thermal protection systems, Int. J. Heat Mass Transfer 145 (2019) 118721, http://dx.doi.org/10.1016/j.ijheatmasstransfer.2019.118721.

[20] H. Zhang, K. Wu, G. Xiao, Y. Du, G. Tang, Experimental study of the anisotropic thermal conductivity of 2D carbon-fiber/epoxy woven composites, Compos. Struct. 267 (2021) 113870, http://dx.doi.org/10.1016/j.compstruct.2021.113870.

[21] P. Ding, J. Zhang, N. Song, S. Tang, Y. Liu, L. Shi, Anisotropic thermal conductive properties of hot-pressed polystyrene/graphene composites in the through-plane and in-plane directions, Compos. Sci. Technol. 109 (2015) 25–31, http://dx.doi.org/10.1016/j.compscitech.2015.01.015.

[22] H. Zheng, K. Jaganandham, Thermal conductivity and interface thermal conductance in composites of titanium with graphene platelets, J. Heat Transfer 136 (2014) 061301, http://dx.doi.org/10.1115/1.4026488.

[23] S. Gustafsson, Transient plane source techniques for thermal conductivity and thermal diffusivity measurements of solid materials, Rev. Sci. Instrum. 62 (1991) 797–804, http://dx.doi.org/10.1063/1.1142087.

[24] Plastics — Determination of thermal conductivity and thermal diffusivity — Part 2: Transient plane heat source (hot disc) method, (ISO 22007-2) 2022, URL https://www.iso.org/standard/81836.html.

[25] D. Hume, A. Sizov, B. Mihiretie, D. Cederkrantz, S.E. Gustafsson, M. Gustavsson, Specific heat measurements of large-size samples with the hot disk thermal constants analyser, in: Thermal Conductivity 33, 2017, p. 10.

[26] N.E. Taylor, D.M. Williamson, Characterising Group Interaction Modelling for Complex Composite Materials, Technical Report, Cavendish Laboratory, University of Cambridge, Cambridge, 2019.

[27] M. Gustavsson, E. Karawacki, S.E. Gustafsson, Thermal conductivity, thermal diffusivity, and specific heat of thin samples from transient measurements with hot disk sensors, Rev. Sci. Instrum. 65 (1994) 3856–3859, http://dx.doi.org/10.1063/1.1145178.

[28] M. Gustavsson, S. Gustafsson, On the use of transient plane source sensors for studying materials with direction dependent properties, in: Thermal Conductivity 26, 2001, p. 367.

[29] S.E. Gustafsson, E. Karawacki, M.A. Chohan, Thermal transport studies of electrically conducting materials using the transient hot-strip technique, J. Phys. D: Appl. Phys. 19 (1986) 727, http://dx.doi.org/10.1088/0022-3727/19/5/007.

[30] Instruction Manual: Hot Disk Thermal Constants Analyser, Hot Disk AB, Sweden, 2022.

[31] B.M. Suleiman, S. Malinarič, Transient techniques for measurements of thermal properties of solids: data evaluation within optimized time intervals, WSEAS Trans. Heat Mass Transf. 1 (2006).

[32] E. Karawacki, B.M. Suleiman, Dynamic plane source technique for simultaneous determination of specific heat, thermal conductivity and thermal diffusivity of metallic samples, Meas. Sci. Technol. 2 (1991) 744, http://dx.doi.org/10.1088/0957-0233/2/8/007.

[33] S. Tarasovs, A. Aniskevich, Identification of the anisotropic thermal conductivity by an inverse solution using the transient plane source method, Measurement 206 (2023) 112252, http://dx.doi.org/10.1016/j.measurement.2022.112252.

[34] A. Elkholy, H. Sadek, R. Kempers, An improved transient plane source technique and methodology for measuring the thermal properties of anisotropic materials, Int. J. Therm. Sci. 135 (2019) 362–374, http://dx.doi.org/10.1016/j.ijthermalsci.2018.09.021.

[35] H. Zhang, Y. Li, W. Tao, Theoretical accuracy of anisotropic thermal conductivity determined by transient plane source method, Int. J. Heat Mass Transfer 108 (2017) 1634–1644, http://dx.doi.org/10.1016/j.ijheatmasstransfer.2017.01.025.

[36] R. Coquard, E. Coment, G. Flasquin, D. Baillis, Analysis of the hot-disk technique applied to low-density insulating materials, Int. J. Therm. Sci. 65 (2013) 242–253, http://dx.doi.org/10.1016/j.ijthermalsci.2012.10.008.

[37] Q. Zheng, S. Kaur, C. Dames, R.S. Prasher, Analysis and improvement of the hot disk transient plane source method for low thermal conductivity materials, Int. J. Heat Mass Transfer 151 (2020) 119331, http://dx.doi.org/10.1016/j.ijheatmasstransfer.2020.119331.

[38] S. Wang, Q. Ai, T. Zou, C. Sun, M. Xie, Analysis of radiation effect on thermal conductivity measurement of semi-transparent materials based on transient plane source method, Appl. Therm. Eng. 177 (2020) 115457, http://dx.doi.org/10.1016/j.applthermaleng.2020.115457.

[39] H. Zhang, Y. Li, W. Tao, Effect of radiative heat transfer on determining thermal conductivity of semi-transparent materials using transient plane source method, Appl. Therm. Eng. 114 (2017) 337–345, http://dx.doi.org/10.1016/j.applthermaleng.2016.11.208.

[40] H. Zhang, M. Li, W. Fang, D. Dan, Z. Li, W. Tao, A numerical study on the theoretical accuracy of film thermal conductivity using transient plane source method, Appl. Therm. Eng. 72 (2014) 62–69, http://dx.doi.org/10.1016/j.applthermaleng.2014.01.058.

[41] A. Berge, B. Adl-Zarrabi, C.-E. Hagentoft, Determination of specific heat capacity by transient plane source, Front. Archit. Res. 2 (2013) 476–482, http://dx.doi.org/10.1016/j.foar.2013.09.004.

[42] J. Yves, A. Zoubir, A quadrupolar complete model of the hot disc, Meas. Sci. Technol. 18 (2007) 1229, http://dx.doi.org/10.1088/0957-0233/18/5/009.

[43] V. Bohac, M.K. Gustavsson, L. Kubicar, S.E. Gustafsson, Parameter estimations for measurements of thermal transport properties with the hot disk thermal constants analyzer, Rev. Sci. Instrum. 71 (2000) 2452–2455, http://dx.doi.org/10.1063/1.1150635.

[44] J.-G. Bauzin, N. Laraqi, New thermal analysis of the hot disc method based on explicit analytical developments, Int. J. Therm. Sci. 195 (2024) 108645, http://dx.doi.org/10.1016/j.ijthermalsci.2023.108645.

[45] V. Mathur, K. Sharma, Thermal response of polystyrene/poly methyl methacrylate (PS/PMMA) polymeric blends, Heat Mass Transf. 52 (2016) 2901–2911, http://dx.doi.org/10.1007/s00231-016-1779-4.

[46] Z. Zeng, W. Dilles, B.M. Mihiretie, Enhancing thermal characterization with TPS method: a study of specific heat capacity and anisotropic heat flow using FEM, in: Proceedings of the 17th International Heat Transfer Conference, 2023, p. 1141.

[47] A.C. Lua, J. Su, Isothermal and non-isothermal pyrolysis kinetics of Kapton® polyimide, Polym. Degrad. Stab. 91 (2006) 144–153, http://dx.doi.org/10.1016/j.polymdegradstab.2005.04.021.

[48] J.V. Beck, K.J. Arnold, Parameter Estimation in Engineering and Science, first ed., Wiley, 1977.

[49] K.J. Dowding, B.F. Blackwell, R.J. Cochran, Application of sensitivity coefficients for heat conduction problems, Numer. Heat Transf. B: Fundam. 36 (1999) 33–55, http://dx.doi.org/10.1080/104077999275767.

[50] N.P. Ramos, L.F. dos Santos Carollo, et al., Contact resistance analysis applied to simultaneous estimation of thermal properties of metals, Meas. Sci. Technol. 31 (2020) 105601, DOI: 10.0.4.64/1361-6501/ab8e6a.
[51] G. D'Alessandro, F. de Monte, On the optimum experiment and heating times when estimating thermal properties through the plane source method, Heat Transf. Eng. 43 (2021) 257–269, http://dx.doi.org/10.1080/01457632.2021.1874655.
[52] M.J. Powell, et al., The BOBYQA Algorithm for Bound Constrained Optimization Without Derivatives, Cambridge NA Report NA2009/06, vol. 26, University of Cambridge, Cambridge, 2009, pp. 26–46.
[53] H. Zhang, C. Shang, G. Tang, Measurement and identification of temperature-dependent thermal conductivity for thermal insulation materials under large temperature difference, Int. J. Therm. Sci. 171 (2022) 107261, http://dx.doi.org/10.1016/j.ijthermalsci.2021.107261.
[54] P.R. Bevington, D.K. Robinson, Data Reduction and Error Analysis, third ed., McGraw Hill Higher Education, New York, 2003.

Supplementary Material

Zijin Zeng, Christian Müller, Besira Mihiretie

Extending the Transient Plane Source Scanning Method for Determining the Specific Heat Capacity of Low Thermal Conductivity Materials through a Numerical Study

1 Mesh independence analysis

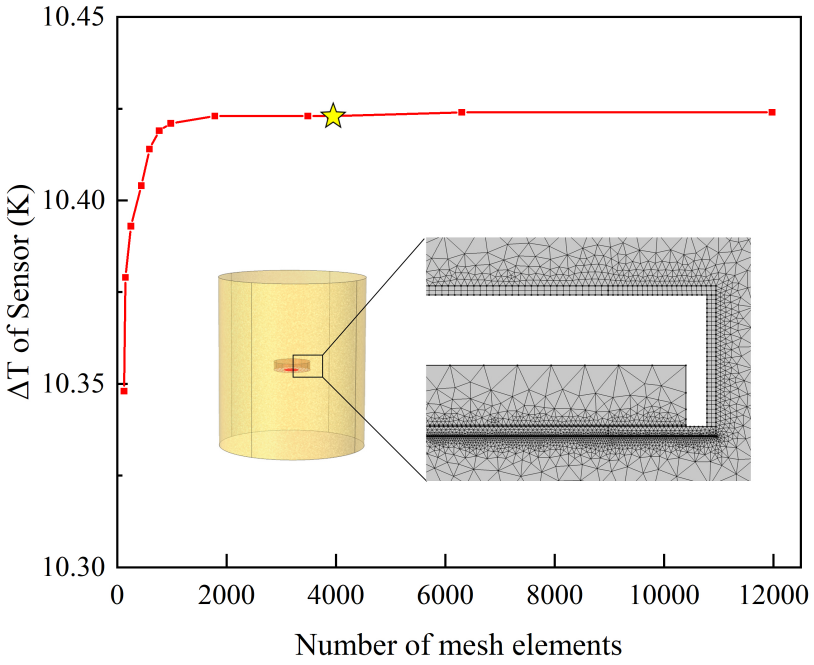

Figure S1: Simulated ΔT at 160 s versus different mesh numbers. The insert shows the mesh utilized in the study, which comprised approximately 4000 elements and achieved an average element quality of 0.82 in terms of skewness.

2 Comparison between $S_x(t)$

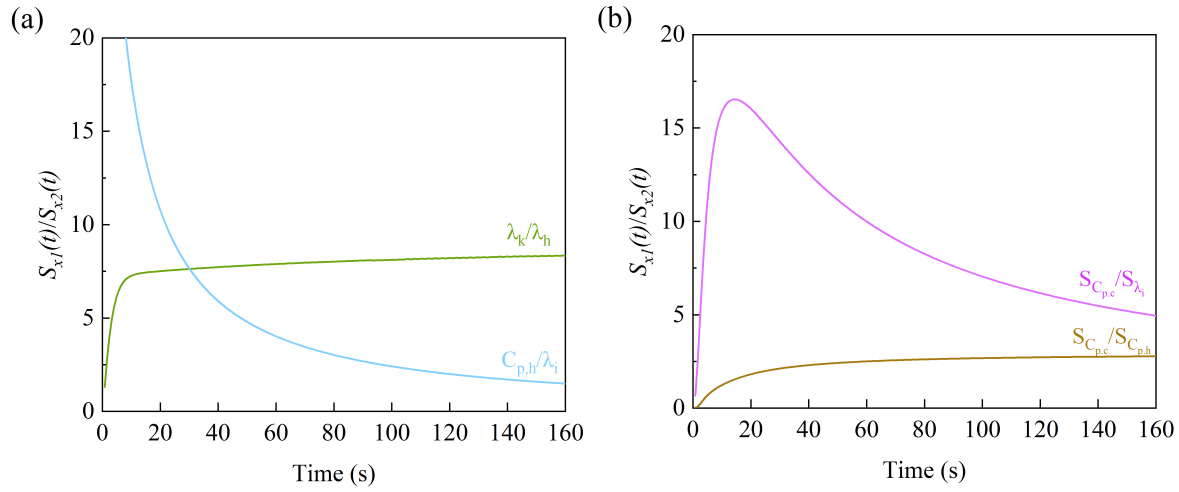

Figure S2: The comparison between $S_x(t)$ to different parameters in (a) holder measurement and (b) sample measurement.

3 Influence of uncertainty of input parameter

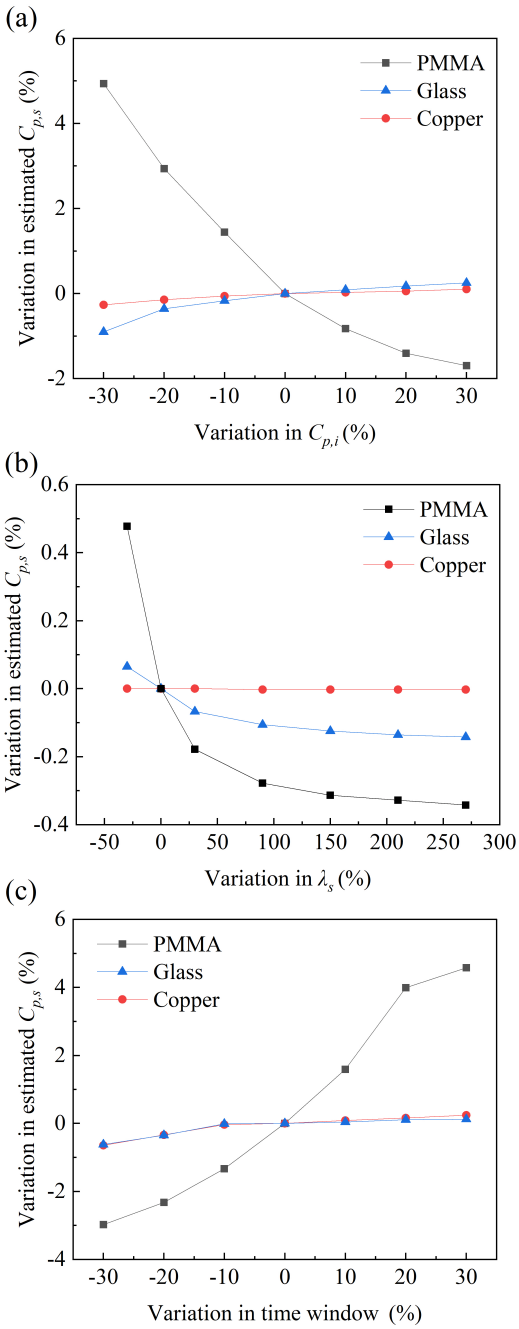

Figure S3: Influence of uncertainty of input parameter on the result of $C_{p,s}$.

4 C_p of additional materials

Table. S1: The specific heat capacity of materials at room temperature determined by the well-tuned model in this work.

Material	C_p (J/(kg · K))	Source	Detail
High density polyethylene	1942 ± 97	Sigma-Aldrich	547999, Mw 95 kg/mol, PDI 5.3
Poly(3-hexylthiophene)	1608 ± 80	Ossila	M1010, Mw 74 kg/mol, PDI 2.1

Paper III

Poly (benzodifurandione) Coated Silk Yarn for Thermoelectric Textiles

Advanced Science

ADVANCED SCIENCE Open Access
www.advancedscience.com

Poly(benzodifurandione) Coated Silk Yarn for Thermoelectric Textiles

Mariavittoria Craighero, Qifan Li, Zijin Zeng, Chunghyeon Choi, Youngseok Kim, Hyungsub Yoon, Tiefeng Liu, Przemyslaw Sowinski, Shuichi Haraguchi, Byungil Hwang, Besira Mihiretie, Simone Fabiano, and Christian Müller**

Thermoelectric textile devices represent an intriguing avenue for powering wearable electronics. The lack of air-stable *n*-type polymers has, until now, prevented the development of *n*-type multifilament yarns, which are needed for textile manufacturing. Here, the thermomechanical properties of the recently reported *n*-type polymer poly(benzodifurandione) (PBFDO) are explored and its suitability as a yarn coating material is assessed. The outstanding robustness of the polymer facilitates the coating of silk yarn that, as a result, displays an effective bulk conductivity of 13 S cm^{-1}, with a projected half-life of 3.2 ± 0.7 years at ambient conditions. Moreover, the *n*-type PBFDO coated silk yarn with a Young's modulus of $E = 0.6$ GPa and a strain at break of $\epsilon_{break} = 14\%$ can be machine washed, with only a threefold decrease in conductivity after seven washing cycles. PBFDO and poly(3,4-ethylenedioxythiophene):poly(styrenesulfonate) (PEDOT:PSS) coated silk yarns are used to fabricate two out-of-plane thermoelectric textile devices: a thermoelectric button and a larger thermopile with 16 legs. Excellent air stability is paired with an open-circuit voltage of 17 mV and a maximum output power of 0.67 µW for a temperature difference of 70 K. Evidently, PBFDO coated multifilament silk yarn is a promising component for the realization of air stable thermoelectric textile devices.

1. Introduction

Miniaturized and integrated electronic devices are poised to become ubiquitous in our daily lives and are increasingly used in several areas, including the Internet of Things (IoT), augmented reality (AR), robotics, health care, and wearable technology. Electronic textiles (e-textiles) constitute a versatile platform that uses textile manufacturing technology to add new functionalities to fabrics and garments, such as health monitoring and diagnostics via sensors,[1–5] communication via keyboards,[6] displays[7,8] or antennae,[9,10] motion via actuators[11] and thermal regulation via heating and cooling elements.[12,13] E-textiles should also incorporate energy harvesting devices that allow the conversion of on-site energy into electricity for powering the integrated electronics. This can include harvesting biomechanical energy through piezoelectric[14,15] or triboelectric generators,[16,17] as well as exploiting energy sources available in our surroundings, such as light through solar cells[18] and heat gradients through thermoelectric devices.[19–22]

M. Craighero, Z. Zeng, Y. Kim, P. Sowinski, S. Haraguchi, C. Müller
Department of Chemistry and Chemical Engineering
Chalmers University of Technology
Göteborg 412 96, Sweden
E-mail: christian.muller@chalmers.se

Q. Li, T. Liu, S. Fabiano
Laboratory of Organic Electronics
Department of Science and Technology
Linköping University
Norrköping 60174, Sweden
E-mail: simone.fabiano@liu.se

Z. Zeng, B. Mihiretie
Hot Disk AB
Sven Hultins gatan 9A, Göteborg 41258, Sweden

C. Choi, H. Yoon
Department of Intelligent Semiconductor Engineering
Chung-Ang University
Seoul 06974, Republic of Korea

B. Hwang
School of Integrative Engineering
Chung-Ang University
Seoul 06974, Republic of Korea

The ORCID identification number(s) for the author(s) of this article can be found under https://doi.org/10.1002/advs.202406770

DOI: 10.1002/advs.202406770

Thermoelectric devices are attractive because they can harvest body heat and do not require light exposure (cf. solar cells) or motion (cf. piezo- and triboelectric generators). Any difference in temperature, i.e., between skin and a colder (or warmer) environment, can be directly converted into an electrical potential through the Seebeck effect. A typical thermoelectric generator (TEG) includes multiple thermocouples, each composed of two legs that are connected thermally in parallel and electrically in series. The legs of a thermocouple should be made of semiconductor materials that feature excellent thermoelectric properties, i.e., a high Seebeck coefficient α, a high electrical conductivity σ and a low thermal conductivity κ, which can be combined into a dimensionless figure of merit ZT:

$$ZT = \frac{\alpha^2 \sigma}{\kappa} T \quad (1)$$

where T is the absolute temperature. Specifically, one type of leg is composed of a *p*-type material characterized by a positive Seebeck coefficient α_p, and the other leg is composed of an *n*-type material characterized by a negative Seebeck coefficient α_n. Each pair contributes to the total open-circuit voltage V_{oc} of a thermoelectric generator according to:

$$V_{oc} = N\left(\alpha_p - \alpha_n\right)\Delta T_{tc} \quad (2)$$

where N is the number of thermocouples and ΔT_{tc} is the temperature difference experienced by the device.[23]

Integrating thermoelectric devices into textiles can be achieved through multiple approaches such as 1) coating or printing a thermoelectric generator architecture onto the surface of existing fabrics,[24–26] 2) stitching or embroidering conducting fibers into fabrics,[19,25,27] and 3) knitting or weaving of the complete fabric using conducting yarns. In all cases, it is crucial to use thermoelectric materials that possess properties, which match the requirements for comfort and safety of fabrics, such as a low weight and flexibility, and the materials must not be toxic. While inorganic semiconductors offer very promising thermoelectric properties, they tend to comprise scarce and harmful elements and require energy-intensive processing methods. Similarly, carbon nanomaterials such as carbon nanotubes and graphene are associated with toxicity concerns.[28]

Organic semiconductors and in particular conjugated polymers can exhibit outstanding mechanical properties and offer advantages such as ease of processing and a low thermal conductivity.[23,29] For instance, many conjugated polymers feature a Young's modulus of $E = 0.01$ to 1 GPa and strain at break $\epsilon_{break} > 10\%$ (note that textile manufacturing typically requires reversible stretching to at least 5%).[30] Furthermore, it is desirable that the polymer does not comprise reactive compounds such as redox dopants or strong acids, which are often used to optimize the electrical conductivity.

Extensive research has been dedicated to *p*-type conjugated polymers, resulting in materials with promising electrical properties. One notable example is poly(3,4-ethylenedioxythiophene):poly(styrenesulfonate) (PEDOT:PSS), which can exhibit a high $\sigma > 1000$ S cm^{-1} and overall a promising $ZT > 0.3$.[31,32] PEDOT:PSS can be used to wet-spin monofilaments.[27,33] Despite displaying outstanding thermoelectric properties as well as a high Young's modulus, single monofilaments face some limitations due to their small cross-sectional area, which results in a breaking force that is too low for many textile manufacturing techniques. Instead, multifilament yarns are typically used in the case of classical textile materials. Nevertheless, the preparation of multifilament PEDOT:PSS yarns has not been successful yet. Another possible approach to obtain electrically conducting multifilament yarns is coating textile yarns with conductive inks. For example, silk or cellulose yarns have been coated with PEDOT:PSS[34,35] and used as building blocks for the design of thermoelectric textiles through embroidery or machine sewing.[19,36] Nonetheless, the utility of these thermoelectric devices was limited because silver-plated yarn had to be used to connect *p*-type legs instead of an *n*-type yarn due to the lack of air-stable *n*-type organic conductors (replacing α_n in Equation (2) with $\alpha_{Ag} = +0.3$ µV K^{-1} limits V_{oc}).[19,36] Alternatively, some studies that explore the design of thermoelectric textiles use *n*-type yarn or monofilaments based on inorganic materials, e.g., Bi_2Te_3 or $Ti_3C_2T_x$ MXene nanoflakes,[37,38] or carbon allotropes, such as nanotubes[21,39] and graphene.[40] While these types of materials yield a promising thermoelectric performance, e.g., a power factor $\alpha^2\sigma$ above 2000 µW m^{-1} K^{-2} in case of yarns based on carbon nanotubes,[41,42] the high mechanical stiffness and limited ductility as well as toxicity concerns may limit their use for wearable devices.

Recently, a first example of a fully polymer-based in-plane thermoelectric textile device was reported that utilized two sets of cellulose yarn coated with *p*- and *n*-type polymer-based materials, i.e., PEDOT:PSS and poly(benzimidazobenzophenanthroline):poly(ethyleneimine) (BBL:PEI).[43] BBL:PEI is a fairly air-stable (up to two days) *n*-type material that is suitable for the manufacture of TEGs,[44] has a σ of up to 8 S cm^{-1}[45] and a high elastic modulus, with neat BBL featuring an $E \approx 8$ GPa.[46] The BBL:PEI yarn showed an adequate mechanical robustness along with some degree of ambient stability for several days, which was achieved through encapsulation and annealing in a glovebox.[43]

To enable the design of truly functional polymer-based thermoelectric textile devices, it will be necessary to develop an *n*-type yarn with greatly improved air stability, mechanical robustness as well as processability. Recently, a new *n*-type polymer, poly(benzodifurandione) (PBFDO) (see **Figure 1a** for chemical structure), with a high electrical conductivity of $\sigma > 1000$ S cm^{-1} has been reported.[47,48] Wet-spun monofilaments of PBFDO feature a similar value of $\sigma \approx$ 1000–1600 S cm^{-1}, which dropped by a factor of two after 14 days, and a high E = 19.5 GPa while maintaining an ϵ_{break} of ≈8%.[49] A remaining question is the mechanical response of PBFDO at different temperatures since the embrittlement at low temperatures would complicate its use as a textile material. Moreover, a multifilament PBFDO yarn or a coated yarn would be needed to facilitate the use of textile manufacturing techniques.

Here, we investigate the mechanical properties of PBFDO to assess its suitability as a yarn coating material. We find that PBFDO can be easily processed into bulk films that remain bendable and feature some degree of stretchability even at temperatures below room temperature. Its processability and outstanding mechanical properties allow us to prepare an *n*-type conducting yarn by coating silk yarn with PBFDO. The resulting *n*-type

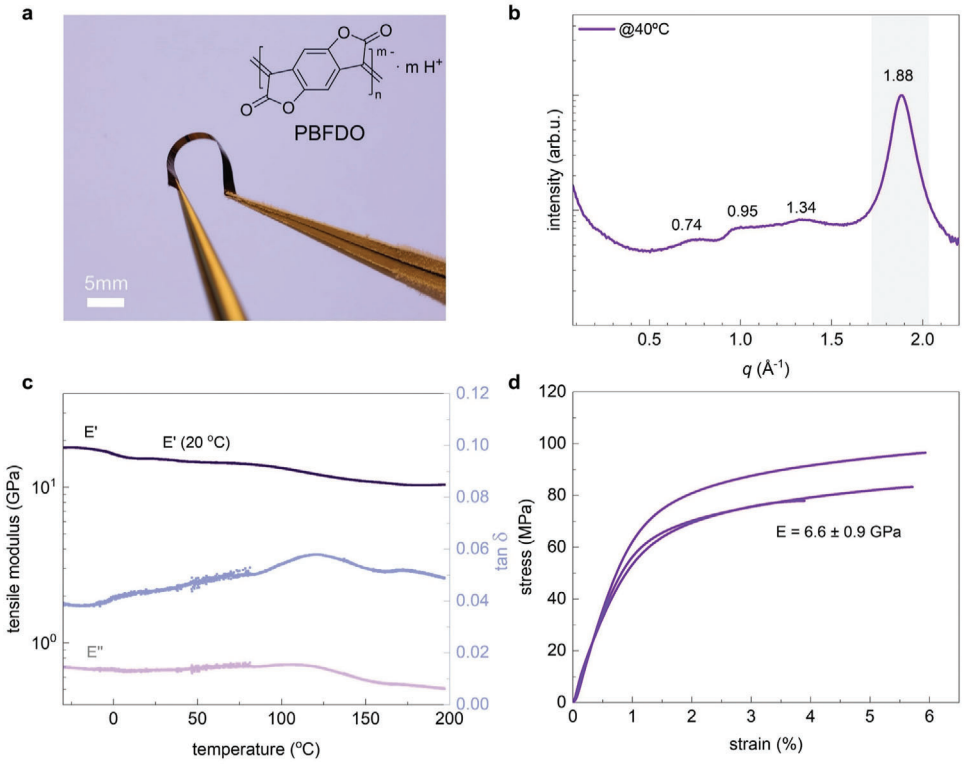

Figure 1. Thermomechanical properties of PBFDO films. a) Chemical structure of reduced PBFDO and photograph of a bent film after being immersed in liquid nitrogen for a few minutes; b) transmission WAXS diffractograms of a free-standing film cast at 40 °C; c) DMTA thermographs of a free-standing film showing the storage modulus E', loss modulus E'' and loss tangent tan δ (see Figure S4, Supporting Information for additional measurements); and d) stress–strain response of three free-standing films measured by tensile deformation at 20 °C (processed and measured in the same way, i.e., drop casting at 40 °C, force rate of 0.01 N min^{-1}).

multifilament yarn features a similar bulk electrical conductivity as PEDOT:PSS coated yarn and, crucially, a very promising stability for at least 14 months at ambient conditions without encapsulation. Moreover, the PBFDO coated yarn can be machine washed at least seven times. Further, the PBFDO coated yarn can be readily used to sew a button and construct a textile thermoelectric device through embroidery, which demonstrates that the yarn exhibits the robustness that is required for textile manufacturing.

2. Results and Discussion

In a first set of experiments, we measured the electrical conductivity of spin-coated films with a thickness of 10 nm. The conductivity increases with temperature starting from a value of σ = 1000 S cm^{-1} at −200 °C to 1600 S cm^{-1} at 130 °C (Figure S1, Supporting Information). The observed electrical conductivity is similar to previously reported values for thin films (2000 S cm^{-1})[47] and wet-spun monofilaments (1000 to 1600 S cm^{-1} depending on the draw ratio),[49] which indicates that the here studied PBFDO batch is of comparable quality.

We then investigated the thermomechanical properties of free-standing films of PBFDO. PBFDO in dimethyl sulfoxide (DMSO) was drop-cast at 40 °C onto glass slides to prepare films with a thickness ranging from 7 to 18 µm, which could be peeled off to obtain free-standing films (see Experimental Section for details). The resulting free-standing PBFDO films were mechanically robust, and could be handled without fracture, even when cooled to below room temperature. Bending without breaking was possible after being immersed in liquid nitrogen for a few minutes (bending radius 5 mm; Figure 1a; Figure S2, Supporting Information). However, thermal annealing, e.g., at 200 °C for 5 min (chosen because the polymer is stable up to 250 °C according to thermogravimetric analysis, TGA; see Figure S3, Supporting Information), resulted in brittle samples that fractured upon bending, which complicated their handling. Evidently, excessive thermal annealing should be avoided to preserve the mechanical robustness of PBFDO. The free-standing PBFDO films featured an electrical conductivity of σ = 627 S cm^{-1} at room temperature, which is lower than the value measured for spin-coated films (Figure S1, Supporting Information). We tentatively assign the difference in electrical conductivity to subtle variations in nanostructure as a result of different processing techniques, i.e., spin coating versus drop casting.

We carried out transmission wide-angle X-ray scattering (WAXS) to investigate the nanostructure of free-standing PBFDO films. The WAXS diffractograms feature a distinct peak at q_{010} = 1.88 Å^{-1} (Figure 1b), which we assign to π–π stacking of the polymer backbone in accordance with a previous report.[47]

Dynamic mechanical thermal analysis (DMTA) in tensile mode at a frequency of 1 Hz was used to investigate the thermomechanical behavior of free-standing PBFDO films. The tensile

Table 1. Elastic modulus and strain at break ϵ_{break} of free-standing PBFDO films at −10 and 20 °C (room temperature) measured by tensile drawing in force-controlled mode using a rate of 0.01 N min^{-1} and DMTA in tensile mode at 1 Hz (mean values and standard deviation of measurements of 2–3 samples; [a]single measurement).

Technique	−10 °C		20 °C	
	Elastic modulus [GPa]	ϵ_{break} [%]	Elastic modulus [GPa]	ϵ_{break} [%]
Tensile drawing	[a]15	[a]2.8	6.6 ± 0.9	5.2 ± 1.1
DMTA	18 ± 0.9	–	16 ± 1	–

storage modulus E' has a value of 18 GPa at −10 °C and slightly decreases with temperature, reaching a value of $E' = 16$ GPa at room temperature and 10 GPa at 200 °C (Figure 1c and **Table 1**; Figure S4, Supporting Information). Evidently, PBFDO maintains its stiffness up to the onset of degradation at T > 200 °C, as inferred from TGA (Figure S3, Supporting Information).

We used tensile deformation of free-standing samples to analyze the stiffness and ductility of PBFDO in more detail. At room temperature, the polymer is stiff but relatively ductile, with a Young's modulus $E = 6.6 \pm 0.9$ GPa and a strain at break $\epsilon_{break} = 5.2 \pm 1.1\%$ when measured in force-controlled mode with a rate of 0.01 N min^{-1} (Figure 1d and Table 1), yielding a toughness of 3.6 ± 1.1 MJ. Cooling resulted in a stiffer but more brittle material, as indicated by tensile deformation at −10 °C, which yielded a high Young's modulus of 15 GPa but low ϵ_{break} of only 2.8% (Table 1; Figure S5, Supporting Information). We explain the somewhat lower Young's modulus values compared with the storage modulus from DMTA with the here employed low tensile deformation rate.

Given that many textile manufacturing processes require materials with at least some degree of mechanical robustness (e.g., bendable and reversibly stretchable to 5%),[30] we decided to use PBFDO in its as-cast state as a coating material. A batch coating process was used to prepare conducting *n*-type yarn, which involved two cycles of immersion of silk yarn in the PBFDO:DMSO ink followed by drying at 40 °C (see Experimental Section for details). Using this method, we produced continuous conductive yarn with a length of up to 1.5 m that comprised ≈10 wt.% of PBFDO (measured by weighing yarn before and after coating).

Scanning electron microscopy (SEM) was used to assess the quality of the PBFDO coating (**Figure 2**). SEM images of the yarn surface and cross section of freeze-fractured yarn sections do not reveal any outer shell layer (Figure 2b–d). Intriguingly, charging artifacts occur within the inner part of each filament, which indicate an insulating silk core surrounded by a conductive outer layer. We argue that PBDFO is present on the surface of individual filaments and may have in part ingressed into each filament. The presence of PBFDO on the silk filaments was confirmed visually by the black color upon coating and by transmission WAXS diffractograms, where a shoulder at $q_{010} = 1.88$ Å^{-1}, i.e., the diffraction peak assigned to the π–π stacking of the conjugated backbone, is observed in case of the coated but not the neat silk yarn (Figure S6, Supporting Information). To understand whether electrostatics govern the interaction between PBFDO and fibroin, the main component of degummed silk, we

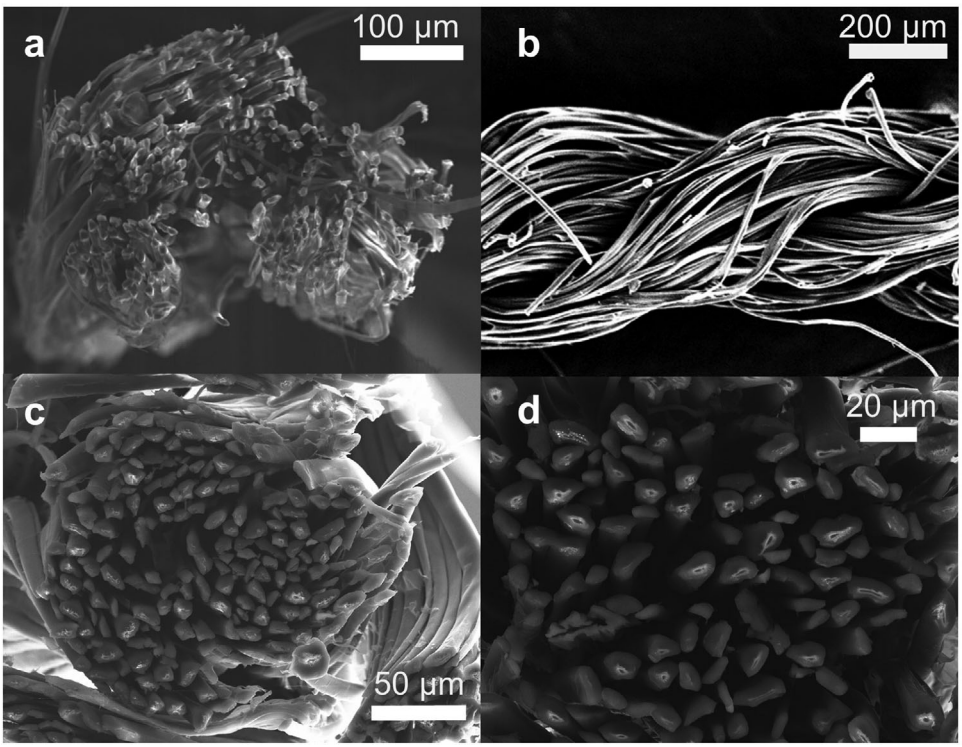

Figure 2. SEM micrographs of a) the cross section of neat and b) a side view of PBFDO coated silk yarn sputtered with gold, and c,d) the cross section of silk yarn coated with PBFDO (no gold sputtering).

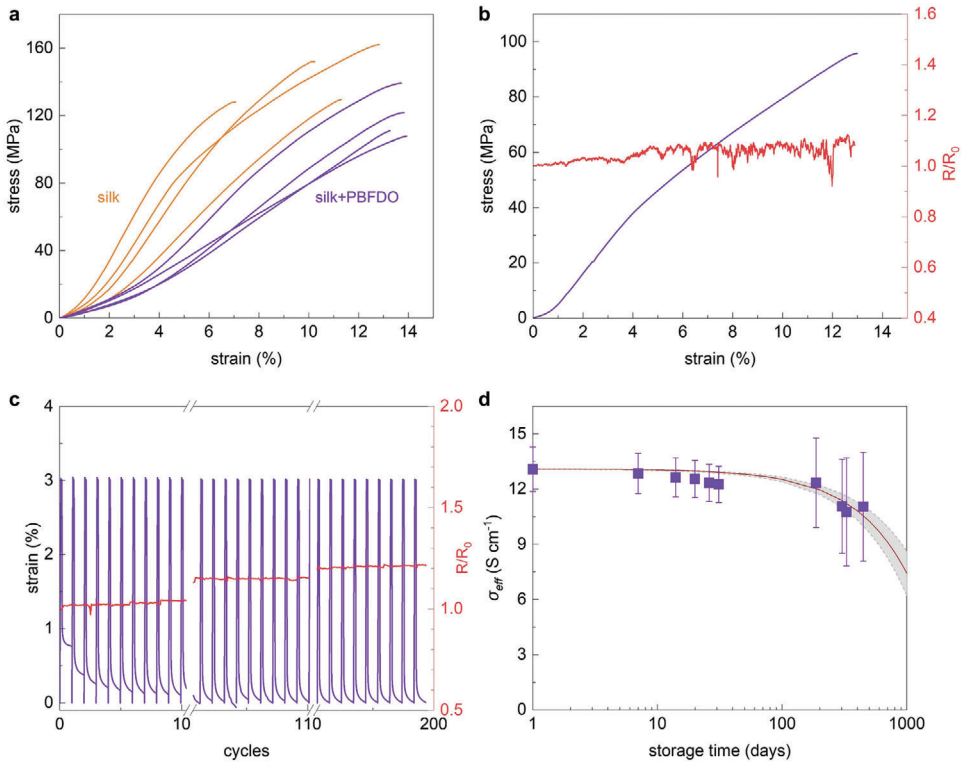

Figure 3. Mechanical and electrical properties of PBFDO coated silk yarn. a) Stress–strain curves recorded during tensile deformation of neat (orange) and PBFDO coated (purple) silk yarn; b) stress–strain curve of the PBFDO coated silk yarn (left) and in situ recorded change in electrical resistance R/R_0 where R_0 is the resistance of the yarn prior to the fatigue test; c) strain during cyclic tensile deformation of the PBFDO coated silk yarn repeatedly stretched to 3% then released for 60 s (purple line) together with the in situ recorded change in electrical resistance (red line); and d) effective electrical conductivity σ_{eff} of PBFDO coated yarn (purple squares) and aging prediction (grey area) as a function of storage time at ambient conditions.

sonicated yarn sections suspended in water with a pH ranging from 2 to 7. Since fibroin has an isoelectric point at pH 4,[34] we would expect that the degree of binding strongly varies as a function of pH if electrostatic interactions dominated, as previously observed for a thiophene based conjugated polyelectrolyte.[50] However, we find that sonication resulted in a significant decrease in electrical conductivity by at least two orders of magnitude, independent of the pH (Figure S7, Supporting Information). Thus, we conclude that physisorption of PBFDO onto silk filaments is not driven by electrostatic interactions.

We proceeded with the mechanical and electrical characterization of the conducting yarn. Tensile drawing of both neat silk yarn and yarn coated with PBFDO was carried out to explore the influence of the coating on the mechanical properties (**Figure 3a**). The recorded stress–strain curves indicate that immersing silk yarn in PBFDO:DMSO ink reduces the Young's modulus from $E = 1.7 \pm 0.5$ GPa, measured for neat silk, to 0.6 ± 0.1 GPa after coating the silk with PBFDO:DMSO ink. Simultaneously, the strain at break increased reaching a value of up to $\epsilon_{break} = 14 \pm 0.3\%$ (**Table 2**). Similar changes are seen when immersing silk yarn in DMSO, indicating that the solvent and not the PBFDO causes the observed changes in mechanical properties (Figure S8 and Table S1, Supporting Information). We monitored the electrical resistance of the *n*-type yarn during stretching to investigate the impact of plastic deformation beyond the yield point. We found that the normalized resistance R/R_0, where R_0 is the resistance prior to tensile deformation, remains largely unaffected until the yarn fractures (Figure 3b; Figure S9, Supporting Information).

To further evaluate how the PBFDO coated yarn responds to repeated mechanical stress, we conducted a series of fatigue tests. The resistance measured in situ during cyclic tensile deformation to 3% strain increased by less than 20% after 200 cycles (Figure 3c). PBFDO coated yarn can also withstand cyclic stretching to 4% or 5% strain without breaking for up to 60 cycles or 30 cycles, respectively, which suggests that the yarn is suitable for textile manufacturing.[30] At the same time the resistance

Table 2. Mechanical and thermoelectric properties of coated silk yarns. Young's modulus *E*, strain at break ϵ_{break}, effective electrical conductivity σ_{eff}, Seebeck coefficient α, and power factor $\alpha^2\sigma_{eff}$; values represent the mean and standard deviation of measurements of 5 samples; [a]values from ref. [51].

Yarn	*E* [GPa]	ϵ_{break} [%]	σ_{eff} [S cm^{-1}]	α [μV K^{-1}]	$\alpha^2\sigma_{eff}$ [μW m^{-1} K^{-2}]
Silk	1.7 ± 0.5	10 ± 2.5	–	–	–
PBFDO coated silk	0.6 ± 0.1	14 ± 0.3	13 ± 1	-18.8 ± 0.8	0.46 ± 0.04
PEDOT:PSS coated silk	2.9 ± 0.6[a]	10 ± 0.3[a]	13 ± 2	17.9 ± 0.1	0.42 ± 0.06

increased by only 10% or 30% (Figure S10, Supporting Information).

We investigated the electrical properties of the *n*-type yarn by determining the effective electrical conductivity σ_{eff}, which is based on the total cross-sectional area of the yarn including the silk, PBFDO as well as voids, and corrected for the contact resistance by using the transmission line method (see Experimental Section for details). We obtained a value of $\sigma_{eff} = 13 \pm 1$ S cm^{-1} for the PBFDO coated silk yarn (Table 2). Considering that PBFDO comprises 10 wt.% of the yarn and taking into account that the coated yarn comprises ≈27.5% voids (obtained by comparing the weight and volume of neat silk yarn with the density of silk $\rho \approx 1.3$ g cm^{-3}), the coating has an effective conductivity $\sigma \approx 250$ S cm^{-1}, which is lower than the value measured for PBFDO films on glass (Figure S1, Supporting Information) or free-standing films. We attribute this difference to an uneven PBFDO coating on the filaments, resulting in an overall reduction of the electrical conductivity. We also measured the Seebeck coefficient α of the *n*-type yarn and obtained a value of $\alpha_n = -18.8 \pm 0.8$ μV K^{-1} (Table 2), which is similar to the value previously reported for PBFDO thin films.[47] The measured electrical conductivity and Seebeck coefficient result in a thermoelectric power factor of $\alpha_n^2 \sigma_{eff} = 0.46 \pm 0.04$ μW m^{-1} K^{-2}, which is comparable to the power factor of PEDOT:PSS coated silk yarn.[19]

In a further set of experiments, we assessed to which extent the thermoelectric properties of PBFDO coated silk yarn can be optimized through partial oxidation. Ke et al. have recently reported that PBFDO can be oxidized by exposing the polymer to strong oxidizing agents such as tris(4-bromophenyl)ammoniumyl hexachloroantimonate (Magic Blue).[52] We submerged PBDFO coated yarn sections in solutions of 0–3 mM Magic Blue dissolved in degassed acetonitrile and subsequently measured the electrical conductivity and Seebeck coefficient (Figure S11, Supporting Information). As anticipated, oxidized yarn sections featured a σ_{eff} that decreased with Magic Blue concentration, while α became more negative (Figure S11, Supporting Information). Overall, the power factor increased by up to one order of magnitude from ≈0.5 to 5 μW m^{-1} K^{-2} for an intermediate Magic Blue concentration of 0.25 mM. However, the thermoelectric properties of partially oxidized PBFDO yarn were not stable at ambient conditions, which we ascribe to gradual reduction of the material. Thus, we opted to use fully reduced PBFDO coated yarn for all further studies since their thermoelectric properties were stable with time.

To assess the long-term stability of PBFDO coated yarn, we repeatedly characterized the electrical resistance during storage at ambient conditions and, in a separate set of experiments, exposed the yarn to machine washing. Notably, the electrical conductivity remains almost constant over a span of 14 months when stored at ambient conditions (Figure 3d), which indicates exceptional stability of the yarn compared to other types of *n*-type polymers. For instance, BBL:PEI coated regenerated cellulose yarn showed a tenfold increase in resistance after only one day at ambient conditions.[43] We extrapolate that the PBFDO coated yarn will lose 50% of its initial conductivity after 3.2 ± 0.7 years (Figure S12, Supporting Information). Strikingly, the PBFDO coated yarn also featured a promising degree of washability. Seven washing cycles at 20 °C resulted in an increase in electrical resistance by a factor of only 3 (**Figure 4**). The decrease in electrical conductivity observed upon sonication of PBFDO coated yarn (cf. Figure S7, Supporting Information) suggests that mechanical wear limits the stability during machine washing. We chose to study the PBFDO coated yarn without a protective coating to obtain a fair assessment of its stability. In the future, it would be possible to add a protective coating to the yarn such as a thermoplastic elastomer to minimize mechanical wear during washing.

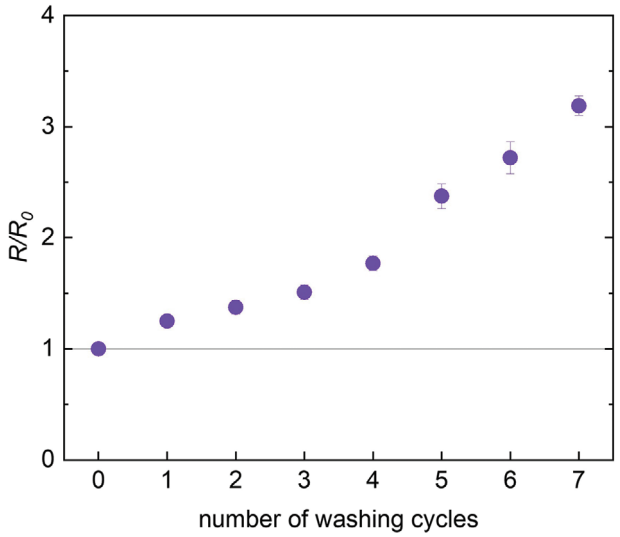

Figure 4. Machine-washing of PBFDO coated silk yarn. Change in electrical resistance R/R_0 as a function of washing cycle at 20 °C.

An out-of-plane textile thermocouple was fabricated by hand-stitching a button with conducting yarn onto three layers of a felted wool fabric (**Figure 5a**; Figure S13, Supporting Information). We used a button to demonstrate the ease of handling and robustness of the *n*-type yarn. Furthermore, the button increases the length of the thermoelectric legs, thereby enhancing the thermal gradient experienced by the thermocouple. The *n*- and *p*-type leg where constructed with PBFDO and PEDOT:PSS coated silk yarn, respectively, with the latter produced with a previously reported roll-to-roll coating method that yielded machine-washable *p*-type conducting yarn.[51] The thermoelectric properties of the *n*- and *p*-type yarns closely match, except for the opposite sign of the Seebeck coefficient (Table 2).

We characterized the performance of the thermoelectric button by placing the device between a hot plate and a heat sink with a temperature T_{hot} and T_{cold}, respectively (Figure 5a, see Experimental Section for details). The temperature of the hot plate was increased to generate stepwise increasing temperature gradients $\Delta T = T_{hot} - T_{cold}$ thus exposing the thermoelectric legs to a temperature gradient ΔT_{tc} (note that $\Delta T_{tc} < \Delta T$ because of thermal contact resistance between the device and the heat source and sink). At each ΔT, the generated voltage V was recorded while a variable load was applied by drawing different currents I with a source-measure unit.

The open-circuit voltage V_{oc}, i.e., the extrapolated voltage at $I = 0$, increased linearly with ΔT (Figure 5c) and we estimate a value of $V_{oc}/\Delta T = 27.5$ μV K^{-1} assuming that $\Delta T_{tc} = \Delta T$. Instead, Equation (2) predicts a higher value of $V_{oc}/\Delta T_{tc} = 36.7$ μV K^{-1}, which we explain with thermal contact resistance and hence

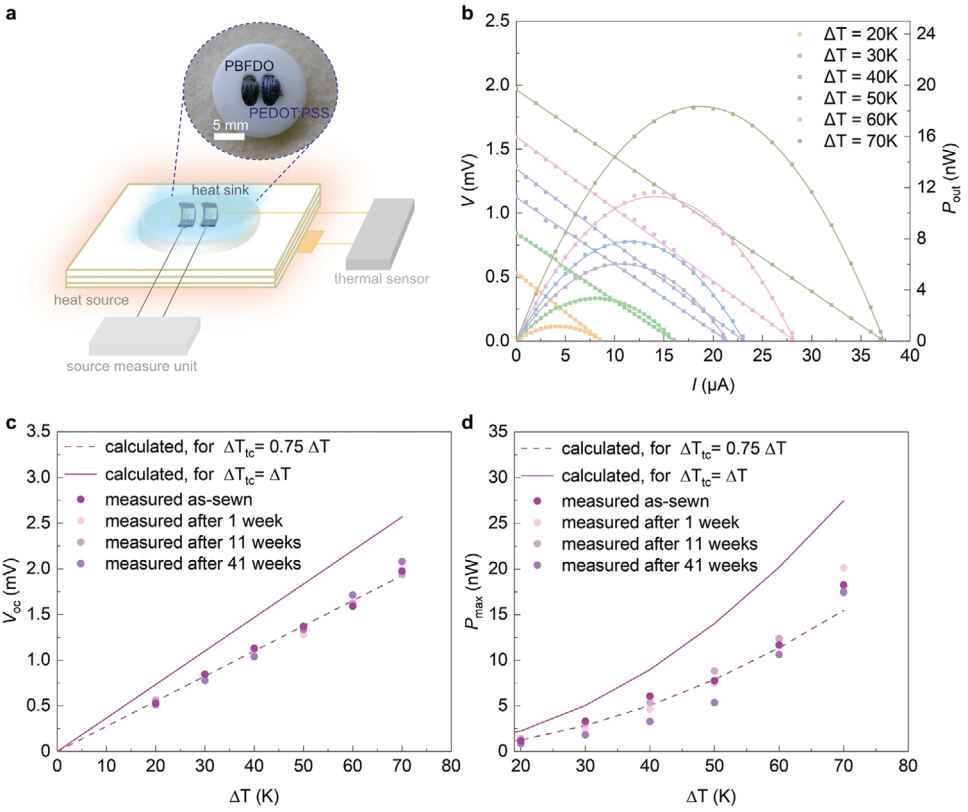

Figure 5. Performance of the thermoelectric button. a) Schematic representation of the thermocouple fabricated by hand-stitching a button onto a wool fabric with the *n*-type leg composed of PBFDO coated yarn and the *p*-type leg of PEDOT:PSS coated yarn; b) voltage V (left) and output power P_{out} (right) of the thermoelectric button as a function of current I for different temperature differences $\Delta T = T_{hot} - T_{cold}$ where T_{hot} and T_{cold} are the temperatures of the hot plate and cooler measured with a pair of thermocouples; c) open-circuit voltage V_{oc} and d) maximum output power P_{max} as a function of ΔT recorded immediately after device fabrication or after storage at ambient conditions for 1, 11 or 41 weeks (circles represent experimental values; solid and dashed lines calculated assuming that $\Delta T_{tc} = \Delta T$ and $\Delta T_{tc} = 0.75 \cdot \Delta T$, respectively).

$\Delta T_{tc} \approx 0.75 \cdot \Delta T$ (cf. solid and dashed lines in Figure 5c). The output power was calculated according to:

$$P_{out} = VI \tag{3}$$

and reached a maximum for the current at which the internal resistance of the device $R_{in} = 50\ \Omega$ and the load R_{load} are equal. The maximum output power P_{max} achieved by the thermocouple increased with ΔT, reaching a highest value of $P_{max} = 20$ nW and a power density of ≈10 nW cm^{-2} at $\Delta T = 70$ K (Figure 5b,d; the projected area of the button was 1.77 cm^{-2}). The measured values are in good agreement with P_{max} predicted according to:

$$P_{max} = \frac{V_{oc}^2}{4R_{in}} \tag{4}$$

which, e.g., yields a value $P_{max} = 22$ nW for $V_{oc} = 2.1$ mV at $\Delta T = 70$ K.

To assess the long-term stability of the thermoelectric button, we repeatedly measured its performance. Both, V_{oc} and P_{max} did not markedly change after at least 41 weeks of storage at ambient conditions, apart from the occasional device characterization during which the device was heated (Figure 5c,d; Figure S14, Supporting Information).

In a further set of experiments, a larger out-of-plane textile thermoelectric generator was fabricated. PBFDO and PEDOT:PSS coated silk yarns were hand-sewn through six layers of felt wool forming 8 n-legs and 8 p-legs, respectively (**Figure 6a**; Figure S15, Supporting Information). We chose to construct *n*- and *p*-type legs with the same number of yarn sections and cross-sectional area because of the similar σ_{eff} of the two types of coated silk yarn (see Table 2), meaning that the performance of the TEG is optimized if the legs have comparable dimensions.[19,44]

We characterized the thermoelectric performance of the generator similar to the thermoelectric button, e.g., by placing the device between a hot plate and a heat sink and by recording the generated voltage V while drawing different currents I with a source-measure unit at each ΔT of interest. Moreover, a numerical simulation model was developed to investigate the impact of the thermoelectric generator design parameters on P_{max}. In our simulation, each thermoelectric leg is depicted as a cubic structure with effective electrical and thermal conductivity (see Supporting Information for further details). We simulated the temperature distribution across the textile thermopile and the resulting V_{oc} at fixed values of ΔT and took into account the thermal contact resistance. P_{max} was subsequently calculated using Equation (4) where the measured internal resistance R_{in} was 119 Ω at room temperature,

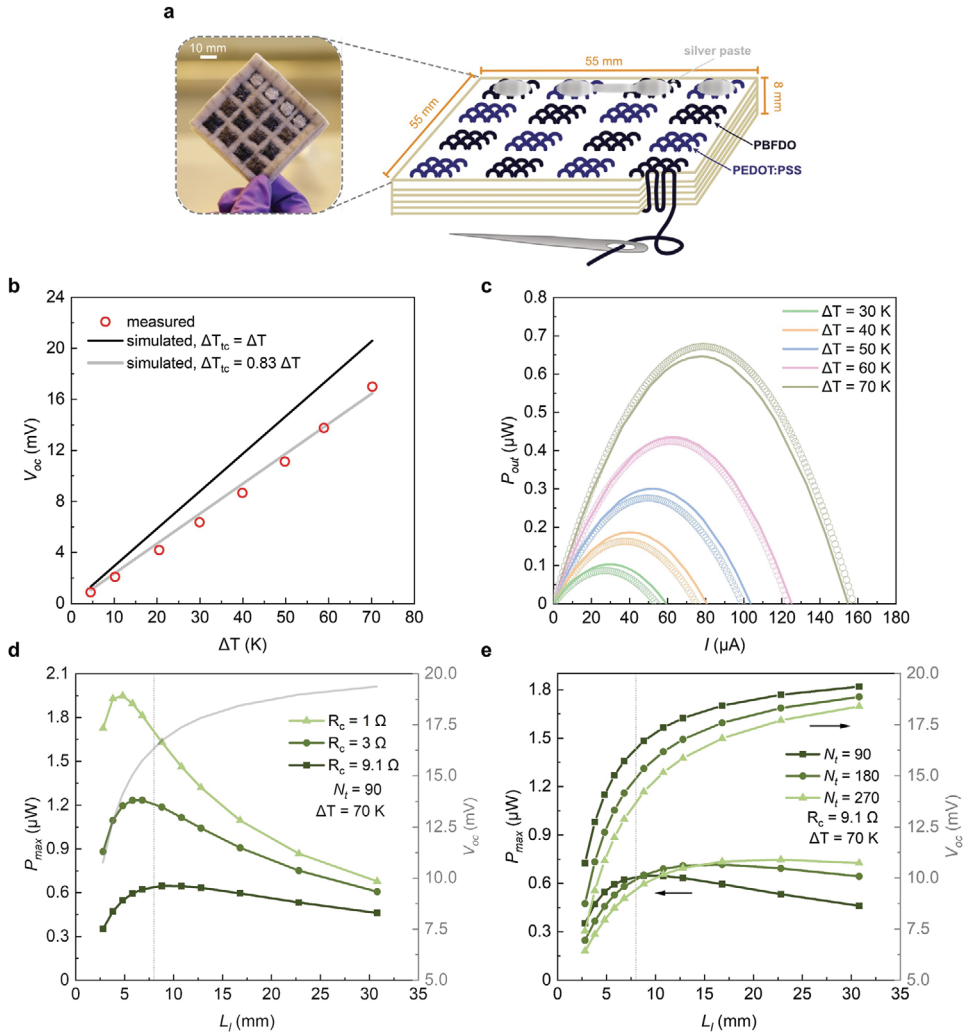

Figure 6. Performance of the thermoelectric generator composed of eight thermocouples. a) Schematic and photograph of the thermoelectric generator. b) Open-circuit voltage V_{oc} as a function of ΔT (circles represent experimental values; black and grey lines calculated assuming that $\Delta T_{tc} = \Delta T$ and $\Delta T_{tc} = 0.83 \cdot \Delta T$, respectively); c) output power P_{out} of the thermopile as a function of current I for different temperature differences ΔT (circles represent experimental values, lines represent the results from the simulation at different ΔT considering a thermal contact resistance of 97 K cm^2 W^{-1}). d) Predicted P_{max} (right) and V_{oc} (left) generated from the thermoelectric generator at $\Delta T = 70$ K and thermal contact resistance of 97 K cm^2 W^{-1} as a function of thermoelectric leg length (L_l) (vertical grey line at $L_l = 8$ mm represents the actual L_l of the device). The electrical contact resistance R_c per thermocouple was 1 Ω (triangles), 3 Ω (circles), 9.1 Ω (squares) (which corresponds to the actual R_c of the device at $\Delta T = 70$ K), and the thread count N_t was set to be 90. e) Predicted P_{max} (right) and V_{oc} (left) generated from the thermoelectric generator at $\Delta T = 70$ K and thermal contact resistance of 97 K cm^2 W^{-1} as a function of L_l (vertical grey line at $L_l = 8$ mm represents the actual L_l of the device). The electrical contact resistance R_c per thermocouple was 9.1 Ω (which corresponds to the actual R_c of the device at $\Delta T = 70$ K), and the thread count N_t was 90 (squares), 180 (circles) and 270 (triangles).

decreasing to 108 Ω at $\Delta T = 70$ K (Figure S16, Supporting Information).

The measured open circuit voltage V_{oc} increased linearly with ΔT (Figure 6b) and we estimate a value of $V_{oc}/\Delta T = 243$ μV K^{-1} assuming that $\Delta T_{tc} = \Delta T$. In agreement with the measured results, the simulated V_{oc} exhibits a linear increase with ΔT. By assessing the ratio between the measured V_{oc} and the simulated V_{oc} under ideal conditions where $\Delta T_{tc} = \Delta T$, we estimate that the thermal contact resistance constitutes 17% of the total thermal resistance of the entire setup, corresponding to a total thermal contact resistance of 97 K cm^2 W^{-1}. The measured P_{max} achieved by the device increased with ΔT, reaching a highest value of $P_{max} = 0.67$ μW at $\Delta T = 70$ K. The value predicted by the simulation agrees with the experimental results (Figure 6c). The thermoelectric module with a total area of 30.25 cm^2 yields a power density of 22 nW cm^{-2} for $\Delta T = 70$ K, which is in good agreement with the power density generated by the button thermocouple considering the different device thickness and area fill factor. The thermoelectric performance of the device is unvaried after 10 days and decreased by 30% after 90 days of storage at ambient conditions (Figure S17, Supporting Information).

Furthermore, the validated model was used to investigate the impact of the length of thermoelectric legs L_l, i.e., the thickness of the device, and the electrical contact resistance R_c of each ther-

mocouple on the performance of the textile device (Figure 6d). A larger L_l results in a higher V_{oc} but also leads to an increase in the internal resistance of the thermoelectric device. The interplay between L_l and R_c determines the optimal L_l for which the highest P_{max} is achieved. For instance, when $R_c = 9.1\ \Omega$, i.e., the actual value calculated for our device, the optimal L_l is 8 mm, resulting in $P_{max} = 0.65\ \mu W$. This aligns with the measured $P_{max} = 0.67\ \mu W$, indicating a good agreement between the numerical model and the experimental data. Additionally, the impact of R_c on the resulting output power is significant. The maximum output power reaches a value of $P_{max} = 1.95\ \mu W$ when $R_c = 1\ \Omega$, exceeding the value achieved for $R_c = 9.1\ \Omega$ by more than three times. This substantial improvement in the highest P_{max} suggests that reducing R_c is an effective means of enhancing the performance of the textile thermopile.

The influence of the thread count N_t for each thermocouple leg was also investigated (Figure 6e). As the thermal conductivity of coated yarns is higher than that of the felted wool (see Experimental Section and ref. [19]), a higher N_t means a higher portion of yarns and a higher effective thermal conductivity of the leg, which decreases the temperature gradient experienced by each leg and hence reduces V_{oc}. On the other hand, a higher portion of yarns greatly decreases the internal electrical resistance of the textile thermopile, leading to a slightly higher P_{max}. If N_t is tripled to 270, a P_{max} of 0.75 μW is predicted for $R_c = 9.1\ \Omega$, which is only 15% larger than the P_{max} for a device with a $N_t = 90$.

In a final set of experiments, we monitored the thermoelectric performance of the textile device upon repeated bending around a coffee mug with a diameter of 10 cm. We measured the internal electrical resistance of the device before and after the mechanical deformation. The internal resistance remained largely unaffected by bending and unbending cycles, with variations of less than 2.5% compared to the initial value after 12 cycles (Figure S18, Supporting Information). Then, we tied the thermoelectric generator around the coffee mug and filled the mug with hot water to create a temperature difference across the device, i.e., between the wall of the mug and the surrounding air. When the temperature difference stabilized at $\Delta T = 30$ K, we measured the thermoelectric performance of the bent device. Gratifyingly, we observed that repeated bending did not affect the thermoelectric performance of the device, which continued to function as before the mechanical deformation was applied (Figure S18, Supporting Information).

3. Conclusion

The *n*-type conjugated polymer PBFDO could be readily processed into free-standing films, exhibiting a high stiffness and relatively high ductility with a Young's modulus $E = 6.6 \pm 0.9$ GPa and a strain at break $\epsilon_{break} = 5.2 \pm 1.1\%$ at room temperature. The high degree of mechanical robustness of as-cast PBFDO enabled the fabrication of *n*-type yarn by batch coating silk yarn with PBFDO:DMSO ink. The resulting multifilament *n*-type yarn featured an effective electrical conductivity of $\sigma_{eff} = 13 \pm 1$ S cm^{-1}, which remained nearly constant over 14 months of storage at ambient conditions and increased only threefold after seven washing cycles, indicating both outstanding long-term stability and washability.

Moreover, the PBFDO coated yarn exhibited a Young's modulus $E = 0.6 \pm 0.1$ GPa and a strain at break of $\epsilon_{break} = 14 \pm 0.3\%$. The yarn could withstand cyclic tensile deformation to 3, 4, and 5% strain, confirming its suitability for textile manufacturing. The robustness and utility of the *n*-type yarn were illustrated by the fabrication of two out-of-plane thermoelectric textile devices: a thermoelectric button and a larger textile thermopile. PBFDO and PEDOT:PSS silk yarns were used to hand-stitch a button onto a pile of wool fabrics, resulting in a thermocouple with a maximum output power of ≈20 nW and good air stability for at least one year. Additionally, PBFDO and PEDOT:PSS silk yarns were used to fabricate a larger thermoelectric textile device consisting of 8 *n*-type and 8 *p*-type legs. The open-circuit voltage V_{oc} of the device reached a value of up to 17 mV and a maximum output power $P_{max} = 0.67\ \mu W$ for a $\Delta T = 70$ K, which, e.g., would be sufficient to power sensors based on organic electrochemical transistors (OECTs) for sensing of electrophysiological signals.[53,54] Numerical simulations were in good agreement with the experimentally obtained device performance and indicated that P_{max} could be increased by minimizing the electrical contact resistance. Evidently, PBFDO coated multifilament silk yarn is a promising material for the realization of stable thermoelectric textile devices.

4. Experimental Section

Materials: PEDOT:PSS (Clevios PH1000) was purchased from Heraeus Holding GmbH. PBFDO was synthesized according to the literature.[47] 3,7-dihydrobenzo[1,2-*b*:4,5-*b*′]difuran-2,6-dione (H-BFDO), duroquinone and DMSO (purity 99.9%) were purchased from Sigma–Aldrich and used as received. H-BFDO (1 eq, 150 mg) and duroquinone (1.5 eq, 194 mg) were dissolved in 10 mL DMSO under nitrogen, followed by heating at 100 °C for 1 h. The final mixture was dialyzed against DMSO using a dialysis bag with a cutoff molecular weight of 10 kg mol^{-1} (Viskase, USA) for 1–2 weeks (DMSO was changed every 3 days until it became colorless). The mixture in the dialysis bag was filtered with a 0.45 μm polytetrafluoroethylene filter to obtain the final PBFDO:DMSO ink.

Sample Preparation and Yarn Coating: Thin films were spin coated (1500 rpm for 120 s and 3000 rpm for 10 s) onto cleaned glass slides (prewashed by sonication in acetone and then isopropanol) and then annealed on a hotplate at 50 °C for 1 h. Free-standing films with a thickness of 7–18 μm were prepared by drop casting PBFDO:DMSO ink onto cleaned glass slides at 40 °C, followed by drying in a vacuum oven for 2 days at 40 °C, and finally removal from the substrate with a sharp blade. The thickness of thin films was determined with atomic force microscopy (AFM) in tapping mode using a Dimension 3000 instrument from Digital Instruments equipped with a standard silicon tip; the thickness of free-standing films was measured with a digital caliper. Silk sewing thread was purchased from Aurora Silk. A prewash of silk yarn in a 1:50 (yarn:water) wash bath using 4 g dm^{-3} (with respect to water) silk detergent (Zenit) and 4 g dm^{-3} ammonia (25%, Merck Millipore) was performed. PBFDO coated silk yarn was prepared by immersion into PBFDO:DMSO ink for 10 to 20 min, followed by drying in an oven at 40 °C. Dip coating in PBFDO:DMSO ink was repeated twice (for the yarns used for the characterization and for sewing the thermopile) or three times (for the yarns used to fabricate the prototype), followed by a final drying step at 40 °C. Oxidation of PBFDO coated yarn was achieved by submerging yarn sections for 20 min in solutions of 0.1–3 mM Magic Blue (obtained from Sigma–Aldrich), dissolved in 2 mL dry and degassed (30 min N_2) acetonitrile (obtained from Sigma–Aldrich). PEDOT:PSS coated yarns were prepared according to a previously reported roll-to-roll method.[51]

Scanning Electron Microscopy: Samples for scanning electron microscopy (SEM) were freeze-fractured in liquid nitrogen, and then sput-

tered with gold, were indicated. SEM imaging was done with a LEO Ultra 55 (Zeiss, Germany) at an acceleration voltage of 2–3 kV.

Wide Angle X-Ray Scattering (WAXS): Wide-angle X-ray scattering was carried out in transmission mode on bulk samples with a Mat:Nordic instrument from SAXSLAB equipped with a Rigaku 003+ high-brilliance microfocus Cu Kα radiation source (wavelength = 1.5406 Å) and a Pilatus 300 K detector placed at a distance of 124.6 mm from the sample.

Electrical Characterization: The electrical resistance of thin films was measured by the four-point probe method in vacuum from 80 to 400 K with 10 K steps using a semiconductor characterization system (Keithley 4200-SCS). The temperature was controlled by a heater and liquid nitrogen. Four parallel line-shaped Cr/Au electrodes were evaporated on glass substrates with a channel width of 12 mm and a channel length of 0.6 mm on top of which PBFDO films were spin coated. To determine the electrical conductivity of conducting yarns, samples were placed on a glass substrate, and contact points with a spacing of L = 10 mm were made on top using silver paint (fast drying silver suspension from Agar Scientific Ltd.). The resistance of each 10 mm long section was measured using a Keithley 2400 source-measure unit in 2-point configuration. The electrical contact resistance $R_{c,\,yarn}$ was estimated through a transmission line method, by plotting the electrical resistance of yarn sections as a function of section length followed by extrapolation of $R_{c,\,\mathrm{yarn}}$ at $L = 0$. The measured resistance R_m was then corrected according to $R = R_m - R_{c,\,\mathrm{yarn}}$. The effective electrical conductivity was calculated according to $\sigma_{\mathrm{eff}} = L/(A \cdot R)$ where L is the length of the characterized yarn section, i.e., 10 mm, and $A = \pi D^2/4$ is the yarn cross-section area determined by assuming an homogenous circular area and measuring the yarn diameter D with an Axio optical microscope from Zeiss. The Seebeck coefficient at 300 K was measured with an SB1000 instrument from MMR Technologies equipped with a K2000 temperature controller using a thermal load of 1–2 K and a constantan wire as internal reference. 5 mm-long yarn segments were mounted on the SB1000 sample stage with silver paint.

Mechanical Characterization: Tensile deformation of free-standing films and yarn sections was performed using a DMA Q800 instrument from TA Instruments in controlled force mode at different temperatures. A force rate of 0.01 N min^{-1} for polymer films and 0.1 N min^{-1} for yarns were used and the preload force was 0.005 N. Cyclic tensile deformation of conducting yarn was performed using the same DMA Q800 instrument by repeatedly applying 3, 4, or 5% maximum strain for 12 s followed by a 60 s release. The electrical resistance during cyclic deformation was monitored with a Keysight U1253B multimeter. Dynamic mechanical thermal analysis (DMTA) was performed using a DMA Q800 in tensile mode at a frequency of 1 Hz while ramping the temperature from −80 to 200 °C at a rate of 3 °C min^{-1}. A dynamic strain with a maximum value of 0.1% and a preload force of 0.001–0.005 N were used.

Machine Washing: Machine washing was carried out using a commercial washing machine (Daewoong Morning Calm) with 30 mL of commercial detergent (Spark, Aekyung Co. Ltd.) in 3 L of water. The detergent was reported to contain linear alkylbenzenesulfonates, α-olefins, zeolite, fatty acids, etc. Several samples were prepared, each comprising three segments of ≈5 cm long *n*-type yarn that were hand-stitched onto a piece of felted wool fabric. Each felt was put into a mesh laundry bag and then washed 1 to 7 times in the washing machine with 3 L of water. Each washing cycle was performed for 15 min at 20 °C. After each washing cycle, the electrical resistance of the three yarns stitched on the felt was measured using a multimeter (Fluke) in 2-point configuration.

Textile Thermoelectric Button and Generator: A button (circular shape with a diameter of 15 mm) was sewn onto three layers of felted wool fabric from Harry Hedgren AB (Wadmal, 3.2 g dm^{-2}, ≈1 mm thick) by hand stitching the conducting yarns with a sewing needle to form a thermopile comprising one *n*-type and one *p*-type leg. After stitching, silver paint (fast drying silver suspension from Agar Scientific Ltd) was applied to both the bottom and top surfaces to establish electrical connections between the legs that also served as contact pads for device characterization.

PBFDO and PEDOT:PSS-coated yarns were hand stitched onto six layers of felted wool fabric from Harry Hedgren AB (Wadmal, 3.2 g dm^{-2}, ≈1 mm thick) using a sewing needle. The sewn yarns formed an out-of-plane thermoelectric generator comprising 8 *n*-type and 8 *p*-type legs. Each leg was characterized by an area of 8–10 mm times 8–10 mm and a length L_l, i.e., the thickness of the felted wool layers, of 8 mm. After stitching, silver paint (fast drying silver suspension from Agar Scientific Ltd) was applied with a circular (diameter ≈ 8 mm) rubber stamp to both the bottom and top surfaces to improve the electrical contact among the conducting yarns of each leg and to establish electrical connections between the legs.

The thermoelectric button and the textile thermoelectric generator were characterized by placing them on top of a variable temperature hot plate (HP60, Torrey Pines Scientific Inc.). K-type thermocouples (Omega Engineering) were placed on the top and at the bottom of the devices to record the surface temperatures using a cDAQ 9174 instrument from National Instruments with an internal temperature reference. A cooling element was placed on top of the devices (separated by a glass slide to avoid direct contact) to maintain a constant cold temperature and to keep the device in place by providing a weight of ≈0.75 kg. The generated voltage was measured with a Keithley 2400 source measure unit. Furthermore, the instrument was used as a variable load by drawing current from the thermoelectric generator to determine the maximum output power.

Modeling and Numerical Simulation: A 3D model of the textile thermopile was constructed in COMSOL Multiphysics. The development of the simulation model was based on the following assumptions: 1) only heat conduction was considered, while heat transfer via convection and radiation was negligible; 2) the influence of Joule heating, the Peltier effect, and the Thomson effect was negligible.

The geometrical and material parameters were selected based on the experimental results (Table 2; Figure S19a, Supporting Information). The side length of the whole model and each leg was 55 and 8 mm, respectively, in line with the actual textile thermopiles. The spacing between each leg was set to be 3 mm. The length of each thermoelectric leg L_l was varied from 2 to 30 mm for investigating the optimal length L_l leading to the P_{max}. Electrodes were constructed for electrically connecting the legs (Figure S19b, Supporting Information). The electrical resistance and thermal resistance of the electrodes were sufficiently small (at least 1000 times smaller than the corresponding contact resistance) to be neglected. The introduction of electrical and thermal contact resistance in the model was achieved by setting an electrical and thermal contact node between the legs and the electrodes.

A 1400 mm long coated yarn was used to fabricate each leg, which corresponds to a thread count N_t of around 90. The cross-sectional area of coated yarn A_y per leg was given by:

$$A_y = \frac{N_t \pi D^2}{4} \approx 2.83\ \mathrm{mm}^2 \tag{5}$$

where D is the yarn diameter.

The internal electrical resistance $R_{\mathrm{int,l}}$ of *p*-type and *n*-type legs were calculated to be 2.19 and 2.16 Ω, respectively, using the equation below:

$$R_{\mathrm{int},l} = \frac{L_l}{A_y \sigma_{\mathrm{eff}}} \tag{6}$$

where L_l is the length of the leg and σ_{eff} is the bulk conductivity of the conducting yarns.

The total internal electrical resistance of the whole textile device was measured to be 119.0 Ω at room temperature and 107.9 Ω at 90 °C, i.e., the set temperature of the hot plate to obtain a ΔT = 70 K (Figure S16, Supporting Information). Assuming that $R_{\mathrm{int,l}}$ of the *n*-type yarn was constant up to 100 °C (see Figure S20, Supporting Information), and that *p*-type yarn shows a similar behavior, a change in the electrical contact resistance R_c per thermocouple with increasing temperature is estimated, ranging from 10.5 Ω at room temperature to 9.1 Ω at 90 °C.

Cubic legs with an effective electrical and thermal conductivity were utilized to represent the legs made of felted wool fabric and coated yarns.

The effective electrical conductivity of the *p*-type or *n*-type legs was given by:

$$\sigma_l = \frac{L_l}{A_l \, R_{\text{int},l}} \tag{7}$$

where A_l is the cross-sectional area of the legs.

Regarding the heat conduction across the legs, it was assumed that the thermal resistances of coated yarns K_y and felted wool fabric K_w were coupled in parallel. K_y is given by $K_y = \frac{L_l}{\lambda_y A_y}$, while $K_w = \frac{L_l}{\lambda_w (A_l - A_y)}$, where λ_y and λ_w are the thermal conductivity of the coated yarn and felted wool fabric, respectively. *p*-type yarn was characterized by a $\lambda_y = 0.18$ W m^{-1} K^{-1}, as previously reported,[19] and the same value for the *n*-type yarn was assumed. The thermal conductivity of felted wool λ_w used in the simulation was 0.056 W m^{-1} K^{-1}, as previously reported.[19] The total thermal resistance K of each leg was given by:

$$\frac{1}{K} = \frac{1}{K_y} + \frac{1}{K_w} \tag{8}$$

The effective thermal conductivity of the cubic legs was calculated by $\lambda_l = \frac{L_l}{K A_l}$.

Supporting Information

Supporting Information is available from the Wiley Online Library or from the author.

Acknowledgements

M.C. and Q.L. contributed equally to this work. The authors gratefully acknowledge financial support from the European Union's Horizon 2020 research and innovation programme through the Marie Skłodowska-Curie grant agreement no. 955837 (HORATES), the Knut and Alice Wallenberg Foundation (2021.0058, 2021.0230, 2021.0295 and 2022.0034), the European Research Council (ERC) under grant agreement no. 101043417, the Swedish Research Council (2020-03243), and the Swedish Government Strategic Research Area in Materials Science on Functional Materials at Linköping University (Faculty Grant SFO-Mat-LiU 2009-00971).

Conflict of Interest

S.F. is a co-founder and chief scientific officer of the company n-ink. All other authors declare no conflict of interests.

Data Availability Statement

The data that support the findings of this study are openly available in Zenodo at https://zenodo.org/doi/10.5281/zenodo.10926630.

Keywords

organic thermoelectrics, PBFDO coated silk yarn, poly(benzodifurandione), Seebeck coefficient, thermoelectric textile

Received: June 18, 2024
Published online: August 5, 2024

[1] G. Chen, X. Xiao, X. Zhao, T. Tat, M. Bick, J. Chen, *Chem. Rev.* **2022**, *122*, 3259.
[2] S. Takamatsu, T. Lonjaret, D. Crisp, J.-M. Badier, G. G. Malliaras, E. Ismailova, *Sci. Rep.* **2015**, *5*, 15003.
[3] G. M. N. Islam, A. Ali, S. Collie, *Cellulose* **2020**, *27*, 6103.
[4] K. Meng, S. Zhao, Y. Zhou, Y. Wu, S. Zhang, Q. He, X. Wang, Z. Zhou, W. Fan, X. Tan, J. Yang, J. Chen, *Matter* **2020**, *2*, 896.
[5] R. Lin, H.-J. Kim, S. Achavananthadith, S. A. Kurt, S. C. C. Tan, H. Yao, B. C. K. Tee, J. K. W. Lee, J. S. Ho, *Nat. Commun.* **2020**, *11*, 444.
[6] S. Takamatsu, T. Lonjaret, E. Ismailova, A. Masuda, T. Itoh, G. G. Malliaras, *Adv. Mater.* **2016**, *28*, 4485.
[7] S. Sinha, R. Daniels, O. Yassin, M. Baczkowski, M. Tefferi, A. Deshmukh, Y. Cao, G. Sotzing, *Adv. Mater. Technol.* **2022**, *7*, 2100548.
[8] Y. Wu, S. S. Mechael, C. Lerma, R. S. Carmichael, T. B. Carmichael, *Matter* **2020**, *2*, 882.
[9] Z. Li, S. K. Sinha, G. M. Treich, Y. Wang, Q. Yang, A. A. Deshmukh, G. A. Sotzing, Y. Cao, *J. Mater. Chem. C* **2020**, *8*, 5662.
[10] R. Salvado, C. Loss, R. Gonçalves, P. Pinho, *Sensors* **2012**, *12*, 15841.
[11] A. Maziz, A. Concas, A. Khaldi, J. Stålhand, N.-K. Persson, E. W. H. Jager, *Sci. Adv.* **2017**, *3*, e1600327.
[12] Y. Fang, G. Chen, M. Bick, J. Chen, *Chem. Soc. Rev.* **2021**, *50*, 9357.
[13] R. Hu, Y. Liu, S. Shin, S. Huang, X. Ren, W. Shu, J. Cheng, G. Tao, W. Xu, R. Chen, X. Luo, *Adv. Energy Mater.* **2020**, *10*, 1903921.
[14] A. Lund, K. Rundqvist, E. Nilsson, L. Yu, B. Hagström, C. Müller, *npj Flex. Electron.* **2018**, *2*, 9.
[15] F. Mokhtari, G. M. Spinks, C. Fay, Z. Cheng, R. Raad, J. Xi, J. Foroughi, *Adv. Mater. Technol.* **2020**, *5*, 1900900.
[16] J.-E. Lee, Y.-E. Shin, G.-H. Lee, J. Kim, H. Ko, H. G. Chae, *Compos. B Eng.* **2021**, *223*, 109098.
[17] C. Dong, A. Leber, T. Das Gupta, R. Chandran, M. Volpi, Y. Qu, T. Nguyen-Dang, N. Bartolomei, W. Yan, F. Sorin, *Nat. Commun.* **2020**, *11*, 3537.
[18] M. Hatamvand, E. Kamrani, M. Lira-Cantú, M. Madsen, B. R. Patil, P. Vivo, M. S. Mehmood, A. Numan, I. Ahmed, Y. Zhan, *Nano Energy* **2020**, *71*, 104609.
[19] A. Lund, Y. Tian, S. Darabi, C. Müller, *J. Power Sources* **2020**, *480*, 228836.
[20] T. Sun, B. Zhou, Q. Zheng, L. Wang, W. Jiang, G. J. Snyder, *Nat. Commun.* **2020**, *11*, 572.
[21] T. Ding, K. H. Chan, Y. Zhou, X.-Q. Wang, Y. Cheng, T. Li, G. W. Ho, *Nat. Commun.* **2020**, *11*, 6006.
[22] H. M. Elmoughni, A. K. Menon, R. M. W. Wolfe, S. K. Yee, *Adv. Mater. Technol.* **2019**, *4*, 1800708.
[23] R. Kroon, D. A. Mengistie, D. Kiefer, J. Hynynen, J. D. Ryan, L. Yu, C. Müller, *Chem. Soc. Rev.* **2016**, *45*, 6147.
[24] L. K. Allison, T. L. Andrew, *Adv. Mater. Technol.* **2019**, *4*, 1800615.
[25] J. Pope, C. Lekakou, *Smart Mater. Struct.* **2019**, *28*, 095006.
[26] Y. Du, K. Cai, S. Chen, H. Wang, S. Z. Shen, R. Donelson, T. Lin, *Sci. Rep.* **2015**, *5*, 6411.
[27] Y. Kim, A. Lund, H. Noh, A. I. Hofmann, M. Craighero, S. Darabi, S. Zokaei, J. I. Park, M.-H. Yoon, C. Müller, *Macromol. Mater. Eng.* **2020**, *305*, 1900749.
[28] R. Madannejad, N. Shoaie, F. Jahanpeyma, M. H. Darvishi, M. Azimzadeh, H. Javadi, *Chem.-Bio. Inter.* **2019**, *307*, 206.
[29] N. Pataki, P. Rossi, M. Caironi, *Appl. Phys. Lett.* **2022**, *121*, 230501.
[30] A. Lund, Y. Wu, B. Fenech-Salerno, F. Torrisi, T. B. Carmichael, C. Müller, *MRS Bull.* **2021**, *46*, 491.
[31] G. H. Kim, L. Shao, K. Zhang, K. P. Pipe, *Nat. Mater.* **2013**, *12*, 719.
[32] D. A. Mengistie, C.-H. Chen, K. M. Boopathi, F. W. Pranoto, L.-J. Li, C.-W. Chu, *ACS Appl. Mater. Interfaces* **2015**, *7*, 94.
[33] R. Sarabia-Riquelme, R. Andrews, J. E. Anthony, M. C. Weisenberger, *J. Mater. Chem. C* **2020**, *8*, 11618.
[34] J. D. Ryan, D. A. Mengistie, R. Gabrielsson, A. Lund, C. Müller, *ACS Appl. Mater. Interfaces* **2017**, *9*, 9045.
[35] S. Darabi, M. Hummel, S. Rantasalo, M. Rissanen, I. Öberg Månsson, H. Hilke, B. Hwang, M. Skrifvars, M. M. Hamedi, H. Sixta, A. Lund, C. Müller, *ACS Appl. Mater. Interfaces* **2020**, *12*, 56403.

[36] H. Xu, Y. Guo, B. Wu, C. Hou, Q. Zhang, Y. Li, H. Wang, *ACS Appl. Mater. Interfaces* **2020**, *12*, 33297.
[37] B. Lee, H. Cho, K. T. Park, J.-S. Kim, M. Park, H. Kim, Y. Hong, S. Chung, *Nat. Commun.* **2020**, *11*, 5948.
[38] J. Li, B. Xia, X. Xiao, Z. Huang, J. Yin, Y. Jiang, S. Wang, H. Gao, Q. Shi, Y. Xie, J. Chen, *ACS Nano* **2023**, *17*, 19232.
[39] J. D. Ryan, A. Lund, A. I. Hofmann, R. Kroon, R. Sarabia-Riquelme, M. C. Weisenberger, C. Müller, *ACS Appl. Energy Mater.* **2018**, *1*, 2934.
[40] J. Liu, G. Liu, J. Xu, C. Liu, W. Zhou, P. Liu, G. Nie, X. Duan, F. Jiang, *ACS Appl. Energy Mater.* **2020**, *3*, 6165.
[41] H. Suzuki, J. Kametaka, S. Nakahori, Y. Tanaka, M. Iwahara, H. Lin, S. Manzhos, A. K. K. Kyaw, T. Nishikawa, Y. Hayashi, *Small Methods* **2024**, 2301387.
[42] J. Choi, Y. Jung, S. J. Yang, J. Y. Oh, J. Oh, K. Jo, J. G. Son, S. E. Moon, C. R. Park, H. Kim, *ACS Nano* **2017**, *11*, 7608.
[43] S. Darabi, C.-Y. Yang, Z. Li, J.-D. Huang, M. Hummel, H. Sixta, S. Fabiano, C. Müller, *Adv. Electron. Mater.* **2023**, *9*, 2201235.
[44] N. J. Pataki, N. Zahabi, Q. Li, P. Rossi, M. Cassinelli, M. Butti, M. Massetti, S. Fabiano, I. Zozoulenko, M. Caironi, *Adv. Funct. Mater.* **2024**, *34*, 2400982.
[45] C.-Y. Yang, M.-A. Stoeckel, T.-P. Ruoko, H.-Y. Wu, X. Liu, N. B. Kolhe, Z. Wu, Y. Puttisong, C. Musumeci, M. Massetti, H. Sun, K. Xu, D. Tu, W. M. Chen, H. Y. Woo, M. Fahlman, S. A. Jenekhe, M. Berggren, S. Fabiano, *Nat. Commun.* **2021**, *12*, 2354.
[46] S. M. West, D. K. Tran, J. Guo, S. E. Chen, D. S. Ginger, S. A. Jenekhe, *Macromolecules* **2023**, *56*, 2081.
[47] H. Tang, Y. Liang, C. Liu, Z. Hu, Y. Deng, H. Guo, Z. Yu, A. Song, H. Zhao, D. Zhao, Y. Zhang, X. Guo, J. Pei, Y. Ma, Y. Cao, F. Huang, *Nature* **2022**, *611*, 271.
[48] Z. Ke, A. Abtahi, J. Hwang, K. Chen, J. Chaudhary, I. Song, K. Perera, L. You, K. N. Baustert, K. R. Graham, J. Mei, *J. Am. Chem. Soc.* **2023**, *145*, 3706.
[49] R. Sarabia-Riquelme, L. E. Noble, P. Alarcon Espejo, Z. Ke, K. R. Graham, J. Mei, A. F. Paterson, M. C. Weisenberger, *Adv. Funct. Mater.* **2024**, *34*, 2311379.
[50] C. Müller, R. Jansson, A. Elfwing, G. Askarieh, R. Karlsson, M. Hamedi, A. Rising, J. Johansson, O. Inganäs, M. Hedhammar, *J. Mater. Chem.* **2011**, *21*, 2909.
[51] A. Lund, S. Darabi, S. Hultmark, J. D. Ryan, B. Andersson, A. Ström, C. Müller, *Adv. Mater. Technol.* **2018**, *3*, 1800251.
[52] Z. Ke, J. Chaudhary, L. Q. Flagg, K. N. Baustert, A. O. Yusuf, G. Liu, L. You, K. R. Graham, D. M. DeLongchamp, J. Mei, *Adv. Funct. Mater.* **2024**, 2400255.
[53] C.-Y. Yang, D. Tu, T.-P. Ruoko, J. Y. Gerasimov, H.-Y. Wu, P. C. Harikesh, M. Massetti, M.-A. Stoeckel, R. Kroon, C. Müller, M. Berggren, S. Fabiano, *Adv. Electron. Mater.* **2022**, *8*, 2100907.
[54] S. Wang, X. Chen, C. Zhao, Y. Kong, B. Lin, Y. Wu, Z. Bi, Z. Xuan, T. Li, Y. Li, W. Zhang, E. Ma, Z. Wang, W. Ma, *Nat. Electron.* **2023**, *6*, 281.

Supporting Information

Poly(benzodifurandione) Coated Silk Yarn for Thermoelectric Textiles

Mariavittoria Craighero[1#], Qifan Li[2#], Zijin Zeng[1,3], Chunghyeon Choi[4], Youngseok Kim[1], Hyungsub Yoon[4], Tiefeng Liu[2], Przemyslaw Sowinski[1], Shuichi Haraguchi[1], Byungil Hwang[5], Besira Mihiretie[3], Simone Fabiano[2]*, Christian Müller[1]*

[1]Department of Chemistry and Chemical Engineering, Chalmers University of Technology, 41296 Göteborg, Sweden

[2]Laboratory of Organic Electronics, Department of Science and Technology, Linköping University, 60174 Norrköping, Sweden

[3]Hot Disk AB, Sven Hultins gatan 9A, 41258 Göteborg, Sweden

[4]Department of Intelligent Semiconductor Engineering, Chung-Ang University, 06974 Seoul, Republic of Korea

[5]School of Integrative Engineering, Chung-Ang University, 06974 Seoul, Republic of Korea

[#]these authors contributed equally

* simone.fabiano@liu.se; christian.muller@chalmers.se

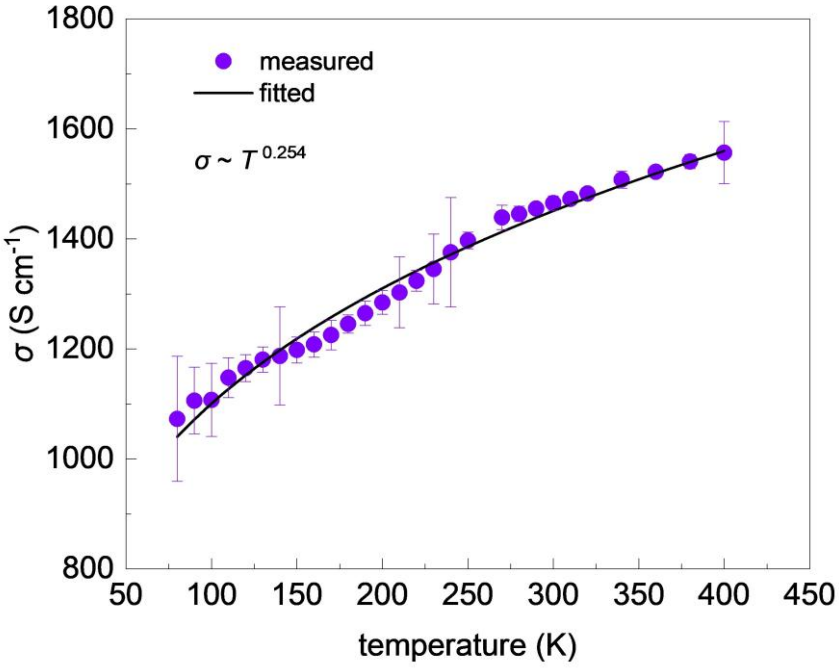

Figure S1. Electrical conductivity σ of spin-coated films as a function of temperature.

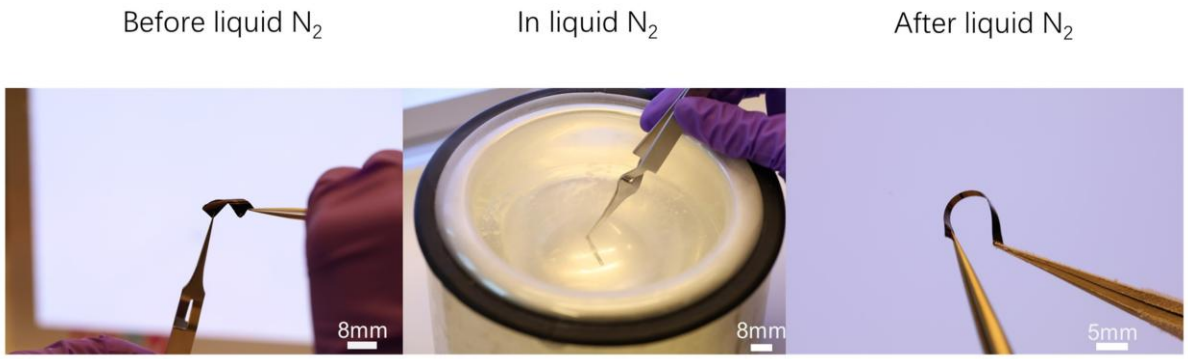

Figure S2. Photographs of PBFDO bent films before, during and after being immersed in liquid nitrogen for a few minutes.

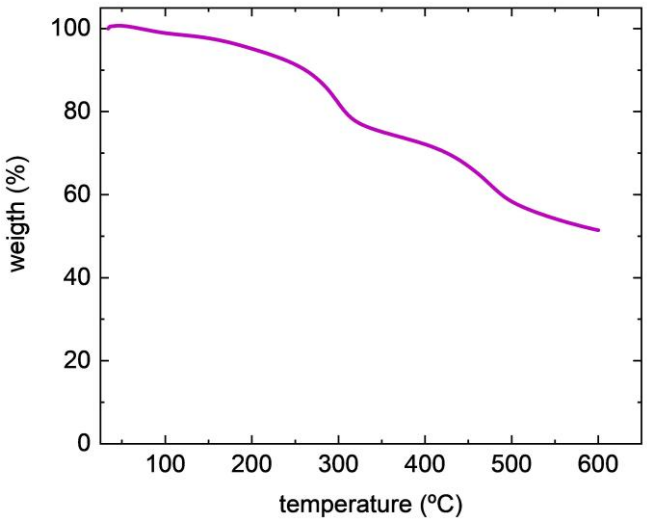

Figure S3. Thermogravimetric analysis (TGA) of PBFDO carried out under nitrogen at a scan rate of 10 °C min^{-1} using a Mettler Toledo TGA/DSC 3+ instrument.

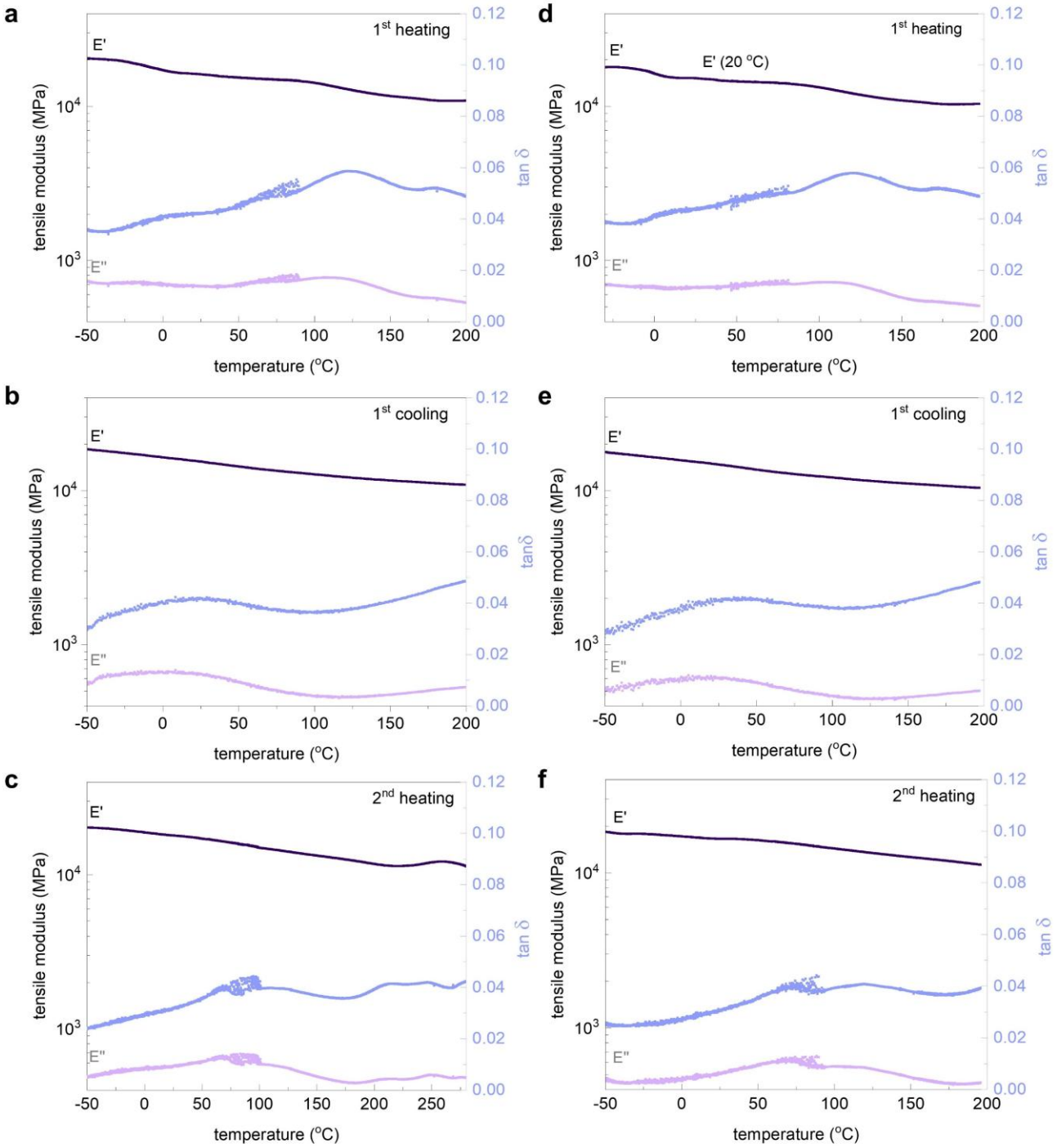

Figure S4. DMTA thermographs of two free-standing films (a-c, d-f) showing the storage modulus E', loss modulus E'' and loss tangent tan δ during the first heating (a, d), first cooling (b, e) and second heating (c, f) steps.

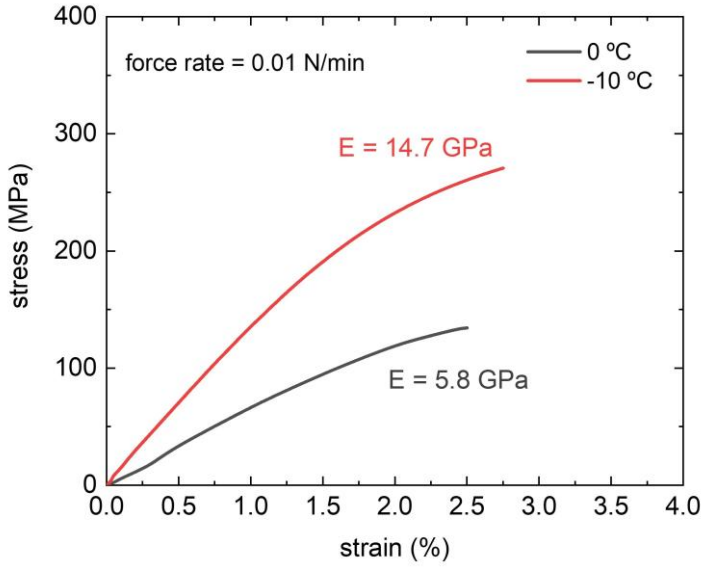

Figure S5. Stress-strain response of free-standing films at different temperatures measured by tensile deformation.

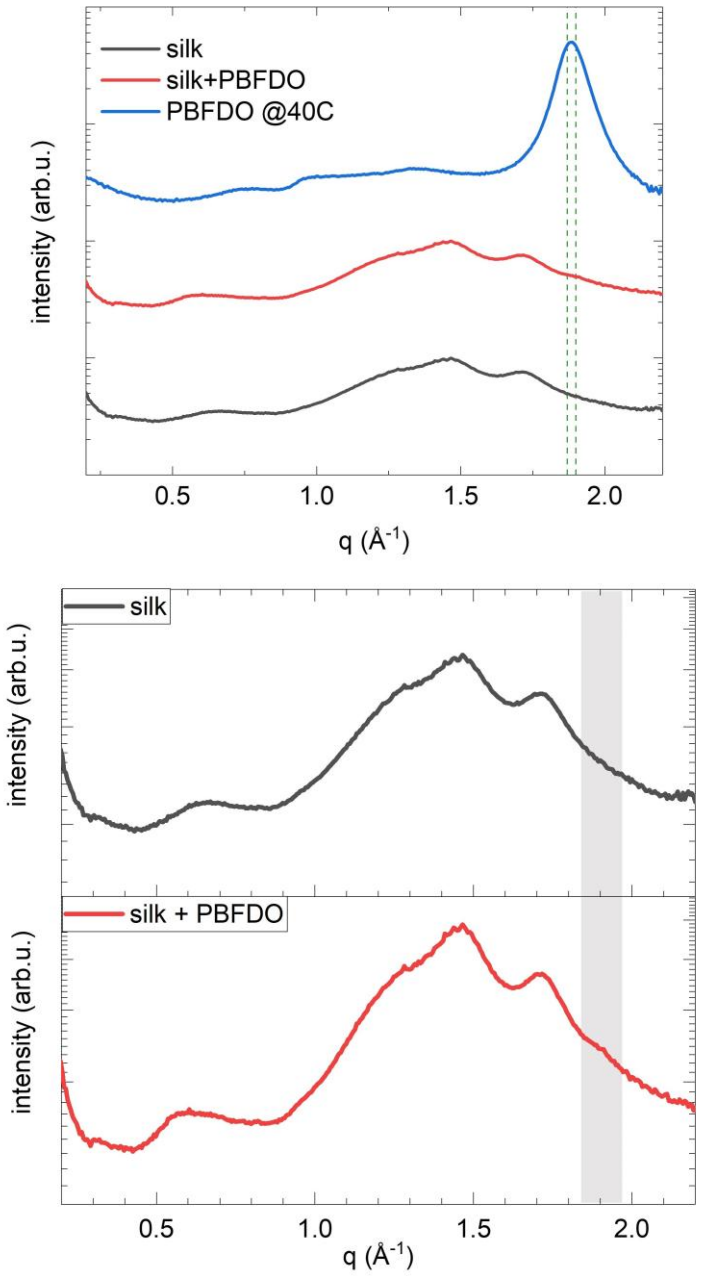

Figure S6. Transmission WAXS of neat and PBFDO-coated silk yarns.

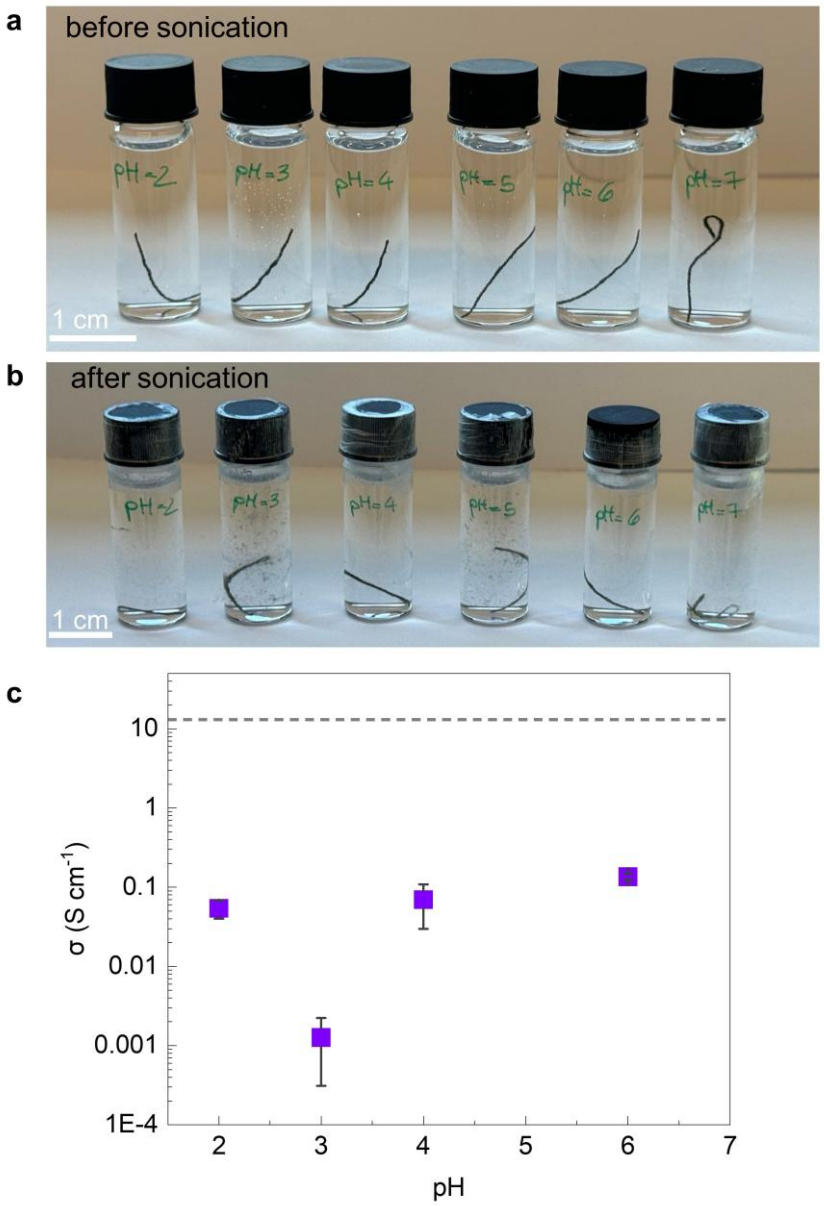

Figure S7. Photograph of PBFDO coated yarns suspended in water with a pH ranging from 2 to 7: before (a) and after (b) sonication for 20 minutes; (c) electrical conductivity of the conductive yarns after sonication (dashed line represents the electrical conductivity value of the yarns before the sonication).

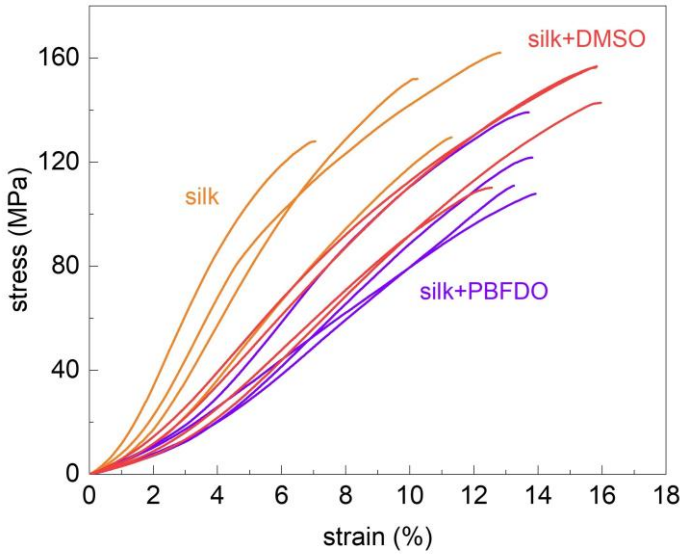

Figure S8. Stress-strain response of silk yarns: neat (orange), treated with DMSO (red), coated with PBFDO:DMSO ink (purple).

Table S1. Mechanical properties of coated silk yarns. Young's modulus E and strain at break ε_{break}. Values represent the mean and standard deviation of measurements of 5 samples.

yarn	E (GPa)	ε_{break} (%)
silk	1.7 ± 0.5	10 ± 2.5
silk treated with DMSO	0.8 ± 0.2	15 ± 1.8
PBFDO:DMSO coated silk	0.6 ± 0.1	14 ± 0.3

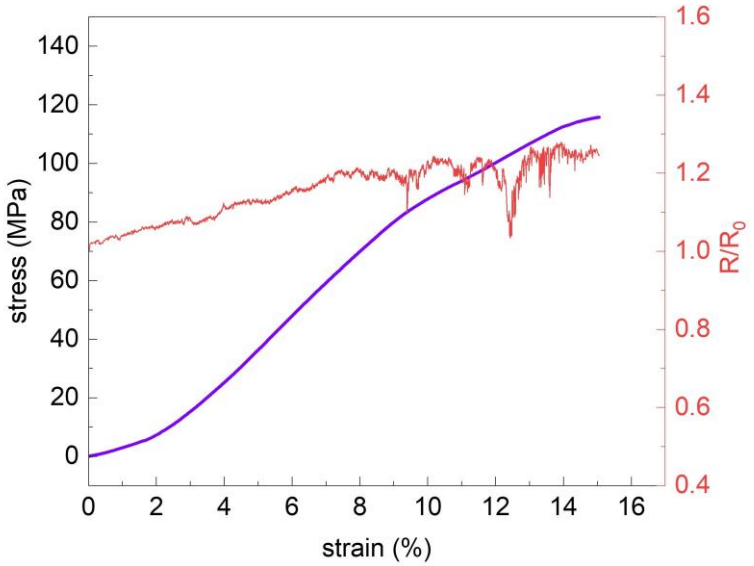

Figure S9. Stress-strain curve of the PBFDO coated silk yarn (left) and in-situ recorded change in electrical resistance R/R_0 where R_0 is the resistance of the yarn prior to the tensile test.

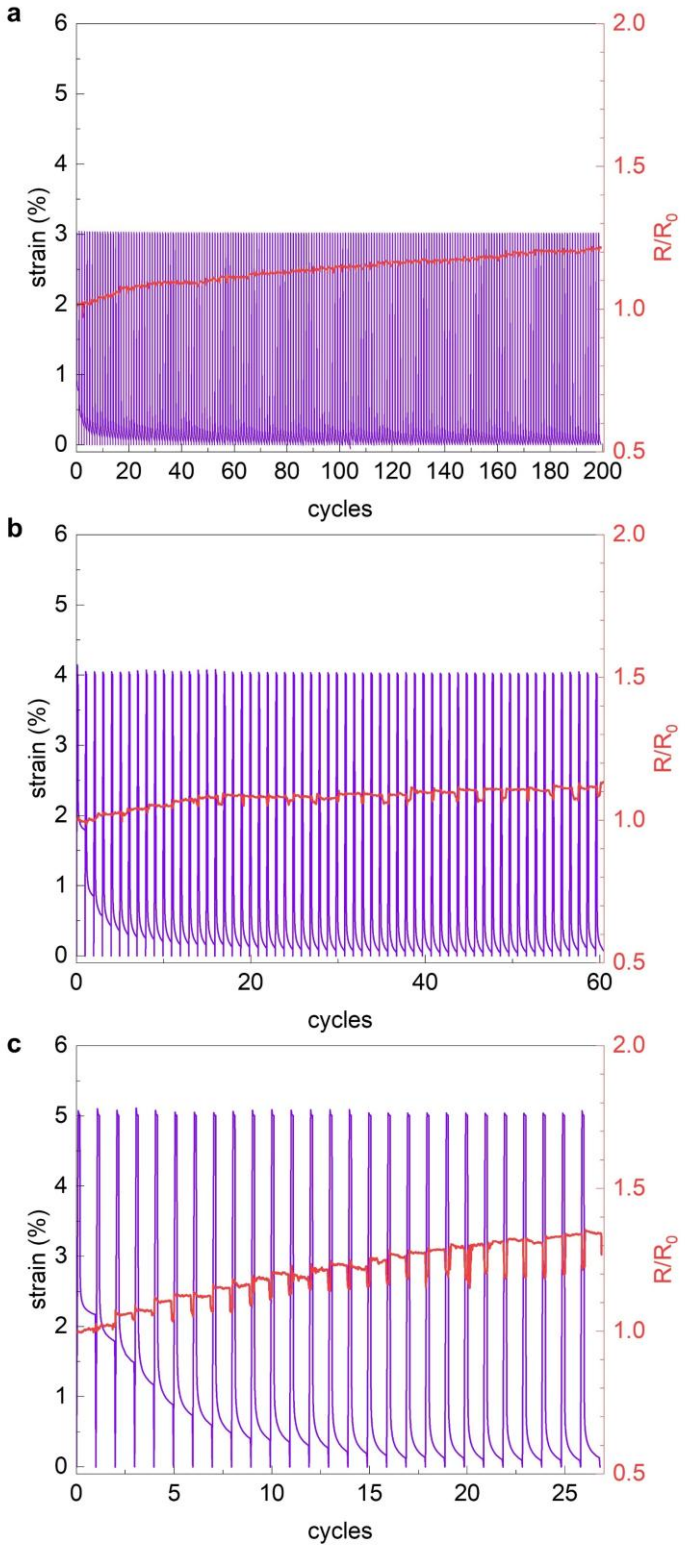

Figure S10. Strain during cyclic tensile deformation of the PBFDO coated silk yarn repeatedly stretched to 3 (a), 4 (b) and 5 % (c) then released for 60 s (purple line) together with the in-situ recorded change in electrical resistance (red line).

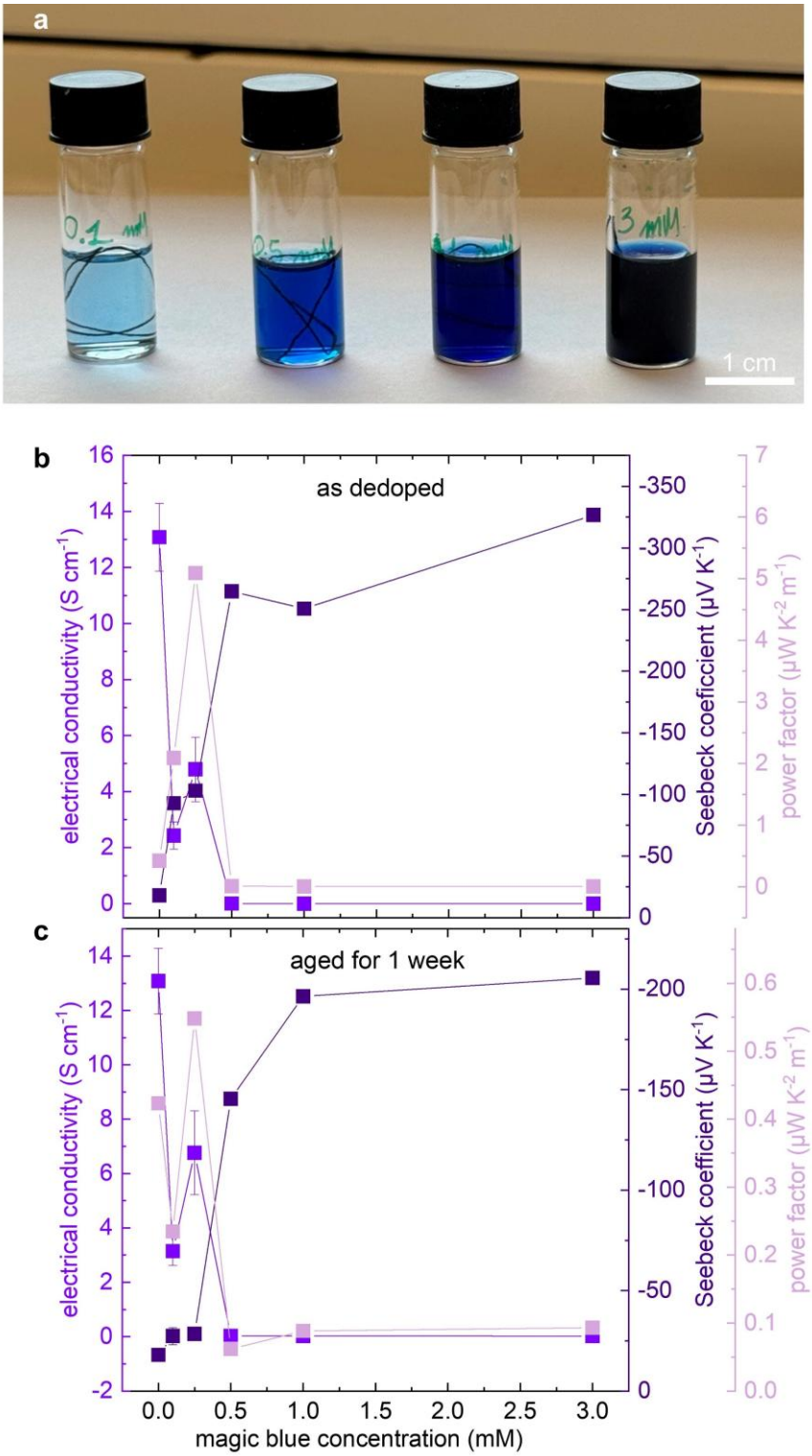

Figure S11. Oxidation of PBFDO coated yarns by Magic Blue. (a) Photograph of PBFDO coated yarns submerged into Magic Blue solutions with different concentrations; electrical conductivity (purple), Seebeck coefficient (dark purple) and power factor (pink) of PBFDO coated yarns as a function of Magic Blue concentration measured (b) as-dedoped and (c) aged for one week at ambient conditions.

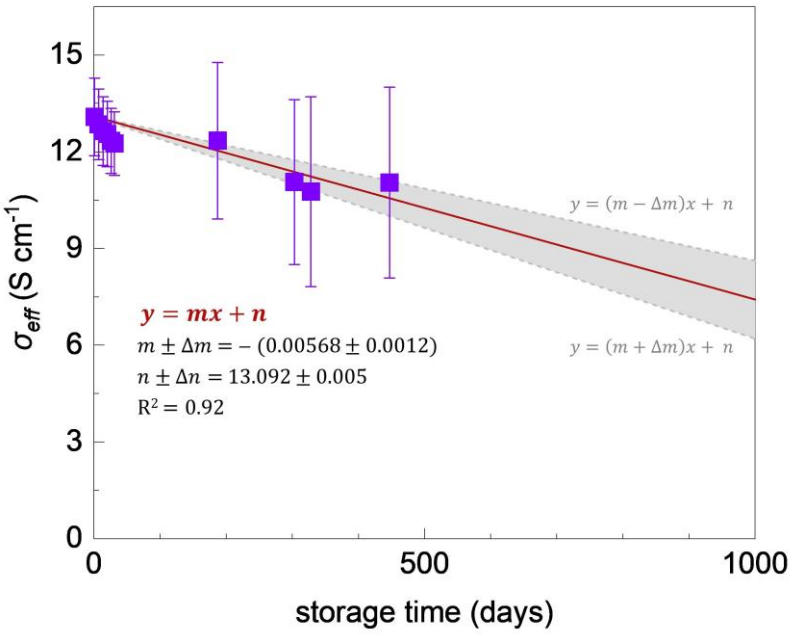

Figure S12. Effective electrical conductivity σ_{eff} of PBFDO coated yarn (symbols) as a function of aging time at ambient conditions and linear fits with statistical results (grey lines: upper and lower boundaries calculated using $y = (m \pm \Delta m)x + n$, respectively; red line: mean fit) from which the half-life time was estimated.

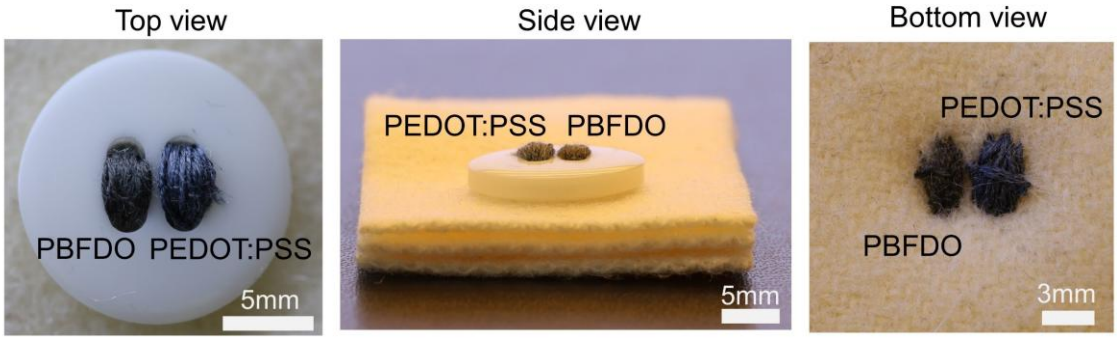

Figure S13. Photographs of the top, side and bottom view of the thermoelectric button.

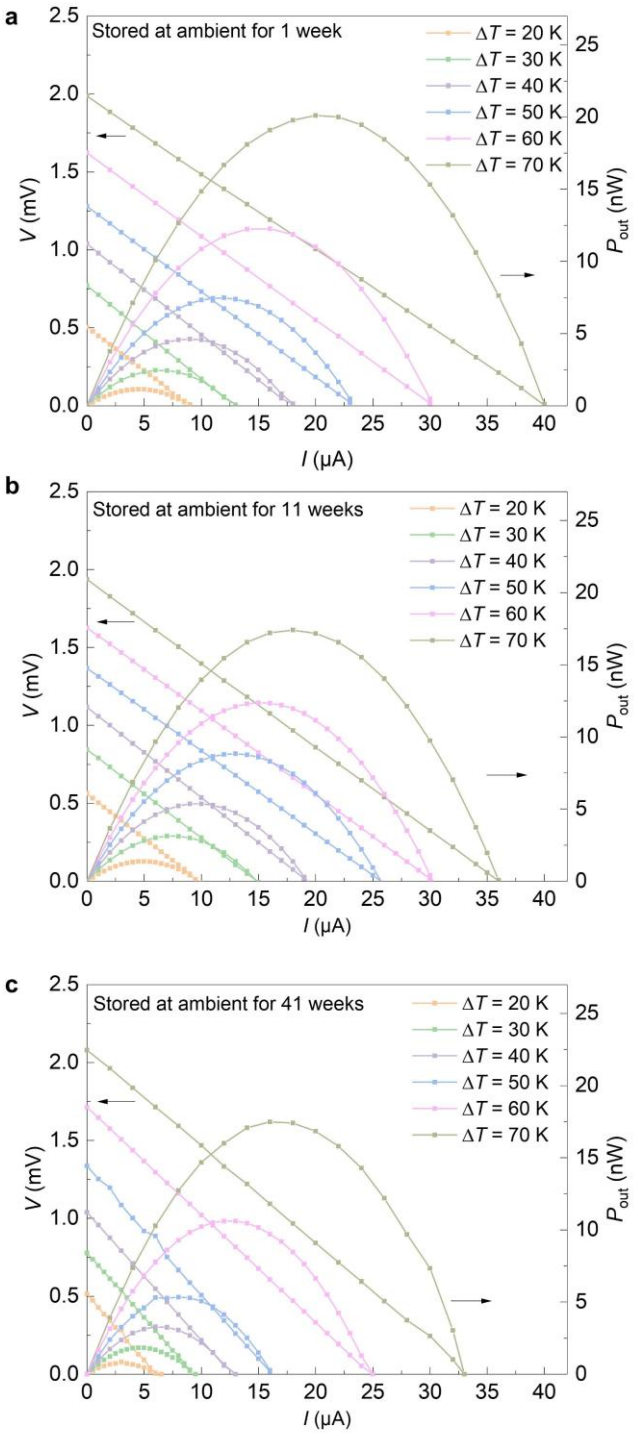

Figure S14. Performance of thermoelectric button stored at ambient conditions for (a) 1, (b) 11, (c) 41 weeks. Voltage V (left) and output power P_{out} (right) of the thermoelectric button as a function of current I for different temperature differences $\Delta T = T_{hot} - T_{cold}$ where T_{hot} and T_{cold} are the temperatures of the hot plate and cooler measured with a pair of thermocouples.

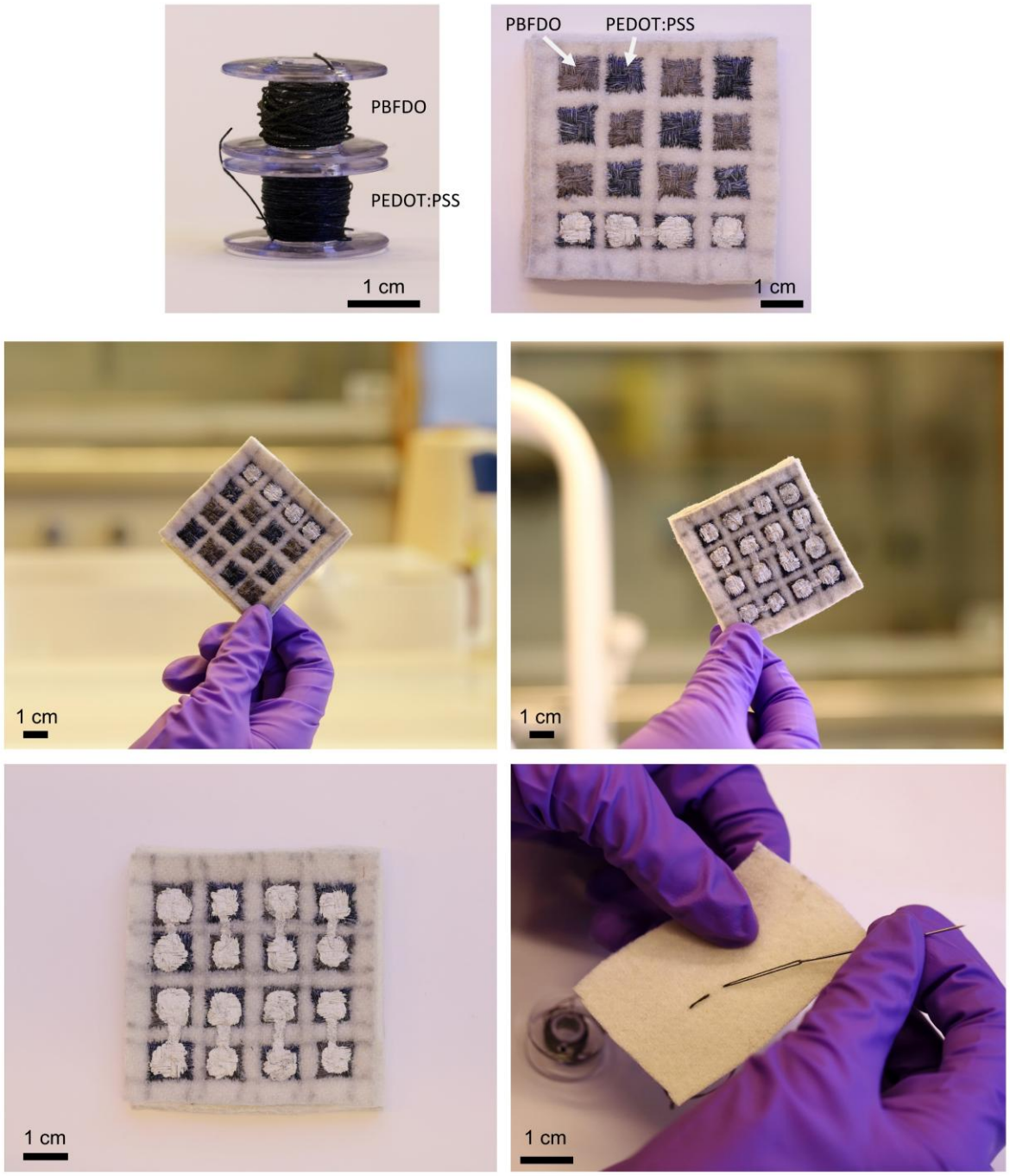

Figure S15. Photographs of PBFDO and PEDOT:PSS coated yarns and the thermoelectric generator.

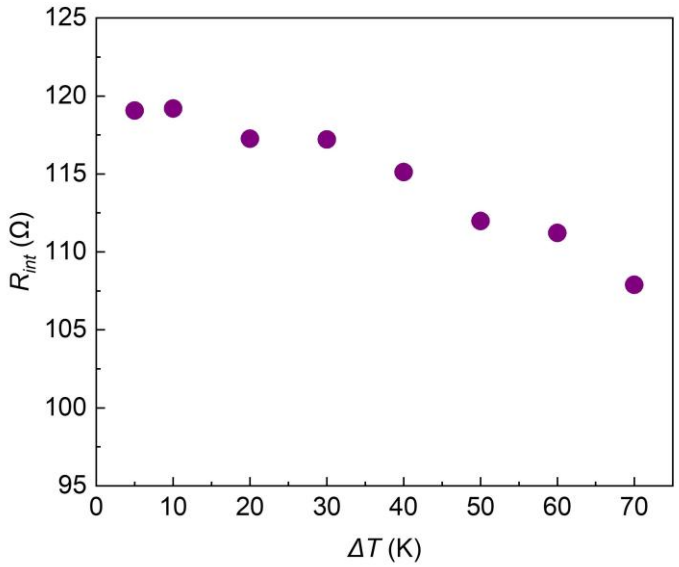

Figure S16. Internal electrical resistance R_{int} of the thermoelectric generator as a function of the temperature gradient across the device.

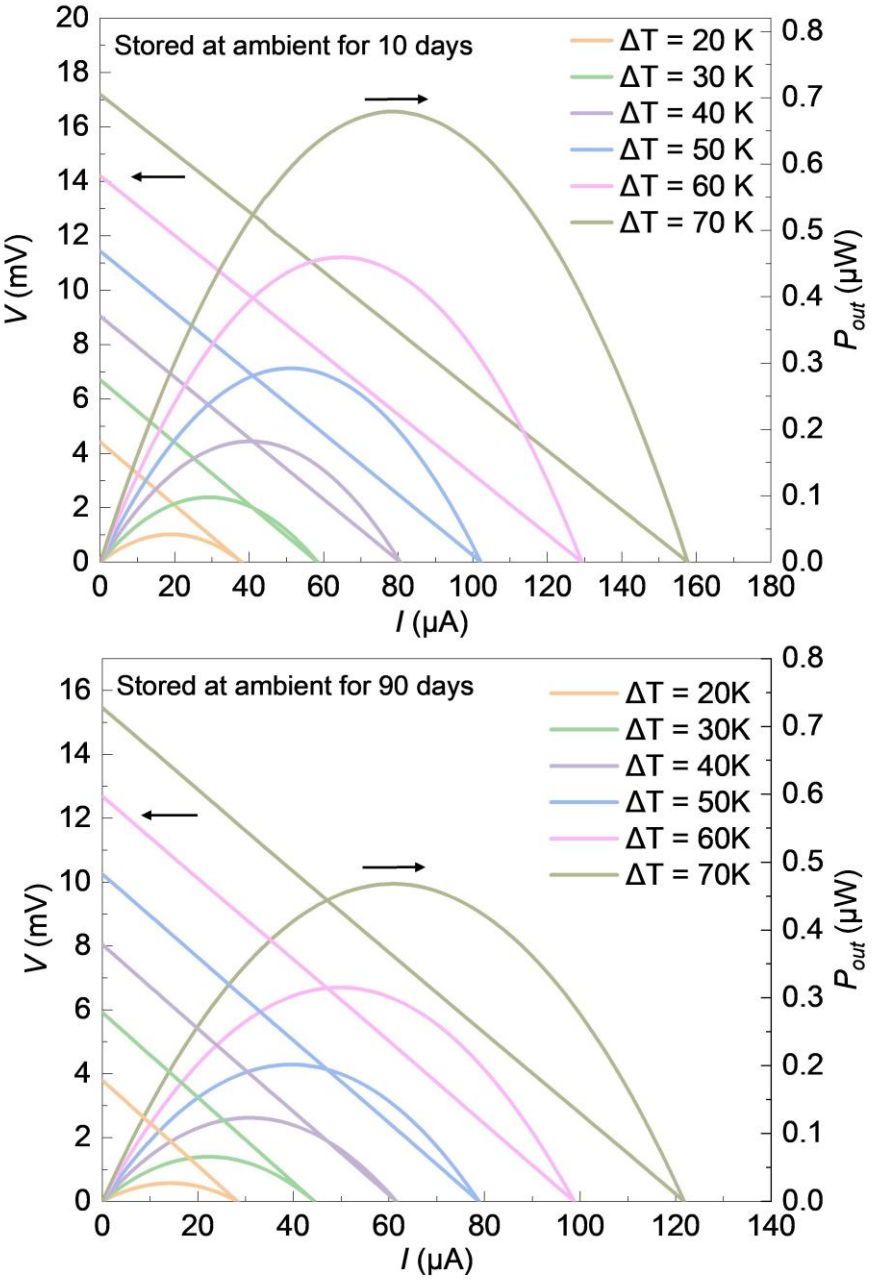

Figure S17. Performance of the larger thermoelectric generator stored at ambient conditions for 10 and 90 days. Voltage V (left) and output power P_{out} (right) of the thermoelectric device as a function of current I for different temperature differences $\Delta T = T_{hot} - T_{cold}$ where T_{hot} and T_{cold} are the temperatures of the hot plate and cooler measured with a pair of thermocouples.

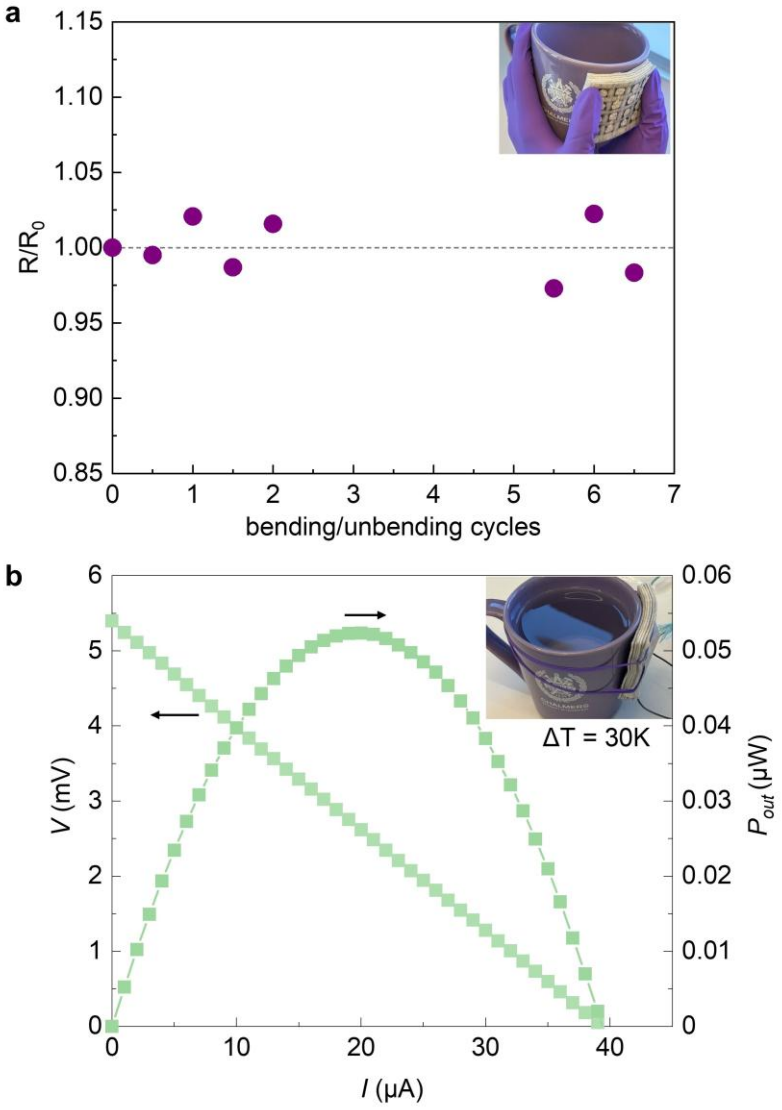

Figure S18. (a) Internal relative electrical resistance of the larger thermoelectric generator during bending-unbending cycles (inset photograph of the bent thermoelectric generator around a coffee mug); and (b) voltage V (left) and output power P_{out} (right) of the bent thermoelectric device as a function of current I at temperature difference $\Delta T = T_{hot} - T_{cold} = 30K$, where T_{hot} and T_{cold} are the temperatures of the warm wall of the mug filled with hot water and room temperature measured with a pair of thermocouples (the inset is a photograph of the thermoelectric generator bent around a coffee mug filled with hot water).

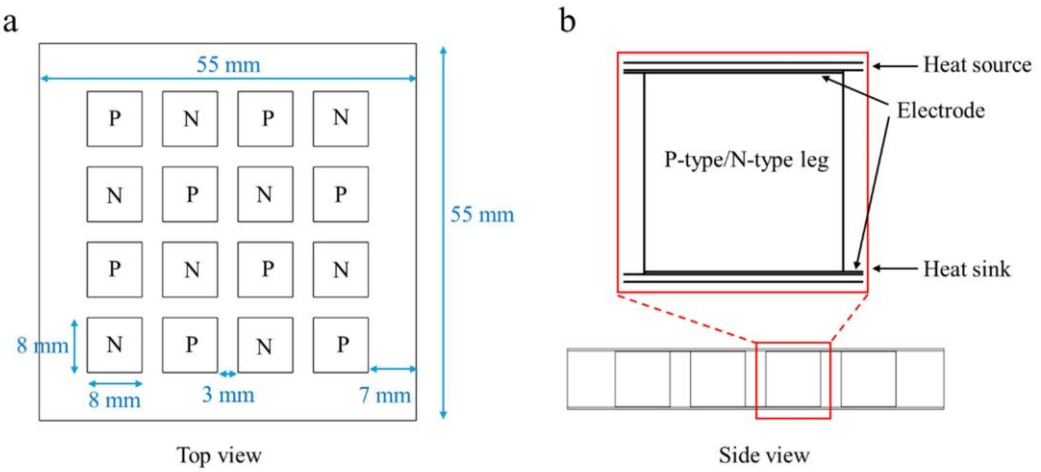

Figure S19. (a) Top view and (b) side view of the simulation model.

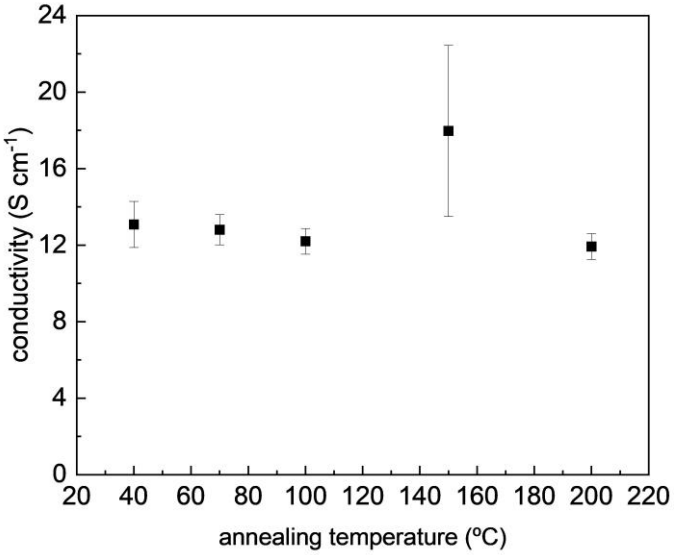

Figure S20. Bulk electrical conductivity of PBFDO coated yarns at different temperatures.

Paper IV

Improved Transient Plane Source Measurements of Layer–Substrate Structures via a Semi-Analytical Temperature Response Model

Manuscript in preparation

Improved Transient Plane Source Measurements of Layer–Substrate Structures via a Semi-Analytical Temperature Response Model

Zijin Zeng[a,b], Christian Müller[a], Johan Gustavsson[c], Besira Mihiretie[b]

a. Department of Chemistry and Chemical Engineering, Chalmers University of Technology, Gothenburg, 41296, Sweden

b. Hot Disk AB, Sven Hultins gatan 9A, Gothenburg, 41288, Sweden

c. Thermetrol AB, Sven Hultins gatan 9A, Gothenburg, 41288, Sweden

Abstract

The Transient Plane Source (TPS) method is widely used to investigate the thermal properties of homogeneous bulk materials and has been further extended to layer–substrate structures. Conventional models on layer–substrate structures typically assume one-dimensional (1D) heat flux across the layer from the heating area into the backing substrate. This assumption imposes a series of constraints on the layer (thermal conductivity < 2 W $m^{-1}K^{-1}$ and thickness < 600 μm) and on the heating area (radius > 11 mm), which greatly limits the scope of the current method. In this study, we present a new semi-analytical model with consideration of non-1D heat flux within the layer, along with an iterative algorithm which automatically selects time range for data analysis. This new model substantially relaxes these constraints, expanding the applicable layer thermal conductivity by an order of magnitude (up to 20 W $m^{-1}K^{-1}$) and thickness by about four times (up to 2000 μm). Moreover, the model enables the use of a new TPS probe for layer-substrate structures, which has a radius of only 6.6 mm. Experiments are described to validate the new model, showing that inaccuracies primarily stem from the thermal contact resistance between the layer and backing substrate. Finite element simulations further indicate that a measurement accuracy better than 10 % can be achieved provided that thermal contact resistance is mitigated.

Key words: Transient Plane Source method, thin layer, thermal conductivity, thermal contact resistance, Finite element method

1. Introduction

Accurate characterization of material thermal properties, including thermal conductivity (λ) and thermal diffusivity (α), is essential for understanding and optimizing a broad range of engineering processes [1-3]. The Transient Plane Source (TPS) method is one of the most widely used characterization techniques, offering fast and non-destructive measurements [4, 5]. Originally proposed in 1991, an international standard for the TPS method was introduced in 2008 [6].

A TPS measurement involves a flat probe — fabricated as a disk [4, 5], rectangle [4] or other planar shape that is embedded between two identical solid or liquid samples. The most widely used design is the disk-shaped "Hot Disk" probe, which consists of a double-spiral metal foil sandwiched between thin insulating layers such as polyimide sheets. The insulation layers provide electrical insulation and protection under different measurement conditions. The probe acts as both a heat source for the surrounding material and a thermometer to measure the resulting temperature response. The thermal properties of bulk samples, including thermal conductivity and thermal diffusivity, can be simultaneously determined based on the recorded temperature response.

Upon heating by the probe, the temperature response (as a function of time *t*) of the sample surface in immediate contact with the probe ($\Delta T_{\mathrm{surf}}(t)$) is raised, typically by a few Kelvin. Based on the assumption that the spiral probe can be approximated by a number of concentric and equally spaced circular rings, the relationship between $\Delta T_{\mathrm{surf}}(t)$ and the thermal properties of the sample can be expressed as:

$$\Delta T_{\mathrm{surf}}(t) = P_0 \left(\pi^{\frac{3}{2}} R\lambda\right)^{-1} D(\tau) \quad \text{and} \quad \tau = \left(\frac{t}{\theta}\right)^{\frac{1}{2}},\ \theta = \frac{R^2}{\alpha} \tag{1}$$

Where P_0 is the power output of the probe, R denotes the radius of the outermost ring of the probe, λ is the thermal conductivity of the sample, and α is the thermal diffusivity. $D(\tau)$ is the dimensionless shape function, defined as:

$$D(\tau) = [m(m+1)]^{-2} \int_0^{\tau} \sigma^{-2} \left[\sum_{n=1}^{m} n \sum_{k=1}^{m} k \exp\left(\frac{-(n^2+k^2)}{4m^2\sigma^2}\right) I_0\left(\frac{nk}{2m^2\sigma^2}\right)\right] \mathrm{d}\sigma \tag{2}$$

Where m denotes the number of concentric ring sources, σ is an integration variable related to dimensionless time, and I_0 is the first kind modified Bessel function of the zeroth order.

In most cases, the insulation layer and thermal contact resistance impede the heat conduction between the probe and the sample, leading to an additional temperature difference ($\Delta T_{\mathrm{add}}(t)$) between the probe and the sample surface in contact with the probe. $\Delta T_{\mathrm{add}}(t)$ approaches a constant value within a short time after the measurement begins. Therefore, the average temperature response of the probe ($\Delta T_{\mathrm{avg}}(t)$) that is recorded by the instrument can be expressed as:

$$\Delta T_{\mathrm{avg}}(t) = \Delta T_{\mathrm{surf}}(t) + \Delta T_{\mathrm{add}} \tag{3}$$

When utilizing a Hot Disk probe with a very small space between the concentric rings, $\Delta T_{\mathrm{surf}}(t)$ approaches the average temperature increase of an ideal circular heating source on a semi-infinite substrate ($\Delta T_{\mathrm{surf,o}}(t)$). In this case, the dimensionless shape function for $\Delta T_{\mathrm{surf,o}}(t)$ becomes [4, 7]:

$$D_{\mathrm{o}}(\tau) = \int_0^{\tau} \mathrm{d}\sigma\sigma^{-2} \int_0^1 v\,\mathrm{d}v \int_0^1 u\,\mathrm{d}u \cdot \exp\left(-\frac{u^2+v^2}{4\sigma^2}\right) I_0\left(\frac{uv}{2\sigma^2}\right) \tag{4}$$

where variable v and u represent normalized radial coordinates.

Laraqi also provided the explicit analytical expression of $\Delta T_{\mathrm{surf,o}}(t)$ [8]:

$$\Delta T_{\mathrm{surf,o}}(t) = \frac{\varphi R}{\lambda}\left(\frac{8}{3\pi} + 2\sqrt{\frac{t^*}{\pi}} - 2\sqrt{\frac{t^*}{\pi}} e^{-\frac{1}{2t^*}}\left[\left(1+\frac{2}{3t^*}\right) I_0\left(\frac{1}{2t^*}\right) + \left(\frac{1}{3}+\frac{2}{3t^*}\right) I_1\left(\frac{1}{2t^*}\right)\right]\right) \tag{5}$$

where $t^* = \tau^2$, $\varphi = P_0/(\pi R^2)$ denotes the power density of an ideal circular heat source and I_1 is the first kind modified Bessel function of the first order.

If the diameter of the probe is roughly two orders of magnitude larger than the insulation layer thickness, the heat flux between the probe and the bulk sample can be regarded as one dimensional (1D). ΔT_{add} can be used to estimate the thermal resistance (R_{th}) between the probe and the background bulk material (referred to as substrate):

$$R_{\mathrm{th}} = \frac{2\pi R^2 \Delta T_{\mathrm{add}}}{P_0} \tag{6}$$

If an additional thin layer is positioned between the probe and the substrate (Fig. 1 c), Eq. 6 still apply and can be used to obtain the corresponding thermal resistance. Consequently, the following equation allows to determine the thermal conductivity of the layer (λ_l):

$$R_{\mathrm{th},l} - R_{\mathrm{th},s} = \frac{L}{\lambda_l} \tag{7}$$

Here, L is the layer thickness, $R_{\mathrm{th},l}$ denotes the total thermal resistance between the probe and the substrate in a layer measurement when an extra layer is inserted, whereas $R_{\mathrm{th},s}$ is the thermal resistance in case of a substrate measurement without a layer.

This approach to utilizing the TPS method for thin layers was proposed in 1997 [9], and has since been adopted for characterizing polymer films [10-12], bio-based films [13, 14], and polymeric composite films [15, 16]. The thermal contact resistance encountered during a measurement can lead to an underestimation of the thermal conductivity [17, 18]. This influence can be effectively mitigated by applying a thermal interface material (TIM), which is also used in conjunction with other contact-based methods such as the guarded hot plate (GHP) method [19-21], the divided bar method [22], the 3*w* method with a reusable sensor [23], and the temperature wave analysis (TWA) method [24]. In

addition, thickness-dependent measurements can be employed to compensate for the influence of thermal contact resistance [10, 25, 26].

While the assumption of 1D heat flux greatly simplifies the equations used to calculate the thermal conductivity, it also imposes a principal limitation. The thermal conductivity and thickness of the layer must be strictly limited ($< 2\ \mathrm{Wm^{-1}K^{-1}}, < 600\ \mu\mathrm{m}$) to ensure that the heat flux across the layer remains strictly 1D. Otherwise, the influence of radial heat flux can lead to significant errors. This limitation means that a wide range of materials, such as alloys, ceramics, carbon-based materials, and composites with a relatively high thermal conductivity, cannot be characterized. Theoretically, the assumption of 1D heat flux is also fulfilled if the sample and the probe are equal in size and perfectly aligned. However, ensuring these conditions requires precise shaping of the samples and careful alignment during assembly, which can significantly increase both the time and effort of the measurement process. Even small mismatches can introduce substantial errors, as evidenced by a study [18] showing that a 7 % difference in radius between the probe and the sample can result in errors of up to 15 %.

To the best of our knowledge, no previous study has addressed non-1D heat flux to extend TPS measurement capabilities in the context of sample layers. Several investigations and model variants have been introduced but continue to adhere to the 1D heat flux assumption. Zhang et al. [27] systematically studied the influence of non-1D heat flux through a numerical simulation. An empirical function was proposed to compensate for non-1D heat flux, which was however only applicable to samples with a low thermal conductivity and limited thickness. By approximating the layer as a lumped thermal resistance, Emanuel et al. [28, 29] presented an analytical equation in integral form describe the temperature fields in an asymmetric configuration, i.e. different layers and substrates on both sides of the heat source. The proposed model was validated by comparing its results with those obtained from a reliable numerical model based on the Finite Element Method (FEM). To decouple the effect of thermal contact resistance at the probe-sample interface, Landry et. al [18] proposed a new measurement configuration with a slab piece between the thin film and the probe. A corresponding 1D model in the Laplace domain was developed and processed using numerical algorithms. Overall, the models developed in these studies are based on the 1D heat flux assumption, which reduces computational complexity but fails to adequately account for the effects of non-1D heat flux.

Accounting for multidimensional heat conduction within the multilayer structures facilitates a more comprehensive understanding of the heat conduction. Beck et al. [30-32] developed mathematical formulations to study the temperature field in multi-dimensional and multi-layer bodies. Gui et al. [33] used the transmission-line technique to study two-dimensional (2D) heat conduction in multilayer thin-film structures exposed to laser-induced surface-heating. Hui et al. [34, 35] developed

a 2D series solution to study the temperature distribution of a heat spreader on a semi-infinite heat sink. Milošević et al. [36] proposed a two-dimensional analytical model for measuring the thermal diffusivity of two-layer slabs. Rassy et al. [37, 38] proposed a three-dimensional semi-analytical model for a coating-substrate material in an unconventional laser flash measurement. This model enables the simultaneous identification of the direction-dependent thermal diffusivities of the coating. Cahill et al. [39] developed an iterative algorithm for calculating the frequency-domain temperature response of layered structures. This temperature is then converted into a transient temperature response to evaluate the accuracy of TPS-based measurements of thermal effusivity. Zheng et. al [40, 41] proposed several analytical models to extend the capability of TPS measurements for bulk samples with low (~ 0.03 $\mathrm{W\,m^{-1}\,K^{-1}}$) or relatively high thermal conductivity (> 30 $\mathrm{W\,m^{-1}\,K^{-1}}$). These studies have provided valuable insights into multi-dimensional temperature responses during thermal property measurements, but these existing methods cannot be directly applied to layer characterization using TPS techniques.

In this work, a novel semi-analytical model is developed for the TPS measurement of layer-substrate structures. The proposed model accounts for the non-1D heat flux within the layer, allowing accurate prediction of the temperature response for materials that have a higher thermal conductivity and larger thickness. A thorough sensitivity analysis was conducted to determine appropriate time windows for determination of the thermal conductivity. Additionally, an iterative algorithm was designed that allows to automatically process the measurement data.

2. Measurement and mathematical models

2.1 Measurement setup

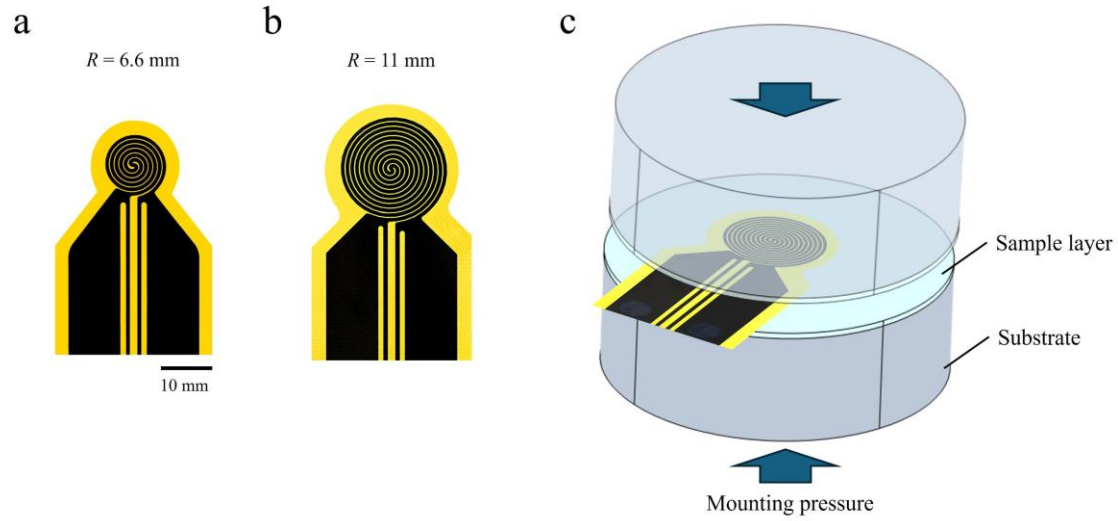

Fig. 1 (a-b) Probe profile featuring a nickel spiral foil sandwiched between polyimide sheets: (a) radius R = 6.6 mm, (b) radius R = 11 mm. (c) The vertically symmetrical configuration of a TPS measurement for layers. Two sample layers are positioned between the probe and the substrate.

The TPS measurements of the layers were conducted using a TPS 2500 S Thermal Constants Analyzer from Hot Disk AB, Sweden. Two types of probes with a radius of 6.6 mm (Fig. 1a) and 11 mm (Fig. 1b) are utilized in the measurements. The sensing element (black) is made of a nickel spiral foil with four extending leads, two thin and two wide ones. The nickel spiral foils have a width of 870 µm and a thickness of 10 µm, with an inner spacing of 130 µm. The polyimide insulation sheets (yellow) have a thickness of 20 µm and ensure electrically insulation and protection. The substrates were stainless steel blocks with a thermal conductivity of 13.5 W m^{-1} K^{-1} (See Table 1 for material properties). The sample layer consist of poly(methyl methacrylate) (PMMA), zirconium dioxide (ZrO_2), stainless steel, or Alumina (Al_2O_3, 96 wt%) with thicknesses ranging from 500 µm to 2000 µm. To reduce thermal contact resistance, a high-thermal-conductivity, easily spreadable TIM is applied at the interface between the components (NT-H2 from Noctua, Austria). In addition, a controlled mounting force was applied to the measurement assembly through a compression stand obtained from Hot Disk, Sweden.

Based on the illustrated measurement setup (Fig. 1c), both analytical and FEM models are developed to describe the heat transfer process. Analytical models are typically fast and capable of capturing the dominant heat transfer behavior, but they require more assumptions to approximate the actual experiment. The first common assumption in analytical models is that the probe can be regarded as an ideal circular boundary heat source, and the measurement setup can be assumed to be axisymmetric

[18, 28, 40]. Accordingly, the analytical models are formulated in two-dimensional (2D) cylindrical coordinates. The second common assumption is that the influence of thermal contact resistance is negligible, which is reasonable when TIMs are applied and the layer does not have an extremely high thermal conductivity.

By contrast, FEM models are generally more robust, capable of investigating complex geometries. Although measurement data can be fitted with FEM models to estimate material properties [42, 43], this approach is currently significantly more computationally demanding than the use of analytical solutions. As a result, FEM is primarily used to generate reference datasets to validate analytical models in this study.

In this study, four models are introduced and summarized as follows:

• **Layer 1D model**: An analytical model that assumes 1D heat flux across the layer (section 2.2.2).

• **Layer 2D model**: A semi-analytical model that accounts for 2D heat flux across the layer (section 2.2.3).

• **Simplified FEM model**: A FEM model based on the same physical configuration as the Layer 2D model, used to preliminarily assess the mathematical accuracy of the analytical models (section 2.3.1).

• **Detailed FEM model**: A high-fidelity FEM model that closely represents the measurement setup, used to generate simulated measurement data for comprehensive evaluation of the analytical models (section 2.3.2).

2.2 Analytical models

2.2.1 Physical configuration and its solution

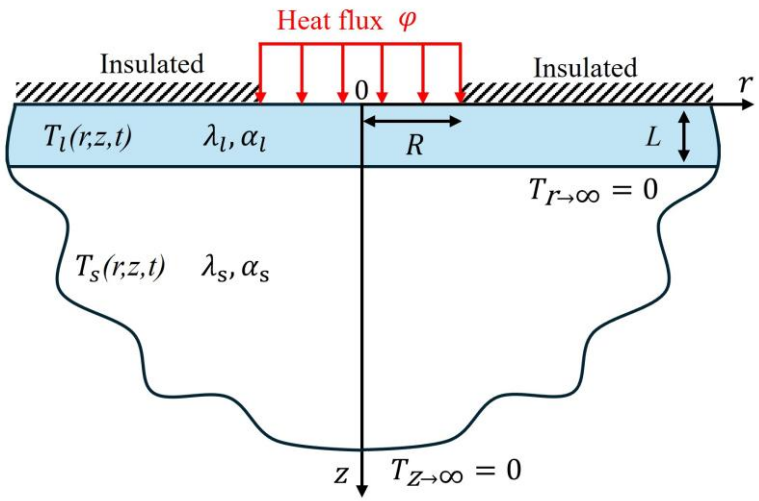

Fig. 2 Schematic of a semi-infinite substrate with a layer on top, subjected to uniform surface heating.

The simplified physical configuration for analytical models is represented in cylindrical coordinates (Fig. 2). A semi-infinite substrate is in perfect thermal contact with a radially infinite overlying layer of thickness L. This layer-substrate assembly, initially at zero reference temperature, is suddenly subjected to heating across a circular area of radius R and a constant and uniform density φ. The governing equation of heat diffusion in the solids is [44]:

$$\frac{\partial^2 T_i}{\partial r^2} + \frac{\partial T_i}{r\,\partial r} + \frac{\partial^2 T_i}{\partial z^2} = {\alpha_i}^{-1}\frac{\partial T_i}{\partial t} \tag{8}$$

where T represents the temperature response of the solids to the heating, α denotes thermal diffusivity, and $i = l$ or s corresponds to the layer and the substrate, respectively.

The boundary conditions are given by:

$$-\lambda_l \frac{\partial T_l}{\partial z}\Big|_{z=0} = \begin{cases} \varphi & (r \le R) \\ 0 & (r > R) \end{cases} \tag{9}$$

$$T_i(r, z, 0) = 0 \tag{10}$$

$$T_l(r \to \infty) = 0 \tag{11}$$

$$T_s(z \to \infty) = 0 \tag{12}$$

where λ represents the thermal conductivity. At the interface between the layer and the substrate where $z = L$ the following conditions apply:

$$T_l(z = L) = T_s(z = L) \tag{13}$$

$$-\lambda_l \frac{\partial T_l}{\partial z}\Big|_{z=L} = -\lambda_s \frac{\partial T_s}{\partial z}\Big|_{z=L} \tag{14}$$

The following Laplace and infinite Hankel transforms can be sequentially applied to Eq. 1-2, and 5-7:

$$\overline{T}_i = \mathcal{L}\{T_i\} = \int_0^\infty T_i e^{-pt}\,\mathrm{d}t \tag{15}$$

$$\widetilde{\overline{T_i}} = \int_0^\infty r\,J_0(\beta r)\overline{T_i}\,\mathrm{d}r \tag{16}$$

where $\mathcal{L}$ represents the Laplace operator, p is the Laplace variable, J_0 denotes the Bessel function of the first kind of order zero, and β is the Hankel variable.

The transformed version of the governing equation and boundary conditions become:

$$\frac{d^2\widetilde{\overline{T_i}}}{\mathrm{d}z^2} - [\beta^2 + p_i/\alpha]\,\widetilde{\overline{T_i}} = 0 \tag{17}$$

$$\widetilde{\overline{\varphi}} = \varphi\,\frac{aJ_1(\beta R)}{p\beta} \tag{18}$$

$$-\lambda_l \frac{d\widetilde{\overline{T_l}}}{dz}\bigg|_{z=0} = \widetilde{\overline{\varphi}} \tag{19}$$

$$\widetilde{\overline{T_s}}\Big|_{z\to\infty} = 0 \tag{20}$$

where J_1 denotes the Bessel function of the first kind of the first order.

At the interface where $z = L$, the transformed equations are:

$$\widetilde{\overline{T_l}}(z = L) = \widetilde{\overline{T_s}}(z = L) \tag{21}$$

$$-\lambda_l \frac{d\widetilde{\overline{T_l}}}{dz}\bigg|_{z=L} = -\lambda_s \frac{d\widetilde{\overline{T_s}}}{dz}\bigg|_{z=L} \tag{22}$$

Combining Eq. 17 and 19 – 22, the following expression can be derived for the temperature at the heating surface (z = 0),

$$\widetilde{\overline{T_l}}(r, 0, p) = \frac{\widetilde{\overline{\varphi}}}{\lambda_l q_l} \cdot \frac{\lambda_s q_s \tanh(Lq_l) + \lambda_l q_l}{\lambda_l q_l \tanh(Lq_l) + \lambda_s q_s} \tag{23}$$

where $q_i = \sqrt{\beta^2 + p/\alpha_i}$.

The following inverse Hankel and Laplace transforms can be applied to obtain the temperature in the Laplace domain:

$$\overline{T} = \int_0^\infty \beta J_0(\beta r) \widetilde{\overline{T}}\, d\beta \tag{24}$$

With this inverse transformation, Eq. 23 can be written as:

$$\overline{T_l}(r, 0, p) = \frac{\varphi R}{\lambda_l} \int_0^\infty \frac{J_0(\beta r) J_1(\beta R)}{q_l p} \cdot \frac{\lambda_s q_s \tanh(Lq_l) + \lambda_l q_l}{\lambda_l q_l \tanh(Lq_l) + \lambda_s q_s}\, d\beta \tag{25}$$

By integrating this expression over r from 0 to R, the expression for the area-average temperature of the heating area can be obtained:

$$\overline{\Delta T_{\text{avg}}} = \frac{2\varphi}{\lambda_l} \int_0^\infty \frac{J_1^2(\beta R)}{q_l p \beta} \cdot \frac{\lambda_s q_s \tanh(Lq_l) + \lambda_l q_l}{\lambda_l q_l \tanh(Lq_l) + \lambda_s q_s}\, d\beta \tag{26}$$

The average temperature of the heating area can be written as:

$$\Delta T_{\text{avg}} = \frac{2\varphi}{\lambda_l} \int_0^\infty \frac{J_1^2(\beta R)}{\beta} \mathcal{L}^{-1}\left(\frac{1}{q_l p} \cdot \frac{\lambda_s q_s \tanh(Lq_l) + \lambda_l q_l}{\lambda_l q_l \tanh(Lq_l) + \lambda_s q_s}\right) d\beta \tag{27}$$

where $\mathcal{L}^{-1}$ denotes the inverse Laplace operator.

Several numerical algorithms are available that allow to predict ΔT_{avg} directly based on Eq. 27. For example, the Talbot method can be employed to obtain the inverse Laplace transform and sequentially the composite trapezoidal rule can be used to calculate the integral with respect to β. However, this

method is relatively time-consuming, hampering the application of Eq. 27 in data analysis. By introducing several reasonable assumptions, two simplified models (the 1D Layer Model and the 2D Layer Model) can be derived, each offering significantly reduced computation time. The details of these models are described below.

2.2.2 Layer 1D Model

When the layer has both a considerable small thickness ($L \to 0$) and a small thermal conductivity compared with the substrate ($\lambda_l \ll \lambda_s$), the heat flux across the layer can be regarded as 1D. In this case, $\tanh(Lq_l) \to Lq_\mathrm{l}$ and $\lambda_l \tanh(Lq_l) \to 0$, which simplifies Eq. 27 to:

$$\Delta T_{\mathrm{avg,1D}} \approx \frac{\varphi L}{\lambda_l} + \frac{2\varphi}{\lambda_s}\int_0^\infty \frac{J_1^2(\beta R)}{\beta}\mathcal{L}^{-1}\left(\frac{1}{q_s p}\right) d\beta \tag{28}$$

The first term on the right side of Eq. 28 corresponds to an additional temperature increase caused by the layer, while the second term is the temperature increase of the bottom surface of the substrate in contact with the layer (Eq. 5). Therefore, Eq. 28 can be written in explicit analytical form:

$$\Delta T_{\mathrm{avg,1D}} \approx \frac{\varphi L}{\lambda_l} + \frac{\varphi R}{\lambda_s}\left(\frac{8}{3\pi} + 2\sqrt{\frac{t^*}{\pi}} - 2\sqrt{\frac{t^*}{\pi}}e^{-\frac{1}{2t^*}}\left[\left(1+\frac{2}{3t^*}\right)I_0\left(\frac{1}{2t^*}\right) + \left(\frac{1}{3}+\frac{2}{3t^*}\right)I_1\left(\frac{1}{2t^*}\right)\right]\right) \tag{29}$$

2.2.3 Layer 2D Model

At a later stage of the measurement, the heat flux across the layer is assumed to achieve a quasi-steady state, where the contribution of α_l to ΔT_{avg} becomes negligible. During this stage, $\alpha_l = \alpha_s$ can be applied to simplify the term inside the inverse Laplace transform (K) in Eq. 25:

$$K = \frac{1}{pq_l}\cdot\frac{q_s\tanh(Lq_l)+c\cdot q_l}{c\cdot q_l\tanh(Lq_l)+q_s} \approx \frac{1}{pq_l}\cdot\frac{c(w^2+3)+3w}{(w^2+3)+3cw} \tag{30}$$

where $w = q_s L$ and $c = \lambda_l/\lambda_s$. Detailed derivation is available in Section S1 of the Supporting Information.

Upon taking the inverse Laplace transform of simplified K, the following equation can be written to predict ΔT_{avg}:

$$\Delta T_{\mathrm{avg,2D}} = \frac{2\varphi}{\lambda_l}\int_0^\infty \frac{J_1^2(\beta R)}{\beta}\frac{(A+D)}{F}\, d\beta \tag{31}$$

where

$$A = c(\beta^4 L^4 - 3\beta^2 L^2 + 9)\cdot \mathrm{erf}\left(\beta\sqrt{\alpha_s t}\right)$$

$$D = 3\beta L(1 - c^2)(3 + \beta^2 L^2)$$

$$F = 9\beta L + 3\beta^3 L^3(2 - 3c^2) + \beta^5 L^5$$

2.3 FEM models

In this study, two FEM models are developed. The first, a simplified FEM model, is used to generate reference data for validating the Layer 2D model and to highlight its improvement. The second one, referred to as the detailed FEM model, is employed to generate simulated temperature responses and investigate systematic measurement errors in the latter part of this paper.

These FEM models were developed using COMSOL Multiphysics (version 6.1) with the *Heat Transfer in Solids Module* and *Heat Transfer in Shell Module*. The simulations were solved using the Parallel Direct Sparse Solver (PARDISO). Mesh number and solver relative tolerance were systematically evaluated to ensure numerical stability, with representative results presented in Fig. S2.

2.3.1 Simplified FEM model

The geometry of the simplified FEM model (Fig. 3a) was developed according to the physical configuration in Fig. 2. The substrate is a stainless steel cylinder with a radius of 50 mm and a thickness of 38 mm (Fig. 3b), which is sufficiently large to be considered a semi-infinite domain during the measurement. The sample layer is PMMA, ZrO_2, stainless steel or Al_2O_3 with thicknesses ranging from 500 μm to 2000 μm. On the top of the layer, there is a boundary heat source with a radius of 6 mm or 11 mm that provides uniform heat flux. Note that only half of the experimental setup was simulated owing to vertical symmetry in the heat conduction domain (See Table 1 for material properties used in the FEM simulations). Thermal contact resistance is not considered in this model.

Table 1. Material properties. [a] Measured by TPS measurements on bulk samples. The measurement accuracies are ±2 % for thermal conductivity and ±7 % for thermal diffusivity [6]. [b] Calculated from mass and volume. [c] Measured by the Transient Plane Source Scanning method [43, 45], with a measurement accuracy of approximately 5 %. [d] Values from reference [46]. [e] Values from reference [47].

Material	Thermal conductivity ($W\ m^{-1}\ K^{-1}$)	Thermal diffusivity (mm^2/s)	Density (kg/m^3)	Specific heat ($J\ kg^{-1}\ K^{-1}$)
Stainless steel	13.5[a]	3.60[a]	8150[b]	460[a]
PMMA	0.21[a]	0.12[a]	1180[b]	1464[c]
Glass	1.34[a]	0.81[a]	2172[b]	766[c]
ZrO_2	3.15[a]	1.23[a]	6220[b]	412[c]
Al_2O_3	22.3[a]	7.26[a]	3775[b]	815[c]
Polyimide	0.12[d]	-	1090[d]	1420[d]
TIM	1.0 / 3.0[e]	-	2800[e]	-

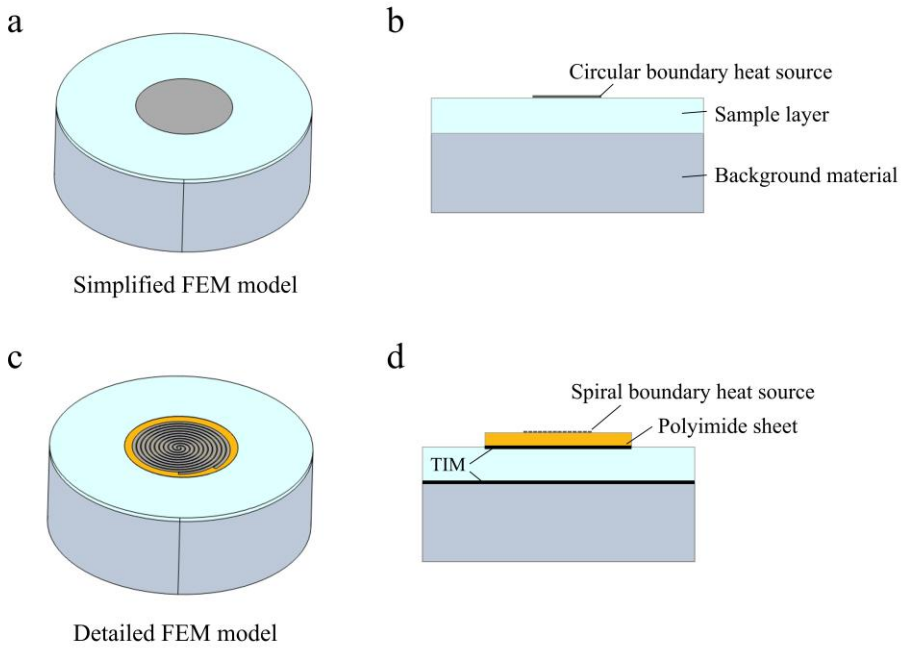

Fig. 3 Schematic of the (a) the Simplified FEM model and (c) the Detailed FEM model, along with their corresponding cross-sectional views in (b, d). Selected components in (b, d) are scaled to account for the wide range of dimensions, ensuring that all elements remain discernible.

2.3.2 Detailed FEM model

The detailed FEM model generates simulated measurement data to comprehensively evaluate the application of analytical models in data analysis. This model includes more details of the measurement setup compared with the simplified model. Specifically, a boundary heat source with a double spiral pattern is utilized to represent the actual heating element (Fig. 3c). The influence of the four leads and heat capacity of the spiral is assumed to be negligible, which is reasonable provided that the samples do not have an extremely low thermal conductivity [40]. In addition, TIM are introduced to align with the experimental conditions.

3. Model verification and parameter estimation

3.1 Model comparison

To evaluate the accuracy of the analytical models, the values of T_{avg} calculated from the Layer 1D model and Layer 2D model are compared with those from a reference model — the Simplified FEM model (Fig. 4).

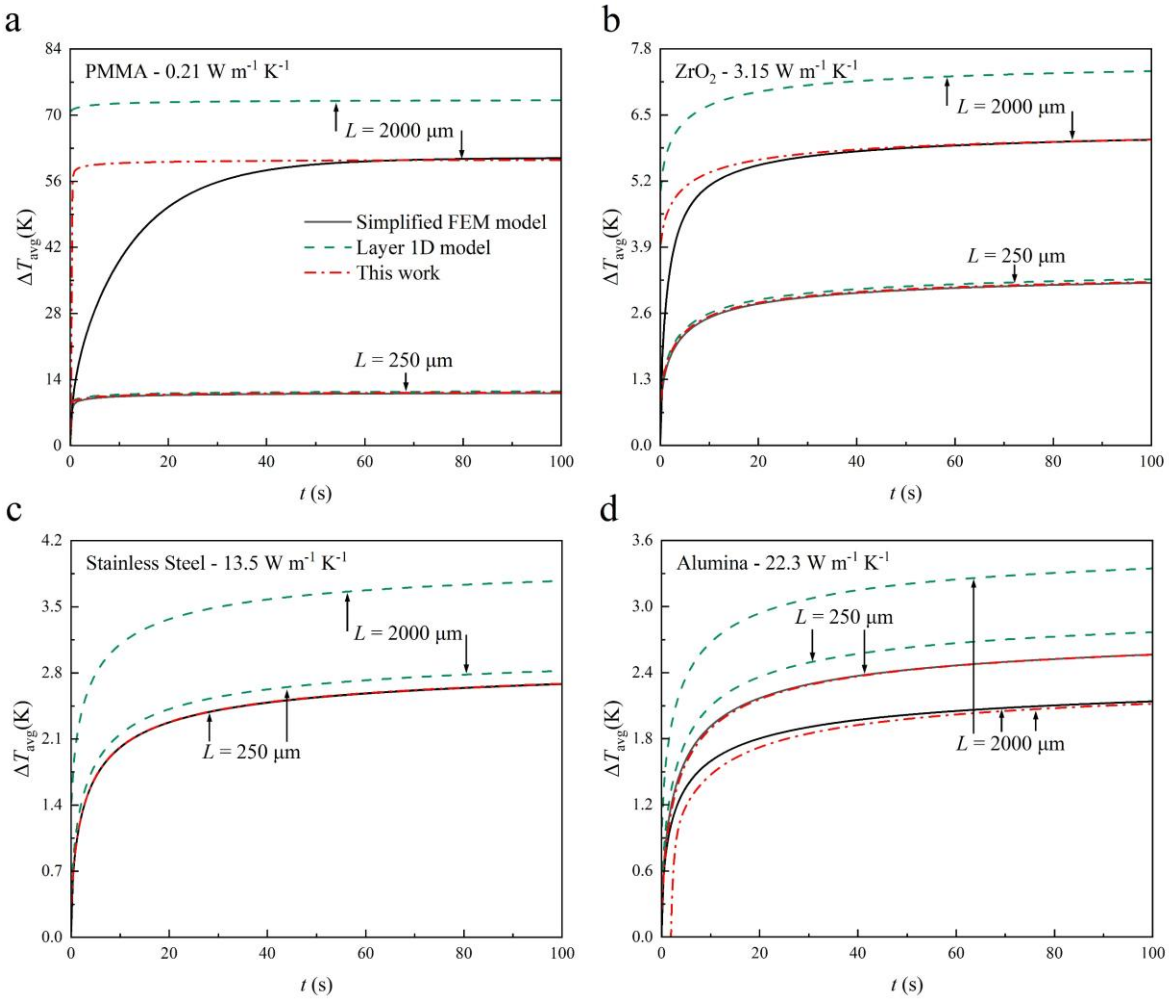

Fig. 4 Comparison of T_{avg} obtained using different models (Layer 1D model: green dashed line, Layer 2D model: red dash-dot line, Simplified FEM model: black solid line) for a heating area radius of 6 mm: (a) PMMA layer, (b) ZrO_2 layer, (c) stainless steel layer, and (d) alumina layer. The substrate in all cases is stainless steel, and the heating power is 1 W.

The conventional Layer 1D model agrees well with the FEM results in some cases — specifically, when the layer has both a low thermal conductivity and a small thickness (Fig. 4 a, bottom group). However, differences arise with higher thermal conductivity or layer thickness (Fig. 4 a-d). By contrast, the Layer 2D model agrees well with the FEM model in the later stage, across a broad range of thermal conductivities and thicknesses. Notably, the good agreement is maintained when the thermal conductivity of the layer exceeds that of the substrate (Fig. 4 d).

In general, there is a time delay before the Layer 2D model achieves close agreement with the FEM results. Theoretically, this delay results from the simplification of heat diffusion within the layer in the equation, namely assuming $\alpha_l = \alpha_s$. Therefore, this delay is linked to both the thickness and thermal diffusivity of the layer. For instance, in the case of PMMA, the delay increases from approximately 2 s to 60 s as the thickness increases from 250 µm to 2000 µm (Fig. 4 a). In the case of ZrO_2, which has a higher thermal diffusivity than PMMA, the delay becomes slightly smaller (Fig. 4 b). Estimating this delay is essential for applying this model and will be detailed in the following sections.

When layer and substrate share the same properties (Fig. 4 c, stainless steel layer on a stainless steel substrate), all scenarios with different thicknesses converge to the case of a semi-infinite substrate heated by a circular heat source. Therefore, the T_{avg} values remain identical across different layer thicknesses in both the simplified FEM model and Layer 2D model. The Layer 2D model closely aligns with the FEM throughout the whole period without any delay, as the assumption of $\alpha_l = \alpha_s$ is always fulfilled in these cases.

When the heating area has a larger radius (Fig. 5 a-d), the difference between the Layer 1D model and the FEM results is slightly reduced compared with the previous cases with a small heating area. Despite this reduction, the difference remains significant in most cases. The reduction is attributed to a higher ratio between the probe radius and the layer thickness, bringing the situation closer to the 1D heat flux assumption. However, even an 80 % increase in heating radius (from 6 to 11 mm) yields only marginal improvement, indicating that enlarging the heating area is not an effective strategy for improving the performance of the Layer 1D model. On the other hand, the Layer 2D model still exhibits significantly better agreement with the FEM results. However, a slightly longer time is required for the Layer 2D model to achieve a good level of agreement with FEM results. For example, approximately 70 s are needed in the case of a 2000 µm thick ZrO_2 layer (Fig. 5b), compared with 40 s when the heating area is smaller (Fig. 4b).

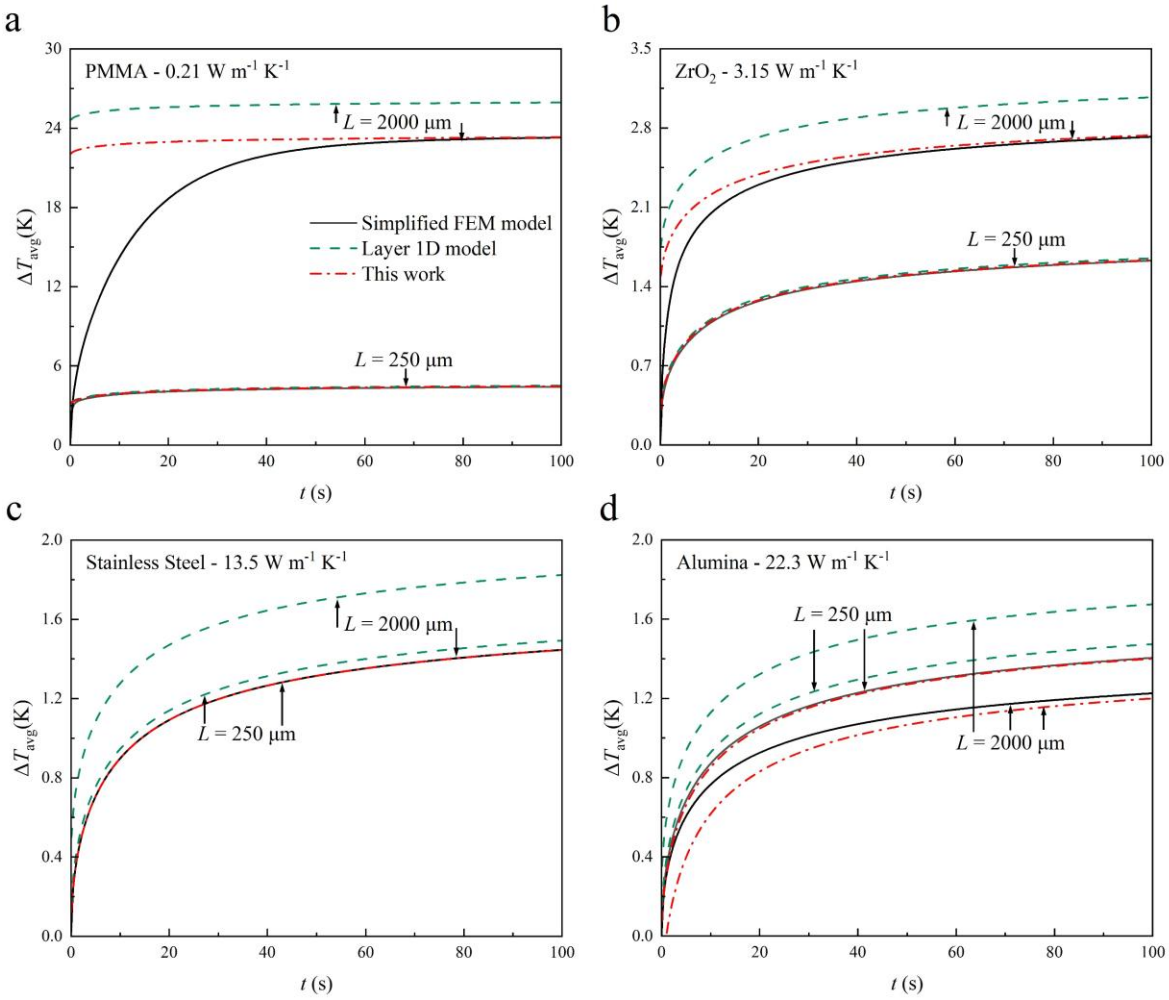

Fig. 5 Comparison of T_{avg} obtained using different models (Layer 1D model: green dashed line, Layer 2D model: red dash-dot line, Simplified FEM model: black solid line) for a heating area radius of 11 mm: (a) PMMA layer, (b) ZrO_2 layer, (c) stainless steel layer, and (d) alumina layer. The substrate in all cases is stainless steel, and the heating power is 1 W.

3.2 Sensitivity analysis

Based on the simplified FEM model, a sensitivity analysis is conducted to gain deeper insight into the interactions among parameters in the measurement, thereby guiding the design of the measurement scheme [41, 48].

The sensitivity of T_{avg} to a specific parameter x is defined as:

$$S_x(t) = \frac{\partial \ln\left(T_{\mathrm{avg}}(t)\right)}{\partial \ln(x)} \approx \frac{x\delta\left(T_{\mathrm{avg}}(t)\right)}{T_{\mathrm{avg}}(t)\,\delta(x)} \tag{32}$$

where δ presents a small perturbation. A large magnitude of $S_x(t)$ indicates that parameter x has a large influence on $T_{\mathrm{avg}}(t)$. A positive $S_x(t)$ implies that $T_{\mathrm{avg}}(t)$ increases as parameter x increases, and vice versa. Here, the data used for calculating $S_x(t)$ were obtained by a parameter sweep study in the FEM model with $\delta x = 0.02x$.

In all cases, the sensitivity to the layer thermal diffusivity (S_{α_l}) is initially high but quickly decreases to a minimal positive value over time (Fig. 6 a-f). The small value of S_{α_l} reflects the validity of the simplification of heat diffusion within the layer in the Layer 2D model, assuming $\alpha_l = \alpha_s$. For thinner layers, the magnitude of S_{α_l} decays more rapidly to a small value, explaining the shorter time delay they required to achieve good agreement with the FEM results (Fig. 6 a–f). Additionally, the increase in layer thickness lowers S_{α_s} in all cases. When the heating area is larger (Fig. 6 d-f), S_{α_l} is slightly higher and requires a longer time to decrease to a low value. This observation is in line with the results shown in Fig. 5, which shows a longer time is needed to achieve good agreement with the FEM model when a larger probe is used.

On the other hand, the sensitivity to layer thermal conductivity (S_{λ_l}) and substrate thermal conductivity (S_{λ_s}) are negative, and their magnitude increase with time (Fig. 6 a-f). In the case of PMMA (Fig. 6 a, d), the magnitude of S_{λ_l} is consistently greater than that of S_{λ_s} owing to its much lower thermal conductivity compared with the substrate. Increasing the layer thickness further increases the magnitude of S_{λ_l} and lowers that of S_{λ_s} at the same time. When both the layer and substrate are stainless steel (Fig. 6 c, f), S_{λ_l} has a higher magnitude in the very beginning (within 5 s) since the layer is in direct contact with the heating area. However, it is quickly surpassed by S_{λ_s} as time progresses. This case illustrates how the position influences the $S_x(t)$ when the layer and the substrate have the same properties. In general, the magnitude of S_{λ_l} is high, suggesting that λ_l can be reliably estimated.

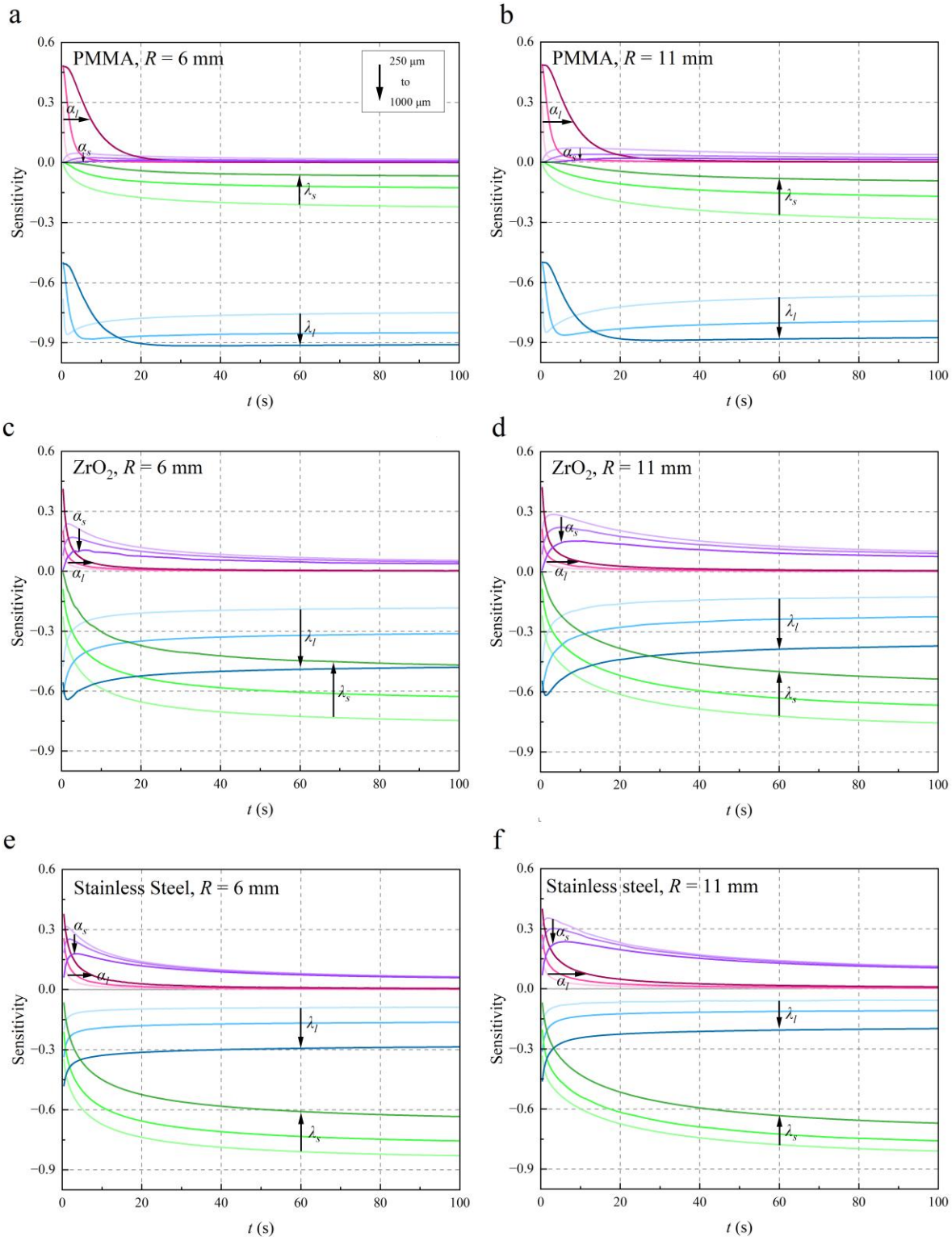

Fig. 6 Exemplary sensitivity of T_{avg} to different material properties at different layer thicknesses: (a-b) PMMA layer, (b-c) ZrO_2 layer, (e-f) stainless steel layer. The radius of heat source in (a), (c), and (e) is 6 mm, and 11 mm in (b), (d), and (f). In all cases, the substrate is stainless steel. The black arrow indicates the direction of increasing layer thickness.

3.3 Estimation of time window

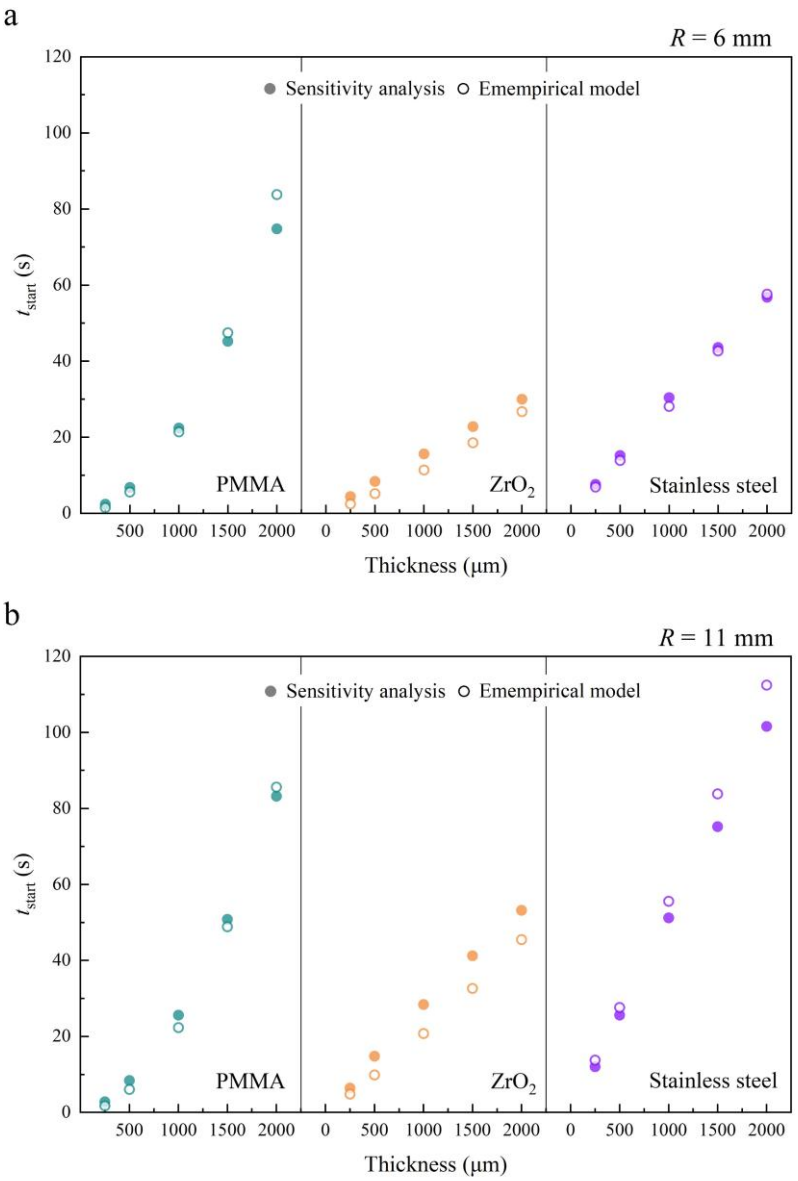

Fig. 7 Comparison of estimated t_{start} between sensitivity analysis (solid symbols) and the empirical model (empty symbols).

To further utilize the Layer 2D model in analyzing the measurement data, it is essential to identify the appropriate time window $[t_{\text{start}}, t_{\text{end}}]$ during which this model can accurately describe the measurement results. Theoretically, a suitable t_{start} can be the time when the influence of the layer thermal diffusivity on ΔT_{avg} is very small, namely a minimal S_{α_l}. This time is denoted as t_{α_l} and can be extracted from sensitivity curves. Here, a value of t_{α_l} is assigned to the earliest time at which S_{α_l} falls below a threshold of 0.02 (Fig. 7 a, b, solid symbols). To predict the extracted values of t_{α_l} and use it in the analysis of measurement data, an empirical equation is written with respect to the thickness and the thermal diffusivity of the layer:

$$\hat{t}_{\alpha_l} = \mathrm{A}\frac{L^2}{\alpha_l} + \mathrm{B}\frac{\alpha_l r^2}{\alpha_s}\left(\frac{L}{R}\right)^C \tag{33}$$

where A, B and C are constant to be determined for different heating radii. The first term is designed to represent the time that heat waves need to go through the layer in the vertical direction, while the second term is intended to be associated with the heat wave propagation in the radial direction. Constants A, B, and C are determined by an optimization process that minimizes the maximum group error (MGE) defined as:

$$\mathrm{MGE} = \max_G \left(\frac{1}{n_G}\sum_{j\in G}\left(\hat{t}_{\alpha_l,j} - t_{\alpha_l,j}\right)^2\right) \tag{34}$$

where G represents a group of t_{α_l} for different thicknesses, classified by material type, n_G is the size of the group G, j indexes t_{α_l} within each group.

For each heating radius, A, B and C were determined through optimization (Table 2). The values of $\hat{t}_{\alpha_l}$ are in good agreement with t_{α_l} (Fig. 7 a, b), showing the generalizability of the empirical equation.

Table 2. Values of coefficients A, B and C used for predicting t_{α_l} with different heating radii.

Heating radius	A	B	C
6 mm	2.186	4.325	1.056
11 mm	2.483	5.889	1.140

3.4 Procedure of parameter estimation

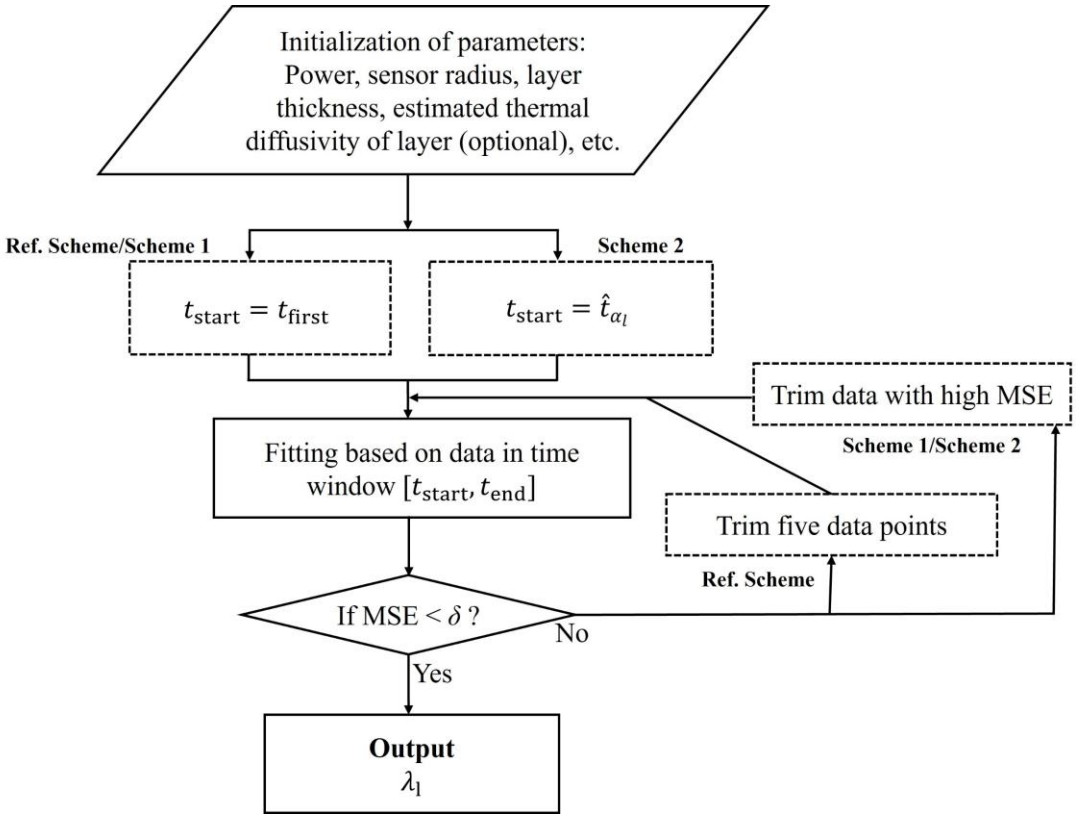

Fig. 8 Flow diagram of the iterative process used to determine the thermal conductivity of the layer.

In this section, several procedures are developed to apply the Layer-2D model for determining the thermal conductivity of layers from input measurement data (Fig. 8). Overall, these procedures start with the initialization of parameters including heating power, probe radius, layer thickness, thermal properties of the substrate, etc. Afterwards, a fitting process is carried out over a specify time window $[t_{\text{start}}, t_{\text{end}}]$, using the Mean Squared Error (MSE) as the objective function:

$$\text{MSE} = \frac{1}{n}\sum_{t=t_{\text{start}}}^{t=t_{\text{end}}}\left(T_{\text{avg},t}(\lambda_l) - \hat{T}_{\text{avg},t}\right)^2 \tag{35}$$

where n is the number of data points in the time window, and $\hat{T}_{\text{avg},t}$ is the temperature response of the probe in the measurement. $T_{\text{avg},t}(\lambda_l)$ is the temperature response of the probe calculated using the Layer 2D model, defined as:

$$\Delta T_{\text{avg,2D}} = \Delta T_{\text{pi}} + \frac{2\varphi}{\lambda_l}\int_0^{\infty}\frac{J_1^2(\beta R)}{\beta}\frac{(A+D)}{F}\,d\beta \tag{34}$$

where ΔT_{pi} is the additional temperature increase caused by polyimide sheets covering the probe. Owing to low thermal conductivity and small thickness of the polyimide sheets, ΔT_{pi} can be approximated as $\frac{\varphi L_{\text{pi}}}{\lambda_{\text{pi}}}$, where L_{pi} and λ_{pi} denote the thickness and the thermal conductivity of the

polyimide sheets, respectively. The value of λ_{pi}, λ_s, and α_s used in Eq. 34 can be determined in a TPS measurement performed with the probe directly sandwiched between two substrates.

Three schemes are proposed to select and adjust the time window in the fitting process: a reference scheme, Scheme 1, and Scheme 2. The reference scheme starts with all data points recorded in the measurement $[t_{\mathrm{first}}, t_{\mathrm{last}}]$ and iteratively adjusts the time window by trimming the first five data points at each step. Here, t_{first} and t_{last} represent the first and the last data point of the recorded data, respectively. The reference scheme is intended to provide baseline information about the relationship between time window, determined thermal conductivity, and MSE.

Similar to the reference scheme, Scheme 1 starts with time window $[t_{\mathrm{first}}, t_{\mathrm{last}}]$ but subsequently trims the segment with large square error, $(T_{\mathrm{avg},t}(\lambda_l) - \hat{T}_{\mathrm{avg},t})^2$. This trimming tactic aims to speed up the iterative process. Scheme 2, in turn, begins with the time window $[\hat{t}_{\alpha_l}, t_{\mathrm{last}}]$ and likewise trims it by excluding the segment with the largest squared error. Here, $\hat{t}_{\alpha_l}$ is estimated from an empirical equation using an approximate value of the layer thermal diffusivity (Eq. 33). Overall, Scheme 1 is more general and can be utilized for random samples with unknown properties, while Scheme 2 can be employed when a rough value of thermal diffusivity is available, thereby further accelerating the iteration process.

Once the MSE falls below a predefined threshold (δ), the value of λ_l becomes the output value. Otherwise, the current time window is adjusted and used for another round of data fitting. After the fitting process, the relative error (ε) is used to evaluate the accuracy of the output thermal conductivity of the layer:

$$\varepsilon = \left(1 - \frac{\lambda_{l,\mathrm{est}}}{\lambda_{l,\mathrm{ref}}}\right) \cdot 100\ \% \tag{36}$$

where $\lambda_{l,\mathrm{est}}$ represents the thermal conductivity estimated via the fitting process, while $\lambda_{l,\mathrm{ref}}$ represent the reference thermal conductivity of the material (Table 1). A positive value of ε corresponds to an overestimation of thermal conductivity, and vice versa.

4. Model application

4.1 Measurement results

The fitting results from the reference scheme are first analyzed. As the iteration progresses (Fig. 9 a, c), MSE decreases and the determined thermal conductivity tends toward a specific value. In particular, the variation of the determined thermal conductivity remains within 1 % once MSE falls below approximately 10^{-4} in cases of both glass and ZrO_2. Although trimming the time window by a small, fixed number of data points continuously lowers the MSE and eventually yields a precise thermal conductivity, this method requires more iteration steps and thus a longer execution time. Using a larger fixed step, e.g., 10 s or 20 s, can shorten the iterations but may cause overshooting and loss of accuracy.

In contrast to the reference scheme, Scheme 1 requires considerably fewer iteration steps to achieve the same MSE (orange symbols, Fig. 9 a, c). In case of glass and ZrO_2, only around five steps are required to achieve a minimal MSE of 10^{-4}, demonstrating a threefold improvement in efficiency compared with the reference scheme. When this tactic of adjusting the time window is combined with $\hat{t}_{\mathrm{start}}$ estimated from the empirical equation (Scheme 2, green symbols, Fig. 9 a, c), only around three steps are required for both glass and ZrO_2, showing a further 30 % improvement in efficiency relative to Scheme 1.

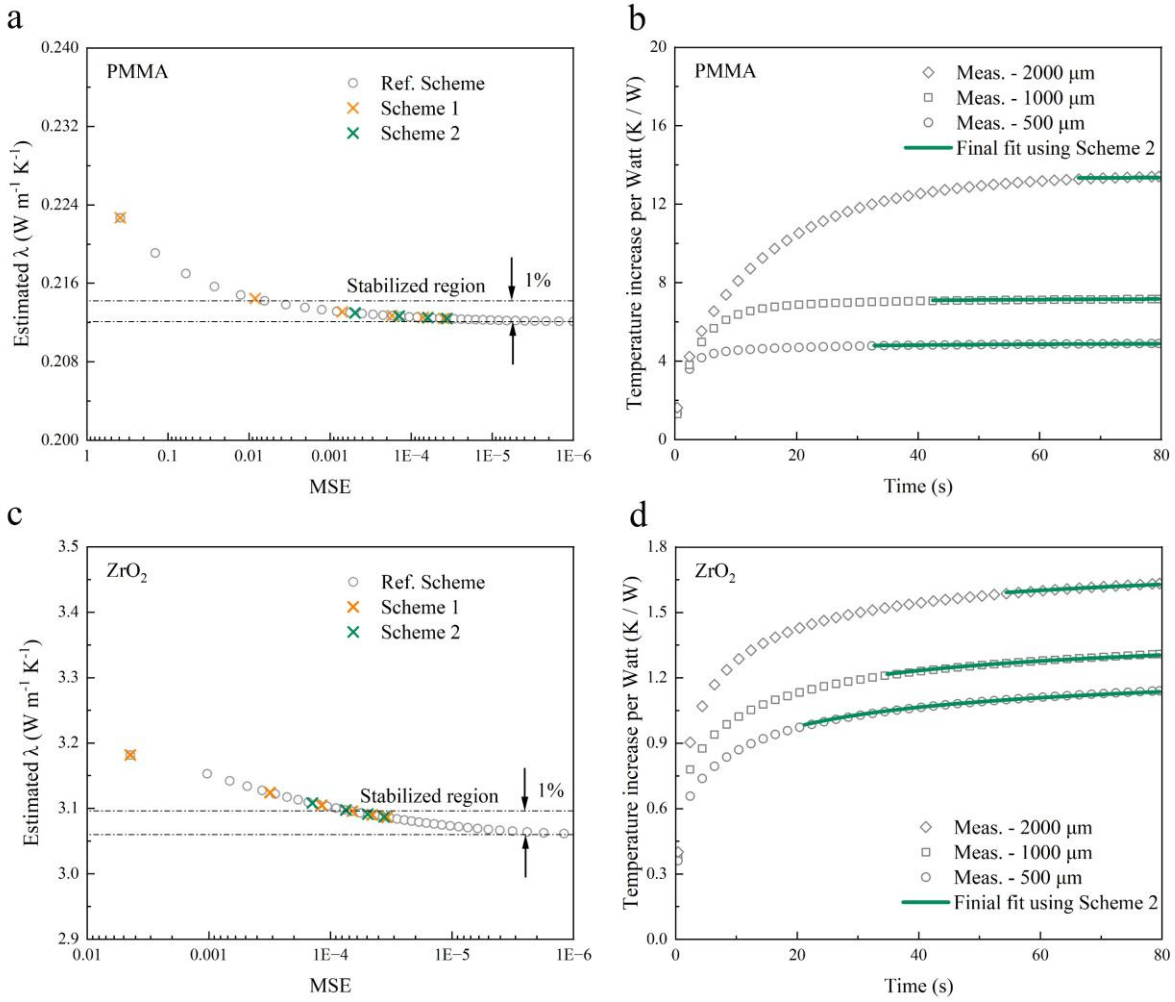

Figure 9. Exemplary results from the fitting process. (a, c) Evolution of thermal conductivity values as a function of MSE using the reference scheme (grey), Scheme 1 (orange) and Scheme 2 (green), for a 500 µm-thick (a) glass and (c) ZrO_2 layer. (b, d) comparison between experimental data and the fitted data for (b) a glass layer and (d) a ZrO_2 layer.

Owing to its superior calculational efficiency, Scheme 2 is utilized to process all the measurement data to determine the thermal conductivity of the layers. The resulting fits show good agreement with the experimental data within the fitting window (Fig. 9 b, d). Moreover, the determined thermal conductivity using the Layer 2D model agrees well with the reference values in most cases (except for thinnest stainless steel and alumina), with error ε less than 7 % (Table 3), thereby validating the fitting procedure. The magnitude of ε increases with higher layer thermal conductivity or reduced thickness, most likely dominated by the influence of thermal contact resistance. For comparison, the thermal conductivity determined by using the Layer 1D model is summarized in Table S1. Only a few cases (PMMA and glass layers thinner than 1000 µm) exhibit an acceptable ε of less than 14 %, highlighting the limitation of the Layer 1D model.

Table 3. The determined thermal conductivity of layers obtained from experimental data using the Layer 2D model. Each value represents the average of three repeated measurements, with the associated error given as the maximum difference among them.

	Layer thickness (µm)	Thermal conductivity ($Wm^{-1}K^{-1}$)				
		PMMA	Glass	ZrO_2	Stainless steel	Alumina
Probe A (R = 6.6 mm)	500	0.198 ± 0.001	1.35 ± 0.01	3.17 ± 0.18	13.8 ± 0.4	14.7 ± 0.1
	1000	0.196 ± 0.001	1.37 ± 0.02	3.15 ± 0.03	13.4 ± 0.3	22.4 ± 0.8
	2000	0.207 ± 0.001	1.33 ± 0.01	3.14 ± 0.01	13.9 ± 0.4	23.8 ± 0.2
Probe B (R = 11 mm)	500	0.206 ± 0.001	1.38 ± 0.03	3.11 ± 0.06	12.7 ± 0.6	18.4 ± 0.7
	1000	0.209 ± 0.011	1.42 ± 0.01	3.13 ± 0.06	13.9 ± 0.1	19.8 ± 0.6
	2000	0.212 ± 0.002	1.39 ± 0.06	3.22 ± 0.02	13.4 ± 0.3	22.6 ± 1.0

To reveal the distribution of ε with respect to layer thickness and thermal conductivity, contour maps are plotted based on the experimental data in Table S1 (Layer 1D model) and Table 3 (Layer 2D model). In the cases of a 6.6 mm probe (Fig. 10 a), the Layer 1D model yields low ε (< 10 %) for low thermal conductivity and thin layers, since the assumption of 1D heat flux across the layer remains valid in these cases. However, ε increases dramatically with increasing thickness or thermal conductivity, which we attribute to the violation of the 1D heat flux assumption. It should be noted that the effect of this violation overshadows that of thermal contact resistance, ultimately leading to an overestimation of the layer thermal conductivity. In the case of a 11 mm probe (Fig. 10 b), the region with low ε (< 10 %) is larger than the previous case, likely due to larger probe-to-layer thickness ratio, which as a result of the heat flux across the layer more closely resembles the assumed 1D scenario. The green frame in Fig. 10 b indicates the original applicability of TPS method for characterizing layers. Note that the data for layers thinner than 500 µm were not experimentally measured but derived by extrapolation from the measurement data.

When utilizing the Layer 2D model, the region with low ε covers the vast majority of the plot (Fig. 10 c,d) in cases of both a 6.6 mm and a 11 mm probe. We attribute this significant improvement to the consideration of two-dimensional heat flux in the Layer 2D model. For layers thicker than approximately 750 µm or with a thermal conductivity lower than about 8 W m^{-1} K^{-1}, ε is lower than 5 %. Only the upper left corner, corresponding to thermally thin layers, shows a magnitude of ε greater than 10 %, which we ascribe to the influence of thermal contact resistance.

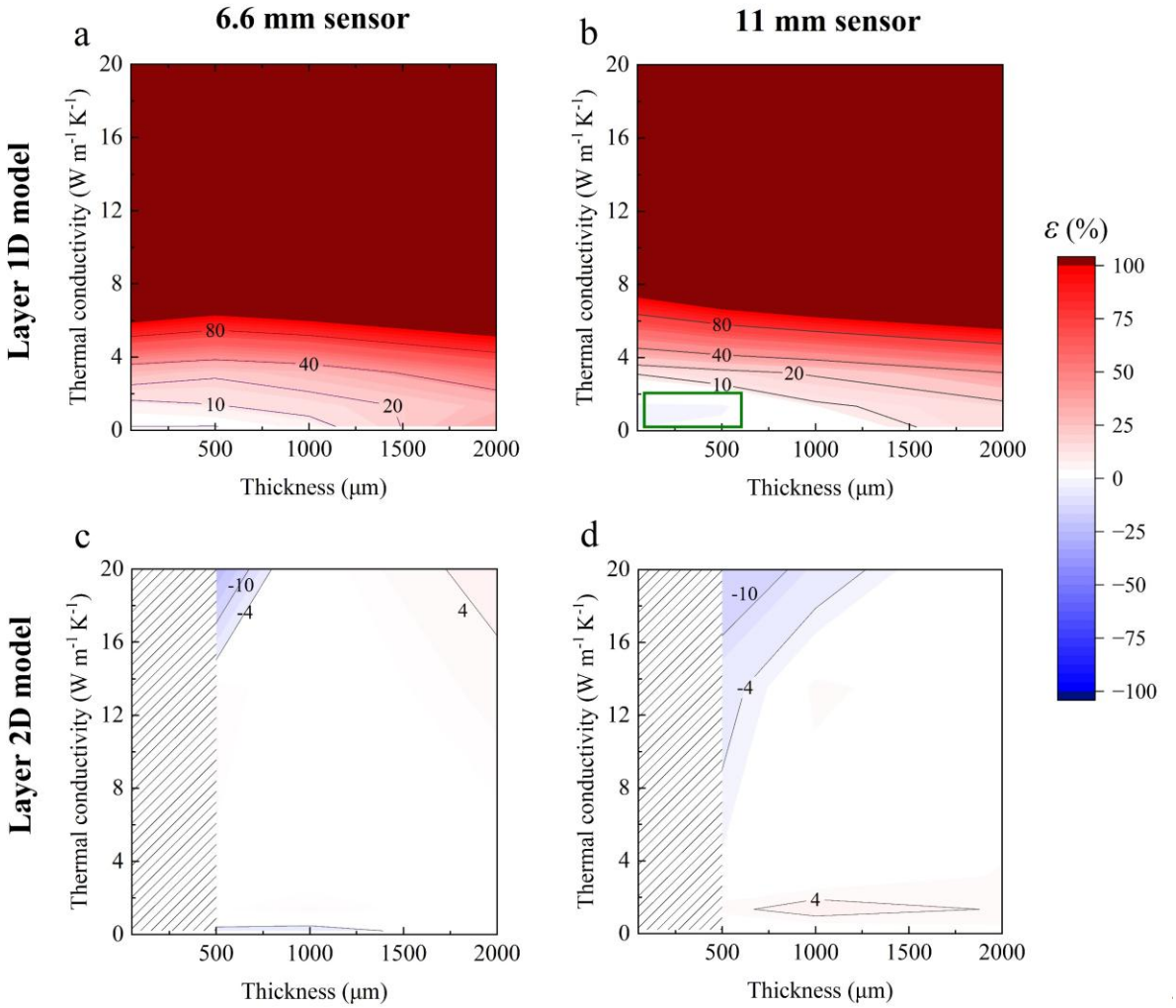

Figure 10. Contour maps of error ε in layer thermal conductivity determined from measurement data using different probes and fitting models: (a) 6.6 mm probe, Layer 1D model, (b) 11 mm probe, Layer 1D model, (c) 6.6 mm probe, Layer 2D model, (d) 11 mm probe, Layer 2D model. Since the data for layers thinner than 500 μm was not experimentally obtained, the corresponding regions in (c,d) are shaded. In (a,b), due to pronounced overall gradient, the data of layers thinner than 500 μm was obtained by extrapolation based on the measurement data in Table S1.

4.2 Analysis of systematic errors

To further quantify systematic errors (e.g., those resulting from thermal contact resistance), the Layer 2D model is employed to determine the layer thermal conductivity from simulated measurement data generated by the detailed FEM model. The determined thermal conductivity is subsequently compared with the input value in the FEM model to calculate the relative error ε.

The simulated measurement data (Fig. 3 c, d) cover two thermal contact conditions between the probe, sample layer, and substrate: (i) good thermal contact, represented by a 5 μm-thick TIM with a thermal conductivity of 3 $\mathrm{W\,m^{-1}\,K^{-1}}$, and (ii) inferior thermal contact, represented by a TIM of 1 $\mathrm{W\,m^{-1}\,K^{-1}}$.

When utilizing a TIM of 3 W m^{-1} K^{-1} (Fig. 11 a, b), ε is generally low (< 10 %) for layers thicker than 250 µm in cases of both a 6.6 mm and 11 mm sensors. For thinner layers, thermal conductivity is slightly underestimated, consistent with the experimental observation. We attribute this underestimation to the thermal contact resistance between the components, which impedes thermal conduction and leads to a higher temperature response of the probe. For low thermal conductivity layers (< 2 W m^{-1} K^{-1}), the magnitude of ε remains small even when the layer thickness is as low as 50 µm. Compared with the conventional Layer 1D model (green frame, Fig. 11b), the measurement applicability has been significantly extended, enabling accurate characterization (ε < 10 %) of layers with thermal conductivities up to 20 W m^{-1} K^{-1} and thickness up to 2000 µm.

When the thermal contact resistance is higher (Fig. 11 c, d), the underestimation for thin layers becomes more pronounced, indicating that the thermal contact resistance is the primary limiting factor of the Layer 2D model. These results are closer to the measurement results observed in Fig. 10 c, d. Overall, although thermal contact resistance introduces minor systematic errors, they remain within an acceptable range for relatively thick layers and can be substantially reduced by improving thermal contact—for example, by using a TIM with higher thermal conductivity of 3 W m^{-1} K^{-1}.

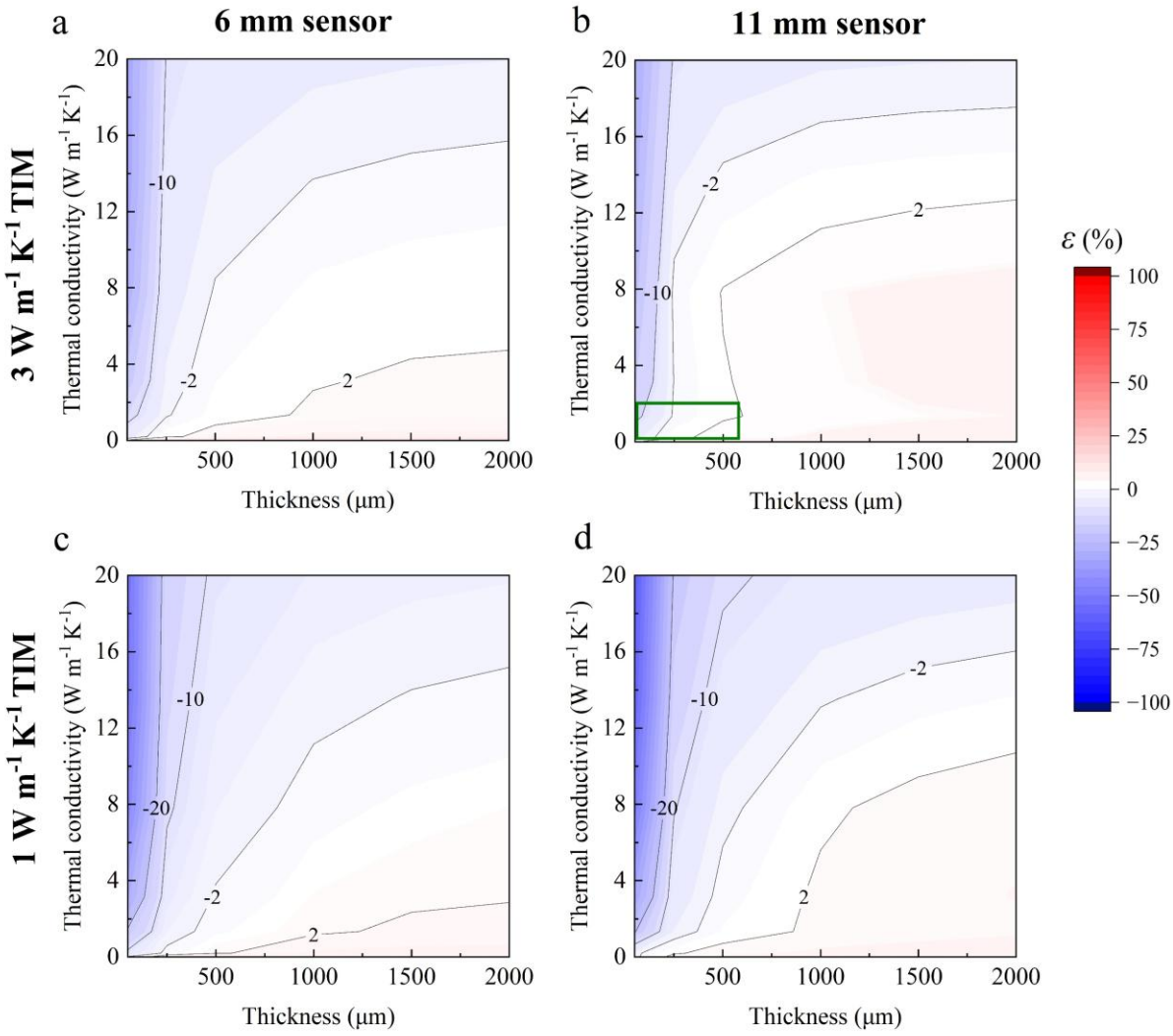

Fig. 11 Contour maps of error ε in the layer thermal conductivity determined using the Layer 2D model from simulated data under different conditions: (a) 6 mm probe, TIM thermal conductivity of 3 W m^{-1} K^{-1}, (b) 11 mm probe, TIM thermal conductivity of 3 W m^{-1} K^{-1}, (c) 6 mm probe, TIM thermal conductivity of 1 W m^{-1} K^{-1}, (c) 11 mm probe, TIM thermal conductivity of 3 W m^{-1} K^{-1}. The thickness of TIM for all cases is 5 μm.

5. Conclusion

Conventional TPS measurements of layer-substrate structures rely on the assumption of 1D heat flux across the layer, which restricts their applicability to sample layers with low thermal conductivity (< 2 W $m^{-1}K^{-1}$), small thickness (< 600 μm), and relatively large probes (radius > 11 mm). In this work, we propose a semi-analytical model that accounts for non-1D heat flux across the layer. This new model is derived from the Laplace-Hankel transform and subsequently simplified for the regime where the heat flux within the layer reaches a quasi-steady state. Sensitivity analysis based on finite element simulations further validates this assumption and enables the development of an empirical equation to estimate the time range for data analysis. Overall, the new model applicable to layers with a thermal conductivity up to 20 W $m^{-1}K^{-1}$ (tenfold higher than before) and a thickness of up to 2000 μm (approximately fourfold thicker). Moreover, this model enables the use of a new TPS probe for layer-substrate structures, featuring a radius of only 6.6 mm. This new model is validated by experiments, demonstrating an accuracy of about 10 % for layers with a thermal conductivity below 16 W $m^{-1}K^{-1}$ and a thickness above 500 μm. The observed measurement deviations and limitations are mainly attributed to thermal contact resistance. FEM simulations suggest that an even wider measurement range (< 20 W $m^{-1}K^{-1}$, > 250 μm) is attainable when the thermal contact resistance is minimized, for example by using a 5 μm thermal interface material with a thermal conductivity of 3 W $m^{-1}K^{-1}$.

Acknowledgement

This project has received funding from the European Union's Horizon 2020 research and innovation program under the Marie Skłodowska-Curie grant agreement No 955837. The authors are grateful to Mr. Jesper Löfman for providing the high-resolution photographs of the Hot Disk probes.

Support information

S1. Derivation of the Layer 2D model

A closed-form algebraic expression for the inverse Laplace transform term in Eq. 27 is sought to reduce computational time. As far as the authors are aware, there is no tabulated inverse transformation that can be directly used to the key term (K) in Eq. 27.

$$K = \frac{1}{pq_l} \cdot \frac{q_s \tanh(Lq_l) + c \cdot q_l}{c \cdot q_l \tanh(Lq_l) + q_s} \tag{S1}$$

where $c = \lambda_l / \lambda_s$.

However, a considerable simplification of K can be achieved by making a modest assumption about the thermal diffusivity of the layer (α_l). It is assumed that the heat flux across the layer reaches a quasi-steady state given a long measurement time, where T_{avg} is not sensitive to α_l. Consequently, α_l can be treated as an arbitrary value without materially influencing T_{avg}. This observation permits the simplification of K by assigning the layer the same thermal diffusivity as the substrate, i.e., $\alpha_l = \alpha_s$, and thus $q_l = q_s$:

$$K = \frac{1}{pq_{\mathrm{s}}} \cdot K_{\mathrm{r}} \tag{S2}$$

$$K_{\mathrm{r}} = \frac{\tanh(w) + c}{1 + c \cdot \tanh(w)} \tag{S3}$$

where $w = Lq_s$.

K_{r} can be further simplified using the Padé approximation of order [2,2] for small w:

$$K_{\mathrm{r}} \approx \frac{c(w^2+3)+3w}{(w^2+3)+3cw} \tag{S4}$$

This simplification yields significantly better agreement with the original equation (Fig. S1) compared with assuming $\tanh(w) \approx w$, which leads to $K_{\mathrm{r}} \approx \frac{w+c}{1+c \cdot w}$ and enables the derivation of the Laye 1D model in section 2.1.

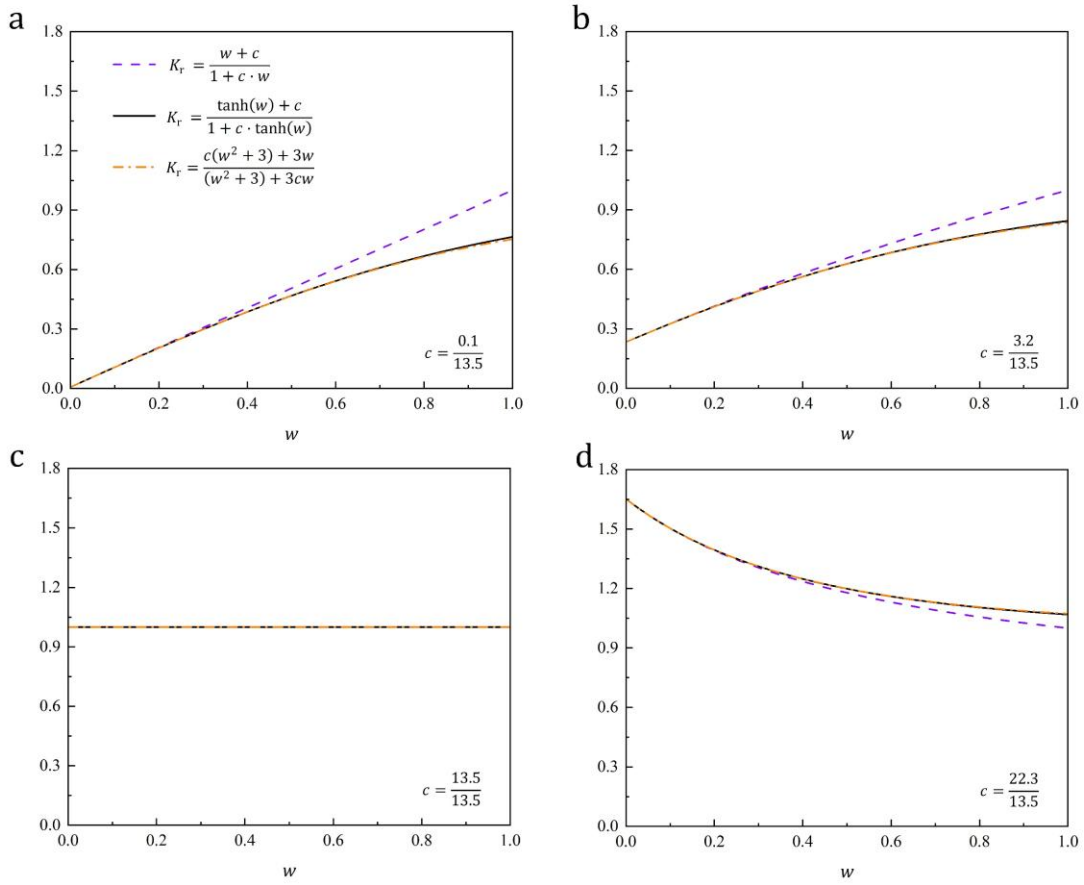

Fig. S1. Comparison between the Eq. S3 (black solid line) and its two approximations: $\frac{w+c}{1+c\cdot w}$ (purple dashed lines) and $\frac{c(w^2+3)+3w}{(w^2+3)+3cw}$ (orange dash-dot line) across different c values.

With the Padé approximation, a close form inverse Laplace transform of K can be found:

$$L^{-1}(K) \approx \frac{c\left(\beta^4L^4-3\beta^2L^2+9\right)\cdot \mathrm{erf}\left(\beta\sqrt{\alpha_s t}\right)+3\beta L\left(1-c^2\right)\left(3+\beta^2L^2\right)}{9\beta L+3\beta^3L^3(2-3c^2)+\beta^5L^5} \tag{S5}$$

Therefore, the final equation for calculating T_{avg} can be written as:

$$\Delta T_{\mathrm{avg}} = \frac{2\varphi}{\lambda_l}\int_0^{\infty}\frac{J_1^2(\beta R)}{\beta}\frac{(A+D)}{F}\,d\beta \tag{S6}$$

where

$$A = c(\beta^4L^4 - 3\beta^2L^2 + 9)\cdot \mathrm{erf}\left(\beta\sqrt{\alpha_s t}\right) \tag{S7}$$

$$D = 3\beta L(1-\ c^2)(3+\beta^2L^2) \tag{S8}$$

$$F = 9\beta L + 3\beta^3L^3(2-3c^2) + \beta^5L^5 \tag{S9}$$

S2. Influence of mesh number and relative tolerance on simulation results

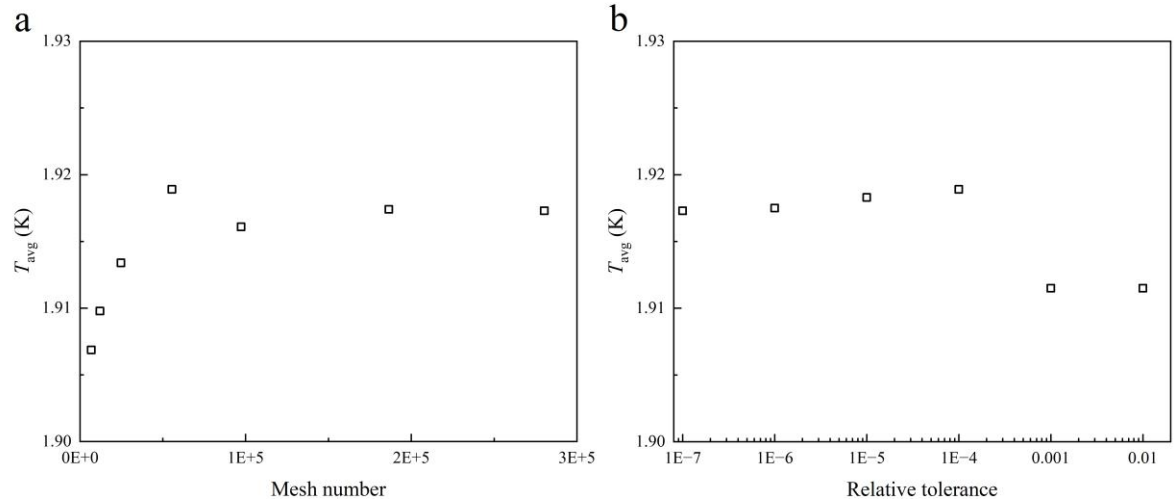

Fig. S2. Simulated ΔT_{avg} at 80 s using the details FEM model as a function of (a) mesh number and (b) relative tolerance.

S3. Results of the conventional Layer 1D model

Table S1. The determined thermal conductivity of different layers obtained from experimental data using the Layer 1D model. The reported values represent the average of three repeated measurements, with the uncertainty expressed as the maximum difference among them. Results for stainless steel and alumina are excluded, as the Layer 1D model is not applicable to these materials.

	Layer thickness (μm)	Thermal conductivity ($W\ m^{-1}K^{-1}$)		
		PMMA	Glass	ZrO_2
Probe A (R = 6.6 mm)	500	0.209 ± 0.010	1.47 ± 0.03	3.85 ± 0.27
	1000	0.221± 0.004	1.53 ± 0.02	4.03 ± 0.11
	2000	0.282 ± 0.026	1.70 ± 0.01	4.87 ± 0.06
Probe B (R = 11 mm)	500	0.211 ± 0.005	1.33 ± 0.03	3.65 ± 0.25
	1000	0.217 ± 0.017	1.45 ± 0.02	3.82 ± 0.07
	2000	0.241 ± 0.012	1.56 ± 0.01	4.39 ± 0.06

References

[1] D. Zhao, X. Qian, X. Gu, S.A. Jajja, R. Yang, Measurement techniques for thermal conductivity and interfacial thermal conductance of bulk and thin film materials, Journal of Electronic Packaging 138(4) (2016) 040802.
[2] H. Wang, W. Chu, G. Chen, A brief review on measuring methods of thermal conductivity of organic and hybrid thermoelectric materials, Advanced electronic materials 5(11) (2019) 1900167.
[3] Ľ. Kubičár, V. Boháč, P. Gaal, D. Apostolescu, Review of several dynamic methods of measuring thermophysical parameters, Proc. of 24th Int. Conf. on Thermal Conductivity/12th Int. Thermal Expansion Symposium", ed. PS Gaal, DE Apostolescu, Lancaster: Technomic Publishing Company, 1999, pp. 135-149.
[4] S.E. Gustafsson, Transient plane source techniques for thermal conductivity and thermal diffusivity measurements of solid materials, Review of scientific instruments 62(3) (1991) 797-804.
[5] S.E. Gustafsson, B.M. Mihiretie, M.K. Gustavsson, Measurement of thermal transport in solids with the hot disc method, International Journal of Thermophysics 45(1) (2024) 1.
[6] ISO 22007-2:2022, Plastics — Determination of thermal conductivity and thermal diffusivty — Part 2: Transient plane heat source (hot disc) method.
[7] Y. Jannot, Z. Acem, A quadrupolar complete model of the hot disc, Measurement science and technology 18(5) (2007) 1229.
[8] N. Laraqi, Thermal impedance and transient temperature due to a spot of heat on a half-space, International Journal of Thermal Sciences 49(3) (2010) 529-533.
[9] J. Gustavsson, M. Gustavsson, S. Gustavsson, On the Use of the Hot Disk Thermal Constants Analyser for Measuring the Thermal Conductivity of Thin Samples of Electrically Insulating Materials, Thermal Conductivity 24, Technomic Publishing Co., Lancaster, PA, 1997, pp. 116-122.
[10] M. Ahadi, M. Andisheh-Tadbir, M. Tam, M. Bahrami, An improved transient plane source method for measuring thermal conductivity of thin films: Deconvoluting thermal contact resistance, International Journal of Heat and Mass Transfer 96 (2016) 371-380.
[11] M. Gustavsson, L. Hälldahl, Thermal conductivity measurements of thin insulating layers deposited on high-conducting sheets, International journal of thermophysics 27(1) (2006) 195-208.
[12] Y. Zhang, T. Wang, X. Mei, M. Chen, L. Wu, Ordered porous polymer films for highly efficient passive daytime radiative cooling, Acs Photonics 10(9) (2023) 3124-3132.
[13] W. Gan, Y. Wang, S. Xiao, R. Gao, Y. Shang, Y. Xie, J. Liu, J. Li, Magnetically driven 3D cellulose film for improved energy efficiency in solar evaporation, ACS Applied Materials & Interfaces 13(6) (2021) 7756-7765.
[14] X. Liu, H. Li, T. Zhang, H. Peng, K. Wang, Y. Dong, Y. Lu, K. Wang, X. Zhan, Y. Liu, Strong, tough, anisotropic, flexible, and transparent bamboo films, Industrial Crops and Products 207 (2024) 117757.

[15] Y. Guo, H. Qiu, K. Ruan, Y. Zhang, J. Gu, Hierarchically multifunctional polyimide composite films with strongly enhanced thermal conductivity, Nano-Micro Letters 14(1) (2022) 26.
[16] T. Gu, Z. Zeng, S. Wu, D.-x. Sun, C.-s. Zhao, Y. Wang, Poly (L-lactic acid)/graphene composite films with asymmetric sandwich structure for thermal management and electromagnetic interference shielding, Chemical Engineering Journal 466 (2023) 143190.
[17] H. Zhang, M.-J. Li, W.-Z. Fang, D. Dan, Z.-Y. Li, W.-Q. Tao, A numerical study on the theoretical accuracy of film thermal conductivity using transient plane source method, Applied thermal engineering 72(1) (2014) 62-69.
[18] D. Landry, R. Flores, R.B. Goodman, Estimating the Thermal Conductivity of Thin Films: A Novel Approach Using the Transient Plane Source Method, ASME Journal of Heat and Mass Transfer 146(3) (2024) 031004.
[19] ASTM D5470-06, Standard Test Method for Thermal Transmission Properties of Thermally Conductive Electrical Insulation Materials, (2010).
[20] ASTM E1530-19, Standard test method for evaluating the resistance to thermal transmission of materials by the guarded heat flow meter technique, (2025).
[21] H.-P. Ebert, S. Vidi, Correct use of the guarded-hot-plate method for thermal conductivity measurements on solids, International Journal of Thermophysics 45(2) (2024) 20.
[22] K. Horai, T. Shankland, Thermal Conductivity of Rocks and Minerals, Methods in experimental physics 24 (1987) 271-302.
[23] D. Chalise, R. Tee, Y. Zeng, S. Kaur, H. Pokharna, R.S. Prasher, High throughput, spatially resolved thermal properties measurement using attachable and reusable 3ω sensors, Review of Scientific Instruments 94(9) (2023).
[24] A. Muscio, P.G. Bison, S. Marinetti, E. Grinzato, Thermal diffusivity measurement in slabs using harmonic and one-dimensional propagation of thermal waves, International Journal of thermal sciences 43(5) (2004) 453-463.
[25] B. Feng, Y.-H. Zhang, J. Tu, L.-W. Fan, Z.-T. Yu, Determination on the thermal conductivity and thermal contact resistance of thin composite phase change films as a thermal interfacial material, Case Studies in Thermal Engineering 33 (2022) 101979.
[26] Z. Zeng, P. Sowinski, C. Müller, B. Mihiretie, Liquid Interface for Accurate Intrinsic Thermal Conductivity Measurements of Polymer Films Using the Transient Plane Source Method, Journal of Thermal Science and Engineering Applications 17(11) (2025) 111008.
[27] H. Zhang, Y.-M. Li, W.-Q. Tao, Theoretical accuracy of anisotropic thermal conductivity determined by transient plane source method, International Journal of Heat and Mass Transfer 108 (2017) 1634-1644.
[28] M. Emanuel, M. Bhouri, S.L. Ackermann, D. Groulx, J. Maassen, Temperature fields generated by a circular heat source (CHS) in an infinite medium: Analytical derivation and comparison to finite element modeling, International Journal of Heat and Mass Transfer 126 (2018) 1265-1274.

[29] M. Emanuel, M. Bhouri, J. Furlotte, D. Groulx, J. Maassen, Temperature fields generated by a circular heat source (CHS) in an infinite isotropic medium: Treatment of contact resistances with application to thin films, International Journal of Heat and Mass Transfer 137 (2019) 677-689.
[30] A. Haji-Sheikh, J. Beck, D. Agonafer, Steady-state heat conduction in multi-layer bodies, International Journal of Heat and Mass Transfer 46(13) (2003) 2363-2379.
[31] D.H. Yen, J.V. Beck, Green's functions and three-dimensional steady-state heat-conduction problems in a two-layered composite, Journal of engineering mathematics 49(3) (2004) 305-319.
[32] L. Yan, A. Haji-Sheikh, J. Beck, Thermal characteristics of two-layered bodies with embedded thin-film heat source, (1993).
[33] P. Hui, H. Tan, A transmission-line theory for heat conduction in multilayer thin films, IEEE Transactions on Components, Packaging, and Manufacturing Technology: Part B 17(3) (2002) 426-434.
[34] P. Hui, H. Tan, Temperature distributions in a heat dissipation system using a cylindrical diamond heat spreader on a copper heat sink, Journal of applied physics 75(2) (1994) 748-757.
[35] P. Hui, H. Tan, A rigorous series solution for a thermal dissipation system with a diamond heat spreader on an infinite slab heat sink, Japanese journal of applied physics 34(9R) (1995) 5056.
[36] N.D. Milošević, M. Raynaud, Analytical solution of transient heat conduction in a two-layer anisotropic cylindrical slab excited superficially by a short laser pulse, International journal of heat and mass transfer 47(8-9) (2004) 1627-1641.
[37] E. El Rassy, Y. Billaud, D. Saury, A direct method for the simultaneous characterization of thermal diffusivities of a bi-layer material consisting of a thin coating deposited on a substrate, Applied Mathematical Modelling 91 (2021) 614-631.
[38] E. El Rassy, Y. Billaud, D. Saury, Unconventional flash technique for the identification of multilayer thermal diffusivity tensors, International Journal of Thermal Sciences 155 (2020) 106430.
[39] S. Yeon, D.G. Cahill, Analysis of heat flow in modified transient plane source (MTPS) measurements of the thermal effusivity and thermal conductivity of materials, Review of Scientific Instruments 95(3) (2024).
[40] Q. Zheng, S. Kaur, C. Dames, R.S. Prasher, Analysis and improvement of the hot disk transient plane source method for low thermal conductivity materials, International Journal of Heat and Mass Transfer 151 (2020) 119331.
[41] G. Jiaqi, S.B. Safiullah, L. Yang, Q. Ziyan, Q. Zheng, Improving the Accuracy of Transient Plane Source Thermal Conductivity Measurements: Novel Analytical Models, Fitting Approaches, and Systematic Sensitivity Analysis, International Journal of Heat and Mass Transfer 247 (2025) 127110.
[42] V. Barragán, M. Izquierdo-Gil, J. Maroto, P. Antoranz, S. Muñoz, Estimation of the through-plane thermal conductivity of polymeric ion-exchange membranes using finite element technique, International Journal of Heat and Mass Transfer 176 (2021) 121469.

[43] Z. Zeng, C. Müller, B. Mihiretie, Extending the Transient Plane Source Scanning method for determining the specific heat capacity of low thermal conductivity materials through a numerical study, Thermochimica Acta 742 (2024) 179883.
[44] H.S. Carslaw, J.C. Jaeger, Conduction of Heat in Solids, Oxford Science Publications, New York2000.
[45] M. Gustavsson, N. Saxena, E. Karawacki, S. Gustafsson, Specific heat measurements with the hot disk thermal constants analyser, Thermal Conductivity 23, CRC Press2021, pp. 56-65.
[46] A.C. Lua, J. Su, Isothermal and non-isothermal pyrolysis kinetics of Kapton® polyimide, Polymer degradation and stability 91(1) (2006) 144-153.
[47] Thermal-Paste Comparison, Igor's Lab, https://www.igorslab.de/en/thermal-paste-comparison/?ids=30,55, (2025).
[48] V. Bohac, M.K. Gustavsson, L. Kubicar, S.E. Gustafsson, Parameter estimations for measurements of thermal transport properties with the hot disk thermal constants analyzer, Review of scientific instruments 71(6) (2000) 2452-2455.

Paper V

Prediction of the thermal conductivity of polypropylenes and propylene copolymers based on crystallinity or elastic modulus

Manuscript in preparation

Prediction of the thermal conductivity of polypropylenes based on crystallinity or elastic modulus

Przemyslaw Sowinski,[a]* Zijin Zeng,[b] Besira Mihiretie,[b] Ewa Piorkowska-Galeska,[c] Mathis Brette Mortensen,[a] Ergang Wang,[a] Christian Müller[a]*

[a] Department of Chemistry and Chemical Engineering, Chalmers University of Technology, 41296 Göteborg, Sweden

[b] Hot Disk AB, Sven Hultins gatan 9A, Gothenburg, Sweden

[c] Centre of Molecular and Macromolecular Studies, Polish Academy of Sciences, Sienkiewicza 112, Lodz, 90 363, Poland

*e-mail: sowinski@chalmers.se; christian.muller@chalmers.se

Abstract

Knowledge about the thermal conductivity of polypropylenes is important for the development of new dielectric materials. However, many research laboratories do not have access to suitable instrumentation. Here, the thermal conductivity of polypropylenes is characterized. The thermal conductivity of isotropic samples is found to linearly increase from approximately 0.18 W m^{-1} K^{-1} for amorphous material to 0.26 W m^{-1} K^{-1} for a crystallinity of about 60%. At the same time, the Young's modulus exponentially increases from 24 MPa to more than 1700 MPa for the most crystalline materials, which is used to predict a logarithmic increase of the thermal conductivity with Young's modulus. Overall, the here presented results allow to

estimate the thermal conductivity of polypropylenes with an uncertainty of about 0.01 W m^{-1} K^{-1} through straightforward differential scanning calorimetry or tensile deformation measurements.

Keywords: polypropylene, crystallinity, elastic modulus, thermal conductivity

Introduction

Polypropylenes are widely utilized for a variety of applications from packaging, kitchenware, and textiles to structural components in automobiles and dielectric layers in power engineering systems [1]. In the context of electrical components, efficient thermal management plays a pivotal role in ensuring the safe and reliable operation of devices. This is of particular importance for high-voltage capacitors, power cables, and similar electrical components, where temperature regulation is crucial for maintaining performance, preventing damage and ensuring low losses. In many electrical systems, polymer-based dielectric layers are the part with the lowest thermal conductivity, making the selection of appropriate materials a critical factor in optimizing heat dissipation. For instance, in high-voltage direct current (HVDC) power cables, the thermal conductivity of the polyolefin-based insulation layer significantly influences the maximum operating temperature at a given transmission voltage [2]. As heat is generated by the electrical conductor, the ability of the dielectric material to effectively manage and dissipate this heat is essential to prevent overheating and to ensure the longevity of the system.

Among various materials under consideration for the design of novel insulation materials, polypropylenes have attracted considerable academic interest in recent years [3-7]. They are being explored as a promising alternative to crosslinked polyethylene, which is widely used for

preparing the insulation layer of extruded HVDC cables [2, 3, 8]. The growing interest in polypropylenes stems from its higher melting temperature compared to polyethylene. However, unlike polyethylene, polypropylene does not conduct heat as effectively [9]. Therefore, a priori knowledge of the thermal conductivity of polypropylenes is crucial for the design, development, and optimization of thermoplastic HVDC cables. Otherwise, it would be challenging to ensure that the cables can handle the thermal demands of high-voltage systems while maintaining performance and safety standards. Thus, the straightforward characterization of the thermal behavior of polypropylenes is of paramount importance for advancing the field of HVDC technology.

It would be advantageous if methods existed that allowed to estimate the thermal conductivity *a priory*, without the need for intricate measurements. The initial selection of materials based on empirical correlations would accelerate development, and the most promising candidates could then be subjected to an in-depth evaluation.

It is not straightforward to estimate the thermal conductivity of a polymer from the chemical structure of its repeat unit alone. In case of amorphous polymers, for instance, crosslinks and strong secondary interactions tend to enhance coupling between polymer chains, thereby improving the thermal conductivity of the polymer [10]. In case of semicrystalline polymers, besides crosslinking the thermal conductivity is strongly influenced by the nanostructure of the material with typical values ranging from $\kappa = 0.2$ to 0.7 W m^{-1} K^{-1} [11-13]. Crystalline lamellae, which typically have a thickness of 5-20 nm, are characterized by a higher thermal conductivity (due to their ordered structure and higher density) compared with the surrounding lower-density amorphous phase. Heat transfer between crystalline regions is hindered by phonon scattering at the interface between crystalline and amorphous regions [10,

14, 15]. Therefore, the degree of crystallinity, lamellar thickness and chain orientation play a substantial role in the thermal behavior of these polymers [14]. The highest thermal conductivity values have been reported for highly ordered polymers reaching values of κ = 1.7 W m^{-1} K^{-1} in case of bulk, high-pressure crystallized ultrahigh molecular-weight polyethylene (UHMWPE) [16], 15-20 W m^{-1} K^{-1} in case of uniaxially oriented fibers composed of UHMWPE or aromatic polymers [17] and 100 W m^{-1} K^{-1} in case of polyethylene nanofibers [17, 18]. Evidently, it can be challenging to predict the thermal conductivity of a polymer without detailed knowledge of its nano- and microstructure.

Thermal conductivity measurements can be intricate and are therefore not available in every polymer characterization lab. A number of techniques are available for measuring the thermal conductivity of bulk polymer specimens, including the Guarded Hot Plate (GHP) method, Laser Flash Analysis (LFA), and the Transient Plane Source (TPS) method. The GHP method is a steady state method that requires the application of a constant temperature difference of up to 50 °C to a slab specimen, [19-21] which may result in a gradient in microstructure as a result of local annealing. The LFA method is a transient method for measuring thermal diffusivity [22, 23]. The thermal conductivity is calculated as the product of the measured thermal diffusivity and the heat capacity. In case of LFA, a specimen is heated by less than 3 °C via a laser pulse and its temperature response is recorded by an infrared detector. A transducer layer, e.g. a graphite film, should be deposited on the specimen surface to absorb the laser pulse and emit detectable optical signals, which increases the complexity and uncertainty of the measurement process. The TPS method is a transient method that utilizes a planar probe to heat the specimen and simultaneously record the resulting temperature response of typically less than 3 °C, thus facilitating accurate and non-destructive measurements [24-26].

Here, the TPS method is used to determine the thermal conductivity of a wide range of polypropylenes [27]. The nanostructure of each material is examined with differential scanning calorimetry (DSC), wide- and small-angle X-ray scattering (WAXS, SAXS) and dynamic mechanical analysis (DMA). Various parameters such as the density, crystallinity, lamellar thickness and Young's modulus are compared with the thermal conductivity. We find that thermal conductivity scales with crystallinity and consequently the elastic modulus of polypropylenes, which facilitates the straightforward prediction of κ using standard polymer characterization techniques.

Experimental section

Materials. Polypropylenes were obtained from Borealis (PP1, 2, 5-12), Basell Orlen Polyolefins (PP3) [28] or Merck Chemicals (PP4). Isododecane (97.8% purity) was purchased from Thermo Fisher Scientific.

Sample preparation. Plaques with a thickness of 1 mm for mechanical analysis and X-ray diffraction or 4.5 mm for thermal conductivity, DSC and density measurements were prepared by compression molding at 200 °C for 5 min using a LabPro 200 Fontijne press, followed by cooling at -10 °C min^{-1} to 40 °C, transfer to a water-cooled press to cool at a rate of about -130 °C min^{-1} to room temperature, or quenched by transferring samples to an ice water bath.

Differential scanning calorimetry (DSC). First heating thermograms of 4.5 mm plaques were recorded under nitrogen with a heating rate of 10 °C min^{-1} from -40 to 200 °C using a Mettler Toledo DSC 5 instrument. The specific capacity C_p was determined by comparing the heat flow Q at a given temperature with the heat flow recorded for sapphire $Q^{saphire}$ according to:

$$C_p = \frac{Q \cdot m^{saphire}}{m \cdot Q^{saphire}} C_p^{saphire} \quad (1)$$

where m and $m^{saphire}$ are the mass of the sample and of sapphire, respectively, and $C_p^{saphire}$ = 0.7788 J g^{-1} C^{-1} is the specific heat capacity of sapphire [29]. The overall crystallinity X_c was calculated according to:

$$X_C = \frac{\Delta H_m}{\Delta H_{m\alpha}^0} K_\alpha + \frac{\Delta H_m}{\Delta H_{m\beta}^0} K_\beta + \frac{\Delta H_m}{\Delta H_{m\gamma}^0} K_\gamma \quad (2)$$

where ΔH_m is the melting enthalpy and $\Delta H_{m\alpha}^0$ = 209 J g^{-1}, $\Delta H_{m\beta}^0$ = 168.5 J g^{-1} and $\Delta H_{m\gamma}^0$ = 150 J g^{-1} are the enthalpies of fusion of 100% crystalline isotactic polypropylene in α, β and γ forms, respectively [30-32], and K_α, K_β and K_γ are the contents of α, β and γ forms, respectively (See SI Section 1).

Density measurements. A Mettler Toledo XS105 scale equipped with a density kit XPR/XSR-Ana was used to determine the density ρ at 25 °C using isododecane with a density of ρ_l = 0.74 g cm^{-3} as the auxiliary liquid according to:

$$\rho = \frac{m_{air}}{m_{air} - m_l} (\rho_{air} - \rho_l) + \rho_l \quad (3)$$

where m_{air} and m_l are the sample weight in air and in the auxiliary liquid, respectively, and ρ_{air} = 0.0012 g cm^{-3} is the density of air at 25 °C.

Wide angle X-ray scattering (WAXS). Diffractograms of 1 mm thick samples were recorded in reflection mode with a D8 Discover instrument from Bruker equipped with a CuK$_\alpha$ source (wavelength = 1.54 Å) and using a fixed slit mode (0.7 mm). The diffraction patterns were deconvoluted using WAXSFIT program [33] and the contents of individual crystallographic phases were calculated (see Figure S1 and SI Section 1).

Small angle x-ray scattering (SAXS). SAXS diffractograms of 1 mm thick samples were recorded with a Mat:Nordic instrument from SAXSLAB/Xenocs equipped with a microfocus CuK_α source (wavelength = 1.54 Å) and a Dectris Pilatus 300K detector. Data was processed with the SAXSGui software. The thickness of crystalline lamellae l_c was calculated according to:

$$l_c = \frac{\rho}{\rho_c} X_C L_p \tag{4}$$

where ρ_c = 0.946 g cm^{-3} is the density of α-form polypropylene crystals [34] and L_p is the long period obtained from SAXS.

Thermal conductivity measurements. Five measurements for each sample were carried out in accordance with ISO 22007-2 at 25 °C using a TPS 2500S thermal constant analyzer from Hot Disk equipped with a 5465 sensor with a radius of 3.18 mm, using a measurement time of 20 s, heating power of 25 mW and fixed C_p, unless specified otherwise. Further details can be found in Supporting Information Section 2. The surface of the samples was polished with sandpaper to ensure good physical contact with the sensor.

Tensile deformation. Dog-bone shaped samples compliant with ISO 527 (5A) were cut from 1 mm thick plaques. Tensile deformation was carried out at a strain rate of 25 mm mm^{-1} and a temperature of 25 °C using an Instron 5564 A instrument. To calculate the modulus, the stress values were used in the range of 0 to 1% deformation, assuming that the deformation was uniform along the entire length of the sample from clamp to clamp (50 mm).

Results and discussion

We selected twelve different polypropylenes for our study (see Table 1). The TPS method was used to determine the thermal conductivity of the polypropylene materials, which were cooled at either -10 or -130 °C min^{-1}, giving rise to different microstructures and crystallinity [35]. Measurements were carried out according to standard ISO 22007-2 at 25 °C. In a first set of experiments, we compared TPS measurements of the same material (PP5 prepared with -10 °C min^{-1} cooling rate) to determine the error in the obtained values for κ. Variations in different measurement parameters and three repeat measurements of a plaque of the same material (PP1 prepared with -10 °C cooling rate) yielded a percentage error of not more than $\Delta\kappa$ = 1.2 % and 0.3 %, respectively, when a predetermined value of C_p was used for the fitting procedure (Figure S2 and S3). We also compared the percentage error when carrying out the measurement without knowledge of C_p, which yielded a value of $\Delta\kappa$ = 1.6 % (Figure S2). Therefore, we chose to work with a percentage error of $\Delta\kappa$ = 1.2% throughout the remainder of our study.

Subsequently, we determined the thermal conductivity of all twelve grades, cooled at -10 and -130 °C min^{-1} and obtained values ranging from κ = 0.191 W m^{-1} K^{-1} for PP4 to κ = 0.277 W m^{-1} K^{-1} for PP7 (Table 1). We therefore proceeded with characterizing the microstructure of the PP materials with density measurements, DSC, WAXS and SAXS to obtain information about the density ρ, peak melting temperature T_m, crystallinity X_c, long period L_p, lamellar thickness l_c and the presence of different crystalline forms (Table 1, Table S1 and Figure 1; see Experimental Section for details). For instance, ρ ranged from 0.871 to 0.914 g cm^{-3} and X_c ranged from 8 to 66 %. The WAXS diffraction patterns indicate that all samples predominantly contain α-phase crystals, however, in all slowly cooled materials, the presence of γ-phase crystals was also

identified, ranging from 3 to 32%. Samples PP1 and PP3 exhibit trace amounts (<1%) of β-phase cystals, whereas in the slowly cooled PP1, the β-phase content increased to approximately 15%. This observation is confirmed by corresponding DSC thermograms, which display two distinct melting endotherms (Figure 1).

Table 1. Melting temperature T_m of samples cooled with a rate $\Delta T/\Delta t$ = -10 °C min^{-1}, thermal conductivity κ_{10} and κ_{130} of samples cooled with a rate of $\Delta T/\Delta t$ = -10 and -130 °C min^{-1}, respectively (measurement by TPS with known C_p; percentage error $\Delta\kappa$ = 1.2%).

	$\boldsymbol{T_m}$ (°C)	$\boldsymbol{\kappa_{10}}$ (W m^{-1} K^{-1})	$\boldsymbol{\kappa_{130}}$ (W m^{-1} K^{-1})
PP1	165	0.253	0.249
PP2	166	0.251	0.232
PP3	168	n.m.	0.241
[a]PP4	155	0.193	0.196
PP5	165	0.250	0.231
PP6	166	0.244	0.230
PP7	163	0.277	0.251
PP8	152	0.251	0.230
PP9	142	0.244	0.226
PP10	159	0.231	0.228
PP11	142	0.237	0.222
PP12	151	0.228	0.216

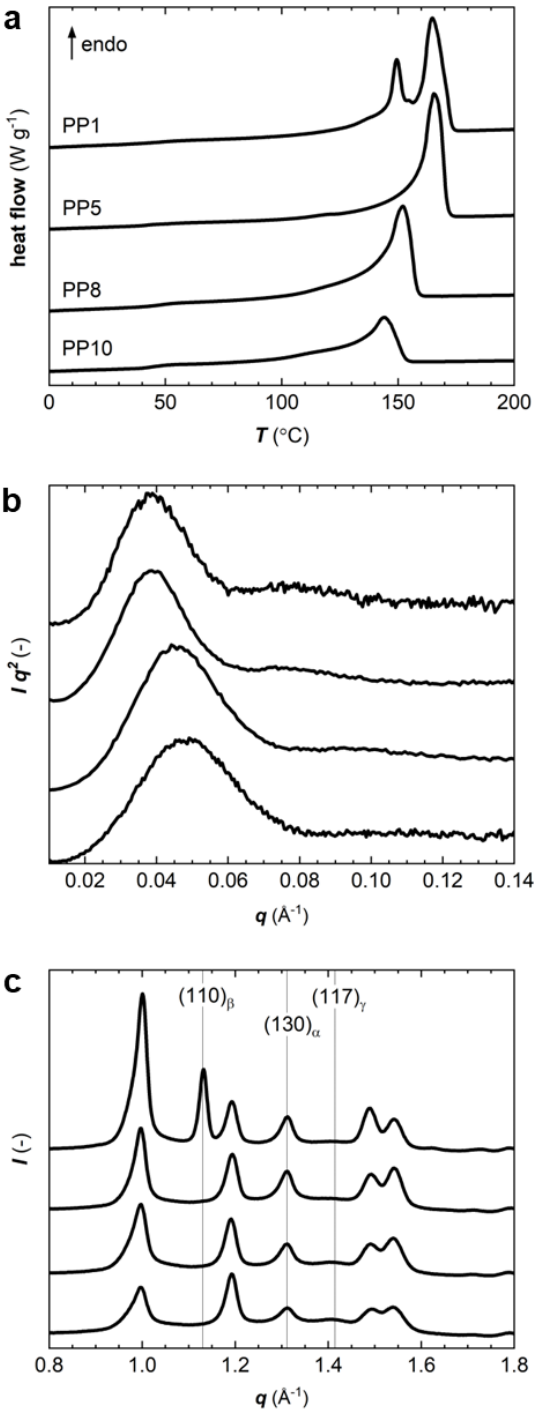

Figure 1. Characterization of PP materials. (a) First-heating DSC thermograms, (b) SAXS and (c) WAXS diffractograms of PP1, PP5, PP8 and PP10 crystallized by cooling at -10 °C min^{-1}.

We then plotted κ against each microstructure parameter to identify those parameters that most strongly correlate. We do not observe any correlation in case of $\kappa(T_m)$ and a weak correlation in case of $\kappa(\rho)$ and $\kappa(L_p)$ (Figure S4). The absence of any correlation with T_m is likely because structural changes can take place during heating and because T_m is related to the size of crystals rather than the crystallinity. For example, PP4 features a relatively high T_m = 155 °C but only a low X_c = 8% when rapidly cooled at -130 °C min^{-1} (see Table 1 and Table S1). A clear linear increase is evident for $\kappa(X_c)$ (Figure 2), which suggests that the number of crystalline domains is the most important parameter that influence κ. A linear function was used to describe $\kappa(X_c)$:

$$\kappa = m \cdot X_c + n \tag{5}$$

where m = (0.00137 ± 0.0001) W m^{-1} K^{-1} %$^{-1}$ and n = (0.179 ± 0.005) W m^{-1} K^{-1} (see Figure 2). The intercept n corresponds to the thermal conductivity κ_{amorph} of purely amorphous polypropylene, which is similar to a value of $\kappa_{aPP} \approx$ 0.15 W m^{-1} K^{-1} that can be extrapolated from literature for atactic PP at ambient conditions [36]. Note that the thermal conductivity of amorphous polymers tends to be independent of chain length above the entanglement molecular weight M_e [37], which is the case for the here investigated materials since $M_e \approx$ 7 kg mol^{-1} for atactic polypropylene [38]. The linear increase in κ with X_c ranging from 8 to 58 % suggests $\kappa = \kappa_{crystalline} + \kappa_{amorph}$ where the contribution from crystalline domains can be estimated according to $\kappa_{crystalline} = m \cdot X_c$ with m = (0.00137 ± 0.0001) W m^{-1} K^{-1} %$^{-1}$ (see Figure 2). Previously reports for, e.g., poly(ethylene terephthalate) and polyethylene have shown that a linear relationship is a reasonable approximation for *isotropic* semi-crystalline polymers [39, 40], while uniaxial orientation will result in an increase in κ along the direction of chain alignment

[41-43]. Evidently, DSC measurements can be used to obtain an estimate of the thermal conductivity of isotropic polypropylenes with an X_c of up to 66% with an uncertainty of $\Delta\kappa \approx \pm$ 0.004 to 0.008 W m^{-1} K^{-1} (see Figure 2). We calculated X_c based on the content of the individual crystallographic phases (see equation 2). Since all investigated materials predominately contain α-form crystals, we can instead use $X_C = \Delta H_m / \Delta H^0_{m\alpha}$ in which case a linear fit remains a very good description of $\kappa(X_c)$ (see Figure S5), which can be used to predict κ an uncertainty of $\Delta\kappa \approx \pm$ 0.005 to 0.01 W m^{-1} K^{-1}. The linear correlation between κ and X_c is promising since many polymer research labs have access to a DSC instrument.

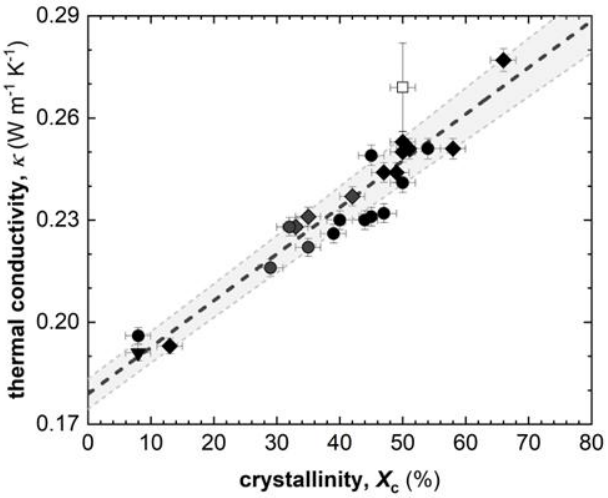

Figure 2. Thermal conductivity κ vs. crystallinity X_c of polypropylenes prepared by cooling with -10 K min^{-1} (♦), -130 K min^{-1} (●), quenching (▼), crystallized under high pressure (purple ▲) and obtained from refs. (open symbols) [35, 44]; the dashed line is a linear fit according to equation 5 and the grey dashed lines are confidence intervals $\kappa \pm \Delta\kappa$ where $\Delta\kappa$ is calculated according to the propagation of errors.

Another property of semi-crystalline polymers that strongly depends on crystallinity is the elastic modulus [45-50], espcially in the temperature range between the glass transition temperature T_g and T_m. Therefore, we chose to determine the Young's modulus E of the investigated polypropylenes with tensile deformation at room temperature. We find that E inceases with X_c from a value of only 24 MPa in case of rapidly cooled low-tacticity PP4 with X_c = 8 % to E > 1700 MPa for the most crystalline materials (Table S1 and Figure 3). Several previous reports have used exponential functions to describe $E(X_c)$ of semi-crystalline polymers [48, 50, 51]. Here, we also chose an exponential function to describe the observed trend of E with X_c:

$$E = a \cdot e^{X_c/b} \tag{6}$$

with a = (26 ± 7) MPa and b = (13 ± 1) % (see Figure 3). We obtain a value of E = 26 MPa for X_c = 0%, which is somewhat lower than the value of 50 MPa, which has been reported for the Young's modulus of the interlamellar amorphous phase of isotactic polypropylene [52].

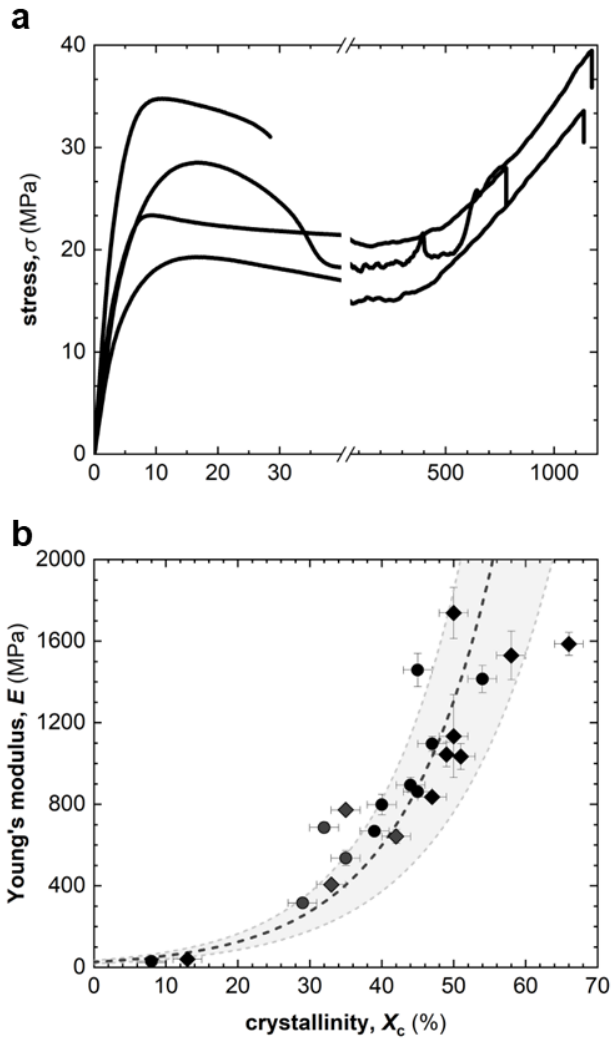

Figure 3. (a) Representative stress-strain curves for polypropylenes, (b) Young's modulus E vs. crystallinity X_c of polypropylenes prepared by cooling with -10 K min^{-1} (♦), -130 K min^{-1} (●) and quenching (▼); the black dashed line is an exponential fit with equation 6 and the grey dashed lines are confidence intervals $E \pm \Delta E$ where ΔE is calculated according to the propagation of errors.

Equations 5 and 6 were combined to predict a logarithmic change in κ with E (Figure 4):

$$\kappa = m \cdot b \cdot \ln(E/a) + n \tag{7}$$

where m, n, b and a are the parameters obtained from fitting $\kappa(X_c)$ and $E(X_c)$. We propose that static or dynamic mechanical measurements can be used to estimate κ of polypropylenes with an uncertainty of $\Delta\kappa \approx \pm 0.01$ W m^{-1} K^{-1} (see Figure 4).

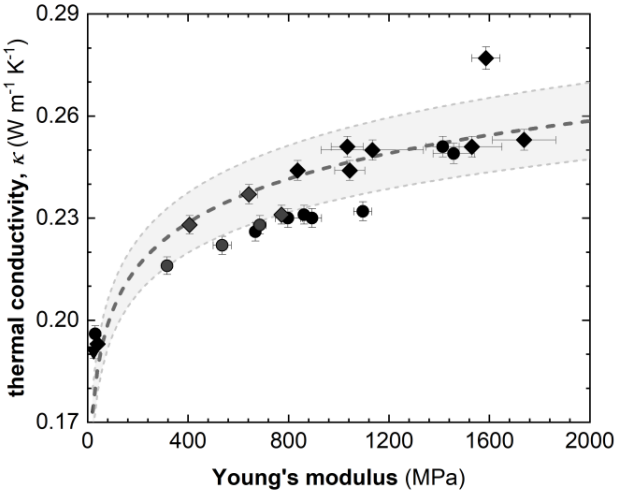

Figure 4. Thermal conductivity κ vs. Young's modulus E of polypropylenes prepared by cooling with -10 K min^{-1} (♦), -130 K min^{-1} (●) and quenching (▼); the black dashed line is a fit obtained by combining the fit functions from Figures 2 and 3 with equation 7 and the grey dashed lines are confidence intervals $\kappa \pm \Delta\kappa$ where $\Delta\kappa$ is calculated according to the propagation of errors.

Conclusions

The thermal conductivity of polypropylenes with a crystallinity of up to 66% that are predominately composed of α-phase crystallites has been characterized. The thermal conductivity was found to linearly increase from about 0.18 W m^{-1} K^{-1} for purely amorphous material to about 0.26 W m^{-1} K^{-1} for the most crystalline samples. In addition, Young's moduli of isotropic samples are found to exponentially increase with crystallinity, which could be used to predict the observed interplay of thermal conductivity and Young's modulus. Hence, differential scanning calorimetry or tensile deformation measurements are proposed as a viable means to obtain an estimate of the thermal conductivity of isotropic polypropylenes, which may accelerate the development of new formulations for dielectric materials. In the future it will be interesting to investigate how the thermal conductivity of polypropylenes with a high content of β- or γ-form crystals scales with crystallinity and elastic modulus.

Acknowledgements

We gratefully acknowledge financial support from Borealis and from the European Union's Horizon 2020 research and innovation program through the Marie Skłodowska-Curie grant agreement no. 955837 (HORATES). This project was in part performed at the Chalmers Materials Analysis Laboratory (CMAL).

Reference

[1] M.T. Hossain, M.A. Shahid, N. Mahmud, A. Habib, M.M. Rana, S.A. Khan, M.D. Hossain, Research and application of polypropylene: a review, Discov Nano 19(1) (2024).
[2] A.M. Pourrahimi, M. Mauri, S. D'Auria, R. Pinalli, C. Müller, Alternative Concepts for Extruded Power Cable Insulation: from Thermosets to Thermoplastics, Advanced Materials 36(52) (2024) 2313508.
[3] T. Andritsch, A. Vaughan, G.C. Stevens, Novel insulation materials for high voltage cable systems, IEEE Electrical Insulation Magazine 33(4) (2017) 27-33.
[4] X.Y. Huang, J. Zhang, P.K. Jiang, T. Tanaka, Material progress toward recyclable insulation of power cables part 2: Polypropylene-based thermoplastic materials, Ieee Electrical Insulation Magazine 36(1) (2020) 8-18.
[5] J.Y. Li, K. Yang, K.N. Wu, Z.H. Jing, J.Y. Dong, Eco-friendly polypropylene power cable insulation: Present status and perspective, Iet Nanodielectr 6(3) (2023) 130-146.
[6] G. Bánhegyi, Compatibility issues in high voltage DC cable insulation development, Adv Ind Eng Poly Res 7(4) (2024) 454-465.
[7] A. Bjurström, H. Edin, H. Hillborg, F. Nilsson, R.T. Olsson, M. Pierre, M. Unge, M.S. Hedenqvist, A Review of Polyolefin-Insulation Materials in High Voltage Transmission; From Electronic Structures to Final Products, Advanced Materials 36(52) (2024).
[8] A.M. Pourrahimi, C. Pitois, A. Abbasi, XLPE high voltage insulation; A link between DC conductivity and microstructure, Polym Test 131 (2024).
[9] Y.W. Ouyang, A.M. Pourrahimi, I. Östergren, M. Mellqvist, J. Ånevall, A. Soroudi, A. Lund, X.D. Xu, T. Gkourmpis, P.O. Hagstrand, C. Müller, Highly insulating thermoplastic blends comprising a styrenic copolymer for direct-current power cable insulation, High Volt 7(2) (2022) 251-259.
[10] D. Mukherji, Thermal Conductivity of Polymers: A Simple Matter Where Complexity Matters, Macromol Rapid Comm 45(24) (2024).
[11] X. Rodríguez-Martínez, F. Saiz, B. Dörling, S. Marina, J.L. Guo, K. Xu, H. Chen, J. Martin, I. McCulloch, R. Rurali, J.S. Reparaz, M. Campoy-Quiles, On The Thermal Conductivity of Conjugated Polymers for Thermoelectrics, Adv Energy Mater 14(35) (2024).

[12] A.U. Chaudhry, A. Mabrouk, A. Abdala, Thermally enhanced pristine polyolefins: fundamentals, progress and prospective, J Mater Res Technol 9(5) (2020) 10796-10806.
[13] X.F. Wei, Z. Wang, Z.T. Tian, T.F. Luo, Thermal Transport in Polymers: A Review, J Heat Trans-T Asme 143(7) (2021).
[14] T. Zhang, X.F. Wu, T.F. Luo, Polymer Nanofibers with Outstanding Thermal Conductivity and Thermal Stability: Fundamental Linkage between Molecular Characteristics and Macroscopic Thermal Properties, J Phys Chem C 118(36) (2014) 21148-21159.
[15] S.N. Leung, Thermally conductive polymer composites and nanocomposites: Processing-structure-property relationships, Compos Part B-Eng 150 (2018) 78-92.
[16] J.C. Yu, B. Sundqvist, B. Tonpheng, O. Andersson, Thermal conductivity of highly crystallized polyethylene, Polymer 55(1) (2014) 195-200.
[17] X.J. Wang, V. Ho, R.A. Segalman, D.G. Cahill, Thermal Conductivity of High-Modulus Polymer Fibers, Macromolecules 46(12) (2013) 4937-4943.
[18] C.L. Choy, Y.W. Wong, G.W. Yang, T. Kanamoto, Elastic modulus and thermal conductivity of ultradrawn polyethylene, J Polym Sci Pol Phys 37(23) (1999) 3359-3367.
[19] ASTM C177-04: Standard test method for steady-state heat flux measurements and thermal transmission properties by means of the guarded-hot-plate apparatus.
[20] BS EN12939: 2001: Thermal performance of building materials and products - Determination of thermal resistance by means of guarded hot plate and heat flow meter methods - Thick products of high and medium thermal resistance, 2001.
[21] U. Hammerschmidt, Guarded hot-plate (GHP) method: Uncertainty assessment, Int J Thermophys 23(6) (2002) 1551-1570.
[22] ASTM E1461-13: 2022: Standard Test Method for Thermal Diffusivity by the Flash Method.
[23] W.J. Parker, R.J. Jenkins, G.L. Abbott, C.P. Butler, Flash Method of Determining Thermal Diffusivity, Heat Capacity, and Thermal Conductivity, J Appl Phys 32(9) (1961) 1679-&.
[24] ISO 22007-2: 2022: Plastics — Determination of thermal conductivity and thermal diffusivity — Part 2: Transient plane heat source (hot disc) method.
[25] S.E. Gustafsson, Transient plane source techniques for thermal conductivity and thermal diffusivity measurements of solid materials, Rev Sci Instrum 62(3) (1991) 797-804.

[26] S. Yeon, D.G. Cahill, Analysis of heat flow in modified transient plane source (MTPS) measurements of the thermal effusivity and thermal conductivity of materials, Rev Sci Instrum 95(3) (2024).
[27] M.F. Bergstra, P. Denifl, M. Gahleitner, D. Jeremic, V. Kanellopoulos, D. Mileva, P. Shutov, V. Touloupidis, C. Tranninger, Polymerization in the Borstar Polypropylene Hybrid Process: Combining Technology and Catalyst for Optimized Product Performance, Polymers-Basel 14(21) (2022).
[28] S. Veluri, P. Sowinski, M. Svyntkivska, Z. Bartczak, T. Makowski, E. Piorkowska, Structure and Mechanical Properties of iPP-Based Nanocomposites Crystallized under High Pressure, Nanomaterials-Basel 14(7) (2024).
[29] D.A. Ditmars, S. Ishihara, S.S. Chang, G. Bernstein, E.D. West, Enthalpy and Heat-Capacity Standard Reference Material - Synthetic Sapphire (Alpha-Al2o3) from 10 to 2250 K, J Res Nat Bur Stand 87(2) (1982) 159-163.
[30] K. Mezghani, P.J. Phillips, The γ-phase of high molecular weight isotactic polypropylene:: III.: The equilibrium melting point and the phase diagram, Polymer 39(16) (1998) 3735-3744.
[31] K. Mezghani, P.J. Phillips, The gamma-phase of high molecular weight isotactic polypropylene .2. The morphology of the gamma-form crystallized at 200 MPa, Polymer 38(23) (1997) 5725-5733.
[32] J.X. Li, W.L. Cheung, D.M. Jia, A study on the heat of fusion of β-polypropylene, Polymer 40(5) (1999) 1219-1222.
[33] M. Rabiej, S. Rabiej, Application of the artificial neural network for identification of polymers based on their X-ray diffraction curves, Comp Mater Sci 186 (2021).
[34] H. Awaya, Morphology of Different Types of Isotactic Polypropylene Spherulites Crystallized from Melt, Polymer 29(4) (1988) 591-596.
[35] P. Sowinski, X.D. Xu, T. Gkourmpis, P.O. Hagstrand, C. Müller, Highly Ductile Polypropylene Based Ternary Blends for High Voltage Insulation, J Appl Polym Sci 142(22) (2025).
[36] S.P. Andersson, O. Andersson, Thermal conductivity, heat capacity, and compressibility of atactic poly(propylene) under high pressure, Int J Thermophys 18(3) (1997) 845-864.
[37] A. Kiessling, D.N. Simavilla, G.G. Vogiatzis, D.C. Venerus, Thermal conductivity of amorphous polymers and its dependence on molecular weight, Polymer 228 (2021).

[38] A. Eckstein, J. Suhm, C. Friedrich, R.D. Maier, J. Sassmannshausen, M. Bochmann, R. Mulhaupt, Determination of plateau moduli and entanglement molecular weights of isotactic, syndiotactic, and atactic polypropylenes synthesized with metallocene catalysts, Macromolecules 31(4) (1998) 1335-1340.
[39] C. Choy, K. Young, Thermal conductivity of semicrystalline polymers—a model, Polymer 18(8) (1977) 769-776.
[40] Y. Jia, Z.P. Mao, W.X. Huang, J. Zhang, Effect of temperature and crystallinity on the thermal conductivity of semi-crystalline polymers: A case study of polyethylene, Mater Chem Phys 287 (2022).
[41] Y. Guo, Y.J. Zhou, Y.F. Xu, Engineering polymers with metal-like thermal conductivity-Present status and future perspectives, Polymer 233 (2021).
[42] C.L. Choy, Thermal-Conductivity of Polymers, Polymer 18(10) (1977) 984-1004.
[43] D. Hansen, G.A. Bernier, Thermal-Conductivity of Polyethylene - Effects of Crystal Size, Density and Orientation on Thermal-Conductivity, Polym Eng Sci 12(3) (1972) 204-&.
[44] Z. Zeng, P. Sowinski, C. Müller, B. Mihiretie, Liquid Interface for Accurate Intrinsic Thermal Conductivity Measurements of Polymer Films Using the Transient Plane Source Method, Journal of Thermal Science and Engineering Applications 17(11) (2025).
[45] S. Humbert, O. Lame, R. Séguéla, G. Vigier, A re-examination of the elastic modulus dependence on crystallinity in semi-crystalline polymers, Polymer 52(21) (2011) 4899-4909.
[46] B. Crist, C.J. Fisher, P.R. Howard, Mechanical-Properties of Model Polyethylenes - Tensile Elastic-Modulus and Yield Stress, Macromolecules 22(4) (1989) 1709-1718.
[47] M.A. Kennedy, A.J. Peacock, L. Mandelkern, Tensile Properties of Crystalline Polymers - Linear Polyethylene, Macromolecules 27(19) (1994) 5297-5310.
[48] J. Molnár, A. Hertner-Horváth, A. Menyhárd, Prediction of tensile modulus from calorimetric melting curves of polylactic acid with pronounced cold crystallization ability, Polym Test 95 (2021).
[49] J.C. Halpin, J.L. Kardos, Moduli of Crystalline Polymers Employing Composite Theory, J Appl Phys 43(5) (1972) 2235-&.
[50] J.Q. Li, Z. Zhu, T.D. Li, X. Peng, S.F. Jiang, L.S. Turng, Quantification of the Young's modulus for polypropylene: Influence of initial crystallinity and service temperature, J Appl Polym Sci 137(16) (2020).

[51] A. Menyhárd, P. Suba, Z. László, H.M. Fekete, A.O. Mester, Z. Horváth, G. Vörös, J. Varga, J. Móczó, Direct correlation between modulus and the crystalline structure in isotactic polypropylene, Express Polym Lett 9(3) (2015) 308-320.
[52] M. Polinska, A. Rozanski, A. Galeski, J. Bojda, The Modulus of the Amorphous Phase of Semicrystalline Polymers, Macromolecules 54(19) (2021) 9113-9123.

Supplementary Information

Prediction of the thermal conductivity of polypropylenes based on crystallinity or elastic modulus

Przemyslaw Sowinski,[a]* Zijin Zeng,[b] Ewa Piorkowska-Galeska,[c] Besira Mihiretie,[b] Mathis Brette Mortensen,[a] Ergang Wang,[a] Christian Müller[a]*

[a] Department of Chemistry and Chemical Engineering, Chalmers University of Technology, 41296 Göteborg, Sweden

[b] Hot Disk AB, Sven Hultins gatan 9A, Gothenburg, Sweden

[c] Centre of Molecular and Macromolecular Studies, Polish Academy of Sciences, Sienkiewicza 112, Lodz, 90 363, Poland

*e-mail: ;

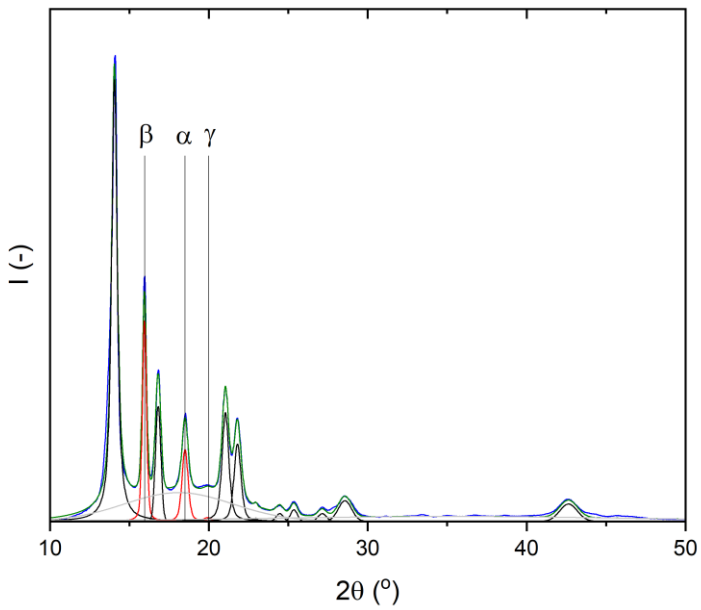

Figure S1. Example deconvolution of a WAXS diffraction pattern using the WAXSFIT program.

Section 1. Deconvolution of WAXS diffractograms.

Parameter optimization was performed using the Rosenbrock method, and peak shapes were fitted using a mixture of Gaussian and Cauchy functions. The background was cut off using a power function. Based on the areas under the individual peaks - $A(110)_\beta$, the content of crystallographic forms (K_α, K_β and K_γ) was calculated according to the following formulas:

$$K_\beta = \frac{A(110)_\beta}{A(110)_\beta + A(110)_\alpha + A(040)_\alpha + A(130)_\alpha + A(117)_\gamma} \quad \text{(S1)}$$

$$K_\gamma = (1 - K_\beta)\frac{A(117)_\gamma}{A(130)_\alpha + A(117)_\gamma} \quad \text{(S2)}$$

$$K_\alpha = (1 - K_\beta)\frac{A(130)_\alpha}{A(130)_\alpha + A(117)_\gamma} \quad \text{(S3)}$$

Section 2. Thermal conductivity measurements

In the TPS method, a sensor composed of a double-spiral nickel foil covered by two thin polyimide films is utilized. This sensor is sandwiched between a pair of samples. The sensor heats up the surrounding material with constant power and the resulting temperature response $\Delta T(t)$ is measured via the resulting change in the resistance of the sensor. Provided the samples are large so that they can be considered as an infinite medium during the measurement, the thermal conductivity κ of isotropic samples is related to the temperature increase of the sensor according to:

$$\Delta T(\tau) = \Delta T_i(\tau) + P\left(\pi^{3/2} r \kappa\right)^{-1} D(\tau) \quad \text{(S4)}$$

where λ is the thermal conductivity of the samples, r is the probe radius, $\tau = r(t\alpha)^{1/2}$ is the dimensionless time, α is the thermal diffusivity of the samples, and $D(\tau)$ is a dimensionless

specific time function [1]. ΔT_i represents the additional temperature increase caused by the thermal resistance between the sample and the sensor, which becomes constant after a short time.

An iterative process can be applied to fit ΔT measured across an appropriate time window ($[t - \Delta t, t + \Delta t]$) using equation S4, which yields values for the two parameters κ and α. Alternatively, if the volumetric heat capacity $C_p = \kappa/\alpha$ is known then α can be replaced so that $\Delta T(\tau)$ only depends on one parameter, i.e. κ, which can be expected to yield more accurate results, which is particularly beneficial for samples with high thermal conductivity.

The probing depth $\Delta P_{prob} = 2\sqrt{t_{max}\alpha}$ where $t_{max} = t + \Delta t$ represents the distance that the heat wave has traveled during the calculation time window. Two requirements concerning ΔP_{prob} should be met for optimal results with small uncertainty. One requirement is that ΔP_{probe} should fall within the range: $1.1\, r < \Delta P_{prob} < 2.0\, r$ to ensure appreciable sensitivity to both λ and α. To fulfill the infinite medium assumption, ΔP_{prob} should also be smaller than the distance between sensor and sample outer boundary, which is 4 mm for our samples.

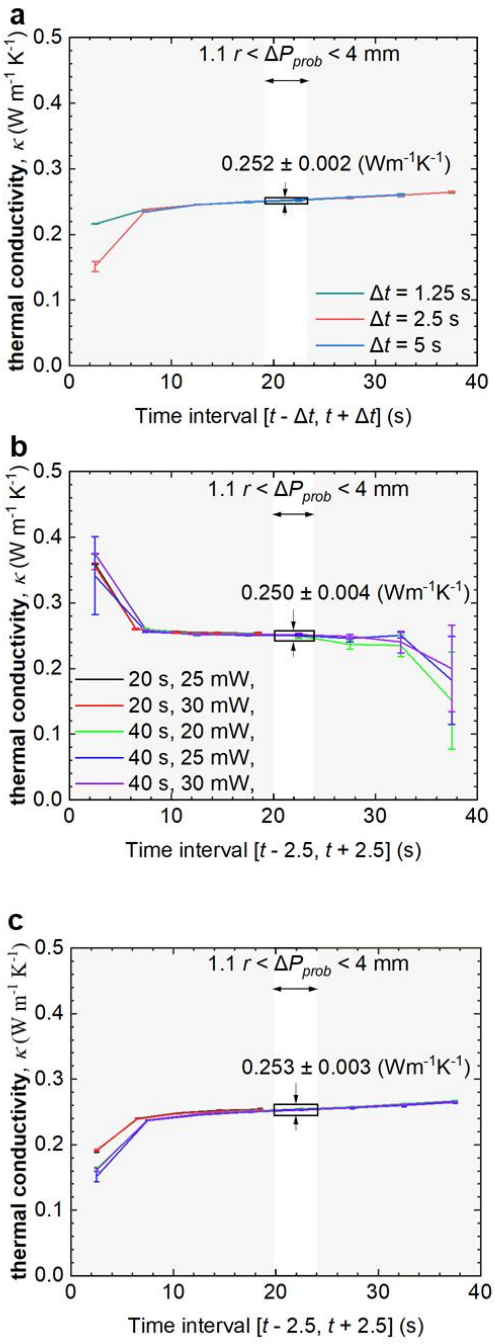

Figure S2. Thermal conductivity κ obtained for different measurement parameters and time windows: (a) influence of time window length $[t - \Delta t, t + \Delta t]$, with Δt ranging from 1.25 to 5 s, on κ obtained from a fit with known C_p; (b) influence of heating power and measurement time on κ from a fit with unknown C_p; and (c) influence of heating power and measurement time on κ from a fit with known C_p; The colored regions indicate the constraints on selection of time windows according to the TPS theory (ΔP_{prob} < 1.1 r in grey; ΔP_{prob} < 4 mm in yellow). The white regions indicate the time range where the constraints $1.1\, r < \Delta P_{prob} <$ 4 mm are fulfilled.

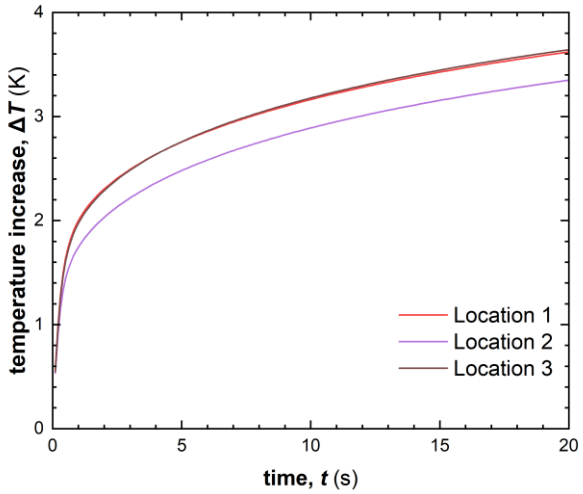

Figure S3. TPS measurements at three different positions on the same plaque of PP5, prepared by -10 °C min^{-1} cooling rate, using the same measurement parameters (20 s, 25 mW), yielding values of κ = (0.2461 ± 0.0001) W m^{-1} K^{-1}, (0.2443 ± 0.0001) W m^{-1} K^{-1} and (0.2447 ± 0.0010) W m^{-1} K^{-1}, yielding a mean value and standard deviation of κ = (0.2450 ± 0.003) W m^{-1} K^{-1}. Although the data magnitude varies due to differences in thermal contact resistance, the calculated thermal conductivity values remain consistent, with only a small standard deviation of 0.3%.

Table S1. Melting temperature T_m, crystallinity X_c, long period L_p, lamellar thickness l_c, $K\alpha$, $K\beta$ and $K\gamma$ crystallographic form content of polypropylenes cooled at $\Delta T/\Delta t$ = -10 or -130 °C min^{-1}; [a]from ref. [2].

	T_m (°C)		X_c (%)		L_p (Å)		l_c (Å)		K_α (%)	K_β (%)	K_γ (%)	K_α (%)	K_β (%)	K_γ (%)
$-\Delta T/\Delta t$ (°C min^{-1})	10	130	10	130	10	130	10	130		10			130	
PP 1	165	169	50	45	183	161	90	71	>99	<1	0	81 ± 1	15 ±3	4 ± 1
PP 2	166	167	58	47	180	135	101	62	>99	<1	0	>96 ± 1	<1	3 ± 1
PP 3	[a]168	169	n.m.	50	n.m.	151	n.m.	73	[a]90 ± 2	0	[a]10 ± 2	100	0	0
PP4	155	155	13	8	n.m.	n.m.	n.m.	n.m.	100	0	0	100	0	0
PP5	165	167	50	45	192	145	110	75	100	0	0	96 ± 1	0	4 ± 1
PP6	166	167	49	40	197	156	112	72	100	0	0	96 ± 1	0	4 ± 1
PP7	163	163	66	54	192	161	124	85	92 ± 1	0	8 ± 1	68 ± 4	0	32 ± 4
PP8	152	154	51	44	165	135	82	57	100	0	0	88 ± 2	0	12 ± 2
PP9	142	144	47	39	n.m.	127	n.m.	48	100	0	0	84 ± 3	0	16 ± 3
PP10	159	158	35	32	171	149	73	58	100	0	0	83 ± 3	0	17 ± 3
PP11	142	146	42	35	172	133	86	56	100	0	0	81 ± 3	0	19 ± 3
PP12	151	150	33	29	180	135	91	60	100	0	0	83 ± 3	0	17 ± 3

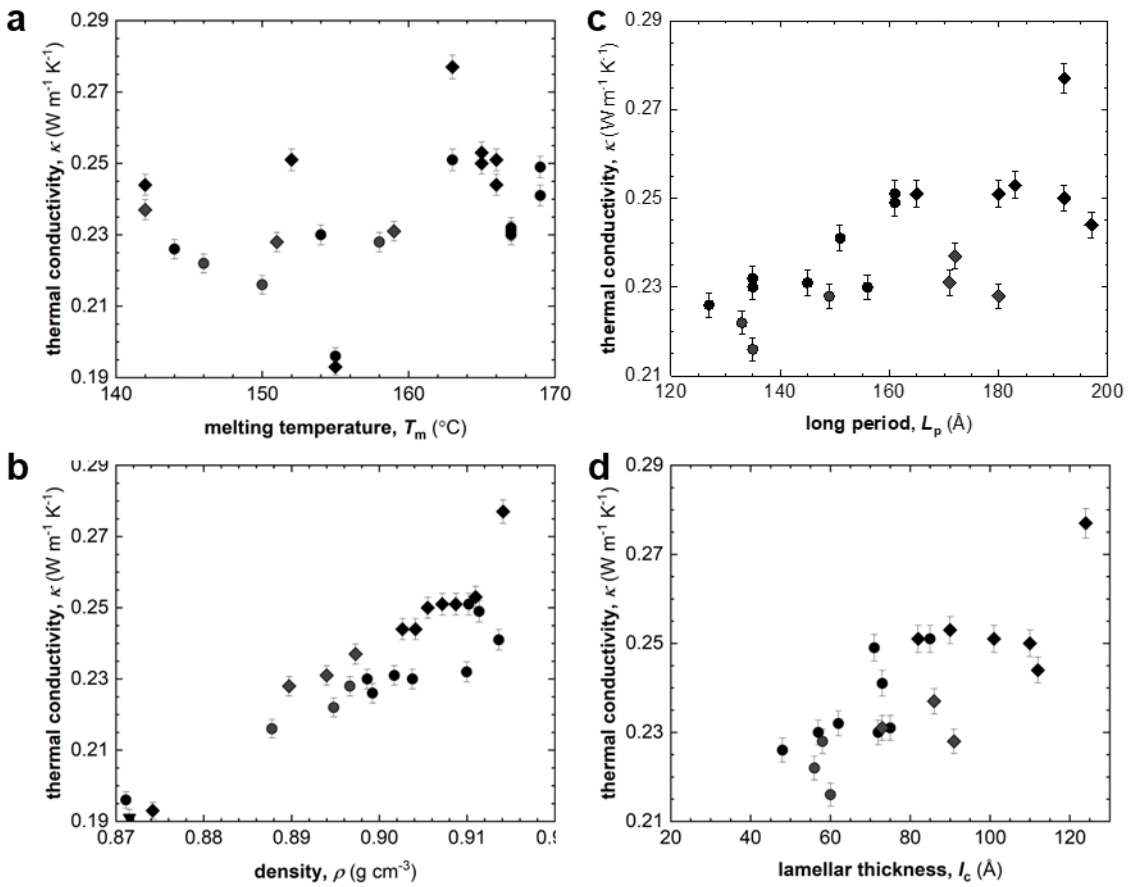

Figure S4. Thermal conductivity κ vs. (a) melting temperature T_m, (b) density ρ, (c) long period L_p, and (d) lamellar thickness l_c of polypropylenes prepared by cooling with -10 ºC min^{-1} (♦) and -130 ºC min^{-1} (●).

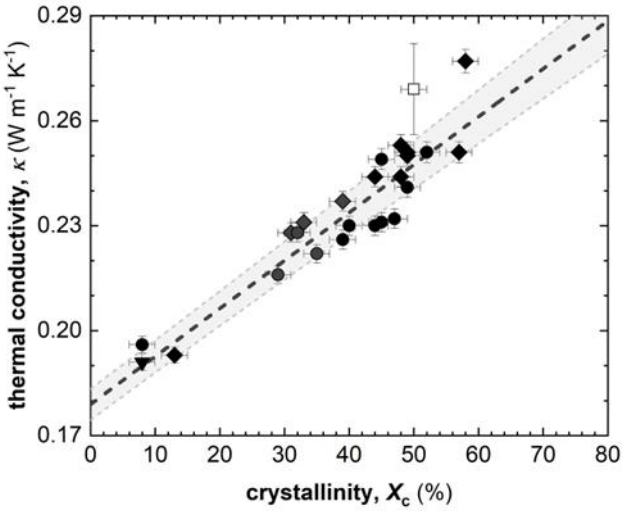

Figure S5 Thermal conductivity κ vs. crystallinity $X_C = \Delta H_m / \Delta H_{m\alpha}^0$ of polypropylenes prepared by cooling with -10 K min^{-1} (♦), -130 K min^{-1} (●) and quenching (▼) and obtained from refs. [3, 4]; the dashed line is a linear fit according to equation 5 and the grey dashed lines are confidence intervals $\kappa \pm \Delta\kappa$ where $\Delta\kappa$ is calculated according to the propagation of errors.

Table S2. Density ρ, heat capacity C_p, Young's modulus E and elongation at break ε_{break} of polypropylenes cooled at $\Delta T/\Delta t$ = -10 or -130 °C min^{-1}.

	ρ (g cm^{-3})		C_p (J g^{-1} C^{-1})		E (MPa)		ε_{break} (%)	
$-\Delta T/\Delta t$ (°C min^{-1})	10	130	10	130	10	130	10	130
PP 1	0.911	0.911	1.97	1.99	1738 ± 126	1458 ± 82	29 ± 4	979 ± 72
PP 2	0.909	0.910	1.89	1.94	1530 ± 120	1096 ± 36	18 ± 2	1021 ± 114
PP 3	n.m.	0.914	n.m.	1.97	n.m.	n.m.	n.m.	n.m.
PP4	0.874	0.871	1.72	2.12	40 ± 4	30 ± 2	27 ± 2	69 ± 9
PP5	0.905	0.902	1.97	1.88	1134 ± 204	862 ± 20	695 ± 187	1044 ± 58
PP6	0.904	0.899	1.93	1.98	1044 ± 30	798 ± 50	920 ± 75	1080 ± 119
PP7	0.914	0.910	1.87	1.91	1586 ± 56	1414 ± 66	736 ± 63	1071 ± 71
PP8	0.907	0.904	1.99	1.92	1034 ± 64	894 ± 38	1180 ± 39	1245 ± 3
PP9	0.903	0.899	2.03	2.02	836 ± 18	668 ± 20	1216 ± 30	1160 ± 92
PP10	0.894	0.897	2.01	2.03	772 ± 14	686 ± 26	1138 ± 21	1111 ± 31
PP11	0.888	0.897	1.87	1.87	642 ± 34	536 ± 36	1198 ± 71	1187 ± 45
PP12	0.890	0.888	2.1	2.12	406 ± 16	316 ± 6	1093 ± 44	1300 ± 63

Reference

[1] ISO 22007-2: 2022: Plastics — Determination of thermal conductivity and thermal diffusivity — Part 2: Transient plane heat source (hot disc) method.
[2] S. Veluri, P. Sowinski, M. Svyntkivska, Z. Bartczak, T. Makowski, E. Piorkowska, Structure and Mechanical Properties of iPP-Based Nanocomposites Crystallized under High Pressure, Nanomaterials-Basel 14 (7) (2024) 629.
[3] P. Sowinski, X.D. Xu, T. Gkourmpis, P.O. Hagstrand, C. Müller, Highly Ductile Polypropylene Based Ternary Blends for High Voltage Insulation, Journal of Applied Polymer Science 142 (22) (2025) e56955.
[4] Z. Zeng, P. Sowinski, C. Müller, B. Mihiretie, Liquid Interface for Accurate Intrinsic Thermal Conductivity Measurements of Polymer Films Using the Transient Plane Source Method, Journal of Thermal Science and Engineering Applications 17 (11) (2025) 111008.